UNIVERSIDAD DE SANTIAGO DE COMPOSTELA

Departamento de Física de Partículas

DETECTION OF HORIZONTAL AIR SHOWERS AND NEUTRINO INDUCED SHOWERS WITH THE PIERRE AUGER OBSERVATORY

Inés Valiño Rielo

Santiago de Compostela, Diciembre 2007.

UNIVERSIDAD DE SANTIAGO DE COMPOSTELA

Departamento de Física de Partículas

DETECTION OF HORIZONTAL AIR SHOWERS AND NEUTRINO INDUCED SHOWERS WITH THE PIERRE AUGER OBSERVATORY

Memoria presentada para optar
al Grado de Doctor en Física por:

Inés Valiño Rielo

Santiago de Compostela, Diciembre 2007

Fdo: Inés Valiño Rielo

Jaime Álvarez Muñiz, Investigador Ramón y Cajal de la Universidad de Santiago de Compostela

CERTIFICA:

que la memoria titulada "Detection of Horizontal Air Showers and Neutrino induced Showers with the Pierre Auger Observatory" ha sido realizada, bajo su dirección, por Inés Valiño Rielo en el Departamento de Física de Partículas de la Universidad de Santiago de Compostela, y constituye el trabajo de Tesis que presenta para optar al grado de Doctor en Física.

Santiago de Compostela, Octubre de 2007

Fdo: Jaime Álvarez Muñiz

Agradecimientos

Mi especial agradecimiento a mi director de tesis Jaime, por su inestimable ayuda, apoyo y amistad. A todos mis compañeros del Grupo de Astropartículas: Ángeles, Dave, Enrique, Gonzalo P., Gonzalo, Iago, Javier, Lorenzo, Patricia, Pedro, Quique, Ricardo, Verónica y Víctor, por su ayuda durante estos años de trabajo.

Quiero también expresar mi agradecimiento al profesor Alan Watson, por su hospitalidad durante mis estancias en Leeds, por su ayuda y sus inestimables enseñanzas durante todos estos años.

Quiero agradecerles a todos los miembros del proyecto "Intersección de Aspectos No-perturbativos y Perturbativos en Física de Solitones y Materia de Alta Densidad y Fenomenología de Astropartículas" dirigido por el catedrático Carlos Pajares por la ayuda económica prestada en la elaboración de este trabajo.

Finalmente quiero dar las gracias a mis compañeros de la facultad de Física, por todos los buenos momentos que hemos pasado juntos: Diego, Elis, Javier, Jose, Néstor y Teresa. A mis amigas Inés, Inma, Isa, Luz, Patricia, Sonia y Sonia Vázquez por todo el ánimo y cariño que siempre me han mostrado. A mi familia y a Juan, por todo su cariño y apoyo.

A mis padres y a Juan.

Contents

List of Figures

List of Tables

Chapter 1

Introduction

The Pierre Auger Observatory is currently the largest cosmic ray observatory. Its goal is to characterize the properties of Ultra High Energy Cosmic Rays (UHECR) with energies above 10^{18} eV in order to understand their origin, mass composition and energy spectrum. The observatory is a hybrid detector combining an array of surface particle detectors and fluorescence telescopes to measure extensive air showers initiated by UHECR at energies greater than 10^{18} eV.

A high energy cosmic ray typically initiates an air shower soon after entering the upper part of the atmosphere, achieving shower maximum at ~ 800 g cm^{-2}. The atmosphere has just the adequate matter depth (~ 1000 g cm^{-2}) so that a vertical shower results in a shower front containing a large number of electrons, positrons and photons (the electromagnetic component) at the ground. As the arrival direction of the cosmic ray increases with the zenith angle, the atmospheric slant depth crossed by the shower rises approximately in proportion with $\sec\theta$. Beyond $\theta = 60^\circ$ the atmospheric slant depth at Auger level increases from 1760 g cm^{-2} to ~ 31000 g cm^{-2} at $\theta = 90^\circ$. As a result, most of the electromagnetic component of showers with $\theta > 60^\circ$, namely horizontal showers, is rapidly absorbed in the atmosphere, and only muons arrive at the ground accompanied by an electromagnetic halo that is mainly due to muon decay. On the contrary, high energy neutrinos might induce an horizontal shower deep into the atmosphere easily identifiable by a significant electromagnetic component at ground. This results in the idea of identifying neutrino showers in the background of horizontal showers initiated by nucleonic cosmic rays.

This thesis is devoted to the study of horizontal (inclined) showers and the capability of the Surface Detector of the Pierre Auger Observatory to detect ultra high energy neutrinos using horizontal down-going showers. The present work is organized as follows: In Chapter 2 we give a brief introduction

to cosmic ray physics and we review some features of air showers, including showers induced by neutrinos. In Chapter 3 we give an introduction to the Pierre Auger Observatory. We describe the reconstruction techniques of the surface detector of the Pierre Auger Observatory and the methods to obtain the cosmic energy spectrum using vertical and horizontal showers. In Chapter 4 we describe a new alternative and fast method to simulate the response of the surface detector. In Chapter 5 we apply the method to the study of the signals in horizontal showers. We study the ratio of the electromagnetic to muonic contributions to the signal in an Auger tank (S_{EM}/S_{μ}). This ratio is used for the energy reconstruction of inclined events. We also study the asymmetries in the ratio S_{EM}/S_{μ} in absence and in presence of the geomagnetic field. In Chapter 6 we develop a criterion to identify neutrino candidates in the data recorded by the surface detector. We describe the algorithms used to select and reconstruct inclined events. We compute the identification efficiencies of the surface detector for neutrino induced down-going showers assuming an ideal infinite array. In Chapter 7 we search for neutrino candidates in the data recorded by the surface detector. We study the potential of the surface detector of the Pierre Auger Observatory to constrain the diffuse flux of UHE neutrinos and we present a prospective upper limit to the diffuse flux of UHE neutrinos assuming a constant with time geometrical area of the surface detector $A = 3000$ km^2 and one year of operation. In Chapter 8 we summarize this thesis and present the main conclusions of this work.

Chapter 2

Ultra High Energy Cosmic Rays

2.1 An overview of the study of Ultra High Energy Cosmic Rays

Cosmic Rays are relativistic particles that are continuously bombarding the Earth's atmosphere from all directions and spanning over a wide range of energies from 10^9 eV to beyond 10^{20} eV.

2.1.1 A brief history of Cosmic Rays

The cosmic ray radiation was discovered almost 100 years ago. At that time, at the beginning of the 20th century, several scientists were very interested in the ionization phenomena and in understanding why a heavily shielded ion chamber still recorded ionization. It was assumed that this was some ionizing radiation associated with the earth's radioactivity, so the detected radiation should be reduced at increasing heights above the ground. However, when Victor Hess and collaborators, in 1912, took ionization chambers in a balloon flight to an altitude about 5 kilometers, it was observed that the amount of radiation increased as the balloon climbed, discovering evidence of a very penetrating radiation coming from outside our atmosphere. This radiation was named "Cosmic Rays" by R.A. Millikan in 1925, and in those days the cosmic rays were supposed to be gamma rays. However, during the 1930s it was found that cosmic rays must be electrically charged particles because of the East-West asymmetry observed in their arrival directions, which is due to the effect of the earth's magnetic field.

During the years before man-made particle accelerators, cosmic rays served

as a source of particles for high energy physics investigations, and led to the discovery of the positron and the muon, among other particles.

In 1938, Pierre Auger and his collaborators, proved the existence of extensive air showers caused by the collision of primary cosmic rays with energies over 10^{15} eV with air molecules, by simultaneously observing the arrival of secondary particles in ground detectors located many meters apart [1].

Studies of extensive air showers continued with increasingly large arrays using different types of detectors recording events with higher energies. The first event with an estimated energy above 10^{20} eV was observed in 1963 [2] by the ground array of scintillation counters of the Volcano Ranch experiment in New Mexico, the first of the giant arrays that have measured the cosmic ray spectrum at the highest energies.

2.1.2 The Cosmic Ray Spectrum and Composition

The energy spectrum of primary protons and nuclei arriving at earth ranges from below 10^9 eV to beyond 10^{20} eV. In Fig. 2.1 we show the differential flux as a function of the primary cosmic ray energy. The differential flux is well described by a power law,

$$\phi = \frac{dN}{dE} \propto E^{-\gamma} \tag{2.1}$$

where γ is the spectral index, which ranges from $\gamma \sim 2.7$ up to an energy of 4×10^{15} eV (called the 'knee') and then changes to $\gamma \sim 3$ between the knee and up to 5×10^{17} eV. In Fig. 2.2 we show a blowup of the cosmic ray spectrum above 10^{17} eV measured by different experiments. Above 5×10^{17} eV, the spectrum seems to steepen to $\gamma \sim 3.2$ up to 3×10^{18} eV (the 'ankle'), after which it flattens to $\gamma \sim 2.7$. The spectral behaviour above 3×10^{19} eV is still being debated with the data collected by the HiRes and AGASA experiments (Fig. 2.1) in clear disagree at the highest energies. HiRes data [4] claims a sharp supression at an energy of 6×10^{19} eV and AGASA data [5] suggest no evidence of this supression. This is perhaps the most puzzling and interesting aspect of UHECR because a cutoff energy is expected at least for extragalactic nucleon primaries (see the next section). The spectrum was also very recently measured with the Surface Detector of the Pierre Auger Observatory (see Chapter 3). The features of the spectral index are usually interpreted in terms of changes in the production mechanism, the origin, the composition or interactions of cosmic rays [6].

The primary composition of the cosmic rays with energies below 10^{14} eV is well known because the flux of cosmic rays is sufficiently large to be measured directly with instruments on balloons and satellites. About 79% of the

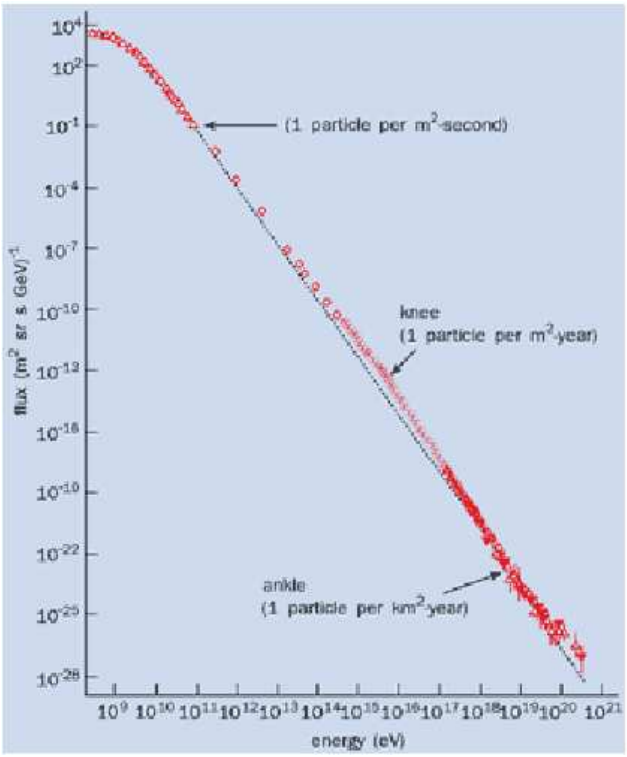

Figure 2.1: *Observed spectrum of primary cosmic rays. See text for a description of the main spectral features.*

primary nucleons are free protons and about 70% of the rest are nucleons bound in helium nuclei [7]. At higher energies, heavier nuclei become more abundant, but the experimental determination of the composition becomes more difficult because the flux decreases rapidly with the energy. For cosmic rays above 10^{14} eV the primary cosmic ray composition can be studied measuring the muon and electromagnetic components of the shower front (see Section 2.2) in the case of ground arrays and measuring the depth of the shower maximum with optical fluorescence detectors. Around the knee the compositional behaviour depends on the assumed interaction model used in the simulations needed for data analysis. Measured events with the fluorescence technique lead to different conclusions than ground particle arrays [8, 9]. A trend towards higher mass primaries [10] through the knee is seen in most experiments when analyzed using the same models. On the basis of composition results from the HiRes Collaboration [11], a transition from heavy to light primary nuclei at an energy around 5×10^{17} eV has recently been proposed, but these predictions are strongly hadronic model depen-

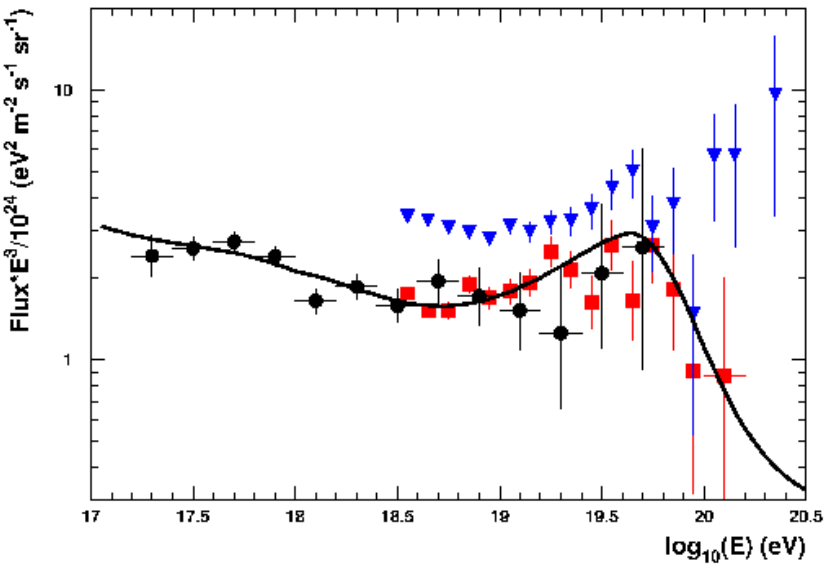

Figure 2.2: *Upper end of the cosmic ray spectrum, multiplied by E^3 to evidence the spectral characteristics. Results from the HiRes-I (circles) and HiRes-II (squares) detectors, and the AGASA experiment (triangles) are shown. The line is a fit to the data assuming a model of galactic and extragalactic sources [3].*

dant and the result was not confirmed by the AGASA experiment. At the highest energies, the composition is completely unknown. Besides the widely adopted assumption that cosmic rays at the highest energies are protons, a number of authors have discussed the possibility of iron nuclei as primaries [12]. Some scenarios of EHECR origin, such as the top-down model in which cosmic rays are massive particle decays, predict the EHECR primaries to be dominated by photons and neutrinos rather than nucleons. These predictions were strongly constrained by recent results of the fluorescence detectors of the Pierre Auger Observatory, a photon limit of less than 16% above 10^{20} eV has been obtained [13].

2.1.3 Propagation and interactions of UHECRs

There is a variety of interactions that cosmic rays can suffer on the propagation from their sources to the earth over large distances through intergalactic matter radiation and magnetic fields. The relevance of each interaction depends on both the cosmic ray origin and the composition.

In the highest energy region, the extragalactic radiation fields relevant for

UHECR interaction include the cosmic microwave background (CMB), the radio background and the infrared and optical background.

For primary protons the main loss processes are the adiabatic losses due to the expanding universe, as well as pair production and photopion production on the CMB. The most important interaction at the highest energies among them being photopion production:

$$\begin{aligned} p + \gamma_{2.7K} &\rightarrow n + \pi^+ \\ &\rightarrow p + \pi^o \end{aligned} \tag{2.2}$$

If the sources are sufficiently distant this process should lead to a cutoff in the spectrum of protons around 4×10^{19} eV. This is known as the GZK cutoff. As a consequence of this the universe becomes opaque to protons with energies above $\sim 10^{20}$ eV on distance scales above ~ 100 Mpc (figure 2.3), that is ultra high energy cosmic ray sources must be relatively close to earth. The actual shape and position of the cutoff in the spectrum would depend on the characteristics of the sources and on their spatial distribution, and also on the cosmic rays composition.

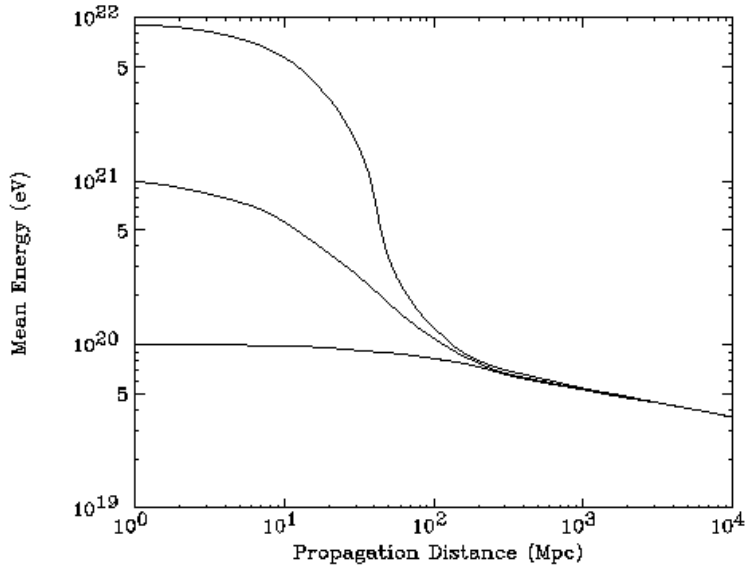

Figure 2.3: *The mean energy of protons as a function of the propagation distance through the CMB. Curves are for different energies at the source (as noted). [14].*

For heavier nuclei the situation is slightly different: the dominant loss processes are photodisintegration in the IR background below $\sim 5 \times 10^{19}$ eV and in the CMB above $\sim 10^{20}$ eV [15].

As in the case of nucleons and nuclei, the propagation of UHE photons and electrons (positrons) is also governed by their interaction with the cosmic photon background. The dominant interaction processes are the attenuation of UHE photons due to pair production on the background of photons ($\gamma\gamma_{2.7K} \rightarrow e^+e^-$) and inverse Compton scattering of the electrons (positrons) on the background photons.

The propagation of UHE neutrinos is governed by the interaction with the theoretically expected relic neutrino background (RNB). The dominant interaction mode of UHE neutrinos with the RNB is the exchange of a W^+ boson in the t-channel ($\nu_i\overline{\nu}_j \rightarrow l_i\overline{l}_j$), or of a Z^o boson in either the s-channel ($\nu_i\overline{\nu}_i \rightarrow f\overline{f}$) or the t-channel ($\nu_i\overline{\nu}_j \rightarrow \nu_i\overline{\nu}_j$). The neutrino-nucleon interactions are negligible compared to interactions with RNB because the RNB particle density is about 10 orders of magnitude larger than the baryon density.

In addition to the interactions with the radiation fields permeating the universe, charged cosmic rays suffer deflections on extragalactic and Galactic magnetic fields. There are different regimes of propagation depending on the strength of the magnetic field, the CR composition and the cosmic ray energy considered. The two extreme limits correspond to rectilinear propagation and diffusive propagation corresponding to the high and low energy limits respectively. Assuming an intergalactic field of 1 nG, a proton of 10^{18} eV would have no memory of its source direction after travelling 10 kpc. However, a proton of 10^{20} eV will not be deviated more than $\sim 3^\circ$.

A complete review of the propagation and interactions of UHECR can be found in [16]

2.1.4 Origin of the bulk of cosmic rays

The question of the origin of the highest energy cosmic rays continues to be regarded as an "unsolved problem". In the following, the two main proposed models to produce cosmic rays at high energy are briefly explained. They can be divided in two general categories: 'bottom-up' and 'top-down' models.

Acceleration Mechanisms and possible sources

In the 'bottom-up' scenario the possible acceleration sites are astrophysical objects. One of the most important proposed acceleration mechanisms is based on a theory introduced by Fermi [18] for the acceleration of particles in magnetized gas clouds ('second order Fermi process'). A more efficient version of the Fermi mechanism is named 'first order Fermi process', in which cosmic rays are accelerated up to $E_{max} \sim 10^{21}$ eV in diffusive shock waves

[19, 20, 21]. The medium in which these shock waves propagate can be the interstellar medium itself or the material resulting from a previous explosion, such as a supernova explosion.

The maximum energy achieved in diffusive shock , E_{max}, acceleration strongly depends on the size and the magnetic field strength in the medium where the shock was propagates. The value of this maximum energy can be estimated by requiring that the gyroradius of the particle be contained in the acceleration region. The condition is summarized in the following expression:

$$E_{max} = kZeBL\beta \tag{2.3}$$

where B (in μG) is the magnetic strength field in the region of the shock, L (in kpc) is the size of the accelerating object, Ze is the electric charge of the accelerated particle and β is the shock speed (in units of c) and $k < 1$. Using the previous relationship, Hillas produced a plot of B vs L to show that very few objects satisfy the conditions needed to achieve the maximum energy [17]. In Fig. 2.4 we show the Hillas plot for $E_{max} \geq 10^{20}$ eV and $Z \simeq 1$. The only known astrophysical sources that are able to accelerate protons to $E \geq 10^{20}$ eV are neutron stars, active galactic nuclei (AGN), radio lobes of AGN and clusters of galaxies. In the case of iron, there are other sources like the galactic halo or extreme white dwarfs. The Hillas plot does not include the effect of energy losses in the accelerating region such as synchrotron radiation in the magnetic field and production of secondary particles, that compete with the acceleration mechanism.

Non-accelerating origin of cosmic rays above 10^{20} EeV

In the 'top-down' scenarios, cosmic rays are generated by the decay of very massive particles (generically, called X particles), $m_X > 10^{20}$ eV, that could have been originated from high-energy processes in the early universe. These X particles typically decay to quarks and leptons. The quarks hadronize producing jets of hadrons, that contain mainly light mesons (pions) with a small percentage of baryons (mainly nucleons). The pions decay to photons, neutrinos (and antineutrinos) and electrons (and positrons). Thus, energetic photons, neutrinos and charged leptons, together with a small fraction of nucleons, are produced directly with energies up to $\sim m_X$ without any acceleration mechanism.

In order for the decay products of the X particles to be observed as UHECR particles today , three basic conditions must be satisfied [16]: (a) the X particles must decay at non-cosmological distances (≤ 100 Mpc), otherwise the decays products of the X particles lose all their energy in interactions with the background radiation and do not survive as EHECR particles; (b)

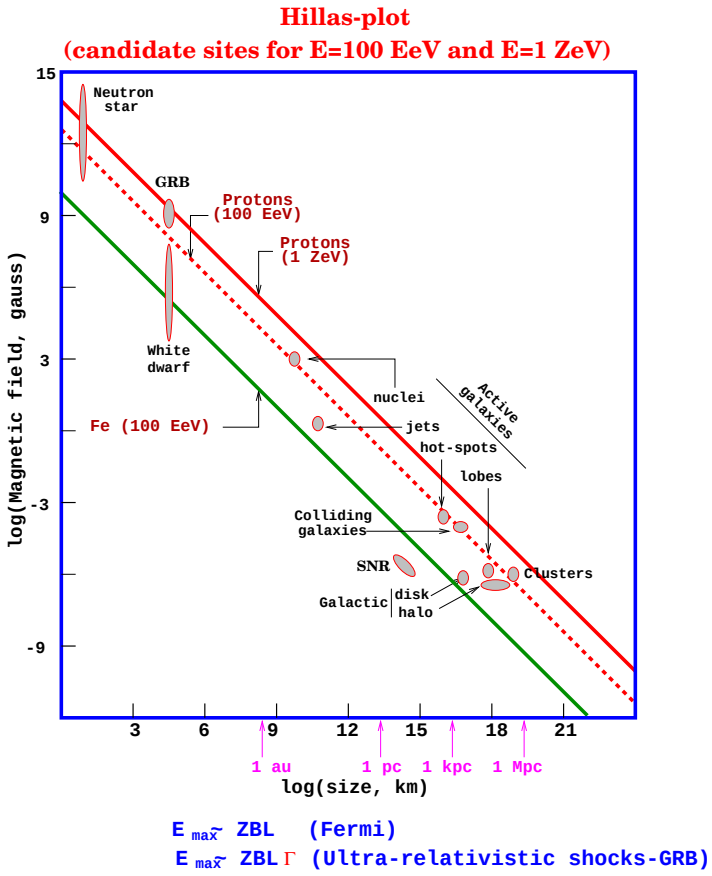

Figure 2.4: *The Hillas plot shows the size and magnetic field strength of astrophysical objects that are candidate sites of cosmic ray acceleration at* 10^{20} *eV. Objects below the diagonal line can not be sources of ultra high energy cosmic rays.*

these particles must be sufficiently massive $m_X >> 10^{20}$ eV; (c) the number density and rate of decay of X particles must be large enough to produce a detectable flux of UHECRs. There are basically two ways of generating X particles that decay at the present time: (1) producing them in the decays of topological defects; (2) making them quasi-stable in the early universe.

2.2 Extensive Air Showers and measurement techniques

Direct observation of cosmic rays is only possible from space by flying detectors with balloons or spacecrafts. Such detectors are very limited in size and because of the steeply falling energy spectrum, direct observations run out

of statistics typically around 10^{14} eV.

Above 10^{14} eV the flux of cosmic rays decreases so much that cosmic rays must be detected indirectly, by observing the shower of secondary particles created in the inelastic collision of the primary cosmic ray with the atmosphere and subsequent interactions. In the collision of a single high energy particle with an atmospheric nucleus of an air molecule (such as nitrogen and oxygen), its energy is distributed among the secondary particles. Then, these products and the remnant cosmic ray continue to propagate and produce after several generations an extensive air shower (EAS). Extensive air showers can be electromagnetic or hadronic depending on the nature of the primary particle.

2.2.1 General features of air showers

A helpful tool to visualize the main features of an extensive air shower development was given by Heitler [22] through a 'Toy Model'. He introduced it in the context of a discussion of purely electromagnetic showers, but its basic structure also applies to air showers initiated by hadrons [23].

In Heitler's approach the particle cascade is seen as a sequence of generations via branching processes. At each generation, each particle undergoes a splitting process into two other particles after traveling a path length (λ), each of them carrying half of the progenitor energy. The splitting continues until the average particle energy is reduced to the critical energy E_c, where the number of particles is maximum (N_{max}) and no more interactions take place. After this, the particles only lose energy or get absorbed.

The model displays the two most important features of air showers: the depth of the shower maximum, X_{max}, depends on the primary energy in a logarithmic way:

$$X_{max} = \lambda \, ln(E_0/E_c)/(ln2) \tag{2.4}$$

and the number of particles at shower maximum, N_{max}, is proportional to the primary energy:

$$N_{max} = E_0/E_c \tag{2.5}$$

Showers induced by proton or nucleus

In an hadronic shower induced by a baryon, typically more than 80% of the particles produced in the first interaction are pions (the rest of particles are kaons, other mesons, hyperons and nucleon-antinucleon pairs). If the secondary hadrons are sufficiently energetic they will themselves initiate new hadronic interactions, produce secondaries and build up a hadron cascade that forms the core of the extensive air shower. Unstable particles such as

pions, kaons and another particles will sometimes decay depending on their energy.

The neutral pions π^os (roughly a third of all the pions produced) have a mean lifetime of 10^{-16} s and so will nearly always decay, except at the most extreme energies (above $\sim 10^{18}$ eV). The most common decay mode is into 2 photons (and electron-positron pairs for a small fraction of the decays), these photons produce an electromagnetic subshower through two processes: photons undergo pair production and electrons/positrons radiate bremsstrahlung photons. The size of the shower grows until the mean energy of the electrons reaches the critical energy ($\sim$ 84 MeV in air) at which the energy losses by ionization and bremsstrahlung are equal. At this shower stage, approximately 90% of the total energy is carried in the electromagnetic cascade. Below the critical energy, the ionization losses overcome bremsstrahlung, and the electromagnetic cascade will begin to die out.

Electrons and positrons in electromagnetic showers suffer multiple scattering, which is mostly going to determine the main features of the transverse structure of these cascades.

Charged mesons, because of a larger mean lifetime (10^{-8} s), not only decay but also interact strongly with atmospheric nuclei. The competition between the two processes depends essentially on the balance between the interaction mean free path (dependent on the cross-section and the density of the medium traversed) and the mean decay length. Both vary substantially with energy and become equal at an energy of $\sim$ 115 GeV for charged pions and $\sim$ 850 GeV for kaons [24]. Thus, at lower energies than these the decay probability is larger than the interaction probability.

Charged pions and kaons give rise to muons and muon-neutrinos in the shower mostly through the following decay modes:

$$\begin{aligned} \pi^{\pm} &\rightarrow \mu^{\pm} + \nu_{\mu} \quad (99.9\%) \\ K^{\pm} &\rightarrow \mu^{\pm} + \nu_{\mu} \quad (63.5\%) \\ &\rightarrow \pi^{\pm} + \pi^{0} \quad (21.2\%) \end{aligned} \tag{2.6}$$

Neutrinos are weakly interacting particles that escape carrying roughly $\sim$ 2% of the primary energy.

Muons are nearly relatively and have a small cross-section for interactions, so they are very penetrating. This component increases its size as the shower develops to reach a plateau that slowly attenuates, because muons mainly lose energy gradually by ionization ($\sim$ 2 MeV/g cm^{-2} in air), bremsstrahlung, electromagnetic and hadronic interactions with nuclei and pair production at very small rate compared to electrons. The radiative processes are only dominant at high energy ($>$ 500 GeV).

Muons are affected by decay in flight when their energies have become quite low (typically below tens of GeV) through the following modes:

$$\begin{aligned} \mu^- &\rightarrow e^- + \overline{\nu}_e + \nu_\mu \\ \mu^+ &\rightarrow e^+ + \nu_e + \overline{\nu}_\mu \end{aligned} \tag{2.7}$$

Muon decay is another source of secondary neutrinos.

So, an air shower induced by a baryon can be understood as a core of high energy hadrons that is continuously feeding an electromagnetic component (electrons, positrons, and photons) mainly through π^0 decay, and both a muonic and a neutrino component through charged pion decay. This is schematically presented in figure 2.5

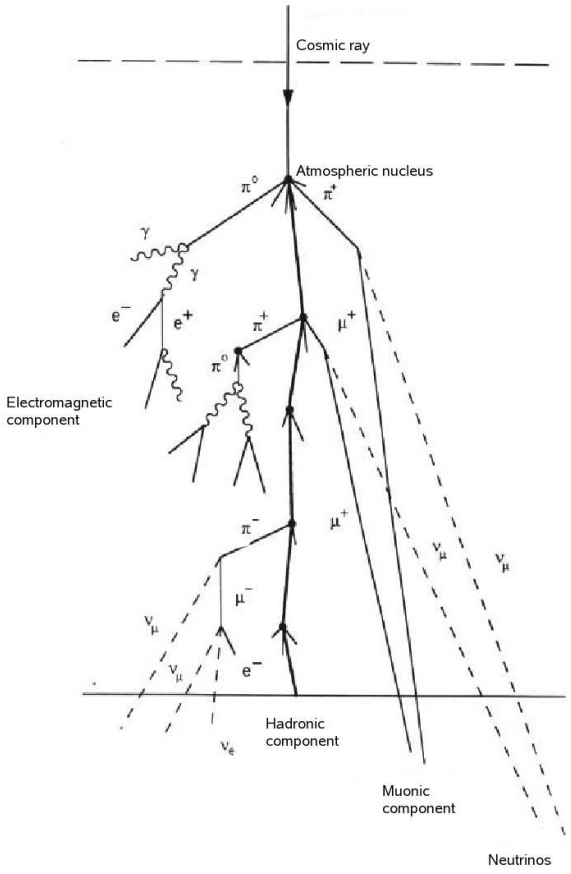

Figure 2.5: *Schematic representation of an hadronic extensive air shower.*

A simplified view of the interaction of a cosmic ray nucleus with the atmosphere is given by the superposition model [25]. A shower induced by a

nucleus with atomic number A develops like a superposition of A independent nucleon air showers all starting at the same point, each carrying $1/A$ of the primary energy. These showers from lower energy primaries do not penetrate as deeply. So, the nucleus shower reaches its maximum size higher in the atmosphere than a proton shower of the same total energy. The resulting shower has more muons than a proton shower at the same total primary energy because pions are produced higher and they are more likely to decay before interacting. For example, an iron shower has ~ 1.8 times as many muons as a proton shower of the same energy and its X_{max} is higher than proton showers by ~ 150 g cm^{-2} at all energies [23].

Showers induced by gamma rays

A shower induced by gamma rays shows slightly different features than a shower induced by a baryon. As figure 2.6 illustrates, it is a purely electromagnetic shower where the dominant processes are pair production and bremsstrahlung in the manner described previously and its behaviour can be accurately predicted from quantum electrodynamics.

At energies above 10^{19} eV, there are other important processes that need to be taken into account. The LPM effect (Landau-Pomeranchuk-Migdal) becomes important reducing the cross-sections for pair production and bremsstrahlung. Additionally, photon interactions with the geomagnetic field induce pair production before entering the atmosphere what effectively reduces the energy of the particles that interact in the atmosphere, which to a large degree compensates for the LPM effect in the final of shower observables.

Shower longitudinal profiles

The longitudinal profile of a shower is the number of charged particles as a function of the atmospheric depth. The longitudinal profile of an electromagnetic shower is quite accurately given by the Greisen formula [26]:

$$N_e(E_0, t) = \frac{0.31}{\sqrt{t_{max}}} \exp\left[t\ (1 - 1.5\ \ln s)\right] \tag{2.8}$$

where t is the atmospheric slant depth measured in radiation lengths ($t = X/X_0$), $t_{max} = \ln(E_0/E_c)$, and s is the shower age: $s \approx \frac{3t}{t+2t_{max}}$. Many shower properties are well parametrized by the shower age. For a given initial energy, the number of shower particles increases with depth when $s < 1$, reaches a maximum when $s = 1$ and declines when $s > 1$.

In the case of hadronic air showers, it is very hard to describe the shower development using an analytical approach. Monte Carlo simulations can be

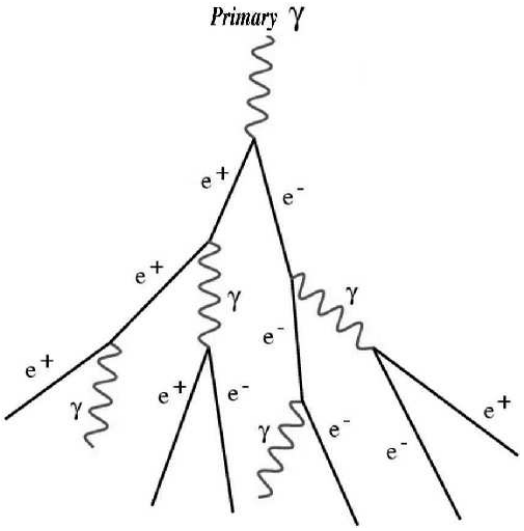

Figure 2.6: *Schematic representation of an electromagnetic extensive air shower.*

performed to model it, but the lack of empirical knowledge of the physical processes which occur at high energies, leads to discrepancies between different models. Laboratory experiments have studied particles collisions (cross sections, inelasticity and multiplicity) only at centre-of-mass energies equivalent to fixed target energies of 10^{15} eV (in the rest frame of one particle), so the results must be extrapolated to the energies of interest 10^{20} eV and assumptions must still be made. Another problem, even at lower energies, is that the interactions are primarily 'soft' interactions, with a low transfer of transverse momentum (P_t) and studies made at accelerators deal primarily with high P_t particles, where the collision fragments are deflected at large angles into the detectors. An experiment is currently under construction at LHC with capability to measuring very forward particles (TOTEM [27, 28]) and may provide important data to help to refine the current models.

The Gaisser-Hillas functional form [29], based on Monte Carlo simulations using the scaling model for nuclear interactions, has proved to be effective in fitting the longitudinal profile of simulated air shower developments resulting from various hadronic models with variable primary masses. The Gaisser-Hillas functional form is:

$$N(X) = N_{\max} \left(\frac{X - X_0}{X_{\max} - X_0} \right)^{\frac{X_{\max} - X_0}{\lambda}} \exp \left(\frac{X_{\max} - X}{\lambda} \right) \qquad (2.9)$$

The four parameters $(N_{max}, X_{max}, X_0, \lambda)$ provide ample size and shape

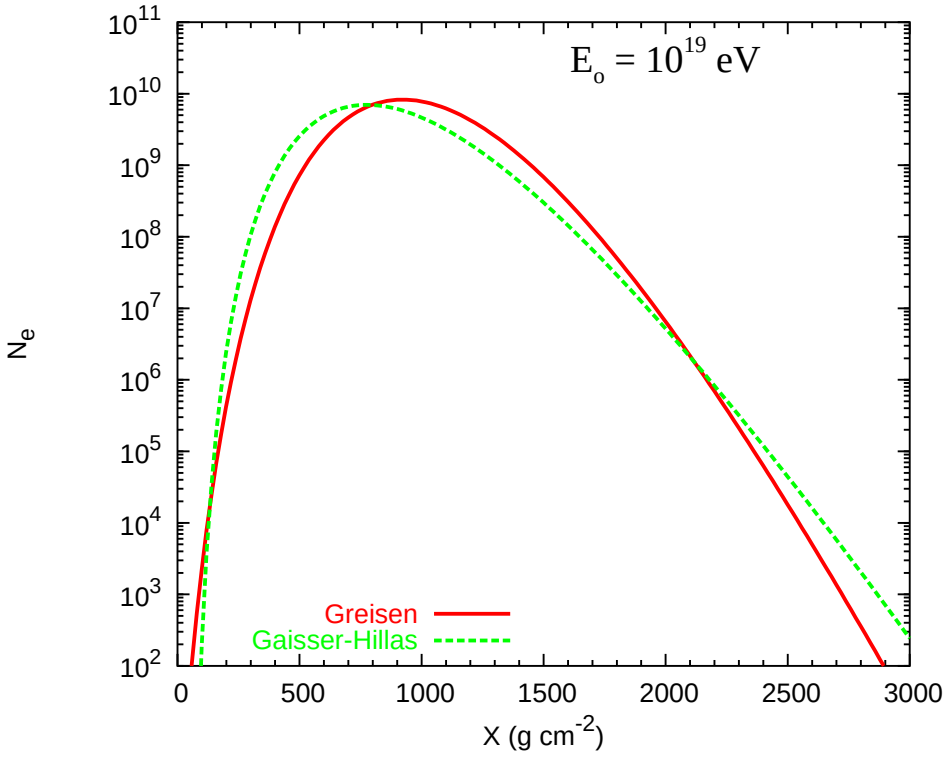

Figure 2.7: *Longitudinal profile of a purely electromagnetic air shower using the Greisen function 2.8 (continuous line) and profile of an hadronic air shower using the model of Gaisser-Hillas 2.9 (dashed line) .*

freedom for fitting longitudinal profiles.

As illustrated Fig. 2.7, the development of a hadronic shower at high energy tends to be faster than that of an electromagnetic shower due to the high inelasticity and multiplicity of hadronic interactions that distribute the primary energy among many particles. Moreover, after the maximum the hadronic shower has a slower attenuation because the electromagnetic component is being fed continuously into the shower by the hadronic core.

Lateral distribution of shower particles

The extensive air shower also develops transversally mainly due to electromagnetic and muonic particles spreading away from the shower axis. Energetic secondary hadrons have transverse momenta that are typically very small compared to their longitudinal momentum. They travel close to the shower axis and essentially are confined in a cylinder around the axis because of decay. In the case of pions, the cylinder radius is less than ~ 22 m

[30].

Electromagnetic particles spread away from the axis primarily by multiple Coulomb scattering of electrons and positrons, and also because of the spreading angles in pair production and bremsstrahlung, which become negligible at high energies. The spread due to Coulomb scattering is given in terms of the Molière radius (r_M), which varies inversely with the density in the medium and it is of the order 100 m at the Auger altitude.

For pure electromagnetic vertical showers, Nishimura and Kamata, and later Greisen, obtained the well-known NKG formula [31, 26] which gives the charged particle density as a function of the distance from the shower axis depending on shower age, s_{NKG},

$$\rho_e = \frac{N_e}{\pi\ r_M^2} \frac{\Gamma(4.5 - s_{NKG})}{\Gamma(s_{NKG})\Gamma(4.5 - 2s_{NKG})} \left(\frac{r}{r_M}\right)^{s_{NKG}-2} \left(1 + \frac{r}{r_M}\right)^{s_{NKG}-4.5} \tag{2.10}$$

where N_e is the total number of electrons.

The NKG formula may also be extended to describe the electromagnetic component of hadronic induced showers by modifying the exponents in Eq. (2.10). Fits to the lateral distribution functions (LDF) of electrons and positrons obtained from simulations as a function of depth (t) yield an age parameter given by $s = \frac{3t}{t+2\beta}$, where the floating parameter β takes into account the deviations from the electromagnetic shower theory in where it is simply the age s_{NKG}.

The modified NKG formula provides a good description of the electromagnetic lateral distribution at all stages of shower development for distances sufficiently far from the hadronic core.

Muons are relatively unaffected by multiple Coulomb scattering, and so their lateral distribution function retains information on the primary interactions in the shower. Muons are distributed in a broader lateral region than electromagnetic particles, and their number does not decrease as rapidly as the shower grows old. The lateral spread of muons is determined by the properties of the hadronic interactions, decays, distances to production point and geomagnetic effects.

There is no standard functional form for the lateral distribution of the the muonic component. One of the earliest parameterizations of the muon LDF in vertical showers was empirically derived by Greisen [26],

$$\rho_\mu(r) = N_\mu(t) f_\mu(r) \approx N_\mu(t) \left(\frac{r}{r_G}\right)^{-0.75} \left(1 + \frac{r}{r_G}\right)^{-2.5} \tag{2.11}$$

where $f_\mu(r)$ is a structure function describing the lateral shape of the shower, and $r_G = 320$ m is analogous to the Moliére radius. Later, Vernov et al proposed an analytical form of the structure function:

$$f_\mu(r) \approx \left(\frac{r}{r_0}\right)^{-\Gamma} \exp\left(\frac{r}{r_0}\right) \tag{2.12}$$

with $\Gamma = 0.4$ and $r_0 = 80$ m.

The LDFs are used to fit experimental data. However, neither function reproduces the whole radial range (distances from the core) of an extensive air shower.

For the case of inclined (horizontal) showers, the muonic lateral distribution is not azimuthally symmetric about the shower axis because of geomagnetic deviations and geometrical and attenuation effects. For very inclined showers the geomagnetic field effect in the muon LDF becomes dominant. A quantitative description of this effect can be found in [32].

2.2.2 Detection Techniques

The classical method of detection of extensive air showers is to use a number of particle detectors distributed over the ground surface to sample the flux of secondary particles at different points of the shower front. This procedure is based on developments of the technique used by P. Auger and his collaborators in their pioneering work [1] leading to the discovery of air showers. Surface arrays include arrays of muon detectors (e.g. SUGAR), scintillators (e.g. Volcano Ranch, Yakutsk and AGASA), and water Cherenkov tanks (e.g. Haverah Park and Auger).

Surface arrays determine the arrival direction of the incoming cosmic ray by recording the relative time at which each detector triggers. The directional precision is limited by the accuracy of the timing measurement, by the sampling area of the detector and by intrinsic fluctuations. The signals collected in the detectors (lateral distribution) can be used to estimate the energy from comparisons with detailed Monte Carlo simulations. Simulations predict the relation between energy and particle density.

A surface array has sensitivity to the primary mass through direct or indirect measurement of the muon and electromagnetic content of the shower and/or indirect measurement of X_{max} (depth of the electromagnetic shower maximum) [33]. Muon counters placed underground can be used to measure directly the muon component.

Scintillator arrays and arrays of water Cherenkov tanks differ in their methods for studying the primary mass distribution. The first are essentially

sensitive to the electrons and positrons of the electromagnetic shower which dominate the charged particles. It can be used to estimate X_{max} by measuring the shape of the LDF. In general a deeper X_{max} will result in a steeper LDF. This gives the opportunity of measuring the fluctuations in X_{max} by measuring the fluctuations in the observed LDF. Its sensitivity is limited by statistical fluctuations of the signal, due to the finite number of incident particles on a limited detector area.

An array of water Cherenkov tanks is roughly equally sensitive to both muons and electromagnetic particles. The most promising mass indicator is the time structure of the signal. Since the muons suffer less Coulomb scattering, they tend to arrive earlier than the electromagnetic component at large core distance. Heavy nucleus showers have a larger muon component, and a fast shower development that leads to less electromagnetic tails [34]. The predicted muon component is very dependent on the multiplicity of hadronic interactions, so this leads to strongly discrepancies between different models ($\sim 40\%$ in number of muons for the same primary).

The second class of air shower detectors are those that record radiation from the shower front as it traverses the atmosphere. Those include fluorescence detectors (e.g. Fly's Eye, HiRes, Auger), air Cherenkov detectors (e.g. HEGRA [35]) and advanced radio frequency antenna arrays (e.g. the LOPES array).

The fluorescence detectors record the fluorescence light ($\lambda \sim$ 300-400 nm) emitted by deexcitation of nitrogen molecules previously excited by the electromagnetic particles traversing the atmosphere. The shower development appears as a rapidly moving spot of light describing a great circle path across the night sky. The fluorescence light is emitted isotropically with an intensity that is proportional to the number of charged particles in the shower. The efficiency of production is very low (about 4 photons per meter of track of ionizing particle), hence only high energy cosmic rays ($> 10^{17}$ eV) can be observed from large distances. Furthermore, observations can only be done in clear moonless nights, resulting in an average 10% duty cycle.

A fluorescence detector consists of a light collector system (mirrors) used to concentrate the fluorescence and several photomultipliers (PMT) that detect the light focused by the mirrors. The timing information and amplitude from the signals together with the pointing direction of the PMTs are used to reconstruct the arrival direction and the longitudinal shower profile. The integral of the longitudinal profile is a direct measurement of the energy deposited by the electromagnetic component of the shower in the atmosphere. The attenuation of the light beam in the atmosphere must be taken into account to determine the energy resolution. The beam attenuation may be due to a combination of absorption and scattering, such as Rayleigh and

Mie scatterings. In addition, the fluorescence method allows to estimate the primary mass by direct measurement of the maximum depth of the shower. The best resolution is obtained when a shower is detected in *stereo*, that is simultaneously by two fluorescence detectors.

Air Cherenkov detectors work at lower energies, detecting the Cherenkov light emitted by the shower particles before they get absorbed in the atmosphere [36]. These detectors are like ordinary telescopes instrumented with a PMT in the focal plane, sensitive to very small number of photons.

The radio technique detects radio-frequency pulses associated with extensive air shower with antennas [37, 38].

2.3 Extremely High Energy Neutrinos and their detection

Cosmic neutrinos provide an unique window on astrophysical processes because they escape from dense regions and typically propagate to the Earth unhindered. Identifying neutrinos among regular cosmic rays at extreme energies would be a great step towards explaining the origin of cosmic rays, but their detection constitutes a real challenge mainly because of their low interaction cross-sections.

2.3.1 Candidate production mechanisms of EeV neutrinos

Several mechanisms have been proposed to explain the origin of EHE neutrinos [39]. All mechanisms also produce UHECR. One of them is the GZK mechanism, where the neutrinos above 10^{18} eV can be produced by photopion production in interactions of EHE cosmic ray nucleons and the cosmic microwave (2.7 K) background photons (CMB) during propagation in intergalactic space. These neutrinos are a direct result of the GZK cutoff and must be produced by high energy cosmic protons of extragalactic origin. Their flux depends heavily on assumptions about the evolution of the cosmic ray sources with cosmological time.

Other candidates sources are astrophysical objects where the protons (or nuclei) can be accelerated and interact by pp or $p\gamma$ producing high energy pions. These include galactic sources as accretion in binary system, supernova remnants,..etc, but those reaching to highest energies are likely to be extragalactic. Active galactic nuclei (AGN) are considered as possible extragalactic acceleration sites for high energy ν production [40]. The energy loss

of the accelerated proton due to pp or $p\gamma$ interactions in the AGN accretion disk or with UV photons in the associated jets are the dominant mechanisms for neutrino production. AGNs can produce EHE neutrinos with energies above 10^{19} eV or greater depending on the proton maximum energy. Gamma Ray Bursts (GRB) are other promising candidate sources of EHE neutrinos [41].

The speculative and exotic models proposed are the production of EHE neutrinos in the annihilation or collapse of topological defects (TD) such as monopoles, cosmic strings, etc [16]. This mechanism predicts EHE neutrinos beyond 10^{20} eV.

2.3.2 Neutrino detection

Up to now, the only directly observed extraterrestrial neutrinos are low energy (MeV-range) neutrinos (from the Sun [42] and Supernova SN1987A [43]). The challenge is the detection of higher energy neutrinos, this can open a new window of astronomy and improve our understanding of fundamental physics. Neutrinos offer several advantages over traditional astronomical messengers. First, they are weakly interacting, so they can travel cosmological distances without being scattered or absorbed. Moreover, they are electrically neutral, so they are not deflected by interstellar magnetic fields.

TeV-PeV neutrinos

The peculiar behaviour of the neutrino interactions has important implications for their detection. The dominant interaction mechanism for neutrinos at $E_\nu > 10^{11}$ eV in matter is deep inelastic scattering (DIS) on nucleons:

$$\nu_l + N \rightarrow l + X \tag{2.13}$$

where l is the lepton flavour, N is the hit nucleon and X represents the outgoing hadron(s).

High energy neutrinos in the TeV-PeV range are detected using large underwater/ice telescopes. These telescopes consist of large volumes of water or ice that are instrumented with PMTs to detect the Cherenkov light from the leptonic product of the interaction (see Eq. 2.13). Among the different flavours, muon detection is favoured because muons take on average $60-70\%$ of neutrino energy [44] and μ-ranges can reach several kilometers enhancing the interaction volume. The determination of the muon direction allows to select muons that travel upwards induced by neutrino interactions, from the down-going muons of air showers. The background is negligible provided that the detector is deep enough and has angular resolution. Muon detection

allows neutrino astronomy because at high energy, the muon track is almost colinear to the interacting neutrino.

Several experiments have been proven the feasibility of these detectors measuring the atmospheric neutrino spectrum at TeV energies without observing an extragalactic contribution: BAIKAL [45] using water of lake Baikal, ANTARES in the Mediterranean sea [46], and AMANDA using the Antarctic ice [47]. These are small scale neutrino telescopes. The first gigaton scale detector will be IceCube, it is being constructed using the AMANDA technique and has already recorded data [48]. Other projected telescopes will use the sea, in particular the Mediterranean, because it offers available depths up to 4000 km and even more. A few projects are being planned: NESTOR [49] and NEMO [50].

EeV neutrinos

Above 1 PeV the Earth becomes opaque to neutrinos and only down-going or Earth-skimming EeV neutrinos can be detected. The challenge lies in the identification of these showers among the background of down-going cosmic rays and atmospheric muons.

Down-Going neutrino-induced air shower

In the collision of a neutrino in the Earth's atmosphere, there are multiple channels to produce down-going ν-induced showers:

- charged current interactions with atmospheric nuclei:

$$(\nu_l, \overline{\nu}_l) + N \rightarrow (l^-, l^+) + X \tag{2.14}$$

- neutral current interactions with atmospheric nuclei:

$$(\nu_l, \overline{\nu}_l) + N \rightarrow (\nu_l, \overline{\nu}_l) + X \tag{2.15}$$

- $\overline{\nu}_e$ resonant interactions with atmospheric electrons:

$$\overline{\nu}_e + e^- \rightarrow W^- \tag{2.16}$$

For instance, at the highest energies in the charged current (CC) interaction of a ν_e a "mixed" neutrino shower (carrying the full ν_e energy) is produced, since an ultra high energy electron having about 80% of the ν_e energy is produced and initiates a large electromagnetic shower parallel to the hadronic shower. The CC interaction of a ν_μ produces a "pure hadronic"

shower (carrying $\sim$ 20% of the energy of the ν_μ) and a long lived muon which is not easily detectable by existing experiments. Tau neutrinos produce tau leptons in CC interactions which, depending on the decay length of the tau, may decay back into tau neutrinos plus other particles, adding to the hadronic shower. If the τ does not decay to add to the hadronic shower channel a shower induced by a ν_τ or a ν_μ become indistinguishable. The neutral current (NC) interaction of all three flavours results in purely hadronic showers.

The interaction of neutrinos with atomic electrons is in general suppresed except for the resonance $\overline{\nu}_e + e^- \rightarrow W^- \rightarrow \textit{anything}$, which dominates over all processes but in a narrow energy range around $E_{\overline{\nu}_e} = 6.4 \times 10^{15}$ eV [51]. The decay of the W^- boson into $q\overline{q}$ pairs dominates due to the six possible final states and induces a "pure hadronic" shower carrying the whole energy of the W^-. If the decay is into $e\overline{\nu_e}$, the electron generates a purely electromagnetic shower with energy $\sim 3 \times 10^{15}$ eV and if it decays into a $\tau\overline{\nu_\tau}$ the shower is produced by τ decay (64% of times it is hadronic and 18% electromagnetic) [52].

Regarding the cross sections of these interactions, they can be found in the literature [51] for $10^{16} \simeq E_\nu \simeq 10^{21}$ eV. They increase with the energy typically as $E_\nu^{1/3}$ reaching $\geq$ 700 pb[1]. This rise induces a reduction of the interaction length. For instance, CC and NC neutrino interaction lengths are given by:

$$L = \frac{1}{N_A \times \sigma^{(\mathrm{NC})\mathrm{CC}}_{(\overline{\nu}\nu)\mathrm{N}}} = 1.7 \times 10^7 \text{ km w.eq.} \left(\frac{\mathrm{pb}}{\sigma^{(\mathrm{NC})\mathrm{CC}}_{(\overline{\nu}\nu)\mathrm{N}}} \right) \tag{2.17}$$

and in the case of the resonance:

$$L = \frac{1}{(10/18) N_A \times \sigma_{\overline{\nu}e}} = 0.94 \times 10^7 \text{ km w.eq.} \left(\frac{\mathrm{pb}}{\sigma_{\overline{\nu}\mathrm{e}}} \right) \tag{2.18}$$

where $(10/18)N_A$ is the number of electrons in a mole of water.

Neutrino interaction lengths are far larger than Earth's atmospheric depth, which has a maximum of 0.36 km w.eq.[2] when traversed horizontally at see level ($\theta = 90°$). As a consequence, neutrinos can induce extensive air showers developing deep in the atmosphere. In contrast, the interaction length of cosmic ray hadrons and gamma rays is $\sim 50 - 100$ g cm^{-2} ($\times 10^{-5}$ in km

[1] 1 pb $= 10^{-36}$ cm^{-2}

[2] km w.eq. are kilometers of water equivalent. 1 km in water $\approx 10^3$ km in air

w.eq.) at 10^{19} eV. Thus, the probability of these particles initiating EAS at depths larger than 2000 g cm^{-2} is very small ($\sim 10^{-9}$). Therefore any shower starting deep enough in the atmosphere would be initiated by a candidate neutrino event. As it was suggested in the 1960s [53], the key in the search of down-going neutrino showers among the ordinary showers is to search for inclined showers that interact deep in the atmosphere and can be detected at ground level. In extensive air showers induced by baryons or photons at high zenith angles, their hadronic and electromagnetic components are completely developed and absorbed before reaching the ground, and only the penetrating component (muons and neutrinos) reaches the ground. On the contrary, neutrinos can be induce air showers deep into the atmosphere with large electromagnetic component at ground level that can be identified.

Air shower arrays, as the AGASA and Haverah Park experiments, have observed inclined extensive air showers. The inclined dataset was studied and shown to be consistent with baryonic origin [54, 55]. The Pierre Auger Observatory is a hybrid detector (fluorescence telescopes and ground array) of ultra high energy cosmic rays designed to observe extensive atmospheric showers. It has the capability to observe very inclined air showers generated by neutrinos with the surface detector and distinguish them from the background of inclined baryonic showers [52, 55].

The rate of neutrino interactions in the atmosphere is low and they are expected to produce at most a few detections of deeply penetrating air showers over the active life of a long-lived experiment such as the Pierre Auger Observatory. There are other phenomena that could produce similar deeply penetrating showers (DPS) [39, 56]. High energy muons (hard muons) can produce DPS by bremsstrahlung, pair production and nuclear interactions. Bremsstrahlung is the hardest process and the most important for producing high energy showers. In any case, the deep showers induced by μ should be typically embedded in a larger shower which produced them. If both are detected it could in principle be possible to distinguish the deep subshower and the primary shower.

Earth-skimming τ neutrinos

Although ν_τ are heavily suppressed at production, neutrino flavour oscillations lead to a flavour proportion $\nu_e : \nu_\mu : \nu_\tau \sim 1 : 1 : 1$ after propagation over cosmological distances. Consequently a considerable number of ν_τ arriving at the Earth are expected. One possibility of detecting ultra high energy ν_τ in the atmosphere is identifying the double down-going extensive air showers produced in the interaction of ν_τ with an air nucleus via charged current. This phenomenon is called Double-Bang (DB) Phenomenon and it does not

occur for other flavours of neutrino. Several recent works have studied the potential of the Pierre Auger Observatory to detect DB events with the fluorescence detector. Moreover, these events do not need to be very near-horizontal (with incident angles from 55° to 75°) [57].

However, τ neutrinos are more effectively detected through the observation of events in which a neutrino skims the Earth, traveling almost horizontally along a chord inside the Earth with length comparable to its interaction length in rock ($\sim$ 500 km w.eq. in rock for an EeV neutrino). Some of them can undergo charged current interactions into charged taus (see 2.14). Tau leptons, produced in the mountains or inside the Earth, can escape even from deep inside the rock emerging in the atmosphere as an up-going particle and produce clear signals if they decay above the detector. The shower induced by τ decay can be considered hadronic and can carry up to 2/3 of the total τ energy. This mechanism does not work so effectively for ν_e and ν_μ If the leptons are electrons, they do not escape from the rocks and if they are muons, despite can travel up to 10 km inside the Earth, they do not produce any visible signal in the atmosphere.

The Pierre Auger Observatory has the potential of detecting τ-showers induced by Earth-skimming neutrinos by means of both the fluorescence detector [58] and the surface detector [59].

Chapter 3

The Pierre Auger Observatory

Understanding the origin, mass composition and spectrum of the most energetic cosmic rays is one of the foremost issues in Astroparticle physics today. The cosmic ray spectrum with energies exceeding 4×10^{19} eV (above the so-called Greisen-Zatsepin-Kuzmin cutoff) is not very well known, due to the poor statistics and the large systematic errors of the few events detected with those energies. The main experimental difficulty to measure the properties of the cosmic rays with these energies is the extremely low flux of cosmic rays at these energies (of the order of 1 particle km^{-2} sr^{-1} yr^{-1} for energies around 10^{19} eV). Only detectors that cover vast areas (thousands of kilometers) could collect a significant number of events.

The Pierre Auger Observatory was conceived to detect thousands of events in the energy region from 10^{19} eV to 10^{21} eV, reconstruct their energy spectrum with unprecedented precision, measure their arrival direction distribution and study the mass composition of the incident cosmic rays over the whole sky. To achieve this coverage, it was decided to build a hybrid two-site observatory, one in the Northern and one in the Southern Hemispheres. The chosen locations are Malargüe in Argentina and Colorado in the USA.

The Southern Observatory is currently under construction and is located at the "Pampa Amarilla" at a mean altitude of 879 g cm^{-2} ($\sim$ 1400 m), near Malargüe in Mendoza Province, Argentina. The site is relatively flat and near the base of the Andes mountains. The weather is classified as "arid" with clear skies and soft temperatures.

3.1 The concept of a Hybrid Detector

The Auger Observatory is a hybrid detector, designed to be fully efficient for showers with energies above 3 EeV combining the strengths of two detection

techniques: an array of surface detectors and 4 fluorescence telescopes. The hybrid detector has important advantages over either surface detectors or fluorescence detectors operating alone. Observing showers simultaneously with the two different detectors allows to identify the sources of systematic uncertainty in each technique, and to measure independently the properties of the showers. The main benefits of the Surface Detector are a 100% duty cycle, a well defined aperture independent of the energy above 3×10^{18} eV and a high sensitivity to showers arriving at large zenith angles. On the other hand, the Fluorescence Detector provides a direct measurement of the longitudinal profile of the extensive air showers and a calorimetric energy measurement (the small unseen fraction of the total energy carried by muons and neutrinos introduces a small systematic uncertainty ($< 4\%$) due to lack of knowledge of the composition of the primary particle and the hadronic interaction model).

In this chapter we will only describe the surface detector since it is the most relevant for the work done in this thesis. More information on the FD detector can be found in [60]. The design of the surface array of the Southern Observatory consists of 1600 water Cherenkov detector stations on a hexagonal grid of 1.5 km spacing spreading over an array of 3000 km^2, overlooked by four fluorescence detector eyes (figure 3.1). Each eye contains 6 fluorescence telescopes allocated inside a building on the edge of the array.

The different types of events that can be detected at the Pierre Auger:

- SD events: events only detected by the surface array.
- FD events:
  - Mono events: 1 FD eye
  - Stereo events: 2 or more FD eyes.
- Hybrid events:
  - Simple hybrid events: 1 FD eye + 1 SD tank or a few SD tanks, but not enough to perform an independent SD reconstruction.
  - Golden events: 1 FD eye + n SD tanks, with n large enough to allow an independent SD reconstruction.
  - Platinum events or Stereo-hybrid events: 2 or more FD eyes + information from SD.

In the following sections, we describe the Surface Detector, the reconstruction of cosmic air showers from the SD, and the most relevant results obtained so far.

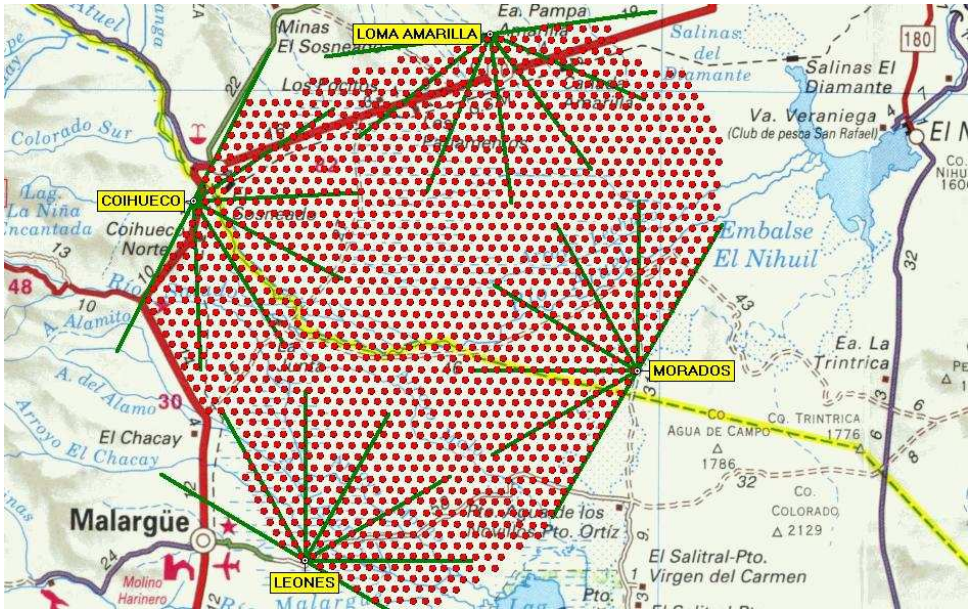

Figure 3.1: *The southern site of the Pierre Auger Observatory near Malargüe, Argentina. The dots represent the current and planned positions of the 1600 Surface Detector tanks. The yellow labels correspond to the localization of the four Fluorescence Detector buildings. The lines mark the* 30° *azimuthal field of view of each of the fluorescence telescopes (6 in each eye) of the Fluorescence Detector.*

3.2 The Surface Detector

The surface detectors used in the Pierre Auger Observatory of the Southern Hemisphere are deep water Cherenkov detectors [61] such as the one shown in Fig 3.2. Each detector unit consists of a cylindrical polyethylene tank, 3.6 m in diameter and 1.55 m in height, enclosing a liner filled with 12000 l of exceptionally pure water. The liner is a plastic cylindrical bag with a height of 1.2 m, which is black in the outside to seal out the external light while it is coated with Tyvek on the inside to diffuse and reflect Cherenkov light. Above the tank, there are three 9" photomultiplier tubes (PMTs) located within the space between the top of the liner and the top of the tank, which are in optical contact with the volume of water through three plastic windows. Each PMT provides two signals: from the last dynode and from the anode. The last dynode signal is amplified 32 times to match the dynamic range. The anode is used for high signals such as seen when the station is near the core of the shower. This six signals are digitized in time slots of 25 ns by a Flash Analog to Digital Converter (FADC) running at 40 MHz. The signals are sent to a Programmable Logic Device, which is used to implement the

local trigger conditions as described in the following section.

Figure 3.2: *Picture of a SD tank installed in the site.*

The electronics include a commercial GPS unit that provides the event time with ~ 8 ns resolution. This was checked by studying the trigger times of two pairs of stations located a few meters from each other.

The wireless LAN communication between the tanks and the Central Data Acquisition System (CDAS) is made by conventional radio systems and each tank has its own antenna.

Each tank is a standalone system. There are two solar panels and two 12 V batteries that supply power to the electronic read-out system and to the high voltage PMTs. The total power consumption is less than 10 W.

A schematic view of the main components of the SD tank is shown in Fig. 3.3.

3.2.1 Calibration of the Surface Detector

The tank FADCs measure the light generated by shower particles crossing the water volume of the tanks by sampling the current generated at the PMT. However, the fact that particles crossing different detectors generate equal light does not result in an equal count in the FADCs. This is due to several factors such as differences in the PMT gains, in the water quality, the

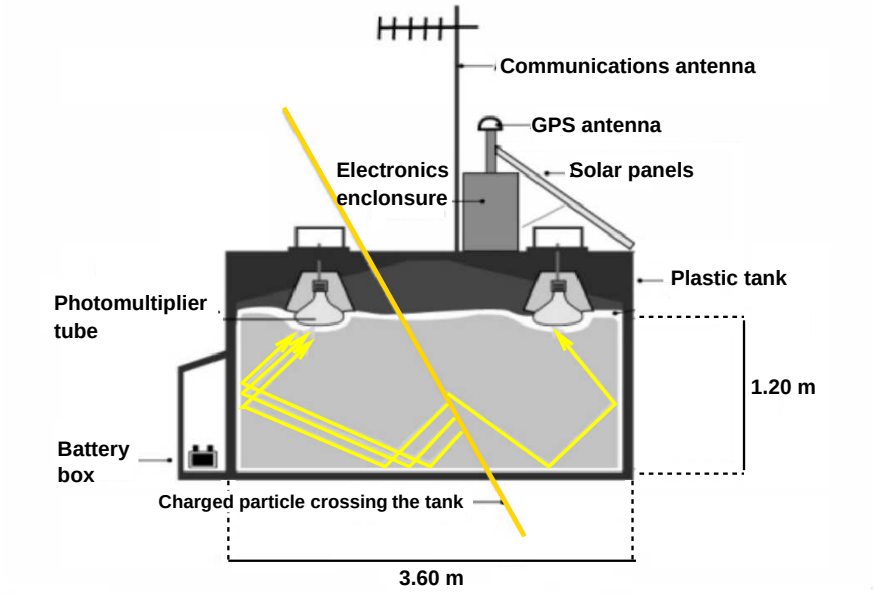

Figure 3.3: *Schematic view of a Surface Detector tank, with the main components labeled.*

Tyvek reflectivity, etc. Therefore, the signal measured by each tank must be normalized to a common calibration unit to cancel out the detector parameter dependence. This normalization factor, called the Vertical Equivalent Muon (VEM or Q_{VEM}), is the signal produced by a vertical muon traveling along the axis of the tank and crossing the entire depth of water.

The goal of the calibration procedure is to measure and monitor with good accuracy the VEM unit for each PMT in electronics units. The calibration is carried out in three steps. Firstly the absolute calibration is determined from a sequence of measurements. Secondly, the PMTs are matched in gain. Finally, the evolution with time of the gains is monitored and inserted into the data flow (see [62] for more details).

To achieve the absolute calibration of the VEM unit, in Auger we use the flux of atmospheric muons which has roughly a constant value (a rate in a tank of ~ 2.5 KHz) producing a peak in a charge histogram. This histogram is understandable as the convolution of distributions of four different classes of incoming particles: (a) muons entering through the top and exiting through the bottom, (b) muons entering through the top and exiting through the side,

(c) muons entering and exiting through the side, and (d) small showers that produce the first peak. The peak produced by the first class of incident muons is the VEM. Unfortunately, vertical and central muons can not be selected. The way to relate the peak value to the VEM unit requires measurements of vertical muons using external triggers by means of a muon telescope. This telescope consists of two pairs of scintillator paddles centered, one on the top and the other underneath the tank. Coincidence between scintillators indicates that a vertical muon crosses the tank.

In Fig. 3.4 we show an example of the charge histogram produced in a SD tank under the flux of atmospheric muons, and the histogram corresponding to the external calibration by a muon telescope. The second peak of the histogram due to atmospheric muons is found to be very stable with a peak charge equivalent approximately to 1.03 VEM for each PMT (1.09 for the sum of the 3 PMTs), allowing to convert the charge measured in any FADC channel to VEM units. All the surface detectors are calibrated remotely with an overall 5% precision with respect to their absolute VEM value.

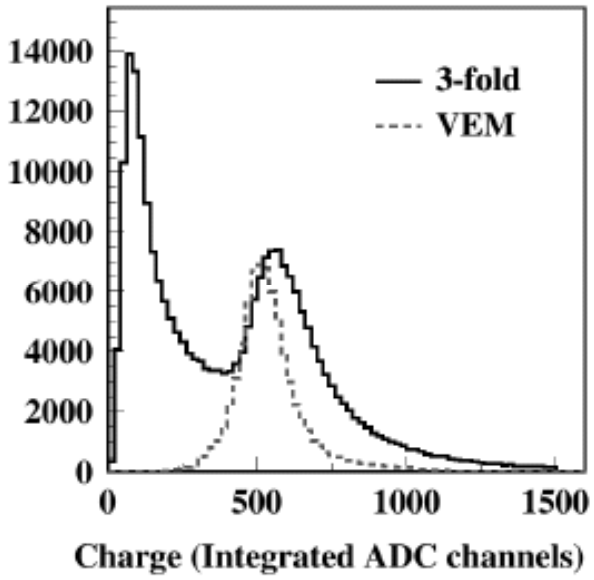

Figure 3.4: *Charge histogram of signals (3 PMTs summed) in a surface detector under the flux of atmospheric muons (black). The first hump is an artifact due to the triggering (3 fold). The second hump corresponds to the signal of single muons going through the tank. The dashed histogram corresponds to events triggered by a muon telescope (see text). The muon peak occurs at 1.09 VEM. Taken from [62].*

Besides the charge distribution, other two histograms are stored in the

tank calibration for each PMT: one with the value of the first bin before the signal to obtain the baseline and another with the maximum values of the measured FADC traces, called the peak distribution. The mean value of this last one is called VEM peak (I_{VEM}^{peak}), and it is used as the common reference unit for trigger issues.

Each station is calibrated online matching the photomultipliers gain by adjusting the voltage on each PMT to get the expected trigger rate for a given VEM threshold.

The calibration is operated online every minute, and sent to CDAS every 6 minutes for monitoring, and in addition every 4 hours a charge histogram of the atmospheric muons is made to compute the position of the muon peak.

3.2.2 The Surface Detector Trigger System

The SD trigger system is used to select high quality extensive air showers from the background of atmospheric muons. This is a hierarchical system with low level triggers (T1 and T2) implemented by the local tank software, the following level trigger (T3) is formed at the central system (at the observatory campus) based on the spatial and temporal correlation of the level T2 triggers. Additional high levels of trigger are implemented offline to select physical events (T4) and finally quality events which can be well reconstructed (T5).

Low level triggers

Currently, there are two different triggers implemented at the T1 level. The first is a simple threshold trigger that requires the 3-fold coincidence of signals exceeding 1.75 I_{VEM}^{peak} threshold. This trigger with a rate of 100 Hz is used to detect fast signals (< 200 ns) corresponding to muons. This trigger is noisier and its rate is used to calibrate the gains of the PMTs (see previous section). The second is a Time over Threshold (ToT) trigger that requires that 13 bins of the FADC trace in a 120 bin window are above a threshold of 0.2 I_{VEM}^{peak} in coincidence of 2 PMTs. This trigger with a rate of 1.6 Hz is very efficient to select small spread-out signals, like those produced by distant showers of high energy or close low energy showers.

All the ToT triggers are directly promoted to the second level trigger T2, whereas the T1 threshold triggers are requested to pass a higher threshold of 3.2 I_{VEM}^{peak} in coincidence of 3 PMTs to be promoted to T2 triggers. The total rate of T2 is close to 20 Hz.

Whenever a station fulfills one of the two T2 trigger conditions, the trigger timestamp (start-time) and the type of the trigger are sent to CDAS. The

central trigger receives the T2s, which are used to check if the following level trigger (T3) is fulfilled.

High level triggers

The higher level triggers are intended to select real events and distinguish them from random coincidences. The third level trigger at the CDAS has been designed to have a trigger efficiency close to 1 above energies $\sim 10^{18.5}$ eV (T3). An offline hierarchy of two additional trigger levels are implemented to reject random coincidences (T4) and ensure a good reconstruction (T5).

At this level, the trigger nomenclature is based on crowns of stations around any given tank among the triggered stations (see Fig. 3.5). We will refer to it as the "central station". The six first neighbours around the central station form the first "crown" with hexagonal shape, named C1. The next crown is named C2. Therefore, the m^{th} crown around the central station is named Cm.

As the T3 triggers are requirements on the number of triggered stations in each crown, the number of required triggered stations (n) contained within certain number of crowns (m) is denoted as nCm.

Once we have introduced the nomenclature, we can present the different trigger levels.

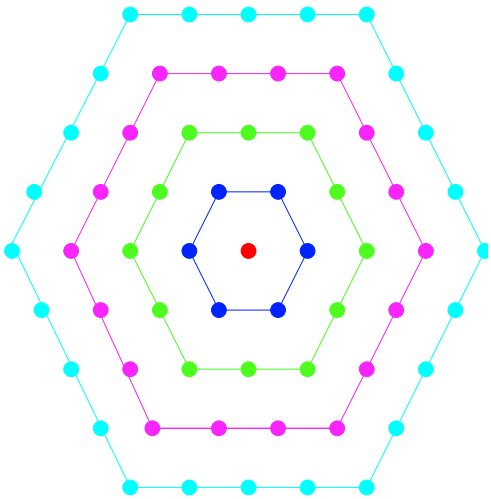

Figure 3.5: *Topology of the concentric crowns-hexagons of tanks around the central station (red) used for the T3 trigger decision. C1 in blue, C2 in green, C3 in magenta and C4 in cyan.*

The T3 trigger is implemented at the CDAS where a search is made for

the coincidence of at least 3 tanks with T2 trigger together with compactness requirements. This trigger requires at least one of the following two conditions:

- $TOT - 2C1$ and $3C2$: this trigger requires a 3-fold coincidence of tanks passing the T2 ToT condition. One of the tanks must have a neighbouring tank in the first crown and another one within the 2 first crowns. This trigger is extremely relevant since 90% of the events selected with it are showers and is most efficient for vertical showers.

- $2C1$ and $3C2$ and $4C4$: this trigger is more permissive, and requires a 4-fold coincidence of any T2 condition with a moderate compactness: one neighbouring tank, 2 tanks inside 2 crowns from the central one and a further tank within 4 crowns. Such a trigger is needed for the detection of horizontal showers but has a lot of noise. From the events selected by this trigger, only $\sim 2\%$ are real showers.

The search of all 3 stations that make up a event is completed as follows. Whenever a station gets a T2 trigger, the trigger time and the type of trigger are sent to CDAS. Placing a 50 μs window around a given T2 (25 μs earlier and 25 μs later), all the stations that have a T2 trigger within this time window are examined the patterns required for T3 trigger are searched for. If a pattern is found, the search stops and the T3 trigger flag is assigned to the event. For every T3, all the stations in the array that had a trigger of any level including T2 in coincidence with the central station (of the crown patterns) are recorded. A final timing criteria is imposed, the trigger times must be within $(6 + 5n)$ μs of the central one, where n indicates the crown number. All the FADC traces of the stations that fulfill that later condition are stored in the event file.

The two offline higher level triggers described were developed for vertical showers $\theta < 60^\circ$ in accordance with the two main characteristics expected in vertical showers: compactness of the pattern of triggered tanks and FADC traces sufficiently spread in time to satisfy the ToT condition. In principle these conditions are not suitable for the inclined showers that are regularly being selected, because their compactness requirements are too restrictive for the wide-spread topological patterns of inclined showers to some extent because the signals of horizontal showers are typically short in time.

The T4 trigger, also known as the "physics" trigger, has been developed to select actual showers from the set of stored T3 data. This trigger requires that the event has at least 3 stations forming a triangle of first neighbours (a $3C1TOT$ event) or a compact configuration of any local trigger called $4C1$.

The tanks satisfying the 3 ToT or 4C1 condition must have their trigger times compatible with the speed of light. Both triggers ensure that more than 99% of the events with $\theta < 60^\circ$ that satisfy it are real showers.

The T5 trigger, also known as the "quality" trigger, selects only those events that can be reconstructed with a controlled energy and angular accuracy among the set of events passing the T4 trigger. Several options have been considered. The current T5 requires that that the tank with the highest signal must be surrounded by at least 6 working tanks within the nearest crown of 6 tanks, and that the reconstructed core must be inside an equilateral triangle of working stations. For vertical events that pass the T5 trigger condition, the acceptance of the detector is computed and the energy spectrum is built.

3.3 Reconstruction of vertical showers with the Surface Detector

The reconstruction of the Surface Detector [64] events is performed in two steps: (1) Angular reconstruction: the arrival direction of the shower is obtained using the timing information from the surface detectors. (2) Reconstruction of the core position and the shower energy.

Before reconstruction, the tanks belonging to the event are selected applying algorithms based on space-time compatibility between stations.

The angular reconstruction is performed assuming the shower front is a plane disk of particles traveling at the speed of light. The plane front can be fitted to the timing data, allowing the reconstruction of the zenith and azimuth angles, with an angular resolution better than 1.2° for the events with multiplicity 4 or 5 and better than 0.9° for higher multiplicity events [65].

After angular reconstruction the core location is obtained by fitting the signals of the stations to a Lateral Distribution Function (LDF), assuming cylindrical symmetry. The LDF fit is based on a likelihood method.

The following LDF is used for the expected signal (in VEMs) at a distance r (in meters) to the shower core:

$$S(r) = S(1000)\left(\frac{r}{1000}\right)^{-\beta}\left(\frac{r+r_s}{1000+r_s}\right)^{-\beta} \tag{3.1}$$

where β is the slope of LDF, $r_s = 700$ m, and $S(1000)$ is the signal of a station at 1000 m from the shower axis. The value of β is fixed and only

depends on the zenith angle of the shower as:

$$\beta = 3.3 - 0.9 \sec\theta \tag{3.2}$$

Eq. (3.2) is valid in the region $\theta < 60°$. At larger zenith angles, there is an azimuthal asymmetry due to geometric and evolution effects as well as the effect of the geomagnetic field, so a simple power law description of the fall of the density with the distance to the core is inadequate.

From the fit of the previous LDF, the values of $S(1000)$ and core position are obtained. The parameter $S(1000)$ is used as an energy estimator because simulations show that the fluctuations of the signals in the tanks have a minimum near the region $r = 1000$ m from the core. This signal fluctuations are typically due to shower fluctuations affecting the shower development (near the core) and to fluctuations of statistical nature (far from the core). The error of $S(1000)$ has been determinated experimentally and found to be better than 12% at the highest energies [65].

The relation between S(1000) and energy can be obtained by air shower simulations. In this case, the result depends on the assumed primary mass and the hadronic model used. These dependences can be avoided to a large extent using the hybrid capabilities of the Pierre Auger Observatory (see Section 3.5).

3.4 Reconstruction of inclined showers with the Surface Detector

The inclined showers ($60° < \theta < 90°$) are characterised by a dominance of the muonic component at ground, and by a very elongated and asymmetrical footprint due to the bending of muon trajectories in the geomagnetic field. Inclined showers are quite different to vertical ones, and require different reconstruction techniques [67].

The trigger hierarchy follows a similar format to that chosen for the vertical reconstruction. The equivalent physics trigger (T4) selects the stations of the event which are compatible with a shower front moving at the speed of light. Later, a Quality Trigger (T5) can be applied to ensure the validity of the reconstruction.

In the case of horizontal showers, the reconstruction of the arrival direction and the reconstruction of energy and position are done all at the same time in an iterative process. The absorption of the electromagnetic component in inclined showers leads to a very flat Lateral Distribution Function (LDF) of particles, together with a broken radial symmetry, which makes the

LDF unsuitable for their analysis. Instead of a LDF, maps of muon number densities at ground, obtained in Monte Carlo simulations for different zenith and azimuth angles in presence of geomagnetic field in the Auger site, are used to fit the core location of the shower and the normalization of the total number of muons relative to a shower initiated by a 10 EeV proton, the so-called N_{19} parameter, which is used as an energy estimator. The shape of the muon maps is not very dependent on energy or composition. On one hand, the map used to fit the core must correspond to the zenith angle of the shower. On the other hand, the angular reconstruction requires timing corrections that depend on core position. Hence, the need for an iterative process.

The first step in the iterative process to obtain a preliminary angular reconstruction is done by fitting the start-time data of a maximum of seven stations (those with the highest signals) to a plane front. This angle is used to select the suitable muon map, and provisionally determine the core location and N_{19}. Once the core position is found, a more sophisticated angular reconstruction is performed including timing corrections to describe the variable curvature of the shower front [34]. The result of this second fit is compared with the original one, and if necessary a more suitable muon map is selected, and a new angular reconstruction is performed with this new map. This process is repeated until the result converges.

To allow the comparison of the muons maps with the station signals, the signal measured in each tank must be converted into an equivalent number of muons. The first step for this conversion is to remove the fraction of the signal due to the electromagnetic halo (see Chapter 4). Then, the muonic signal is converted into a number of muons in each tank using parameterizations based on the tank response to muons [68].

To reconstruct the position of the core, 20×20 cells are scanned to find the location that minimizes the difference between muon maps and the corrected station signals converted into muon numbers. This is followed by a maximum likelihood method with a fixed core to determine the map normalization N_{19}.

Once the shower size, N_{19}, is well determinated, the following step is to estimate the energy shower. For SD events, the relation between energy and N_{19} can be explored by shower simulations. From simulations performed with AIRES, N_{19} has been shown to scale with energy through the following relation:

$$\log_{10} E(EeV) = \alpha + \frac{1}{\beta} \log_{10} N_{19} \tag{3.3}$$

where α and β are constants. The values of these parameters are different depending on both the interaction model and the mass composition. How-

ever the hybrid nature of the Pierre Auger Observatory allows to establish the relation between energy and N_{19} in an almost model and composition independent manner (see Section 3.5).

3.5 Energy spectrum with vertical showers

The hybrid nature of the Pierre Auger Observatory allows to establish the relation between S(1000) obtained in the SD reconstruction and the energy measured by the Fluorescence Detector in a manner that is almost independent of air shower and detector simulations. The analysis is also essentially free of assumptions about the primary nuclear mass and it is based on the well-known constant intensity cut (CIC) method [69]. The attenuation of $S(1000)$ with zenith angle for a fixed energy is derived empirically by exploiting the nearly isotropic intensity of cosmic rays from which the shape of the attenuation of $S(1000)$ with θ, the $CIC(\theta)$, is obtained. $CIC(\theta)$ has been parametrized as $CIC(\theta) = 1.049 + 0.0091\,\theta - 0.00029\,\theta^2$. From a reconstructed $S(1000)$ and θ, the value of $S(1000)$ at 38° (S_{38}) is obtained using the $CIC(\theta)$. S_{38} is then related to energy using a sample of good quality hybrid events in which S_{38} and energy is known. A fit similar to that Eq. (3.4) is performed and α and β are obtained. By fixing a specific intensity I_0 (counts per $\sin^2\theta$ bin), one finds for each zenith angle the value of S(1000) such that $I(> S(1000)) = I_0$. The assumption of isotropy of the cosmic ray flux implies equal fluxes for all the angles.

The latest observation of the energy spectrum J with vertical showers [70] obtained by means of this procedure using data collected at the Pierre Auger Observatory between January 1$^{\text{st}}$ 2004 and February 28$^{\text{th}}$ 2007 is shown in Fig. 3.6. The statistical and systematic uncertainties are indicated in the figure.

3.6 Energy spectrum with inclined showers

The hybrid nature of the Pierre Auger Observatory also allows to establish the relation between N_{19} obtained in the SD reconstruction and the energy measured with data from the Fluorescence Detector, a method that is almost independent of air shower and detector simulations and on primary mass.

The calibration of the normalization parameter N_{19} is performed correlating it with the energy obtained using the fluorescence technique for a set of high quality hybrid events of zenith angle exceeding 60°. From a simple linear fit to the data, the following relation between energy and N_{19} is obtained

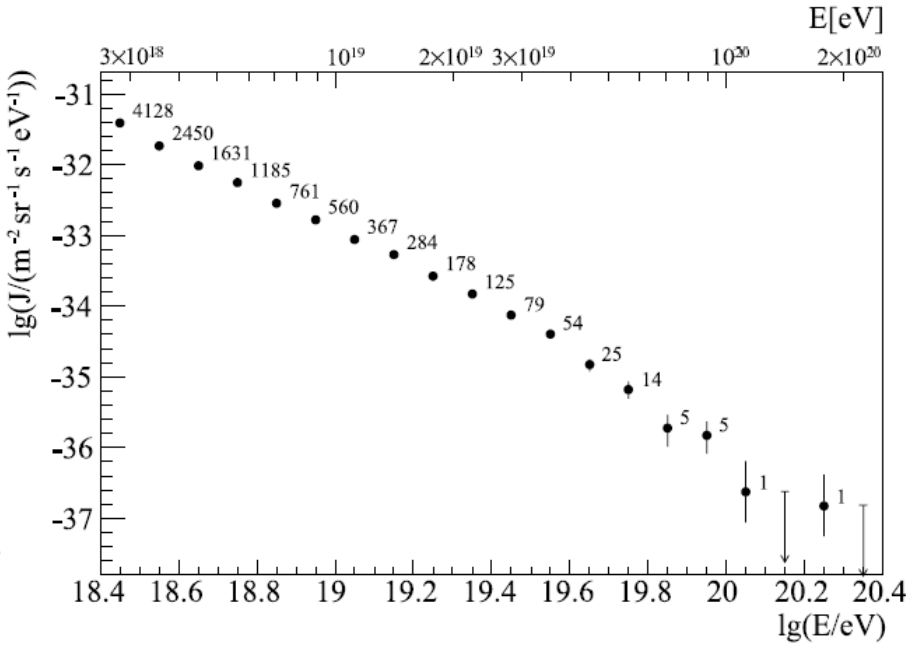

Figure 3.6: *Cosmic ray spectrum obtained with showers with $\theta \in [0°, 60°]$. Statistical uncertainty is indicated by error vertical bars. The statistical and systematic uncertainties in the energy scale are of the order of $\simeq 6\%$ and $\simeq 22\%$, respectively. Presented in [70].*

[71]:

$$\log_{10} N_{19} = \alpha + \beta \log_{10} E_{Hyb}(EeV) \tag{3.4}$$

with $\alpha = -0.77 \pm 0.06$ and $\beta = 0.96 \pm 0.05$.

For the determination of the cosmic ray spectrum with inclined showers, a high level trigger (T5) is applied to the data set. This trigger requires that the tank closest to the reconstructed core is surrounded by an hexagonal crown of working stations. The aperture is also calculated applying this trigger.

Considering only events with $N_{19} > 1$ ($E \sim 6.3$ EeV) where the array efficiency exceeds 98%, the first cosmic ray spectrum ever obtained with showers in the angular range between 60° and 80° as measured by the Pierre Auger Observatory between January 1st 2004 and February 28th 2007 is shown in the top panel Fig. 3.7. In the bottom panel of Fig. 3.7 the cosmic ray spectrum obtained with inclined showers is shown along with the spectrum obtained with vertical showers. The agreement between both is very good.

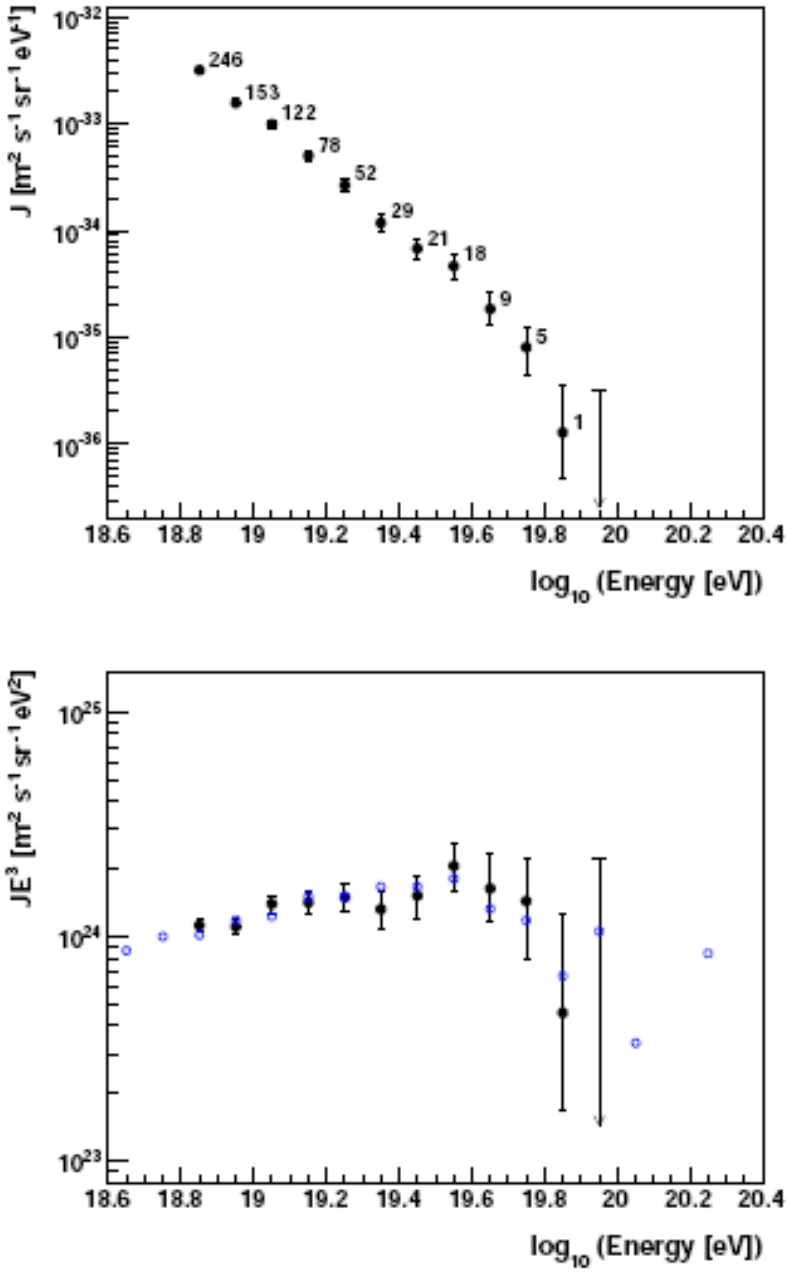

Figure 3.7: *Top panel: Cosmic ray spectrum obtained with showers with $\theta \in [60°, 80°]$. The statistical uncertainty is indicated by error bars (95% upper limit). Bottom panel: Spectrum obtained with inclined showers (black full circles) multiplied by E^3. The spectrum obtained with vertical events is superimposed (blue empty circles). Presented in [71] and [70].*

Chapter 4

Study of the signals in the Surface Detector stations of the Pierre Auger Observatory

4.1 $S(1000)$ USC code: an alternative method to simulate the Tank Response

The study of the response of the Auger tank to the passage of shower particles (mainly muons, electrons and photons) is a fairly complex task that requires the use of quite sophisticated simulation techniques to model the behaviour of the detector. The response of the tank can be simulated with a number of packages, the most sophisticated one being the well-known Geant4 [72]. This package consists on tools to accurately simulate the passage of particles through matter. It provides routines to describe the behaviour of the Auger tank, and the relevant physical processes suffered by $e^{\pm}$, $\mu^{\pm}$ and γ inside it. As these detailed simulations typically require a large CPU time, we have developed an alternative fast method ($S(1000)$ USC) to calculate the response of the Auger tanks. An early version of this method is described in Ref. [73]. In this chapter, we describe the physical basis of the method and we compare it to the output of Geant4.

4.1.1 Description of the method

This approach is based on parameterizations of the response of the tank to the passage of shower particles. The method stems from two basic ideas: Muons produce signals approximately proportional to their track inside the tank. Electrons, positrons and photons typically induce small electromag-

netic showers which give a signal approximately proportional to the energy deposited by the secondary electrons and positrons, which in turn is proportional to their tracklength inside the tank.

The signal computed from the tracklength constitutes a first approximation to the average signal produced by a particle entering the tank. In the following we will account for a number of physical effects in the muonic and electromagnetic components and we will determine the signal produced by a shower reaching ground with larger accuracy.

Besides the primary observables of the shower such as zenith and azimuth angles (θ, ϕ), the method uses as input from the shower simulator the following information about the particles reaching ground:

- Type: muons, electrons, positrons and photons.
- Statistical weight.
- Kinetic energy (in GeV).
- Distance from the shower core.
- Arrival direction of the particle : θ_p, ϕ_p.

This information can be provided by Monte Carlo codes that perform the simulation of extensive showers in the atmosphere such as AIRES [74] and CORSIKA [75].

Although the default reference plane to record the particle information is the ground plane, it is useful to work in the plane transverse to the shower axis. In this case, the particle positions from the ground are projected onto the shower plane by means of a simple rectangular projection.

The results in this study are based on a library of proton showers simulated with AIRES 2.6.0 with a thinning level of 10^{-6}. Showers were generated with an energy E = 10 EeV, and with θ ranging from 0° to 88° for the hadronic model QGSJET01. A total of 100 showers were simulated for each zenith angle. The simulations were performed in the conditions of the southern site of the Pierre Auger Observatory. In this study, the geomagnetic field effect is neglected but will be accounted for later in the following chapter.

We describe step by step the procedure to compute the signal in the tank from the number densities of particles (ρ) and energy densities of particles (ϵ) given by the simulations. We will work in the shower plane unless otherwise indicated.

Unthinning procedure

The number of particles that are produced in an air shower at the energies relevant for Auger can be very large and the computing time needed to follow all of them becomes excessively large. A way out is to use a statistical sampling algorithm (thinning algorithm) which allows to propagate only a small representative fraction of the total number of particles. Statistical weights (W_i) are assigned to the sampled particles in order to compensate for the rejected ones [76].

As the output of the simulations is a ground particle file with weighted entries, we need to perform a unthinning procedure that allows us to extract a set of unweighted particles entering a given tank. The standard procedure [77] consists of selecting all the particles in the simulation that fall inside a sampling region. Then, their weight needed to calculate the signal produced inside the tank, can be computed as a first approximation as follows:

$$w_i = W_i \frac{A_{tank}}{A_{sampling}} \tag{4.1}$$

Here A_{tank} is the total area of the tank projected onto the shower plane (Eq. 4.11) and $A_{sampling}$ is the area of the sampling region projected onto the shower plane. Later in this chapter, we will take into account the zenith angle of the particle entering the tank (θ_p) and project the areas onto the plane transverse to particle direction instead of onto the plane transverse to the shower axis.

We can use different sampling regions depending on the results that we want to calculate. For instance in this chapter, we study the Lateral Distribution Functions (LDF), and we consider particles falling within concentric rings in the shower plane. Using polar coordinates (r, ξ), a ring limited by $r - \delta r$ and $r + \delta r$ has a sampling area:

$$A_{ring} = 2\pi r \; 2\delta r \tag{4.2}$$

If we wanted to calculate signals maps on the transverse plane (x vs y), we could consider square cells of area $A_{cell} = l \times l$ as sampling regions. In any case the sampling region has to be large enough so that a significant amount of particles falls inside it, but at the same time it should be small enough so that the properties (energy, etc...) of the particles are representative of their expected properties in the particular region in the ground in which the sampling area is located.

The unthinning procedure may induce biases and artificial fluctuations. Also note that the sampling ratio may be abnormally large if the zenith angle used in the projection onto the shower plane is close to 90°. To avoid

this problem, particles arriving at $\theta = 90^{\circ}$ are not accounted for in our calculations.

Energy lost by a particle inside the wall of the Auger tank

Since what we get from the shower simulation is the kinetic energy of the shower particles reaching the ground (K_0^{part}), we must calculate the energy lost by them inside the walls of the tank in order to obtain their energies just before they enter inside the instrumented volume of water. To implement this effect, the detector has been modeled as a cylinder of 1.2 m height, 1.8 m radius and with mean wall thickness $d \sim 1.27$ cm.

The energy lost by muons, electrons and positrons when crossing the walls of the tank is given by:

$$\Delta K_{\rm wall} = \alpha_{ion}\ \rho_{\rm wall}\ < t_{\rm wall} > \tag{4.3}$$

where $\rho_{\rm wall} = 0.94$ g cm^{-3} [61] is the density of the wall material (polyethylene C_2H_4), α_{ion} is the average energy loss in that medium, assumed to be ~ 2.079 MeV g^{-1} cm^2 for muons [83] and ~ 1.655 MeV g^{-1} cm^2 for electrons, and $< t_{\rm wall} >$ is the tracklength of the particle inside the wall of the tank averaged over the impact parameter.

The mean tracklength is obtained taking into account that particles can enter through the top or the side of the tank (Fig. 4.1):

$$< t_{\rm wall} >= P_{top} < t_{\rm top} > \ + P_{side} < t_{\rm side} > \tag{4.4}$$

where $< t_{\rm top} >$ and $< t_{\rm side} >$ are the mean tracklengths inside the top and side of the tank wall, respectively and P_{top} (P_{side}) is the probability that a particle crosses through the top (side) wall of the tank, The mean tracklengths are calculated as:

$$< t_{\rm top} >= V_{top}^{eff}/A_{top}^{eff}(\theta) \qquad < t_{\rm side} >= V_{side}^{eff}/A_{side}^{eff}(\theta)$$

where V^{eff} and A^{eff} are the effective volume and area of the side and top walls of the tank. By effective we mean that if a particle hits the effective area it will enter the water volume and produce a signal. In fact, a particle could cross the wall without entering inside the tank and therefore, it would not contribute to the signal inside the tank. Therefore, to calculate the average track of the particles through the wall that enter inside the tank, we must apply a correction to account for this effect. This involves subtracting from the area and volume of the side and top walls, the area and volume of the sectors painted in 'cyan' colour in Fig.4.1.

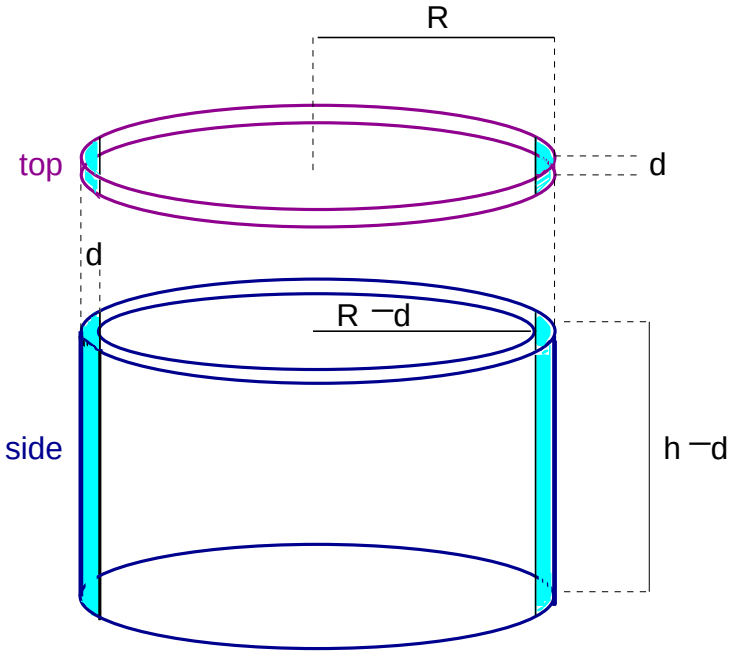

Figure 4.1: *Schematic view of the wall tank: top and side regions.*

The areas of the sectors in the top and side walls *as viewed by the incoming particle* are:

$$A_{sector}^{top} = \pi R^2 - 2\,(R-d)\sqrt{R^2-(R-d)^2} - 2R^2 arcsin\left(\frac{R-d}{R}\right)$$

$$A_{sector}^{side} = 2\,(h-d)\,\sqrt{R^2-(R-d)^2} \tag{4.5}$$

The corresponding volumes are:

$$V_{sector}^{top} = A_{sector}^{top}\,d$$

$$V_{sector}^{side} = A_{sector}^{top}\,(h-d) \tag{4.6}$$

Therefore, the effective area and the effective volume of the side wall projected onto the shower plane are:

$$A_{side}^{eff}(\theta) = \left[2R\,(h-d) - A_{sector}^{side}\right]\,\sin\theta \tag{4.7}$$

$$V_{side}^{eff} = \pi\left[R^2-(R-d)^2\right]\,(h-d) - V_{sector}^{side} \tag{4.8}$$

The effective area and the effective volume of the top wall projected onto the shower plane are:

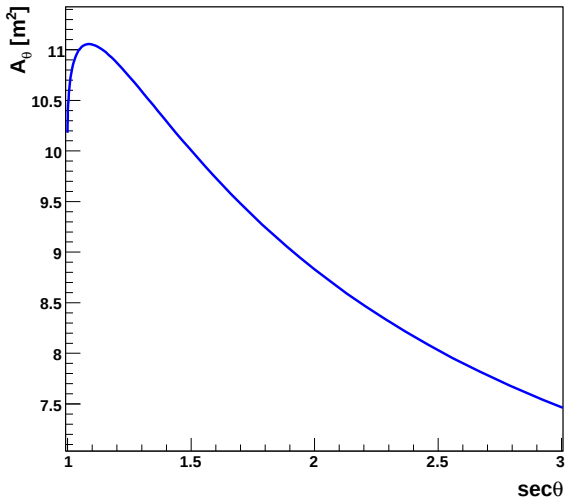

Figure 4.2: *Area of an Auger tank projected onto the traverse plane to the θ direction.*

$$A_{top}^{eff}(\theta) = (\pi R^2 - A_{sector}^{top})\cos\theta + 2Rd\sin\theta \tag{4.9}$$

$$V_{top}^{eff} = \pi R^2 d - V_{sector}^{top} \tag{4.10}$$

On the other hand, the probabilities that the particle crosses through the top and side walls are calculated using the total areas projected onto the direction of the incoming particle:

$$P_{top} = A_{top}/A_{tank} \quad P_{side} = A_{side}/A_{tank}$$

where the total projected area of the wall (see Fig.4.2) is the sum:

$$A_{tank} = A_\theta = A_{top} + A_{side} = \pi R^2\cos\theta + 2Rh\sin\theta \tag{4.11}$$

Once we have calculated the mean tracklength of the particle in the tank wall, the average energy of a charged particle after entering inside the water volume is obtained as:

$$K^{part} = K_0^{part} - \Delta K_{\text{wall}} \tag{4.12}$$

Energy cuts on the input particles

The Auger tank is a water Cherenkov detector, hence we only account for particles with energies inside the instrumented volume above the Cherenkov threshold in water. The minimum kinetic energy that a charged particle must have to produce Cherenkov light in water is:

$$K_{\rm th}^{part} = m_{part}\left(\frac{1}{\sqrt{1-(1/n_w)^2}}-1\right) \sim \begin{cases} 264 & \text{keV} & \text{for } e^{\pm} \\ 54.6 & \text{MeV} & \text{for } \mu^{\pm} \end{cases} \tag{4.13}$$

where m_{part} is the mass of the particle and $n_w = 1.33$ is the refractive index of water for optical wavelengths. For photons the minimum energy is chosen that so that the photon produces an electron-positron pair with at least one of them having energy above $K_{\rm th}^{e}$. The threshold energy for photons is:

$$E_{\rm th}^{\gamma} = K_{\rm min}^{e^+e^-} + K_{\rm th}^{e} = 1.286 \text{ MeV} \tag{4.14}$$

First estimate of S(r)

As a first approximation for the average value of the signal S at a distance r from the shower core, $S(r)$, we calculate the so-called uncorrected $S(r)$, separating the contributions from the muonic (μ) and the electromagnetic (EM) components of the shower:

$$S(r) = S_{\mu}(r) + S_{EM}(r) \tag{4.15}$$

In this preliminary estimate we have assumed the following approximations:

- Muons give signals proportional to their tracks.
- The EM component induces typically small electromagnetic showers that give a signal approximately proportional to the energy deposited inside the tank.
- All particles travel parallel to the shower axis at the speed of light $\beta = v/c = 1$.
- As a result of $\beta = 1$, all particles have maximum and equal Cherenkov emission efficiency.

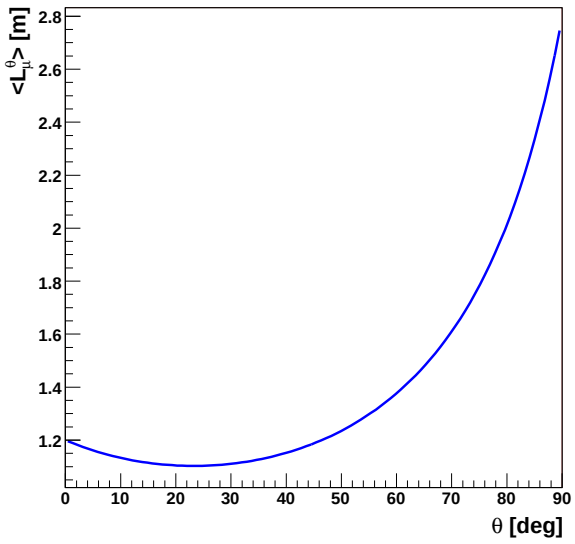

Figure 4.3: *Average tracklength of muons as a function of the zenith angle.*

Under these assumptions, the average signal in VEM units induced by a muon number density ρ_μ in an Auger tank is given by:

$$S_\mu(r) = \rho_\mu A_\theta \frac{< L_\mu^\theta >}{L_\mu^{VEM}} = \rho_\mu A_\theta \frac{< L_\mu^\theta >}{h} = \rho_\mu \frac{V}{h} = \rho_\mu A_0 \tag{4.16}$$

where L_μ^{VEM} is the average tracklength of a vertical muon (a VEM unit) which under the above approximations is equal to the height h of water, and $< L_\mu^\theta >= V/A_\theta$ is the average tracklength of a muon entering at zenith angle θ averaged over impact parameter. Here, A_θ is the area of the tank projected onto the direction θ (Eq. 4.11), and $V = \pi R^2 h$ is the tank volume. In particular $A_0 = \pi R^2 \simeq 10$ m^2 is the area of the tank as seen by a particle entering at $\theta = 0°$. In Fig. 4.3 we show $< L_\mu^\theta >$ as a function of the zenith angle. It has a minimum at around $\theta \sim 23°$.

Therefore, the signal induced by the muonic component of the shower is simply:

$$S_\mu(r) = \rho_\mu(r) A_0 = \frac{A_0}{A_{ring}(r)} \sum_{i=1}^{N_\mu} w_i \tag{4.17}$$

with $A_{ring}(r)$ the sampling area in the shower plane. The sum runs over all muons inside the ring area A_{ring}.

The electromagnetic particles induce subshowers in the tank which produce signals assumed to be proportional to the total tracklength of electrons and positrons (L_{EM}), which at the same time and as a first approximation is assumed to scale linearly with energy [78]. Under the assumption that all the energy of the electromagnetic shower is deposited inside the tank, the EM tracklength is proportional to the total energy of the EM particles entering the tank:

$$L_{EM} = kE_{EM} = k\epsilon_{EM}A_\theta \tag{4.18}$$

where ϵ_{EM} is the electromagnetic energy density and k is a proportionality constant. Therefore, the average signal induced by the EM component in VEM units in an Auger tank is given in this approximation by:

$$S_{EM}(r) = \frac{L_{EM}}{h} = A_\theta \frac{k}{h} \epsilon_{EM}(r) = \frac{A_\theta}{A_{ring}(r)} \frac{k}{h} \sum_{i=1}^{N_{EM}} E_i w_i \tag{4.19}$$

The sum runs over all electromagnetic particles inside the ring area A_{ring}. Photons are included in the sum since they induce EM subshowers inside the tank.

The value of the proportionality constant was obtained by performing shower simulations in water using the ZHS Monte Carlo code [78], giving $k = 5.25$ m GeV^{-1} for the proportionality constant [1].

We have applied our method to the calculation of the signal at $r = 1000$ m from the core $S(1000)$, and in particular we compute its dependence on $\sec\theta$. This dependence was chosen as an example to illustrate the relative importance on the muonic and electromagnetic signals of the different corrections with respect to the first estimate that we will introduce later in this chapter. As we mentioned in Section 3.5, $S(1000)$ has been chosen as the energy estimator for the air showers detected at the surface detector of the Pierre Auger Observatory.

In Fig. 4.4 we show the dependence of $S(1000)$ on $\sec\theta$ for 10 EeV proton showers. The relative contributions to the signal from the electromagnetic and muonic components of the shower are shown in the same figure. of $S(1000)$ increases by $\sim$ 8% from 50.9 VEM for a vertical shower up to $\sim$ 55.0 VEM at $\sec\theta \simeq 1.06$ ($\theta \simeq 20^\circ$) and then decreases monotonically. The increase from 0° to 20° is mainly due to the fact that the transverse area of the tank also rises in this range of θ (see Fig. 4.2). However, the increase of the area does not affect the average muon signal in Eqs. 4.16 and 4.17 although it

[1] It is worth remarking that the ZHS code shows a very good agreement with Geant4 [79] at the 9% level in the total tracklength of electromagnetic showers in water.

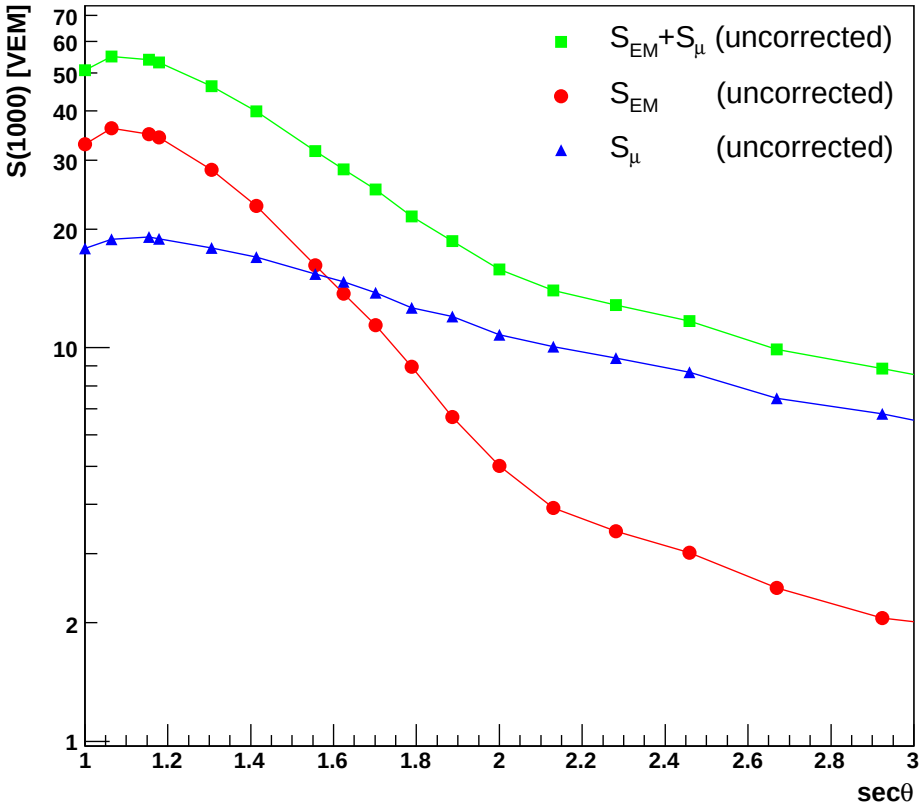

Figure 4.4: *First approximation of* $S(1000)$ *(see text) as a function of* $\sec\theta$ *for 10 EeV proton showers simulated with AIRES + QGSJET. Also shown are the uncorrected signals produced separately by the electromagnetic and muonic components.*

does affect the electromagnetic signal in Eqs. 4.18 and 4.19. Also the particle content in a shower at the ground evolves with zenith angle, and therefore the behaviour with θ of the uncorrected electromagnetic signal is due to a combination of both effects, whereas the behaviour of the uncorrected muonic signal is solely due to the dependence on θ of the muon number density at ground.

The previous estimate of the signal is an oversimplication. A number of effects in the tank were ignored. In the next sections, we will discuss these effects and their quantitative implementation as corrections in the estimate of the signal. We group the corrections into those specific to muons; those specific to electrons, positrons and photons; and finally those that apply to

both components.

4.1.2 Corrections to the muonic signal

The muonic signal must be corrected accounting for the following physical effects:

Cherenkov efficiency and stopping muons

Cherenkov emission is proportional to tracklength but the proportionality depends on the particle velocity β which is always smaller than 1. The number of Cherenkov photons produced per unit of tracklength by a particle with charge ze, velocity β, per unit of wavelength interval is:

$$\frac{d^2N}{d\lambda dx} = \frac{2\pi\,\alpha z^2}{\lambda^2}\left[1-\beta^{-2}n^{-2}(\lambda)\right] = \Phi(\beta) \tag{4.20}$$

where $\alpha = 1/137$ is the fine-structure constant and $n(\lambda) = 1.33$ is the refractive index of water at optical wavelengths.

Also, as muons lose energy continuously in water, they become less efficient in producing Cherenkov light, until their energy falls below the Cherenkov threshold ($E^{\mu}_{\rm th}$) and they produce no light at all.

To quantify the effect of muon energy loss on the Cherenkov efficiency, we calculate the effective muon tracklength L^{eff}_{μ} by integrating the muon path inside the tank, accounting for energy loss as given by [80],

$$-\frac{dE}{dx} = a(E) + b(E)E = f_{loss}(E) \tag{4.21}$$

where E is the total muon energy, $a(E)$ accounts for ionization losses and $b(E)$ is the stopping power due to hard processes (bremsstrahlung, pair production and nuclear interactions).

The effective muon tracklength is given by:

$$L^{eff}_{\mu} = \int_{E_f}^{E_i} \frac{f_{Ch}}{f_{loss}(E)}\,dE \tag{4.22}$$

where f_{Ch} is the Cherenkov efficiency factor given by,

$$f_{Ch} = \frac{\Phi(\beta \neq 1)}{\Phi(\beta = 1)} = \frac{1-n^{-2}\beta^{-2}}{1-n^{-2}} \tag{4.23}$$

which is shown in Fig. 4.5 as a function of the total muon energy. The Cherenkov efficiency factor for muons with energy above ~ 1.5 GeV is practically 100%.

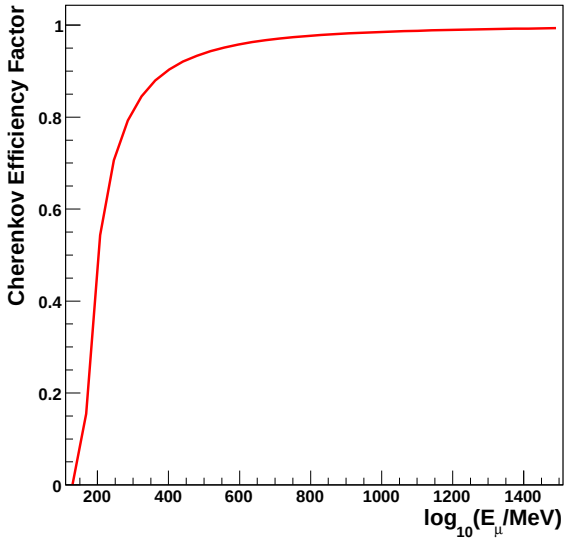

Figure 4.5: *Factor of the Cherenkov efficiency as a function of the total muon energy.*

The upper limit of the integral 4.22 is the total muon energy entering in the water E_μ (see Eq. 4.12). Regarding the lower limit of the integral E_f, its value depends on whether the muon stops inside or outside the tank. Both cases are discerned by comparing the uncorrected muon tracklength L_μ^θ which represents the maximum physically available average trancklength in the tank and the real muon tracklength (without considering the Cherenkov efficiency) L_μ^{real}. The real tracklength is calculated as:

$$L_\mu^{real} = \int_{E_{th}}^{E_i} \frac{1}{f_{loss}(E)}\, dE \tag{4.24}$$

with E_{th} the minimum total energy of a muon to produce Cherenkov light in water (see Eq. 4.13).

The two possible cases are:

- $L_\mu^\theta \geq L_\mu^{real}$, i.e., the muon becomes subthreshold inside the tank, and therefore the final energy of the muon is the Cherenkov energy threshold $E_{th} \sim 54.6$ MeV.

- $L_\mu^\theta < L_\mu^{real}$, i.e., the muon leaves the tank with energy above threshold. In this case, the lower limit E_f corresponds to the muon energy just

when it leaves the tank. We obtain the value of the final energy in this case by imposing that $L_\mu^{real} = L_\mu^\theta$ which gives the following equation,

$$L_\mu^\theta = \int_{E_f}^{E_i} \frac{1}{f_{loss}(E)}\, dE = g(E_i) - g(E_f)$$

$$g(E_f) = g(E_i) - L_\mu^\theta \tag{4.25}$$

We solve this equation for E_f numerically using the iterative method of Newton-Raphson.

Summarizing, the integral 4.22 gives us the equivalent track of an ultra-relativistic muon, accounting correctly for energy losses, the reduced Cherenkov emission as the muon loses energy continuously, and the fact that muons might become subthreshold inside the tank. At this stage, we neglect the contribution to the total signal from the electron produced when a muon decays inside the tank[2].

In Fig.4.6 we show the effective tracklength of a vertical muon as a function of energy. One can see that a vertical muon of energy above 2 GeV produces essentially the maximum possible amount of light that an ultra-relativistic muon can produce, that is, its Cherenkov efficiency is 100%. By inspecting figure 4.6, it is clear that this correction must also be applied to the calibration muons used to estimate the VEM unit. In fact, the peak corresponding to the VEM unit in the single muon spectrum used in calibration (see Section 3.2.1) is equivalent to monochromatic muons of 1.05 GeV of total energy [81]. At this energy, muons are relativistic and $f_{Ch}(1.05\text{ GeV}) \simeq 0.987$, so the VEM tracklength becomes reduced from 1.2 to 1.18 m.

The effect of this correction on the dependence of $S_\mu(1000)$ with zenith angle is shown in Fig. 4.8. The behaviour can be understood by looking at the top panel of Fig. 4.7, where we show the energy spectrum of muons at a distance of 1000 m from the shower axis for different zenith angles. For instance, the large reduction in $S_\mu(1000)$ of about 18% observed with respect to the uncorrected signal in Fig. 4.8 for vertical showers, is mainly due to the fact that about $\sim 35\%$ of the muons at r =1000 m have energies below 500 MeV and $\sim 60\%$ of these have energies below ~ 350 MeV. One can see in Fig. 4.6 that the large number of low energetic muons at this distance induces a large reduction in the muon tracklength of $\sim 10\%$ at 500 MeV and $\sim 70\%$

[2]It is interesting to note that even a subthreshold muon decaying inside the tank might produce an electron with energy above the Cherenkov threshold for electrons in water ($K_{th} \sim 250$ keV) that will contribute to the signal in the tank. This typically produces a pulse which is delayed by at least the lifetime of the muon.

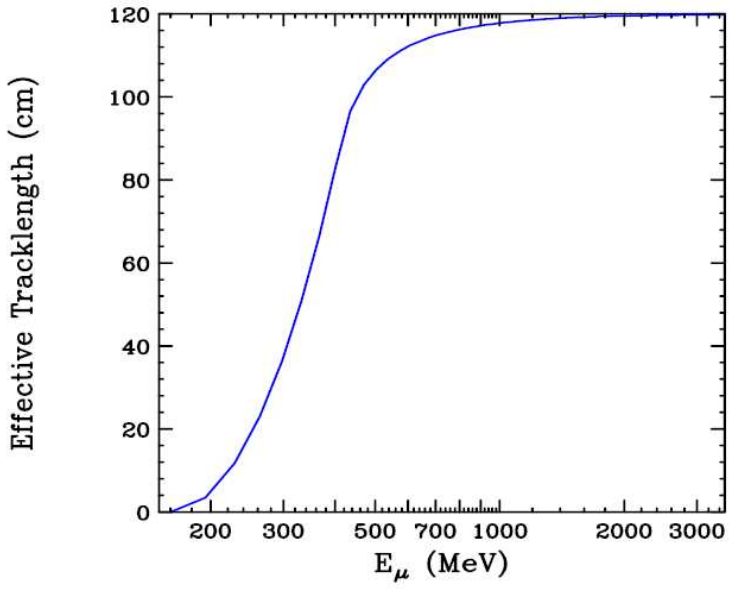

Figure 4.6: *Effective tracklength of muons crossing vertically as a function of the total muon energy.*

at 300 MeV with respect to the maximum track of 1.2 m. As a consequence, the muonic signal corrected for this effect is smaller than the uncorrected one. As the zenith angle increases, there are two compensating effects: on one hand the mean muon energy increases because muons have to travel longer distances in the atmosphere to survive at ground level and therefore, the lower energy muons decay before reaching the ground. For instance, in showers with θ =70° roughly 80% of the muons have energies larger than 2 GeV and a corresponding $\sim$ 100% Cherenkov efficiency (see Fig. 4.5). Hence the correction is expected to be less important as θ decreases. However, and on the other hand muons travel on average larger depths inside the tank (see Fig. 4.3) and therefore they lose more energy. It turns out that the first effect dominates and this correction becomes less and less important as zenith angle increases.

It should be remarked that our treatment of both effects namely, energy loss of muons coupled to Cherenkov efficiency, gives a much larger reduction in signal than a simpler approach using a constant energy loss for muons and the average value of E_μ of the entry and exit points in the tank, which only gives $\sim$ 7% of signal reduction with respect to the uncorrected one in vertical showers.

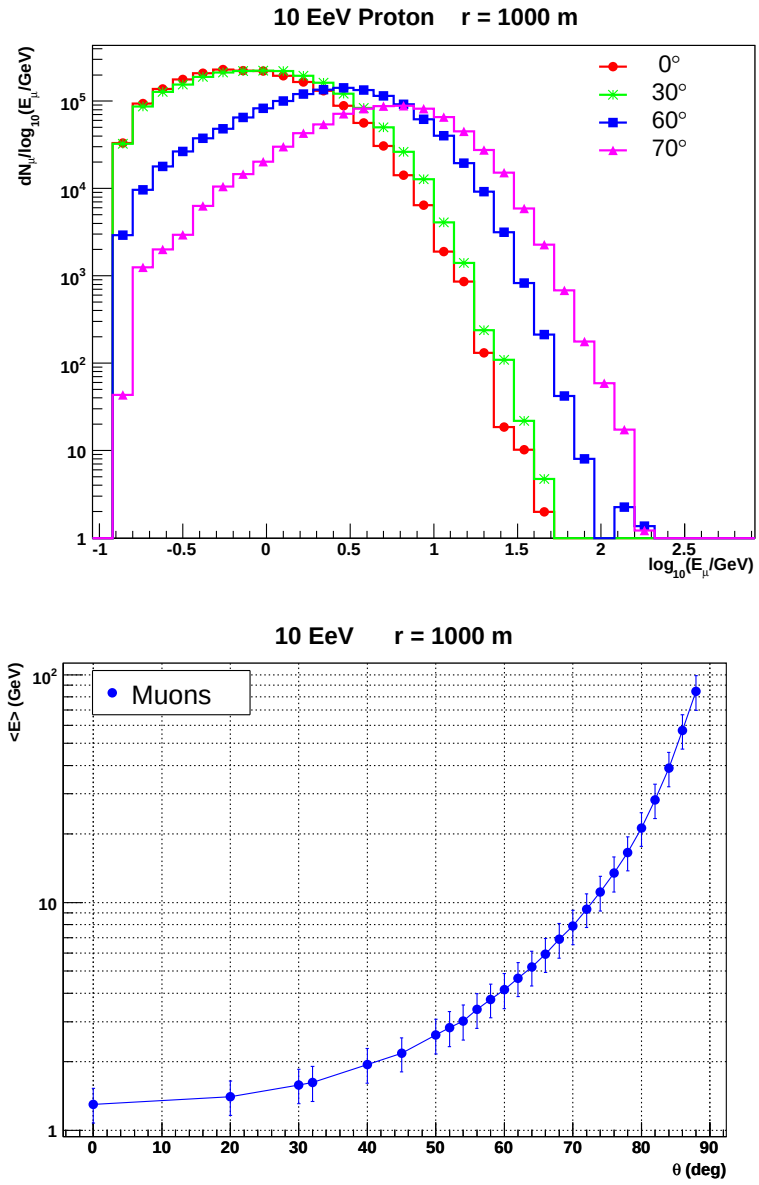

Figure 4.7: *Top panel: Energy spectrum of muons at 1000 m from the shower axis in the shower plane in 10 EeV proton showers simulated at zenith angles 0°, 30°, 60° and 70°. Bottom panel: Mean muon energy as a function of the shower zenith angle for muons at r =1000 m from the shower axis in 10 EeV proton showers.*

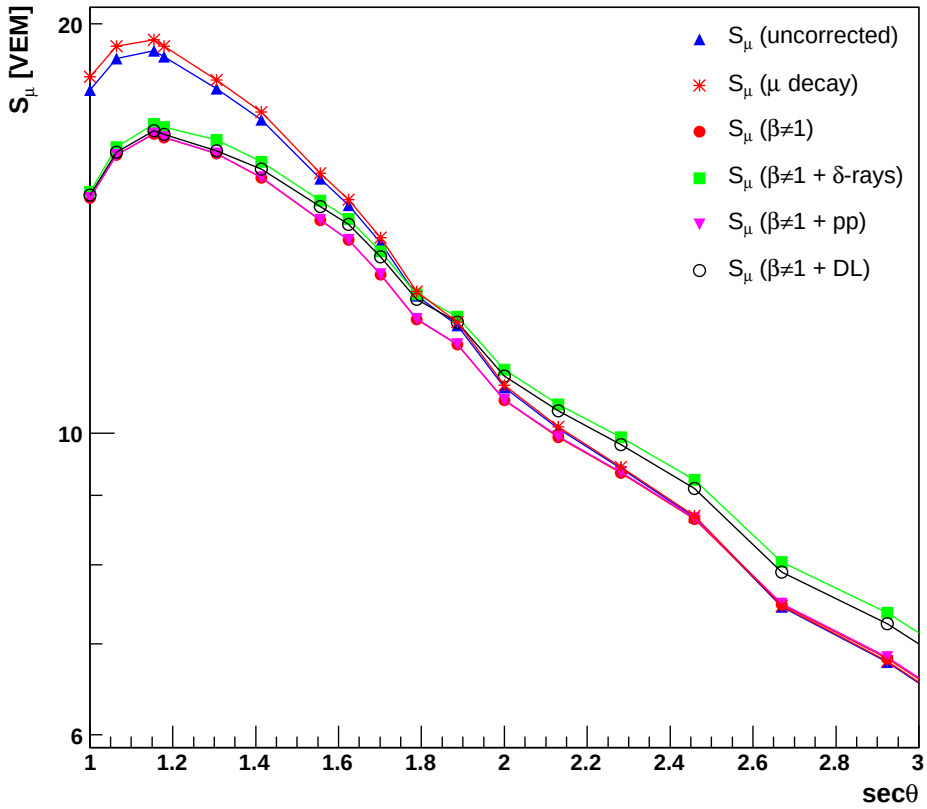

Figure 4.8: *Corrections specific to the muonic signal* $S_\mu(1000)$. *(1) The upward triangles correspond to the uncorrected signal. (2) The stars correspond to* S_μ *after including the corrections due to muon decay inside the tank. (3) The full circles show how* S_μ *is reduced after accounting for Cherenkov efficiencies and muon energy loss* ($\beta \neq 1$). *All the remaining curves include this first correction. (4) The squares correspond to* S_μ *after including the corrections due to* $\delta-$*rays. (5) The downward triangles correspond to* S_μ *including Cherenkov efficiency and pair production. (6) The empty circles correspond to* S_μ *including direct light hitting the PMTs in the tank. In this plot, we are assuming that particles travel parallel to shower axis. The simulation was performed for 10 EeV proton showers, with AIRES and the QGSJET hadronic model.*

Energetic knock-on electrons (δ-rays)

Muons also produce secondary electrons, called δ-ray electrons, along their paths inside the tank. They are mainly produced by the incident muon interacting primarily with a single atomic electron which is ejected from the atom with a considerable kinetic energy $K \gg I$ (I is the mean excitation energy). The kinetic energy distribution of secondary δ-rays per unit thickness x is given by [7, 82]:

$$\frac{d^2N}{dKdx} = C\frac{1}{\beta^2 K^2}\left(1 - \beta^2\frac{K}{K_{\max}} + \frac{K^2}{2E^2}\right) \tag{4.26}$$

for $I \ll K \leq K_{\max}$. Here $C = 2\pi r_e^2 m_e c^2 N_A z^2 Z/A$ is a constant that depends on the material ($C = 0.08445$ MeV cm^{-1} for water), β is the particle velocity, E is the total electron energy, and K_{max} is the maximum kinetic energy carried by δ-ray and given by:

$$K^e_{\max} = \frac{2m_e c^2\beta^2\gamma^2}{1 + 2\gamma(m_e/M) + (m_e/M)^2} \tag{4.27}$$

where M is the muon mass. The secondary δ-rays with kinetic energies above $K^e_{\rm th} = 0.264$ MeV will produce Cherenkov light, and will contribute to the total signal. The number of δ-rays produced by a muon track that will contribute to the signal is given by the integral of Eq. 4.26 from $K^e_{\rm th}$ to $K^e_{\max}$:

$$\frac{dN}{dx} = \frac{C}{\beta^2}\left[\left(\frac{1}{K^e_{\rm th}} - \frac{1}{K^e_{\max}}\right) - \frac{\beta^2}{K^e_{\max}}\ln\frac{K^e_{\max}}{K^e_{\rm th}} + \frac{K^e_{\max} - K^e_{\rm th}}{2E^2}\right] \tag{4.28}$$

The effect of the δ-rays contribution is equivalent to an increase in the effective muon tracklength,

$$L_\mu^{eff\,*} = L_\mu^{eff}\ (1 + r_\delta) \tag{4.29}$$

Using Geant4 simulations, a parameterization of this contribution as a function of muon kinetic energy (K_μ) and the real muon tracklength (Eq. 4.24) was obtained in [68] with the result:

$$r_\delta(K_\mu, L_\mu^{real}) = 0.135\ (0.8\sqrt{L_\mu^{real}} + 1)\ \frac{K_\mu}{0.8\sqrt{L_\mu^{real}} + K_\mu} \tag{4.30}$$

which is valid in the kinetic energy range [0.5,1000] GeV and in the tracklength range [0.3,3.8] m. For muons below 0.5 GeV, which stop inside the tank, we use an approximate constant correction: $r_\delta\ (K_\mu = 0.5\ \text{GeV}) \simeq 0.09$

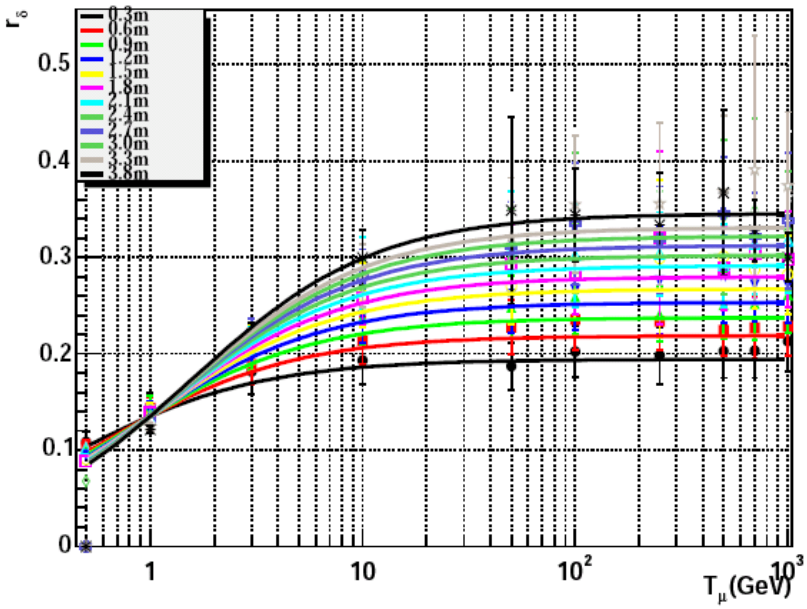

Figure 4.9: *Fraction of Cherenkov light produced by δ-rays taken from [68]*

which produces an increase in the effective muon tracklength of $L_\mu^{eff\,*} = L_\mu^{eff} + 0.09\ (K_\mu/0.5)$. In Fig. 4.9 (taken from [68]), r_δ is plotted as a function of the muon kinetic energy for different muon tracklengths. As one can see δ-ray production increases with the muon energy. The behaviour with the muon tracklength depends on the muon energy, so for muons below 1 GeV, r_δ decreases as the muon path rises due to muon energy loss. However, above this energy the larger the muon path, the bigger the increase because the muon can produce more energetic $\delta-$ray electrons before leaving the tank.

The correction to the muonic signal due to δ-rays must be taken into account in both the tracklength of the incident muon and the tracklength of a vertical muon, L_μ^{VEM}, which is needed to express both S_μ and S_{EM} in VEM units. The effective tracklength of vertical muons h^{eff} is obtained using the parameterization in Eq. 4.30 assuming a single spectrum of monochromatic muons of 1.05 GeV passing through the tank. We obtain a contribution of $r_\delta = 0.13$ for vertical muons, which corresponds to $h^{eff} \sim 1.35$ m. It is important to note that in this correction we have included the previous correction accounting for reduced Cherenkov efficiency and stopping muons.

The effect of the δ-rays correction on the dependence of S_μ with θ is shown in Fig. 4.8. One can see the increase of S_μ in all the $\sec\theta$ range with respect to the correction accounting only for the Cherenkov efficiency. For vertical

showers, the increase is smaller due to the large fraction of muons below 1 GeV that have $L_\mu^{eff\,*} < h^{eff}$. As zenith angle increases, the growth is larger because the average muon energy in the shower increases (see bottom panel of Fig. 4.7) and also the muon tracklengths inside the tank are larger.

Hard muon interactions

Muons can suffer hard interactions in the tank namely, bremsstrahlung (bs), pair production (pp) and nuclear interactions via photo-nuclear processes (ni). Eq. 4.21 is the corresponding expression for the energy loss per unit thickness, where $a(E)$ represents the ionization losses (ion) and $b(E)$ accounts for the hard processes,

$$b(E) = b_{bs}(E) + b_{pp}(E) + b_{ni}(E) \tag{4.31}$$

In Fig. 4.10 we show the rate of muon energy loss in water as a function of its kinetic energy [80]. The critical energy of muons in water is ~ 1 TeV, at this energy the ionization losses are equal to the losses due to hard processes. Pair production becomes the most relevant mechanism of energy loss followed by bremsstrahlung and finally photo-nuclear interactions. A detailed study of the contribution of the hard processes to the total signal was performed in [68]. On one hand, it was found that the pair production contribution (r_{pp}) increases with the muon energy and with its tracklength, a parameterization of this contribution is:

$$r_{pp}(K_\mu, L_\mu^{real}) = \frac{2.1 \times 10^{-4}\, L_\mu^{0.88}\, K_\mu}{1 + 3.7 \times 10^{-4}\, L_\mu^{-0.16}\, K_\mu} \tag{4.32}$$

In Fig. 4.11 taken from [68], we show the fraction r_{pp} as a function of the muon kinetic energy for different muon tracklengths.

It was also found in [68] that the contribution due to bremsstrahlung and photonuclear interactions can be neglected. Therefore, the effective muon tracklength corrected by hard muon interactions is:

$$L_\mu^{eff\,*} = L_\mu^{eff}\,(1 + r_{pp}) \tag{4.33}$$

Note that this correction also includes through L_μ^{eff} the correction due to Cherenkov efficiency and stopping muons. This correction must be also taken into account in the estimate of the VEM tracklength (h^{eff}) although it is practically negligible (about 0.02%).

The effect of the correction on the dependence of S_μ with zenith angle is shown in Fig. 4.8. We observe that the effect is completely negligible for the range of zenith angles considered because this correction starts to be

important at $K_\mu \simeq 250$ GeV and as one can see in the bottom panel of Fig. 4.7, the mean muon energy is much smaller than this value in this angular range. This correction will be only relevant if the muon energy is sufficiently high, i.e., close to the shower axis and for very large zenith angles.

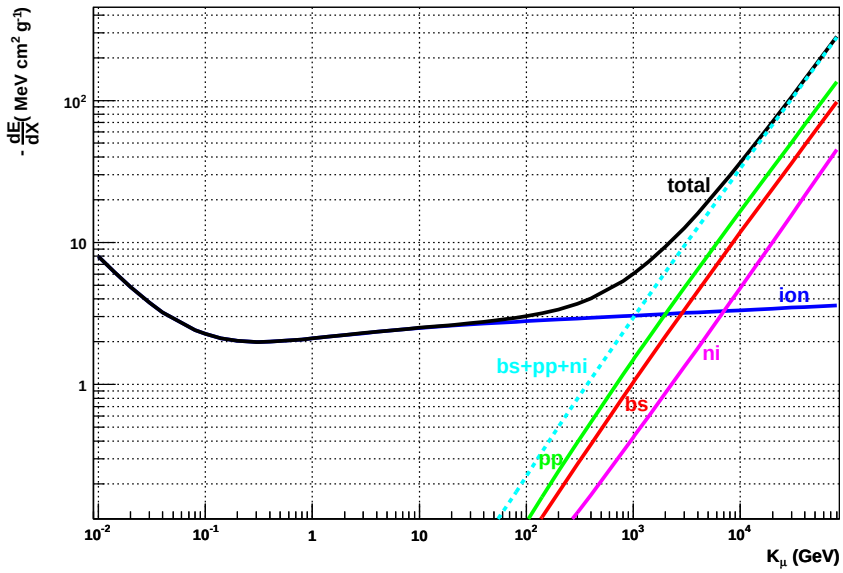

Figure 4.10: *Rate of muon energy loss in (liquid) water. The blue line shows the energy loss by ionization. The green line is the energy loss by pair production. The red line indicates the energy loss by bremsstrahlung. The pink line is the energy loss by nuclear interactions. The cyan dashed line is the energy loss by all the hard processes. The black line is the total energy loss.*

Muon decay inside the tank

A muon decays into an electron and two neutrinos (see Eq. 2.7) with a branching ratio $\simeq 100\%$. The probability that the muon decays inside the tank is:

$$P_{decay} = 1 - \exp\left(-\frac{< L_\mu^\theta >}{\lambda}\right) = 1 - \exp\left(-\frac{< L_\mu^\theta >}{\gamma\, c\tau}\right) \tag{4.34}$$

where $\gamma = E_i/m_\mu$ and $c\tau = 658.654$ m is the mean decay length of the muon. This probability is taken into account in this work as a correction to the muonic signal. If a muon decays inside the tank its tracklength is

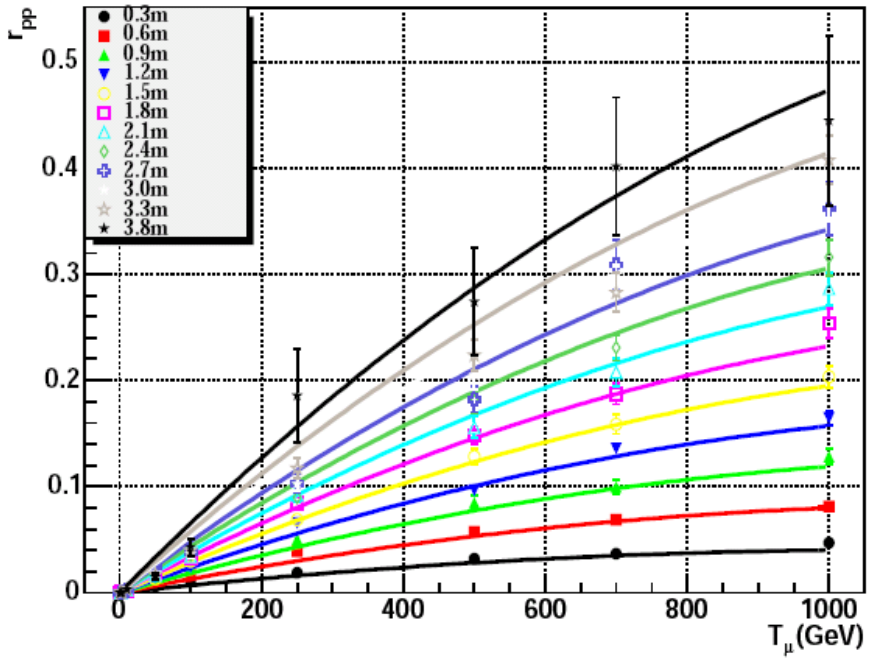

Figure 4.11: *Fraction of Cherenkov light produced by pair production processes taken from [68].*

reduced and hence the muon signal diminishes. We follow here a very simple treatment of this reduction and write that on average the reduction of the muon signal is:

$$S_\mu(r) = S_\mu(r)(1 - P_{decay}) \tag{4.35}$$

This correction is very small. Assuming that the muon decays at rest ($E_\mu = m_\mu$) and assuming the maximum possible tracklength ~ 2.7 m (see Fig. 4.3), the correction $(1 - P_{decay}) \simeq (1 - 4 \times 10^{-3})$ at most.

When a muon decays, the energy distribution of the resulting electron is known as the Michel spectrum, which has an endpoint at 53 MeV and an average electron energy of 37 MeV. The Michel electron may produce a signal in the tank if its energy is larger than the Cherenkov threshold, which we take into account as a correction to the muonic signal.

Following this simplistic treatment we assume that a muon decays only when it stops inside the tank. From the moment the muon becomes sub-threshold $E_{th} = 160.3$ MeV until it stops ($E_{th} = 105.7$ MeV), the muon crosses a distance of about $l = 0.274$ m inside the tank. Therefore, the muon

needs to travel a distance $L_{decay} = L_{\mu}^{eff} + l$ inside the tank to decay.

We assume that the stopping muon decays into a Michel electron of energy $< E_{Michel} >= 37$ MeV and two neutrinos after crossing a depth of L_{decay}. The subshower initiated by the Michel electron might not always be fully contained inside the tank. In fact there is a maximum distance available for the shower to develop given by:

$$d_{Michel} =< L_{\mu}^{\theta} > -L_{decay}$$

In this case, we correct the signal of each muon that stops inside the tank adding the signal produced by the Michel electron:

$$S_{\mu} = S_{\mu}(1 - P_{decay}) + S_{EM}^{Michel} \tag{4.36}$$

where the Michel electron signal is:

$$S_{EM}^{Michel} = \frac{k(E_{Michel})}{h_{eff}(1 + r_{h\delta} + r_{hpp})} E_{Michel} f^{cont} \tag{4.37}$$

with $k = 5.15$ m GeV^{-1}.

In the treatment of the signal produced by the Michel electron, we have accounted for all the corrections that affect the VEM unit (h_{eff}) and the corrections that affect the electromagnetic component of the shower that will be described in the following sections, namely: Fraction of the shower contained inside the tank (f^{cont}) and departure from linearity of the relation between energy and tracklength $k(E_{Michel})$. For a fully contained subshower initiated by a Michel electron of $< E >= 37$ MeV the signal is $S_{EM}^{Michel} \simeq 0.14$ VEM

Two important remarks: The effect of this correction is expected to be more relevant the lower the energy of the muons (they have a larger probability of stopping inside the tank) and the more inclined they are (they have a larger depth of water for the subshower initiated by the Michel electron to be fully contained). Also the signal produced by the Michel electron will be delayed in time by $\sim (l/c + \tau_0)$ with respect to the signal produced by the muon and in fact, S_{EM}^{Michel} might fall outside the time window in which the signal is collected by the detector. This effect is neglected here. The effect of the correction due to μ decay on the dependence of S_{μ} with θ is shown in Fig. 4.8.

4.1.3 Corrections to the electromagnetic signal

The electromagnetic signal must be corrected accounting for the following physical effects:

Shower containment in the tank

The uncorrected approximation to the EM signal assumes that all the energy in the electromagnetic component is fully deposited inside the tank. The fact is that the electromagnetic subshower initiated by secondary electrons, positrons and particularly photons, is not always completely contained in the tank. In fact it is possible for photons to go through the whole tank without producing no signal at all. To implement this effect, we have simulated a large number of photon, electron and positron induced showers in a large volume of water for different energies using the ZHS code to calculate the fraction of EM tracklength that develops inside a given depth. In the bottom panel of Fig. 4.12 we show examples of the resulting curves for photon showers for a wide range of energies. For a fixed depth, the fraction of energy deposited by a photon subshower inside that depth decreases with energy. For instance, on average a 10 MeV (20 MeV) photon deposits $\sim 90\%$ ($\sim 85\%$) of its energy in 1.2 m of water. For a fixed photon energy, the fraction increases with depth, or equivalently with the zenith angle of the shower (see Fig. 4.3).

We calculate the average depth of water available for the subshower to develop as $< d > (\theta) = V/A_\theta$ (this is the same equation that gives $< L_\mu^\theta >$). We parameterize the fraction of tracklength contained inside the tank as a function of the average depth available $< d >$ and of the particle energy for positrons, electrons and photons, and we obtain the following expression:

$$f^{cont}(E_i, \theta) = [\tanh(A < d >)]^B + C \tag{4.38}$$

where the parameters A, B and C depend on the particle energy, and the two first depend also on the particle type. Their values can be read in Table 4.1.

After correcting the total tracklength used in the first estimation for this effect, the electromagnetic signal becomes:

$$S_{EM}(r) = \frac{A_\theta}{A_{ring}(r)} \frac{k}{h} \sum_{i=1}^{N_{EM}} E_i w_i f_i^{cont}(E_i, \theta) \tag{4.39}$$

The effect of the correction on the dependence of S_{EM} with zenith angle is shown in Fig. 4.13. This correction produces a reduction on the electromagnetic signal with respect to the uncorrected one, and in fact it is the most important EM correction at all zenith angles. There is a decrease in the uncorrected S_{EM} by about 16.5% at 0° and about 18.9% at 60°. This behaviour can be understood looking at Fig. 4.14 where we show the energy spectrum of electrons and positrons (top panel) and photons (bottom panel) at a distance of 1000 m from the shower axis for different zenith angles. For

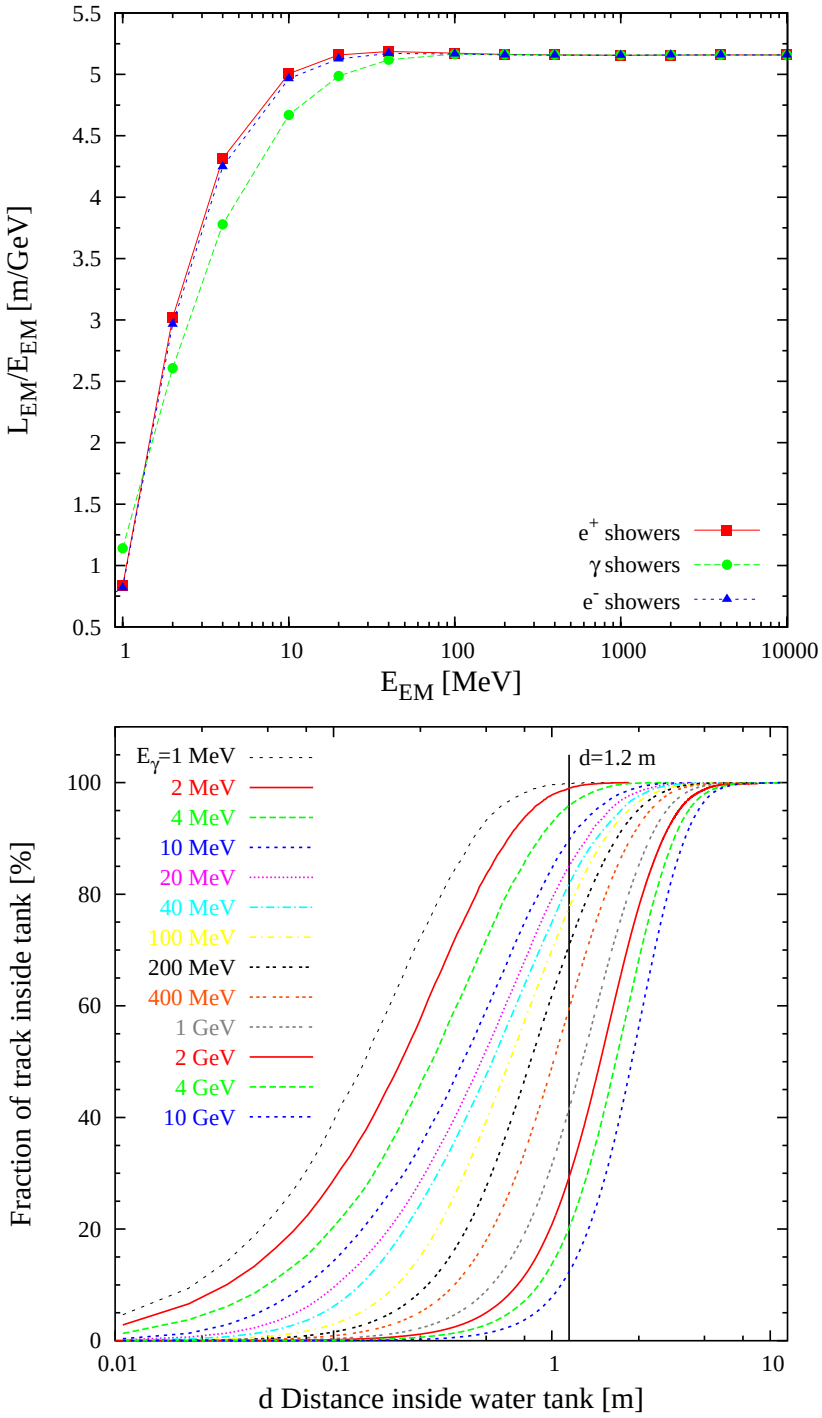

Figure 4.12: *Top panel : k_i as a function of electromagnetic energy showing the departure from linear scaling with energy. Bottom panel: Fraction of tracklength contained inside the tank in photon induced subshowers of different energies as a function of distance inside the tank.*

E (MeV)	A_γ	B_γ	A_{e^-}	B_{e^-}	A_{e^+}	B_{e^+}	C
1.	3.19336	0.80024	0.	0.	2.40062	0.0028627	1.
2.	2.21491	0.805152	0.	0.	1.81648	0.00408368	1.
4.	1.60917	0.823809	231.018	15.1113	97.3032	0.977079	0.
10.	1.16089	0.826219	38.4995	1.35635	32.7209	1.15589	0.
20.	1.0136	0.881936	16.6198	1.2748	13.5751	1.05314	0.
40.	0.92851	0.913472	7.01112	1.09468	5.08748	0.817457	0.
100.	0.9109	1.11474	2.29793	0.91754	1.89732	0.795238	0.
200.	0.86014	1.37832	1.31594	0.994075	1.23131	0.962837	0.
400.	0.76394	1.62843	0.966934	1.24693	0.946752	1.23706	0.
1000.	0.65279	2.05272	0.751189	1.6555	0.74017	1.65012	0.
2000.	0.59384	2.46554	0.652856	2.0446	0.664692	2.03622	0.
4000.	0.54622	2.8765	0.600476	2.38313	0.59809	2.36559	0.
10000.	0.51189	3.59528	0.538004	2.8438	0.532596	2.80372	0.

Table 4.1: *Results of the fitted parameters for the fraction of total electromagnetic track-length contained inside the tank given by Eq. 4.38.*

instance, for $\theta = 0°$ roughly 50% of the photons have energies larger than 40 MeV, and by looking at the curves in the bottom panel of Fig. 4.12 this implies that they are depositing about 20% of their energy outside the tank.

It is also important to keep in mind that the electromagnetic component contributes only about 20% to the total signal above 60°, so the relative contribution of this effect is small, on the order of $\sim 4\%$ reduction in the total signal at large zenith angles.

Effect of δ-rays on the VEM unit

As previously mentioned, the effect of the δ-rays emitted by muons must be taken into account in the effective tracklength of a vertical muon, i.e., in the normalization used to express S_{EM} in units of VEM (see Eq. 4.19). This is not a correction due to a process that affects the electromagnetic component, but it is included in this section because it affects the EM signal by increasing the effective tracklength of a calibration muon and producing a constant reduction of the signal by a factor 1.13 (a constant reduction in $S_{EM}(1000)$ of about 10%) as shown in Fig. 4.13. This effect turns out to be the next in importance after the containment of the shower described above.

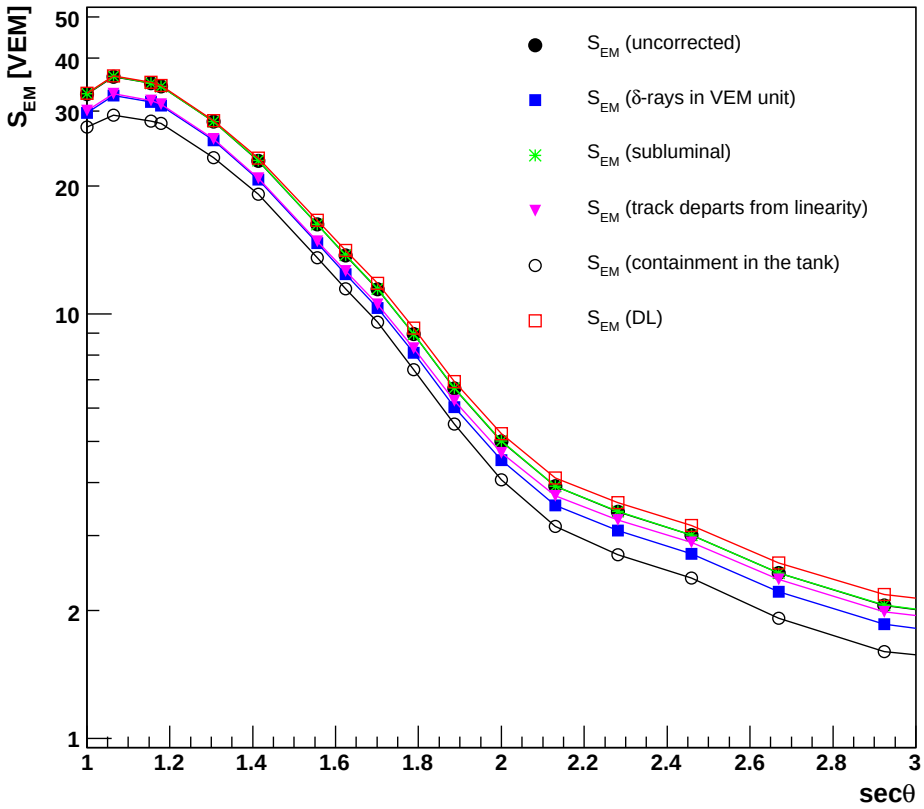

Figure 4.13: *Corrections specific to the electromagnetic signal* $S_{EM}(1000)$. *(1) The full circles correspond to the uncorrected signal. (2) The full squares correspond to* S_{EM} *accounting for subluminal particles* ($\beta \neq 1$). *(3) The stars correspond to* S_{EM} *after accounting for the departure of the tracklength from linearity. (4) The triangles correspond to* S_{EM} *after including the corrections due to* $\delta-$*rays in the normalization to VEM units. (5) The empty circles correspond to* S_{EM} *taking into account that the secondary shower might not be completely contained inside the tank. (6) The empty squares correspond to* S_{EM} *including direct light hitting the PMTs in the tank. In this plot, we are assuming that particles travel parallel to shower axis. The simulation was performed for 10 EeV proton showers, with AIRES and the QGSJET hadronic model.*

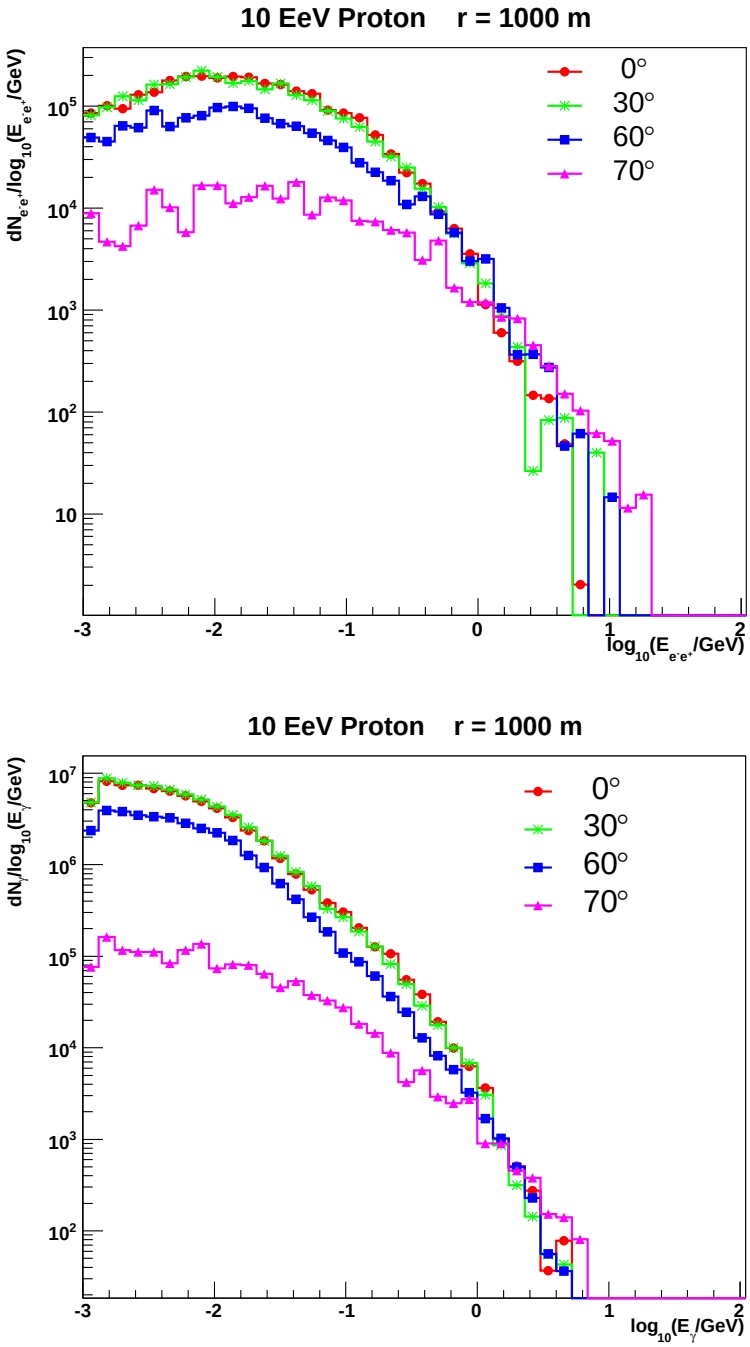

Figure 4.14: *Energy spectrum of electrons+positrons (top panel) and photons (bottom panel) at 1000 m from the shower axis in the shower plane for simulated 10 EeV proton showers at zenith angles 0°, 30°, 60° and 70°.*

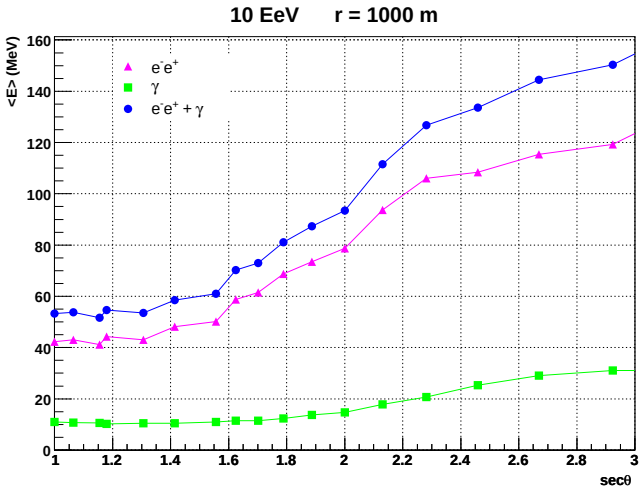

Figure 4.15: *Mean energy of the electromagnetic component as a function of the shower zenith angle at 1000 m from the shower axis at the shower plane for 10 EeV proton showers.*

Departure of the EM tracklength from linear scaling with energy

In the calculation of the uncorrected EM signal, the total tracklength of an electromagnetic shower was assumed to scale linearly with the particle energy. This scaling breaks down for low energies mainly because of the steep rise of the energy loss of electrons. At low energy, electrons and positrons lose energy by collisional processes, primarily ionization, although other processes (Möller scattering, Bhabha scattering, e^+ annihilation) also contribute. The ionization loss rate varies only logarithmically with the electron energy. At higher energies, electrons also lose energy by radiative processes, mainly bremsstrahlung whose loss rate is nearly proportional to the electron energy. The total energy loss for electrons is the sum of the collisional and radiative losses:

$$\frac{dE}{dx} = \left(\frac{dE}{dx}\right)_c + \left(\frac{dE}{dx}\right)_r \tag{4.40}$$

In Fig. 4.16 we show the fractional energy loss rate of an electron in water as a function of its kinetic energy [83]. This graph illustrates how the electrons lose energy rapidly by ionization at low energies. This rapid energy loss is the main cause of the break of the linear scaling of tracklength with energy at energies below $\sim$ 20 MeV. This can be seen in the top panel of Fig. 4.12 where we plot $k = L_{EM}/E_{EM}$ obtained with the ZHS code as a function of E_{EM} for electron, positron and photon showers. The break of the linear behaviour of L_{EM} with E_{EM} is apparent below $E_{EM} \sim 20$ MeV in

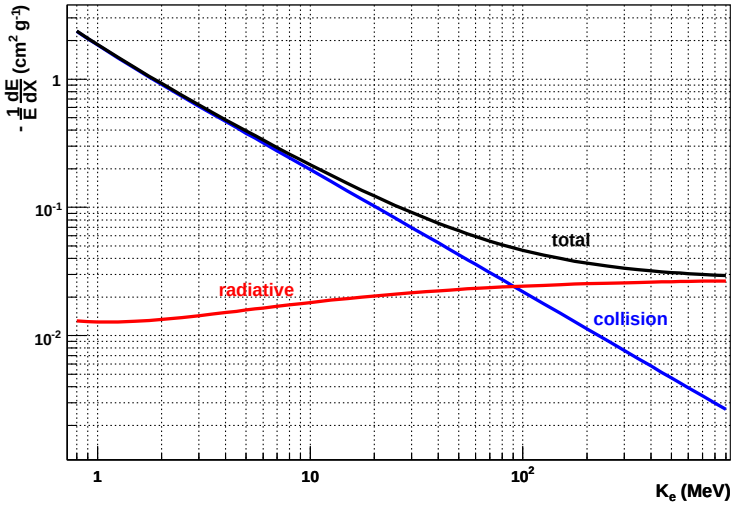

Figure 4.16: *Fractional energy loss per radiation length in (liquid) water as a function of electron kinetic energy. The blue line corresponds to the energy loss by ionization (collisional processes). The red line indicates the loss by bremsstrahlung (radiative processes). The black line is the total energy loss. Data taken from [83]*

electron initiated showers. To implement this on the signal calculation, we have parameterized $k_i = L_{EM}/E_{EM}$ as a function of the total energy of the electromagnetic particle:

$$k_i = \frac{\tilde{A} \times 1000}{1 + \tilde{B}\,(E_i/GeV)^{\tilde{C}}} \tag{4.41}$$

where the parameters $\tilde{A}$, $\tilde{B}$ and $\tilde{C}$ depend on the particle type. Their values are given in Table 4.2.

The appropriate tracklength sum over the electromagnetic particles reaching the sampling area A_{ring} can be easily performed taking into account their energy and type. Therefore, the electromagnetic signal in the tank is given by:

$$S_{EM}(r) = \frac{A_\theta}{A_{ring}(r)}\,\frac{1}{h}\,\sum_{i=1}^{N_{EM}} k_i(E_i)\;E_i w_i \tag{4.42}$$

	$\tilde{A}$	$\tilde{B}$	$\tilde{C}$
e^-	0.0051579538	4.29031	-2.32855
e^+	0.0051584995	4.30260	-2.41297
γ	0.0051565933	3.16719	-1.57263

Table 4.2: *Results of the fitted parameters for k_i (Eq. 4.41).*

where the index i runs over the total number of electrons, positrons and photons generated by AIRES in the sampling area A_{ring}. The effect of this correction on the electromagnetic signal $S_{EM}(1000)$ can be seen in Fig.4.13. This correction produces a reduction in the electromagnetic signal of the order of 8.7% at 0° with respect to the uncorrected one (as expected). The reduction becomes smaller as the zenith angle increases because the mean energy of the electromagnetic particles reaching ground rises with θ (see Fig. 4.15).

Subluminal particles

The secondary electrons and positrons are also subject to inefficiencies in generating Cherenkov light because their energies and hence velocities decrease as they are generated in the subshower that develops inside the tank. Following the procedure applied to the muonic correction, we have calculated the effective tracklength for electrons and positrons in the ZHS code, weighting the contribution to the total track by each particle by the efficiency factor $(1-n^{-2}\beta^{-2})/(1-n^{-2})$. For this purpose, the track of each particle is subdivided in small steps and the mean β in each step is calculated. Finally, the electromagnetic track is obtained as $L_{EM} = \tilde{k}E_{EM}$ where the proportionality constant is $\tilde{k} = 5.16$ m GeV^{-1} instead of $k = 5.25$ m GeV^{-1} which was obtained assuming the Cherenkov efficiency was 100% regardless of electron or positron energy. The overall effect on the uncorrected S_{EM} is a reduction by a constant factor of $k/\tilde{k} \sim 1.02$. However, this correction is nearly canceled out by the same correction applied to the vertical calibration muons, which has the effect of increasing the electromagnetic signal by a factor $1.2/1.18 \sim 1.02$ (see Section 4.3.1.). The result of both effects is an increase in S_{EM} of only 0.13% with respect to the uncorrected one (see Fig. 4.13).

4.1.4 Corrections to both muonic and electromagnetic signals

For the moment we have assumed that the signal is proportional to the tracklength of the muon entering the tank or to the tracklength of the subshower initiated by an electron, positron or photon interacting inside the tank. However a fraction of the light emitted by these particles arrives directly to the PMTs and has been shown in [68] to be approximately independent of the tracklength of the particle. Also for the moment we have assumed that all particles travel parallel to the shower axis while in reality each particle enters the tank with a different zenith angle. These two effects will be discussed in this section.

Direct light in the tank

The Pierre Auger tanks were designed to have an uniform response to shower particles in azimuth angle. For this purpose the inner reflective surface of the tank favours the light diffusion process. As a result, the fraction of light collected by each PMT is to some extent independent of the impact parameter of the incoming particle. This approximate uniformity is not fulfilled for particles which incide on the tank with an angle exceeding the complementary of the Cherenkov angle in water, $\theta_0 = 48.8°$. In this case, the Cherenkov light cone can intercept a PMT and a fraction of the Cherenkov light may fall directly onto it. This has been extensively studied using Geant4 in [84, 85, 86], concluding that direct light is strongly dependent on zenith and azimuth angles, and on the impact parameter. Recently in [68] the dependence of the contribution of the average direct light to the signal as a function of the zenith angle, $f_{DL}(\theta)$, was studied for several energies, and the following parameterization (independent of particle energy) was obtained:

$$f_{DL}(\theta) = 0.005 + \Theta(\theta - 40.)\,(-0.0746 + 0.00186\theta) \tag{4.43}$$

with Θ the Heaviside step function. The small and constant direct light contribution of 0.005 is due to the direct light produced by $\delta-$rays and also by muons that hit the PMTs directly.

This correction to the signal affects both the EM and muonic signals that are given by,

$$S_{EM,\mu} = S_{EM,\mu}^{uncorrected}\,(1 + f_{DL}) \tag{4.44}$$

where f_{DL} in Eq. 4.43 corresponds to the mean value of the direct light contribution of muons when we average over the azimuth angle, which is exactly what we need to implement this effect in the calculation of the mean signal in the tank.

The correction accounting for direct light in the EM component is expected to be less important because at small zenith angles, at which the EM component contributes most to the total signal, it is practically non-existent, and at large zenith angles the total signal is dominated by muons. Although there are not specific studies in which this effect has been addressed, we use the same parameterization for the EM component as in the muonic case as a first order approximation.

The effect of direct light in both the EM and muonic signal is the production of an extra signal in the tank. In Fig.4.8 the effect on S_μ is an increase of the signal with θ so that for very inclined showers the correction can be as large as 10%. The same effect is seen in Fig.4.13 for the electromagnetic signal.

Particle deviations from the shower axis

So far we have worked under the assumption that all the particles travel parallel to the shower axis, and therefore we have assumed that they all enter the tank with an angle θ_i equal to the zenith angle of the shower. The fact is that the particles deviate from the shower axis and therefore we must take into account the true zenith angle of the particle in many of the corrections described above:

- The area of the detector has to be projected onto the plane perpendicular to the arrival direction of each particle. As a consequence, in Eq. 4.19 the area A_θ must be replaced by A_{θ_i}, where the index i runs over all the particles produced in the shower simulation. The sampling area A_{ring} must be also projected onto this plane $A_{ring}(r, \theta_i)$. The latter correction affects the calculation of both muon number densities and electromagnetic energy densities:

$$\rho_\mu(r) = \sum_{i=1}^{N_\mu} \frac{w_i}{A_{ring}(r, \theta_i)}$$

$$\epsilon_{EM}(r) = \sum_{i=1}^{N_{EM}} \frac{E_i\, w_i}{A_{ring}(r, \theta_i)} \tag{4.45}$$

- The corrections of Cherenkov efficiency and muons becoming subthreshold depend on the zenith angle of the particle because they depend on the maximum available depth of water: L_μ^θ

- The correction that accounts for the probability of muon decaying inside the tank also depends on the path traveled by the muon inside the tank L_μ^θ, and hence on the angle of the particle.

- Particle deviations from the shower axis also affects to the containment of the shower induced by an electron, positron or photon inside the tank. This is due to the fraction of total tracklength contained inside the tank (Eq. 4.38) depending on the available depth of water $< d > (\theta_i) = V/A_{\theta_i}$ for the shower to develop.

- The correction due to direct light depends on the angle of incidence of the particles: $f_{DL}(\theta_i)$.

To quantify the effect of this correction we firstly compute the total signal taking into account all the corrections but assuming that particles are parallel to shower axis. The signal can be expressed as:

$$S_\mu(r) = \sum_{i=1}^{N_\mu} w_i \frac{A_\theta}{A_{ring}} (1 - P_{decay}) \, (1 + f_{DL}) \, \frac{1}{h_{eff}(1 + r_{h\delta} + r_{hpp})} \; L_\mu^{eff} (1 + r_\delta + r_{pp}) + \sum_{i=1}^{N_\mu} w_i \frac{A_\theta}{A_{ring}} S_{EM_i}^{Michel} \tag{4.46}$$

$$S_{EM}(r) = (1 + f_{DL}) \, \frac{A_\theta}{A_{ring}} \, \frac{1}{h_{eff}(1 + r_{h\delta} + r_{hpp})} \; \sum_{i=1}^{N_{EM}} k_i \, E_i w_i \, f_i^{cont} \tag{4.47}$$

We also compute the total signal but this time accounting for the actual direction of the particles obtained in the simulation. The two signals are shown in Fig. 4.17. As one can see, accounting for the directions of the particles modifies very little the $S(1000)$ curve especially at large zenith angles. To gain more insight on the relevance of this correction, we plot in Fig. 4.18 the distribution of incidence zenith angles of the particles at 1000 m from the shower axis for vertical (left panel) and inclined showers (right panel). The fact that this correction is very small at large zenith angles is due to the muonic component being dominant as one can see in Fig. 4.18, and to the fact that muons deviate very little from the shower axis partly because only the more energetic muons reach the ground. There is also some degree of compensation because in a non vertical shower, and in the early region of the shower, the particles will typically enter the tank with zenith angles

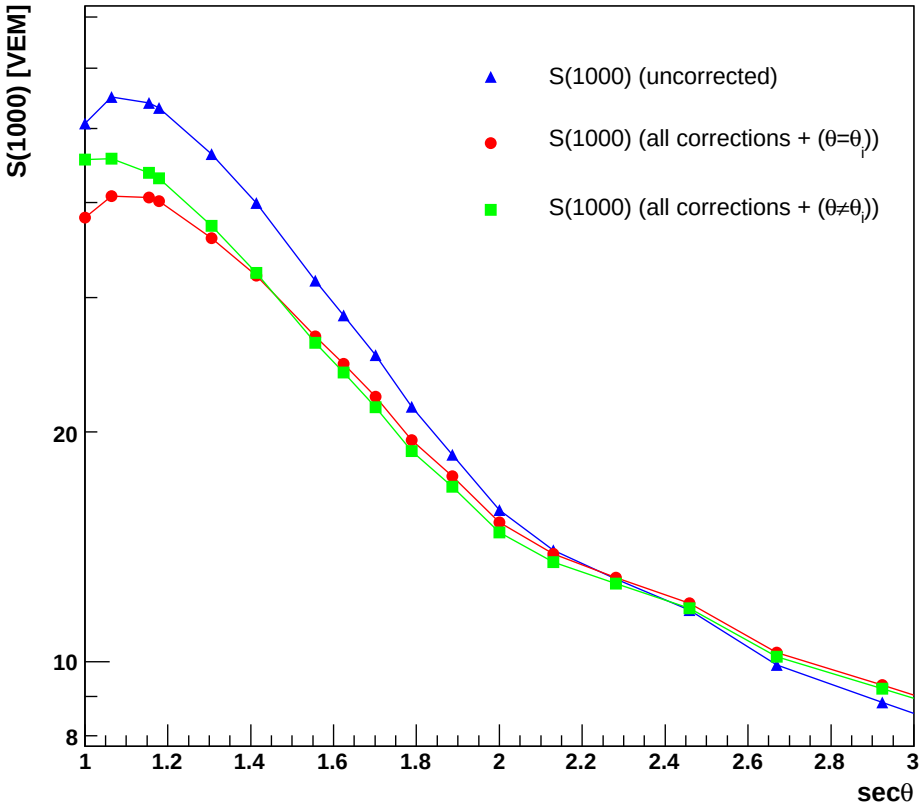

Figure 4.17: *Attenuation of* $S(1000)$ *with the zenith angle of the shower including all the corrections. The circles represent the signal assuming that particles travel parallel to the shower axis,* $\theta_i = \theta$*. The triangles represent the signal accounting for particles not travelling parallel to the shower axis. The squares correspond to the uncorrected signal. The simulations were done for 10 EeV protons with AIRES and the QGSJET model.*

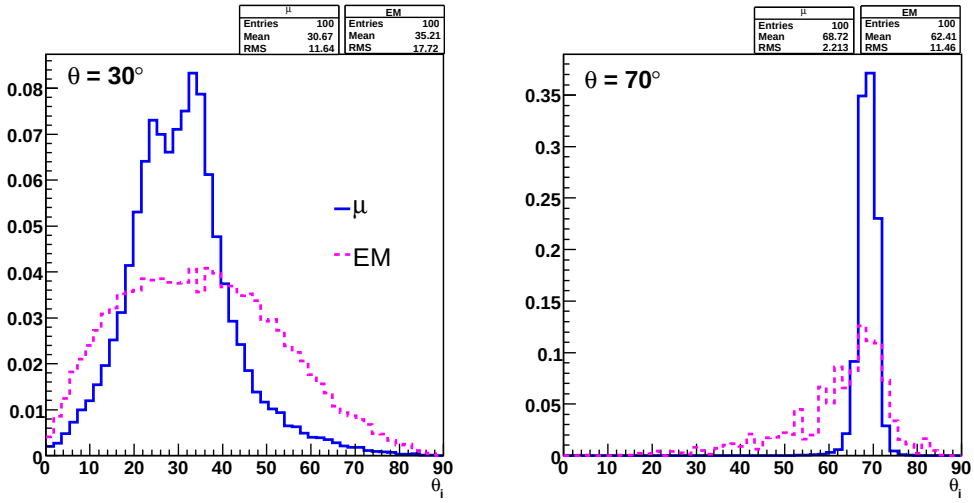

Figure 4.18: *Distribution of the zenith angle of incidence of a particle in at 30° (left panel) and 70° (right panel) showers at 1000 m from the shower axis. The continuous lines correspond to the distribution for muons. The dashed lines correspond to the distribution for electrons, positrons and gammas.The simulations were done for 10 EeV proton with AIRES and the QGSJET model.*

smaller than the shower zenith angle, while in the late region the opposite behaviour occurs (see Fig. 5.7).

However, in showers with small zenith angles the large spread in the arrival directions of muons and electromagnetic particles (left panel of Fig. 4.18) produces an increase of both the muonic and electromagnetic signals with respect to the case in which the direction of the particles was not accounted for. Moreover, for $\sec\theta \lesssim 1.1$ ($\theta \lesssim 30°$) the increase is such that the $S(1000)$ curve flattens. This is mainly due to the combination of two effects. On one hand, a large fraction of electromagnetic particles in showers with $\theta \lesssim 30°$ arrive at ground with θ_p around 25°, and therefore their corresponding projected tank areas reach the highest possible value. On the other hand, the EM particles in showers with $\theta \lesssim 30°$ practically have the same energy spectrum regardless of the zenith angle (see Fig. 4.14). As a consequence and since the effects of all corrections to the EM signal depend only on the energy and θ_i of the particles (see Eq. 4.47), one expects $S(1000)$ to be rouhgly independent of θ for $\theta \lesssim 30°$.

4.1.5 Corrected signal

The final total signal at r =1000 m from the shower core, after accounting for all the effects described in the previous sections, is shown in Fig. 4.19. The most important correction to the electromagnetic component of the signal is due to the secondary shower not being completely contained inside the tank. For the muons it is the energy loss and inefficiencies in the Cherenkov yield. Most of the corrections tend lower the signal. As a result the corrected $S(1000)$ curve is below the uncorrected one for $\theta < 64°$. For zenith angles $\theta > 64°$, the signal is larger then the uncorrected one mainly due to the effect of the direct light.

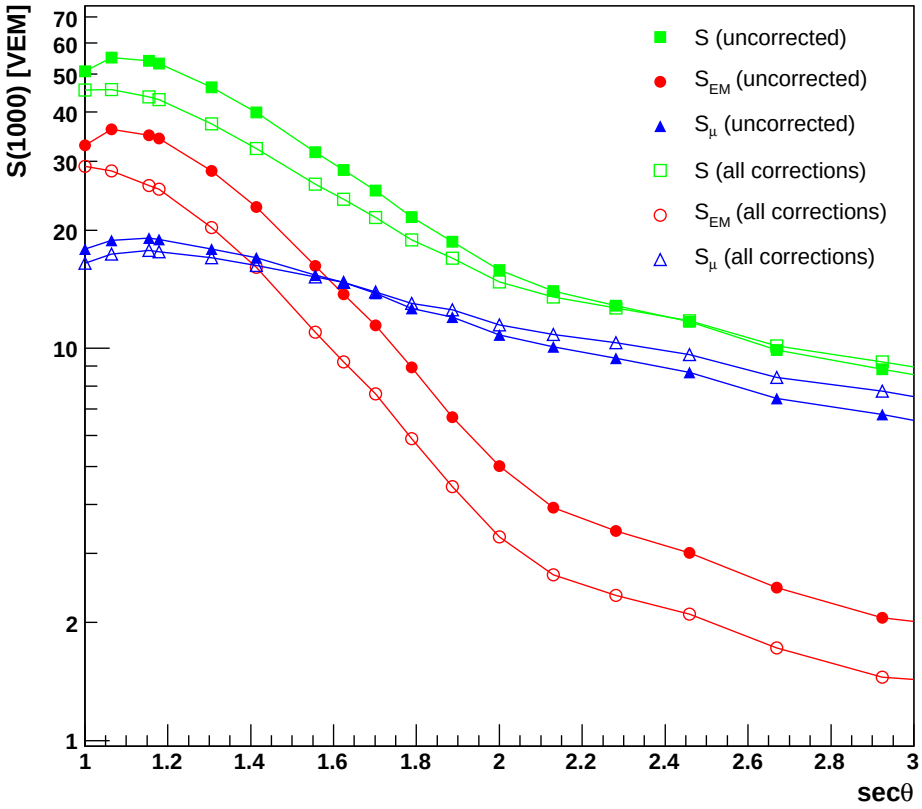

Figure 4.19: *Comparison between uncorrected and corrected electromagnetic, muonic and total signals vs* $\sec\theta$ *at 1000 m from the shower axis. The simulations were done for 10 EeV proton with AIRES and the QGSJET model.*

4.2 Comparative study between S(1000) USC code and Geant4

The aim of this section is to compare our code with a well known, accurate and tested simulation of the passage of particles through matter such as Geant4. For this purpose, we compare the response of the tank to single particles instead of the response to particle showers. In this way we avoid having to employ unthinning algorithms that might be different in our $S(1000)$ code and in the Offline framework where Geant4 is implemented which can introduce artificial differences. We have performed a comparative study of the response to vertical and inclined individual particles of the $S(1000)$ USC code and Geant4 code for different particle kinetic energies.

We used the fast version of the package Geant4 [72] implemented in the G4FastTankSimulatorPS Offline module. The fast version of Geant4 was developed by the Pierre Auger Collaboration [96] to optimize the performance of the existing Geant4 tank simulator, re-writing the code for fast and efficient tracking of the Cherenkov photons in the Auger tank. The goal was to reach the best compromise between accuracy in the detector response and CPU time. The computing speed is 5 times faster than the original Geant4. The output of Geant4 and the fast Geant4 is statistically indistinguishable.

The particles were injected (using the ParticleInjectorOG Offline module) at 1.35 m of height all over the tank surface after projecting it onto the plane tranverse to the particle direction, in order to average over all the impact parameters [3]. The signal in Geant4 is given in number of photoelectrons (pe), and it must be converted into VEM units. The simulation of the tank calibration needed for this purpose was performed using as input vertical and centered muons of 1.05 GeV, obtaining that 1 VEM corresponds to 89.53 ± 9.06 pe.

The signal in VEM produced by muons, electrons, positrons and photons was obtained for different kinetic energies and zenith angles of the injected particles using Geant4 and the $S(1000)$ USC code.

The results of the comparison of the response of both codes to muons, electrons, positrons and gammas are shown in Tables 4.3, 4.4, 4.5 and 4.6 respectively. The relative differences between both codes taking Geant4 as reference are within the RMS of the Geant4 output.

For muons, the relative differences between both codes are less than 10% at all energies. At intermediate energies, we expect part of the discrepancy to be due to the fairly simplistic treatment of the muon decay process in the

[3] Note that in the $S(1000)$ approach the average over impact parameter is done implicitly when calculating the average μ, e^-, e^+ and γ tracklengths.

$S(1000)$ USC code. For instance at $K = 0.4$ GeV and $\theta = 75°$, a muon stops after crossing a mean distance (L_{decay}) which is just a bit smaller than the maximum physical distance inside the tank ($< L_{\mu}^{\theta} >$). In this case and in the $S(1000)$ USC code, the muon always decays inside the tank into a Michel electron with $< E_{Michel} >= 37$ MeV. However in Geant4, the muon might not decay inside the tank because Geant4 takes into account the different tracklengths of the muon inside the tank depending on the sampled impact parameter, evaluates the corresponding decay probability and accounts for the energy distribution of the Michel spectrum. More generally, if the muon decays well outside the tank ($L_{decay} \gg < L_{\mu}^{\theta} >$) or well inside the tank ($L_{decay} \ll < L_{\mu}^{\theta} >$), we do not expect a significant discrepancy between codes due to the implementation of the muon decay process. Only at those energies and angles at which L_{decay} is approximately equal to the available tracklength inside the tank we expect large differences due to the different treatment of the muon decay in Geant4 and S(1000) USC.

K **(GeV)**	θ_i (deg)	S_{G4} (VEM)	S_{USC} (VEM)
0.1	45.	0.179 ± 0.112	0.196 (9)
0.1	75.	0.171 ± 0.118	0.192 (12)
0.4	45.	0.801 ± 0.349	0.878 (10)
0.4	75.	0.965 ± 0.441	1.260 (30)
1.	45.	1.010 ± 0.481	1.016 (0.6)
1.	75.	1.565 ± 0.940	1.611 (3)
10.	45.	1.138 ± 0.630	1.123 (-1)
10.	75.	1.921 ± 1.341	1.814 (-6)

Table 4.3: *Muon signal in VEM in an Auger tank as obtained in Geant4 and the $S(1000)$ USC code for different kinetic energies and angles of incidence. The results of Geant4 show the average over all impact parameters. The numbers in parenthesis indicate the relative differences ($(S_{G4} - S_{USC})/S_{G4}$ in %) using the Geant4 result as reference.*

For the electromagnetic particles, the relative differences are $\sim 25\%$ at most, with the electromagnetic signal obtained with the $S(1000)$ USC typically higher. This discrepancy is expected because the total tracklength of an EM subshower in the the ZHS code (the results of which are used in $S(1000)$ USC) is about 10% larger than the track obtained with Geant4 as discussed in [79]. This difference between ZHS and Geant4 is due to the different implementation of the relevant electromagnetic processes. The difference seems to be larger at high θ, however the contribution of the EM component to the total signal in large θ showers is expected to be small ($< 15\%$) and hence the

impact of these differences in the total signal is expected to be smaller than 3%.

In conclusion, the agreement between $S(1000)$ USC code and Geant4 is generally good with differences of less than 10% for muons and 20% for electrons, positrons and gammas, all within the RMS of the Geant4 output. Finally it is important to remark that the distributions of the signal obtained with Geant4 have fairly large RMSs, mainly due to the correct account for the variations in particle tracklengths correlated with the different impact parameter of the particles [97].

K **(GeV)**	θ_i (deg)	S_{G4} (VEM)	S_{USC} (VEM)
0.01	45.	0.022 ± 0.024	0.022 (0)
0.01	75.	0.016 ± 0.015	0.013 (-19)
0.04	45.	0.138 ± 0.063	0.142 (3)
0.04	75.	0.124 ± 0.071	0.140 (13)
0.1	45.	0.330 ± 0.129	0.376 (14)
0.1	75.	0.351 ± 0.172	0.390 (11)
1.	45.	2.115 ± 1.143	2.248 (6)
1.	75.	2.681 ± 1.472	3.305 (23)

Table 4.4: *Signal produced by an electron in an Auger tank in Geant4 and the $S(1000)$ USC code for different kinetic energies and angles of incidence. The results of Geant4 show the average over all impact parameters. The numbers in parenthesis indicate the relative differences ($(S_{G4} - S_{USC})/S_{G4}$ in %) taking the Geant4 result as reference.*

K **(GeV)**	θ_i (deg)	S_{G4} (VEM)	S_{USC} (VEM)
0.01	45.	0.021 ± 0.018	0.023 (9)
0.01	75.	0.016 ± 0.015	0.014 (-12)
0.04	45.	0.137 ± 0.077	0.142 (4)
0.04	75.	0.124 ± 0.069	0.140 (13)
0.1	45.	0.314 ± 0.128	0.373 (19)
0.1	75.	0.352 ± 0.160	0.389 (10)
1.	45.	2.056 ± 1.133	2.219 (8)
1.	75.	2.797 ± 1.391	3.278 (17)

Table 4.5: *Signal produced by an positron in an Auger tank in Geant4 and the* $S(1000)$ *USC code for different kinetic energies and angles of incidence. The results of Geant4 show the average over all impact parameters. The numbers in parenthesis indicate the relative differences* $((S_{G4} - S_{USC})/S_{G4}$ *in %) taking the Geant4 result as reference.*

K **(GeV)**	θ_i (deg)	S_{G4} (VEM)	S_{USC} (VEM)
0.01	45.	0.028 ± 0.018	0.032 (14)
0.01	75.	0.029 ± 0.019	0.037 (28)
0.04	45.	0.107 ± 0.076	0.128 (20)
0.04	75.	0.126 ± 0.087	0.154 (22)
0.1	45.	0.262 ± 0.158	0.304 (16)
0.1	75.	0.314 ± 0.196	0.380 (21)
1.	45.	1.653 ± 1.255	1.632 (-2)
1.	75.	2.359 ± 1.527	2.795 (18)

Table 4.6: *Signal produced by a gamma in an Auger tank as obtained in Geant4 and the* $S(1000)$ *USC code for different kinetic energies and angles of incidence. The results of Geant4 show the average over all impact parameters. The numbers is parenthesis indicate the relative differences* $((S_{G4} - S_{USC})/S_{G4}$ *in %) taking the Geant4 results as reference.*

Chapter 5

Study of the signals in inclined showers: the role of the electromagnetic halo

The conventional separation between vertical and horizontal (inclined) showers is based on the zenith angle θ of the particle that induces the shower: horizontal showers are defined as those with $60° < \theta < 90°$. The differences between vertical and horizontal showers come from the different atmospheric grammage that the showers have to cross before reaching the ground which increases approximately as $\sec(\theta)$. For instance, the slant depth of atmosphere for a completely vertical shower $\theta = 0°$ is ~ 879.6 g cm^{-2} for the Pierre Auger Observatory altitude, increasing to ~ 1760 g cm^{-2} for a shower at 60° and being about 35 times larger for a completely horizontal shower.

Nucleonic cosmic rays initiate air showers at the top of the atmosphere in the first few 100 g cm^{-2}. For instance in Fig. 5.1 we show the typical longitudinal development of a 10 EeV proton shower. The electromagnetic (EM) component of the shower rises as the shower penetrates and reaches a maximum that in this example is at a depth $X_{max} \sim 780$ g cm^{-2}. After X_{max} the EM component is rapidly absorbed in the atmosphere due to low-energy processes and the photoelectric effect. Meanwhile, non-decaying muons propagate practically unattenuated to the ground, except for energy loss and deflections in the geomagnetic field. Therefore, a 10 EeV energy shower at $\theta = 0°$ reaches the ground level shortly after reaching maximum and the electromagnetic component dominates at ground. However, in horizontal showers muons dominate at the ground level because the electromagnetic component due to cascading processes, i.e. from π^0 decay is largely absorbed before reaching the ground [89]. However though small there is still an electromagnetic component in inclined showers. This is the so-called

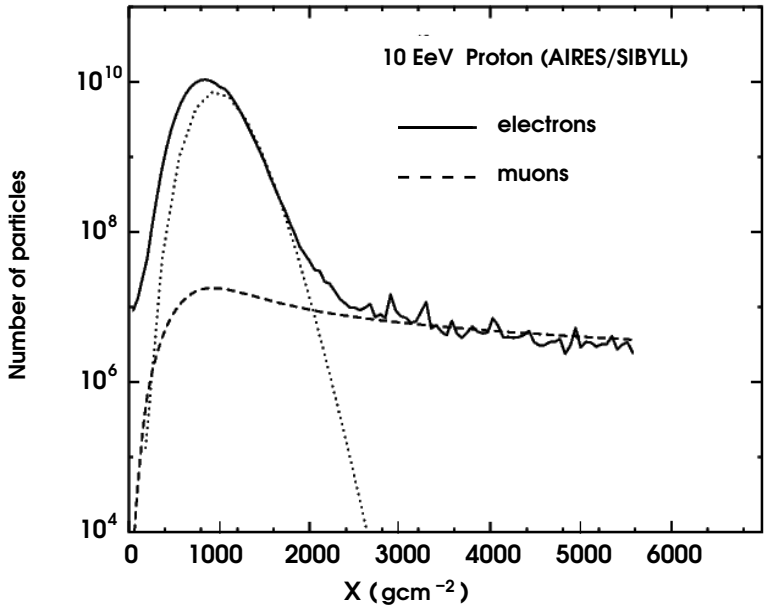

Figure 5.1: *The longitudinal development of the muon and electron components averaged over 100, proton showers of 10 EeV. After the shower maximum, the electromagnetic component is attenuated with an attenuation length of* $\sim$ *160 g cm*$^{-2}$ *and the muonic component with an attenuation length of* $\sim$ *1700 g cm*$^{-2}$*. At depths exceeding* $\sim$ 2500 *g cm*$^{-2}$ *the electromagnetic component is mainly due to muon decay.*

electromagnetic halo which is produced by the following mechanisms:

- Muon decay. The EM contribution due to muon decay appears in inclined showers in which low energy muons (a few GeV) decay due to the long paths they have to travel to reach the ground. In their decays they generate small electromagnetic subshowers that can trigger the surface detector stations.

- Hard muon interactions (pair production, bremsstrahlung and hadronic interactions). These interactions are more relevant as the muon energy increases. Therefore these processes are expected to contribute to the EM halo especially in highly inclined showers in which most of the muons are typically very energetic (hundreds of GeV), because they were produced at higher altitudes where the atmosphere is less dense, and also because the muons with a few GeV of energy typically decay before travelling the enlarged distances from their production height

to the ground. Hard muon interactions are also expected to be more important close to the core of the shower where a larger content of energetic muons is expected since energetic muons deviate less from the shower axis.

The halo EM is roughly proportional to the number of muons and contributes roughly to 15% of the total signal in a tank, as long as the tank is sufficiently far from the shower core (see below). The study of the electromagnetic halo has a special importance in the analysis of inclined showers, because the core and energy reconstruction of inclined events is currently performed comparing the measured signal to theoretical predictions of the muon densities at the ground adding a correction due to the electromagnetic halo assumed constant with distance to the shower axis and zenith angle [67].

In this section, we perform a very detailed study of the signal induced by the EM halo. More precisely we study the dependence of the ratio S_{EM}/S_{μ} on the shower zenith angle and distance to the shower axis, we study its azimuthal asymmetries and the effect of the geomagnetic field. For this study, we have simulated proton showers at an energy E = 10 EeV, and θ ranging from 60° to 88° in steps of 2° for the hadronic model QGSJET01, with a thinning level of 10^{-6}. A total of 100 showers were simulated for each energy and zenith angle. The simulations were performed in the conditions of the southern site of the Pierre Auger Observatory, with and without the geomagnetic field. The signals in the Auger tanks were calculated using the $S(1000)$ USC code.

5.1 Lateral behaviour of the ratio of the EM signal to the muonic signal

Firstly we have calculated from our simulations the distributions of the muonic and electromagnetic signals as a function of the distance to the shower core, the lateral distributions from now on. We compute these distributions in the shower plane, i.e., the plane perpendicular to the shower axis. We also define the azimuthal angle of a tank ζ [1] such that $\zeta = 0°$ (180°) corresponds to a station before (after) the core of the shower along the projection of the shower axis onto the ground. For the moment we assume the lateral distribution depends only on energy and the zenith angle of the shower, with no dependence on ζ, and calculate the signals at a fixed r averaging over ζ. We

[1]The azimuth angle ζ is measured in a coordinate system with center in the shower core and with respect to the projection of the shower axis on the ground.

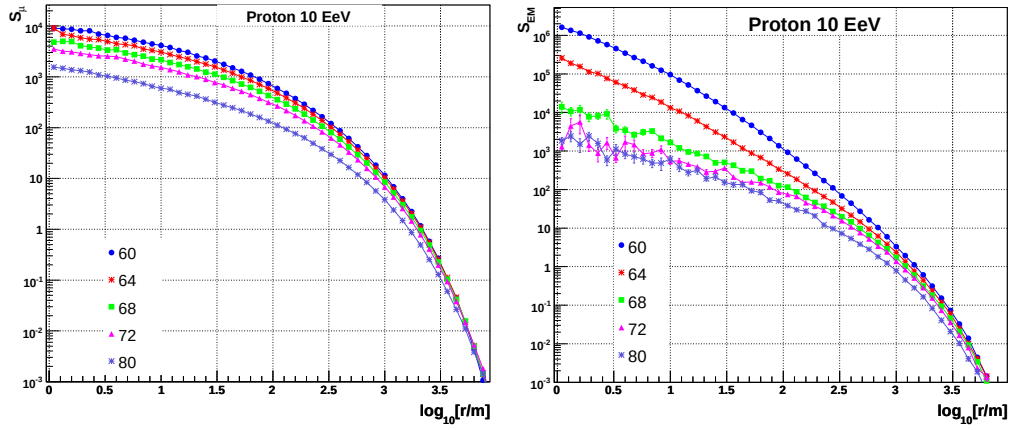

Figure 5.2: *Muonic (left panel) and electromagnetic (right panel) signals in VEM as a function of the distance to the shower axis in the shower plane for 10 EeV proton showers at different zenith angles simulated with AIRES + QGSJET + S1000 USC.*

divide the shower plane in different sampling regions from $r = 0$ to 10^4 meters from the shower axis. The sampling area is defined in the shower plane as a concentric ring with width of 0.08 in $log_{10}r$ around the core (see Eq. 4.2).

In Figure 5.2 we show the lateral distributions of the muonic (left panel) and electromagnetic (right panel) signals in inclined showers at ground level in the shower plane, for protons of 10 EeV energy and different zenith angles. In the following we give a qualitative explanation of the behaviour seen in Fig. 5.2.

The muonic signal S_μ decreases with θ because as the distance to the ground increases the number of muons decreases mainly due to the decay of those with the lowest energies. The decrease with θ is slower as the distance to the core increases, because muons are able to reach larger distances to the shower core as θ increases partially compensating for their decay.

The behaviour of the lateral distribution of the EM signal in inclined showers, can be qualitatively understood as a combination of the different behaviour of the two contributions to the EM component namely, that from π^0 decay and that produced by the electromagnetic halo. Near the core, the EM signal S_{EM} decreases when θ increases from 60° to 72° because the EM component induced by π^0 decay is increasingly absorbed. Still near the core but for larger zenith angles, the EM component due to π^0 decay is negligible and the behaviour with θ is dominated by the EM subshowers induced by electrons produced mainly in hard interactions of highly energetic muons. In that case the decrease of the EM component with θ is slower. At large enough

distances to the core, hard muon processes are less important because muons are less energetic, and only π^0 and μ decays contribute to the EM signal. For $\theta \lesssim 70^\circ$ the EM component from μ decay becomes more and more dominant as the distance to the core increases. For $\theta > 70^\circ$ the EM component from π^0 decay is negligible and the EM halo dominates at essentially all distances. In the ranges of distances to the core where the EM halo dominates, the lateral distribution of the EM signal exhibits an analogous behaviour to the muonic signal as can be seen in the figure.

In Fig. 5.3, we show the ratio of the electromagnetic to the muonic signals (S_{EM}/S_μ) as a function of r for different θ. We can see that near the core, the ratio decreases with zenith angle up to $\theta \sim 72^\circ$, and then increases again mainly due to hard muon processes that are expected to dominate near the core and in very inclined showers as explained above. Far from the core, the ratio is almost compatible with a constant value due to the contribution of the EM halo. The larger the zenith angle, the smaller the distance at which the ratio levels off. The slight increase of the ratio for $\theta \lesssim 68^\circ$ and far from the core ($r \gtrsim 3$ km) might be attributed to the fact that the number of low energy muons decreases more rapidly at large distances because they decay before reaching the ground, and only energetic muons survive. There is also a hint of the same effect at $\theta \gtrsim 68^\circ$ and distances even larger than $log_{10}r = 3.5$.

We have performed a fit of the ratio of the electromagnetic to muonic signals as a function of the distance from the shower axis and the zenith angle:

$$S_{EM}/S_\mu(r,\theta) = A(\theta)\; r^{C(\theta)} \;-\; B(\theta)\; log_{10}r \tag{5.1}$$

with the distance r in meters and θ in degrees. The fit is valid in the ranges $\theta \in [60^\circ, 88^\circ]$ and $log_{10}r \in [1., 3.8]$ m.

The parameter $A(\theta)$ can be parameterized as:

$$A(\theta) = \begin{cases} 42.16 + \exp(-0.605 + 0.23\,\theta) & \text{for } \theta \leq 72^\circ \\ 10^{-4.605+0.0605\,\theta} & \text{for } \theta > 72^\circ \end{cases} \tag{5.2}$$

The parameter $C(\theta)$ has been parameterized in two different ranges of θ as:

$$C(\theta) = \begin{cases} 240 - 10.973\,\theta + 0.165\,\theta^2 - 0.0008\,\theta^3 & \text{for } \theta \leq 72^\circ \\ 119 - \;\; 4.518\,\theta + 0.057\,\theta^2 - 0.0002\,\theta^3 & \text{for } \theta > 72^\circ \end{cases} \tag{5.3}$$

Finally the parameter $B(\theta)$ can be fitted to a Gamma distribution as:

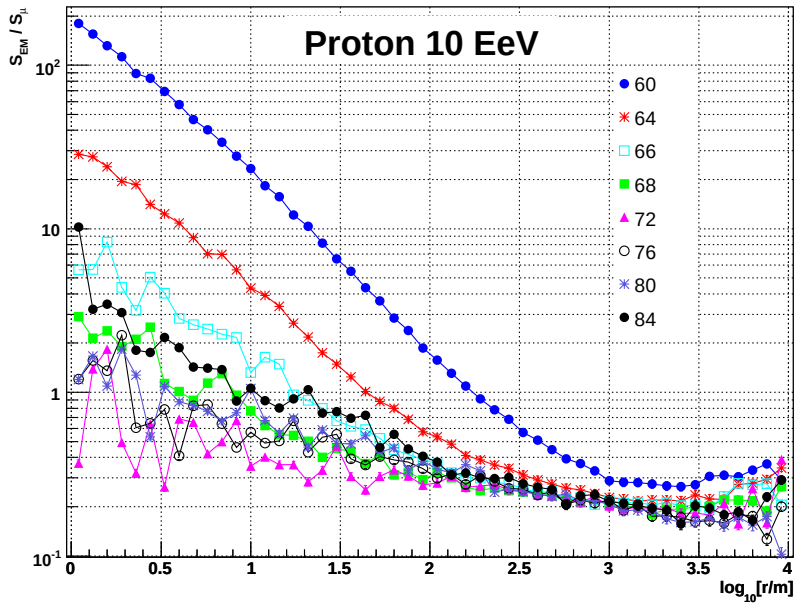

Figure 5.3: *The ratio of the electromagnetic to muon contributions to the tank signal as a function of the distance from the shower axis in the shower plane for 10 EeV proton shower at different zenith angles simulated with AIRES + QGSJET + S(1000) USC in absence of geomagnetic field.*

$$B(\theta) = -0.071 + 1.263 \ \frac{(\theta - 58.411)^{5.108-1}}{4.711^{5.108}\ \Gamma(5.108)} \ \exp\left(\frac{\theta - 58.411}{4.711}\right) \tag{5.4}$$

In Fig. 5.4 we compare the parameterization to the results of the simulation. To test the accuracy of the parameterization, we have compared the averaged ratio S_{EM}/S_μ obtained in the simulations ($< R_{sim} >$) with the value predicted by the corresponding parameterization (R_{param}) in each bin in $log_{10}r$:

$$\frac{R_{param} - < R_{sim} >}{R_{param}}(r)$$

The results of this comparison are histogrammed in Fig. 5.5 for 3 different zenith angles. One can see that the mean values of the ratio are well reproduced by the parameterization within $< 10\%$ (the RMS values of the distributions are below $< 15\%$).

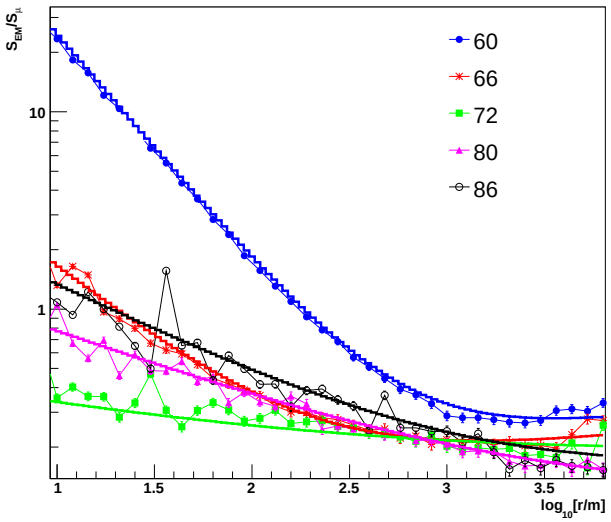

Figure 5.4: *Fit of the ratio of the electromagnetic to muonic contributions to the tank signal for 10 EeV proton showers.*

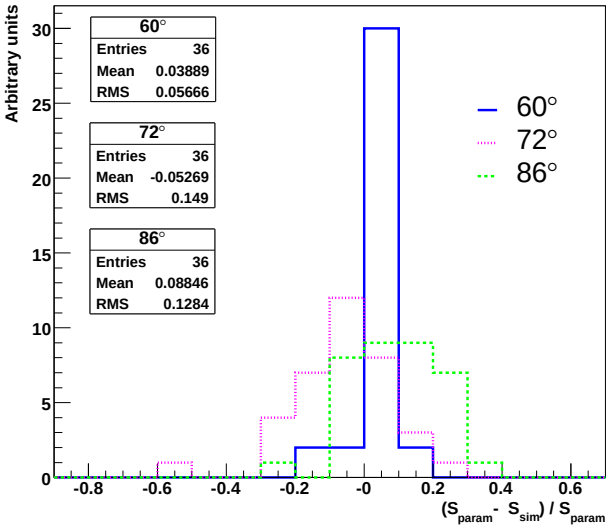

Figure 5.5: *Comparison between the simulated ratio of the electromagnetic to the muonic signals and the prediction of the parameterization for 10 EeV proton showers at* 60°, 72° *and* 86°.

5.2 Azimuthal asymmetries without the geomagnetic field

In the previous section, we have studied the lateral distribution of the ratio S_{EM}/S_{μ} under the assumption that the signals are equal at the same distance from the shower axis in the shower plane regardless of the azimuthal angle ζ. This assumption is only an approximation, and in fact there is an azimuthal asymmetry in the signal due to the several effects, the most important being the so-called geometrical effect, the longitudinal development effect and ground screening [90, 91, 92]. Furthermore, the geomagnetic field is another source of asymmetry in inclined showers which for the moment we will neglect and defer its study to the next section.

5.2.1 The geometrical effect

In Fig. 5.6 we show a sketch of an inclined shower hitting the ground. This sketck serves us to illustrate that the shower particles do not travel parallel to the shower axis and hence cross different paths before reaching the ground depending on their azimuthal angles. Moreover, particles hit the detectors in the "early" region (before the shower axis hits the ground) "more vertically" than the ones that hit the tanks located in the "late" region. This is essentially the basis of the so-called geometrical effect. To demonstrate this behaviour, we show in Fig. 5.7 the distributions of angles of incidence θ_i of early and late particles in simulated showers at different zenith angles (θ). One can see that the mean θ_i of the late muons is always larger than the corresponding mean of the early muons. Also the difference between the mean values decreases with θ. For the electromagnetic particles the same behaviour occurs. As a conclusion by inspecting Fig. 5.7, the asymmetry induced by the difference in the angle of incidence between the particles reaching the early and late regions of a shower, i.e. the geometrical effect, is expected to be more important in showers with small zenith angle.

The geometrical effect is expected to affect differently the EM and muonic components of a shower:

- The electromagnetic signal is roughly proportional to the area of the tank projected onto the plane perpendicular to the particle direction (see Eq. 4.47). The area decreases with zenith angle θ_i (see Fig. 4.2). As a consequence we expect the electromagnetic signal to be larger in the early region than in the late one.

- The muonic signal is roughly proportional to the track-length in wa-

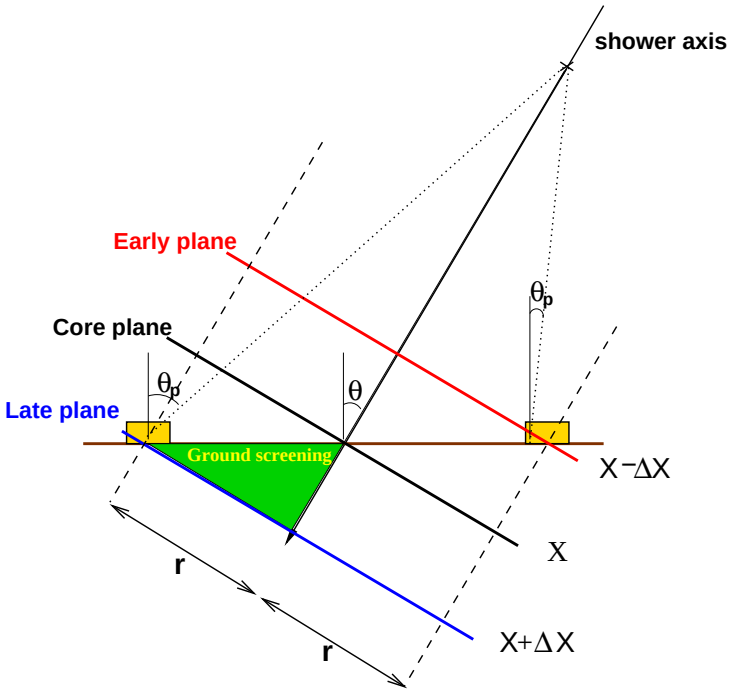

Figure 5.6: *Schematic picture of an inclined shower reaching the ground. Three planes are displayed intersecting the ground plane, each one at different depths on the shower development: early (red), late (blue) and core (black) planes. The latter is also called shower plane.*

ter (see Eq. 4.46), and the mean track-length increases with θ_i (see Fig. 4.3). On the other hand, the area of the tank projected onto the plane perpendicular to the particle direction decreases with θ_i. Therefore, there should be a large degree of compensation between both behaviours and we expect the muonic signal to be approximately the same in the early and late regions [2].

5.2.2 The longitudinal development effect

The longitudinal development effect can be understood as follows. Particles at the same distance to the core in the shower plane r, but arriving with different azimuthal angles ζ travel along different paths, and they belong to different stages in the evolution of the shower. The importance of this effect depends on the evolution with depth of the lateral distribution and

[2] In fact the uncorrected muon signal is independent of θ (see Eq. 4.16)

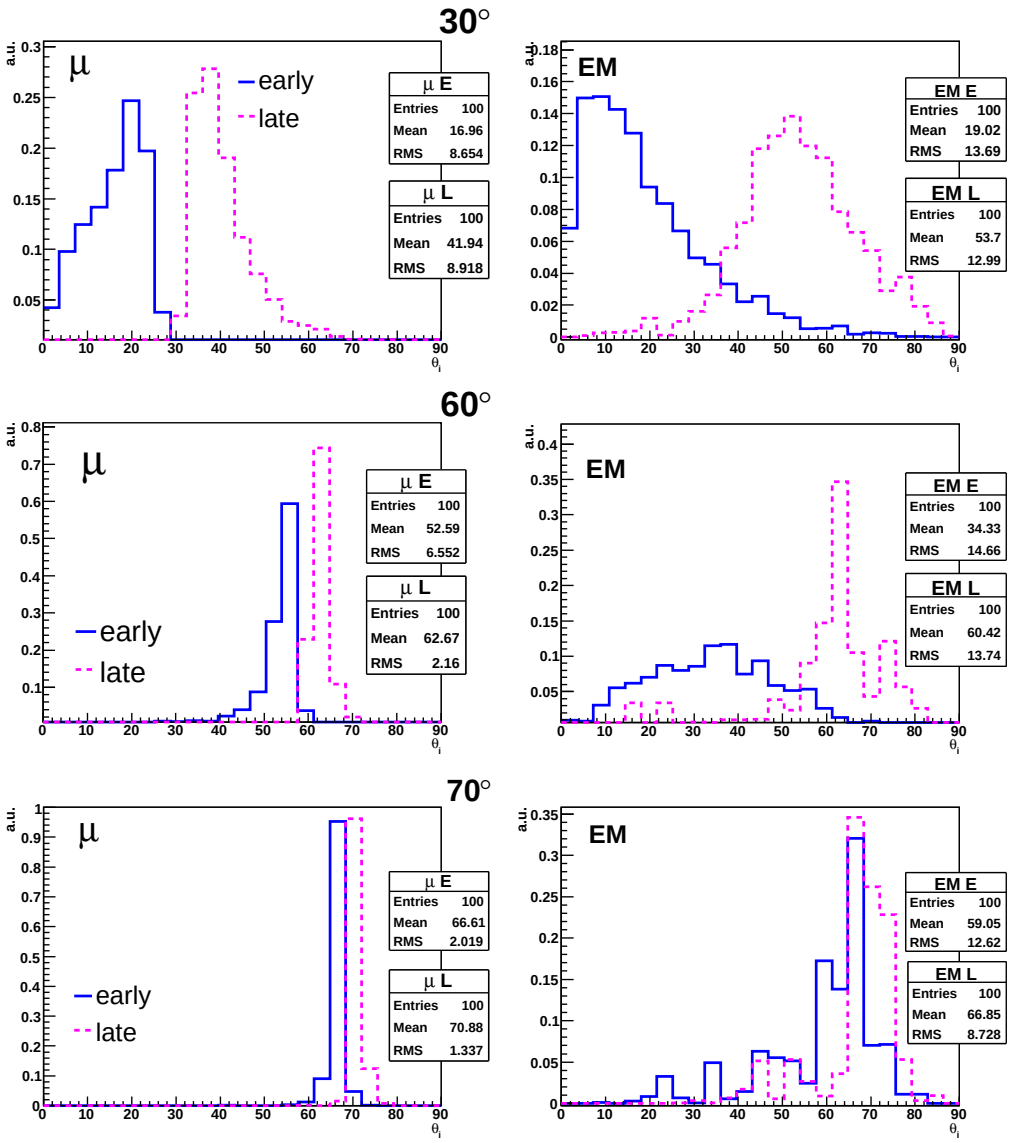

Figure 5.7: *Distribution of the zenith angle of incidence of the shower particles in the early (solid line) and late regions (dashed line) at 1000 m from the shower axis for different shower zenith angles. Top panels: $\theta = 30°$. Middle panels: $\theta = 60°$. Bottom panels: $\theta = 70°$. For each angle we show the distributions for the muonic (left panel) and electromagnetic (right panels) components. The simulations were done for 10 EeV proton showers with AIRES and the QGSJET model.*

on the attenuation of the total number of particles. In Fig. 5.6 we show two detectors at the same distance from the core and two planes transverse to the shower axis containing their positions. These planes serve to illustrate the different values of atmospheric depth crossed by the particles, and therefore the different stages of shower development. We also draw the transverse plane containing the impact point of the shower axis on the ground (shower plane). From Fig. 5.6 it is evident that the tank in the early region is hit by a younger stage on the evolution of the shower than the tank in the late region (for more details see Section 6.3). For instance, in an event produced by a 10 EeV proton shower at $\theta = 60^\circ$ the depth crossed by an early and a late particle hitting tanks at $r = 1000$ m in the shower plane differs by ~ 370 g cm^{-2} in slant depth. The difference of grammage crossed by the early and late particles increases with the distance from the core.

The asymmetry introduced by the effect of the longitudinal development is more important for the electromagnetic component from π^0 decay. This component is exponentially suppressed after the shower maximum, and as a consequence small changes in the depth crossed induce large differences in the number of EM particles on the ground. However, the muonic component is less attenuated and therefore the asymmetry induced by this effect is smaller. Therefore, we expect that the contribution of this effect to the azimuth asymmetry of the signal is small at large zenith angles ($\theta > 70^\circ$) at which the electromagnetic component from π^0 decay on the ground is practically suppressed at all azimuth angles and the electromagnetic halo inherits the behaviour of the muonic component.

In Fig. 5.8 we illustrate the effect of the longitudinal development on the electromagnetic and muon components of the signal by plotting the lateral distributions of electromagnetic energy density (top panels) and the lateral distributions of muon number density (bottom panels) in two ranges of the azimuthal angle: early (ζ around 0°) and late (ζ around 180°) The size of the azimuthal bins in these plots is $\Delta\zeta = 30^\circ$ in order to have an acceptable particle statistics. For showers at $\theta = 60^\circ$ the difference in the EM energy density between the early-late regions is important at even small distances to the core ($r \sim 100$ m) because the EM component from π^0 decay is still significant in the early region, while it is practically absorbed before reaching ground in the late region. However, at $\theta = 70^\circ$ the difference between the densities in the early and late regions is small because the component from π^0 decay is absorbed for all ζ (see Fig. 5.1) and the EM halo, produced by the decay of muons which are less affected by the longitudinal development effect, dominates. In the bottom panels of Fig. 5.8 we plot the lateral distributions of the muon number density. It can be seen that the difference between the densities in the early and late regions is always small regardless of the zenith

angle.

The behaviour of the early-late asymmetry with r is shown in Fig. 5.9, where we plot the relative differences between the early and late electromagnetic energy densities (left panel) and muon number densities (right panel). At $\theta = 60^\circ$ the asymmetry in the EM energy density increases rapidly with r. However, at $\theta = 70^\circ$ there is only a slight increase above $r = 1000$ m which follows the same behaviour seen in the muon number density (see right panel), because at $\theta = 70^\circ$ the electromagnetic component is mostly due to muon decay.

5.2.3 The screening effect

Finally, the azimuthal asymmetry in the signal is also induced by the so-called screening effect. This effect is produced by the absorption of the shower core after its impact on the ground. As a consequence, the hadronic core of the shower stops feeding the EM and muonic components in a portion of the late region (see Fig.5.6).

The combination of these 3 effects produces an azimuthal asymmetry in the lateral distribution of the electromagnetic and muonic components of the signal. The asymmetry in the signal at a fixed ζ can be quantified defining an asymmetry parameter $Asym$:

$$Asym(r) = \frac{S(\zeta) - < S >}{< S >} \tag{5.5}$$

where $< S >$ is the signal averaged over all ζ.

In Fig. 5.10 we plot the asymmetry parameter of the muonic (left panel) and electromagnetic (right panel) signals as a function of the distance to the core for showers at $\theta = 60^\circ$. We have plotted the asymmetry parameter in 4 azimuthal bins of size $\Delta\zeta = 30^\circ : \zeta = 0^\circ$, 90°, 180° and 270°. The behaviour of the asymmetry depends strongly on the type of signal (EM or muonic) and therefore, the asymmetry will not cancel out when the ratio of the EM signal to the muonic signal is calculated. For example, in the left panel of Fig. 5.11 we show the 2-dimensional map of the ratio S_{EM}/S_μ in the shower plane for 10 EeV proton showers at $\theta = 60^\circ$. The arrow shows the shower direction. One can clearly see the azimuthal asymmetry in the ratio S_{EM}/S_μ at a fixed distance to the core (indicated with the head of the arrow). The fraction of electromagnetic signal is larger in the early region. However, at zenith angles greater than 70° as shown in the right panel of Fig. 5.11, no azimuthal asymmetry in the ratio is observed because there are only muonic

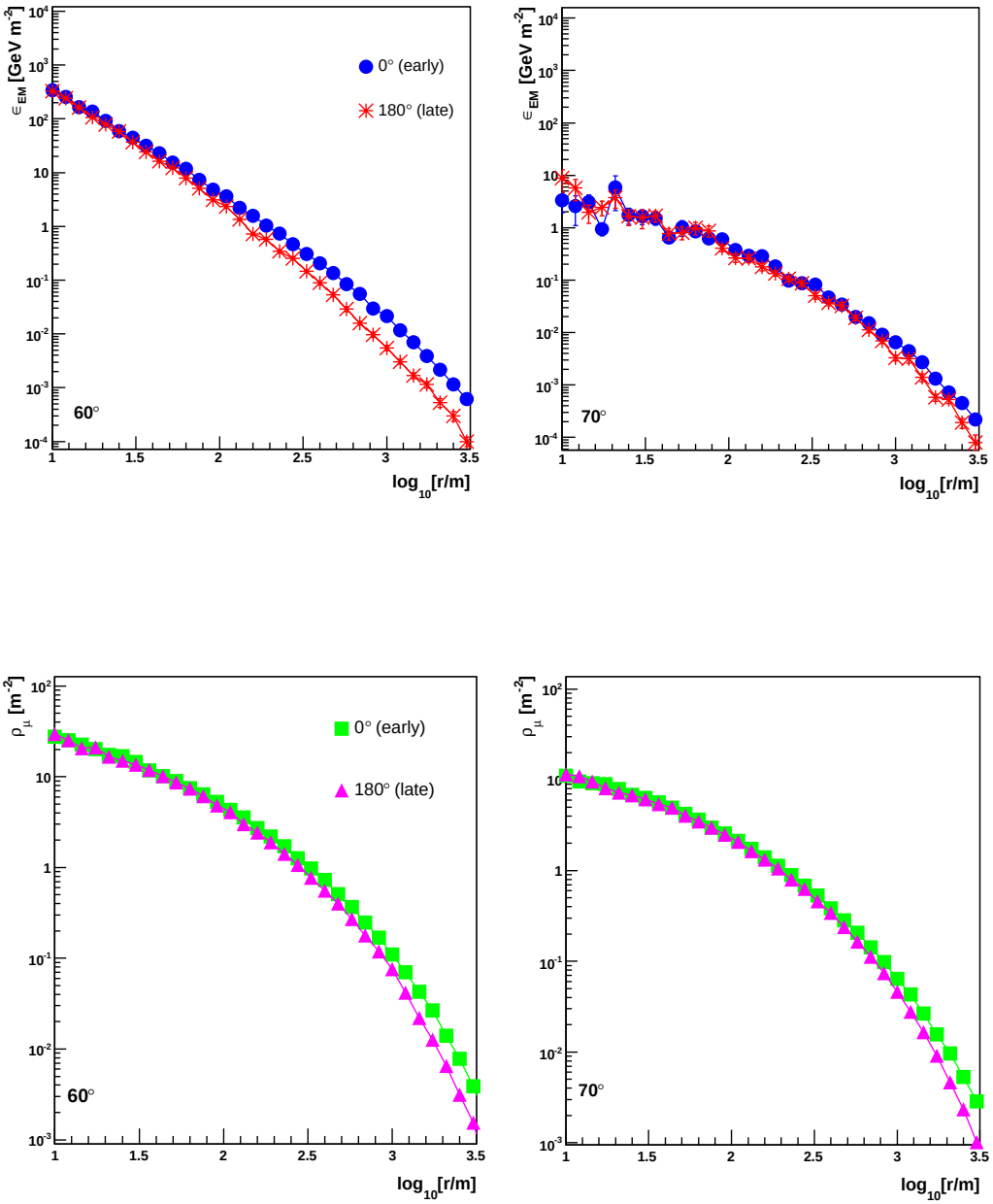

Figure 5.8: *Top panels: Lateral distributions of the electromagnetic energy density in the early (ζ around 0°) and late (ζ around 180°) regions of the shower plane of showers at $\theta = 60°$ (left panel) and 70° (right panel). Bottom panels: Lateral distributions of the muon number density in the early (ζ around 0°) and late (ζ around 180°) regions of the shower plane of showers at $\theta = 60°$ (left panel) and 70° (right panel). Each distributions corresponds to the average of 100 proton showers of $E = 10$ EeV simulated with AIRES.*

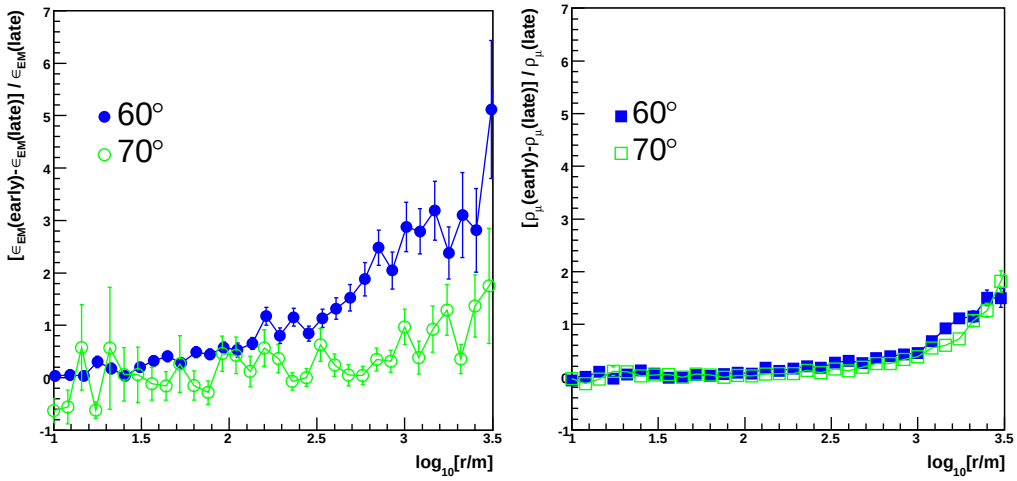

Figure 5.9: *Left panel: Early-late asymmetry of the electromagnetic energy density as a function of the distance from the core in the shower plane for showers at* $\theta = 60°$ *(full circles) and* $\theta = 70°$ *(empty circles). Right panel: Early-late asymmetry of the muon number density as a function of the distance from the core in the shower plane for showers produced at* $\theta = 60°$ *(full squares) and* $\theta = 70°$ *(empty squares).*

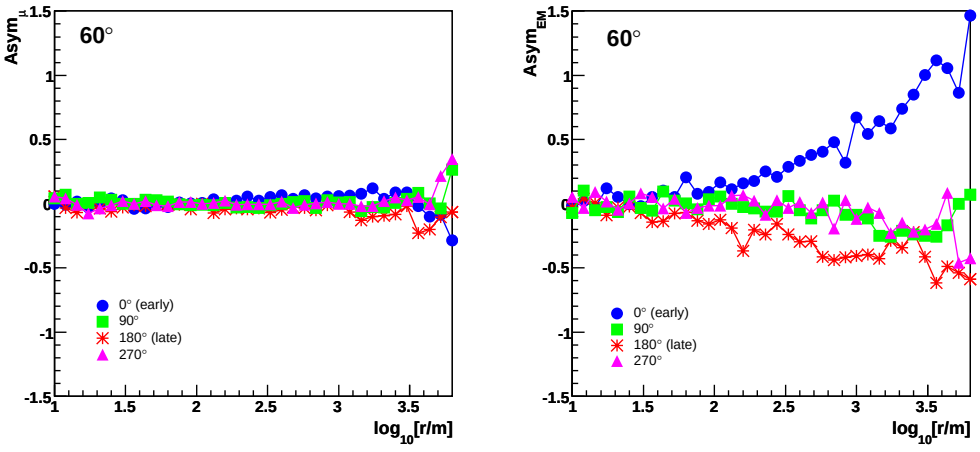

Figure 5.10: *Asymmetry of the lateral distribution of the muonic (left panel) and electromagnetic (right panel) signal components with respect to the mean value for different azimuth regions. The distributions correspond to the average of 100 proton showers of 10 EeV simulated at* $60°$ *with AIRES + QGSJET + S(1000) USC code.*

component and the EM halo on the ground. Since these two components approximately have the same asymmetry, the final asymmetry is practically canceled out when making the ratio of EM and muonic signals.

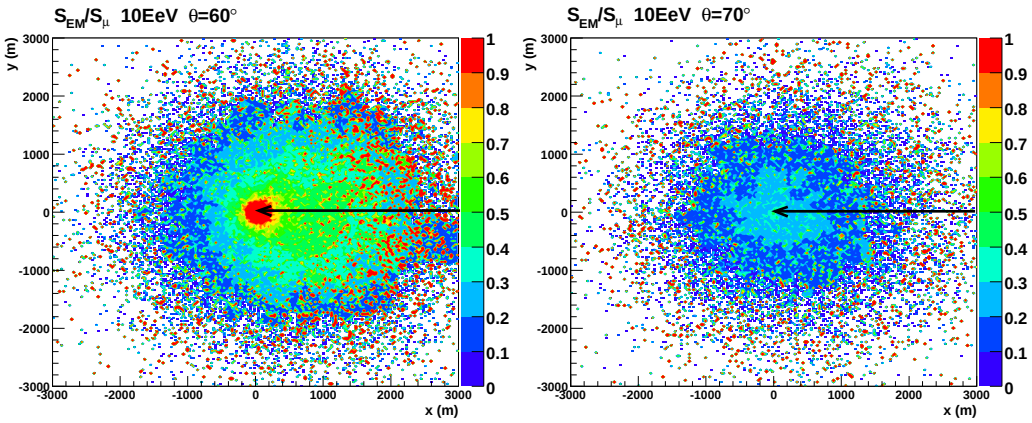

Figure 5.11: *Left panel: Contour map of the ratio S_{EM}/S_μ on the transverse (shower) plane in $\theta = 60°$ showers. Right panel: Contour map of the ratio S_{EM}/S_μ on the transverse (shower) plane in $\theta = 70°$ showers. The arrow shows the shower direction and the head of the arrow shows the core position. Each map is obtained using the average of 100 proton showers of $E = 10$ EeV simulated with AIRES + QGSJET + S(1000) USC code.*

In Fig. 5.12 we plot the ratio S_{EM}/S_μ as a function of the azimuth angle for a fixed distance $r = 1000$ m. We use a system of polar coordinates (S_{EM}, ζ). At $\theta = 60°$ (blue points) there is a large asymmetry, the signal ratio at $\zeta = 0°$ is more than twice the ratio at $\zeta = 180°$. Note also the symmetry in the ratio at $\zeta = \pm 90°$. At $\theta = 70°$ (red squares) there is essentially circular symmetry for the reasons explained before.

The fact that the ratio S_{EM}/S_μ depends on the azimuthal angle must be taken into account in the analysis and reconstruction of inclined showers. For this purpose we have performed a parameterization of the ratio S_{EM}/S_μ as a function of the distance from the core r, zenith angle θ, and azimuth angle ζ,

$$S_{EM}/S_\mu\,(r,\theta,\zeta) \;= < S_{EM}/S_\mu\,(r,\theta) > \;(1 + A_{asym}(r,\theta,\zeta)) \tag{5.6}$$

where $< S_{EM}/S_\mu >$ is the parameterization of the ratio of signals averaged over all ζ angles given in Eq. 5.1 and the parameter A_{asym} characterizes the azimuthal asymmetry (in absence of geomagnetic field). This correction is more important in the range $\theta < 70°$. For larger angles the asymmetry is expected to be negligible as shown before (see for instance Fig. 5.11).

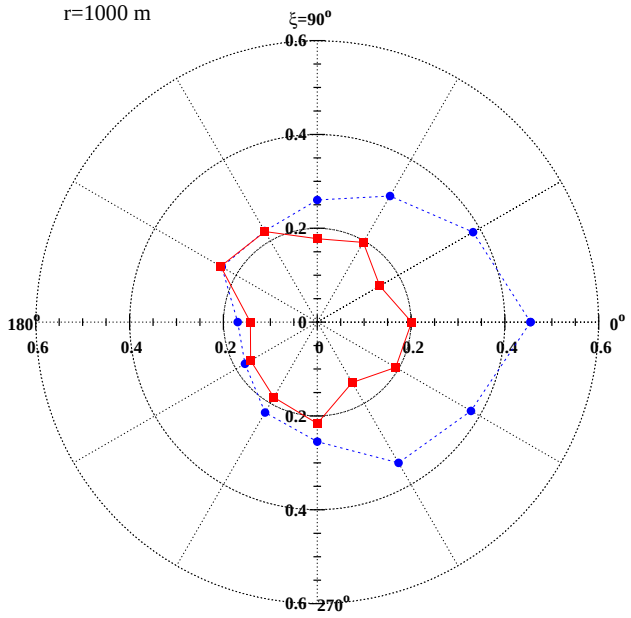

Figure 5.12: *The ratio of the electromagnetic to the muonic signals as a function of the azimuth angle ζ for $r = 1000$ m in polar coordinates $(S_{EM}/S_\mu, \zeta)$. The blue circles correspond to the average of 100 proton showers of $E = 10$ EeV at $\theta = 60°$. The red squares correspond to showers at $\theta = 70°$. The showers were simulated with AIRES + S1000 USC code.*

In Fig. 5.13 we show the ratio S_{EM}/S_μ as a function of r in different bins in ζ compared to the mean value (left panel) for showers at 60° and their corresponding asymmetry parameter A_{asym} (right panel). We parameterize A_{asym} using the following equation:

$$A_{asym}(r, \theta, \zeta) = D(\theta, \zeta)\, r \;+\; E(\theta, \zeta)\, log_{10} r \tag{5.7}$$

with the distance r in meters and the angles θ and ζ in degrees. The fit is valid in the range $\theta \in [60°, 69°]$, $log_{10} r \in [1., 3.8]$ m and $\zeta \in [-180°, 180°]$.

$D(\theta, \zeta)$ in Eq. 5.7 is parameterized as:

$$D = 10^{-5} \times [D_1 + D_2 \, \left(\mathrm{sinc}(\pi \mathrm{D}_3 \zeta) + \mathrm{sinc}^2(\pi \mathrm{D}_3 \zeta)\right)] \tag{5.8}$$

where $\mathrm{sinc(x)} = \sin \mathrm{x}/\mathrm{x}$ and:

$$D_1 = -193.143 + 9.454\,\theta - 0.154\,\theta^2 + 0.0008\,\theta^3$$

$$D_2 = 1.6 - \frac{7.909 \times 10^{-6}\,\theta^2}{1 - 0.014\,\theta}$$

$$D_3 = 21.401 - 1.005\,\theta + 0.016\,\theta^2 - 8.208 \times 10^{-5}\,\theta^3 \tag{5.9}$$

$E(\theta, \zeta)$ in Eq. 5.7 is parameterized as:

$$E = E_1 \cos(E_2 \zeta) \tag{5.10}$$

with:

$$E_1 = 2.052 - 0.053\,\theta + 0.0003\,\theta^2$$

and

$$E_2 = 1.08 - \frac{4.467 \times 10^{-8}\,\theta^3}{1 - 0.014\,\theta} \tag{5.11}$$

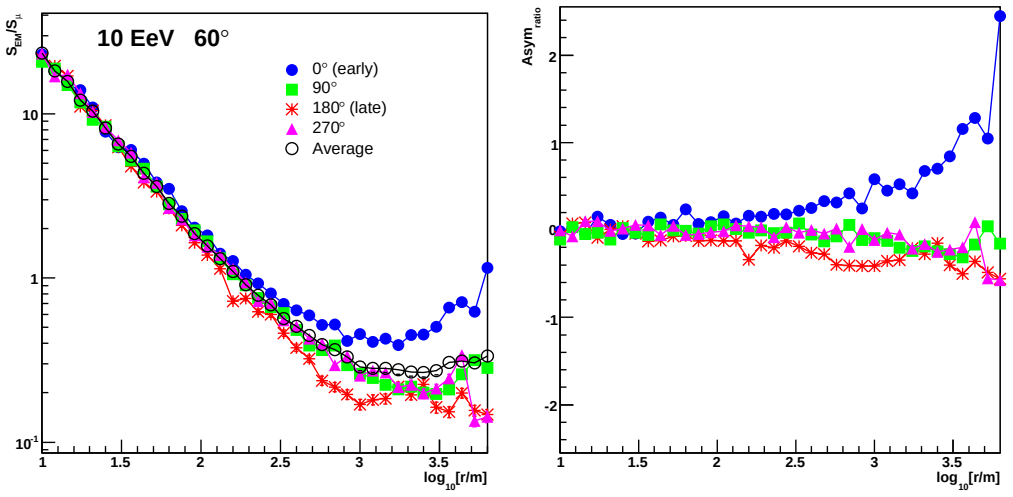

Figure 5.13: *Left panel: The ratio of the electromagnetic to muon contributions to the tank signal as a function of the distance from the shower axis in the shower plane in different bins in ζ. Right panel: Asymmetry of the lateral distribution of the ratio S_{EM}/S_μ in different ζ bins. The distributions correspond to the average of 100 proton showers with $E = 10$ EeV at $\theta = 60°$, simulated with AIRES+QGSJET+S_{1000} USC.*

To test the accuracy of this parameterization, we have compared the simulated ratio and the parameterization at $\zeta = 0°$ and $\zeta = 180°$ in different bins in $\log_{10} r$. In Fig. 5.14 we show the histogram of the results of this comparison for two zenith angles: $\theta = 60°$ (left panel) and $\theta = 68°$ (right panel). The mean values of the ratio are well reproduced by the parameterization within $< 10\%$ (the RMS of the distributions are all $< 25\%$).

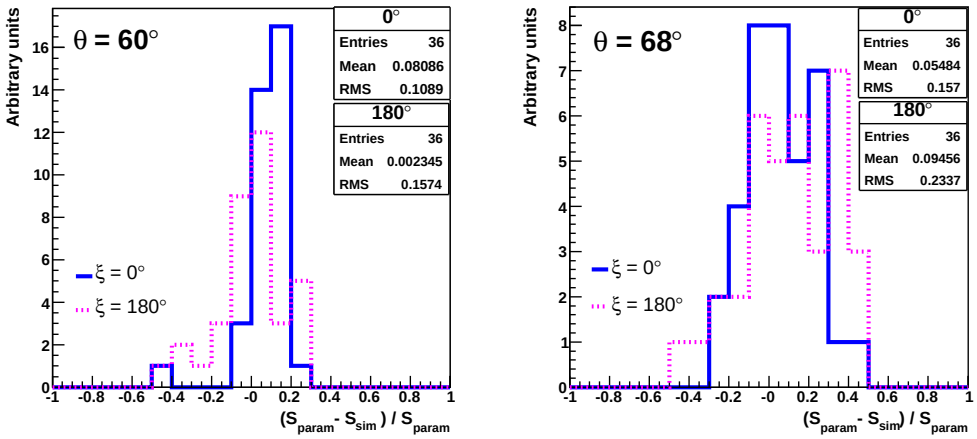

Figure 5.14: *Comparison between simulated ratio of the electromagnetic to the muon signals and the prediction of the parameterization accounting for azimuth asymmetry. The continuous line shows the difference corresponding to the ζ bin centered on* $0°$*. The dotted line corresponds to the ζ bin centered on* $180°$*. The distributions correspond to 10 EeV proton showers simulated at* $\theta = 60°$ *(left panel) and* $68°$ *(right panel).*

5.3 The effect of the geomagnetic field

Finally we study the ratio S_{EM}/S_{μ} including the effect of the geomagnetic field.

The geomagnetic field bends the trajectories of the charged particles due to the Lorentz force, which is perpendicular to both the motion of the particles ($\vec{v}$) and direction of the magnetic field ($\vec{\mathrm{B}}$):

$$\vec{F} = q\vec{v} \times \vec{\mathrm{B}} \tag{5.12}$$

In horizontal showers, muons travel along very long paths in the atmosphere, (of the order of a few km depending on the zenith angle of the shower) without interacting, and can suffer significant deflections with respect to the rectilinear trajectories that they would follow in the absence of geomagnetic field. On the contrary, electrons and positrons typically travel along small paths without interacting, so that the effect of the geomagnetic field on their trajectories is less important. As we will show below, the geomagnetic field becomes a relevant source of asymmetry in the lateral distribution of the muon number and therefore, in the lateral distribution of the muon signal.

Moreover, since the electromagnetic halo preserves the muon spatial distribution, the lateral distribution of its signal will also be influenced by the presence of the geomagnetic field.

In [88] a model to describe the effect of the geomagnetic field on the muon trajectories was developed. The basic ideas of the model are described below for completitude.

In absence of geomagnetic field, a relativistic muon of energy $E \simeq cp$ that travels a distance d will only be deviated due to the transverse momentum ($\vec{p_t}$) inherited from its parent meson, reaching a distance $\overline{r}$ to the shower axis in the tranverse plane given by:

$$\overline{r} = \frac{p_\perp}{p} d \simeq \frac{c p_\perp d}{E} \tag{5.13}$$

The geomagnetic field can be decomposed in two components $\mathrm{B}_\parallel$ and $\mathrm{B}_\perp$, parallel and perpendicular to the shower axis respectively. Assuming that muons travel parallel to the shower axis, we can neglect the effect of $\mathrm{B}_\parallel$ and use $\mathrm{B}_\perp$ to describe the effect of the geomagnetic field. Under this approximation, the radius of curvature R of the trajectory of a relativistic muon in the magnetic field is:

$$R = \frac{p}{q\mathrm{B}_\perp} \simeq \frac{E}{ce\mathrm{B}_\perp} \tag{5.14}$$

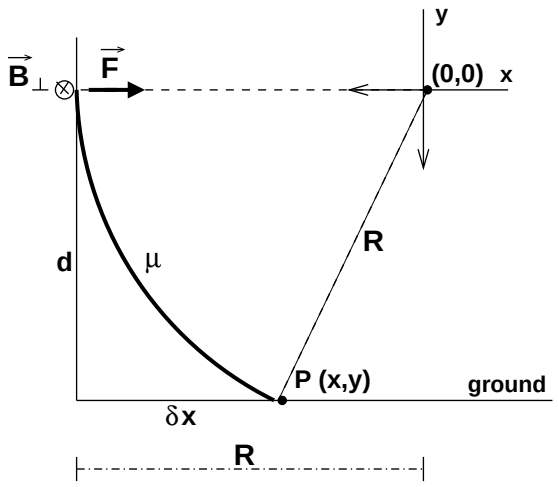

Figure 5.15: *Deviation from the rectilinear trajectory due to the magnetic field. of a positive muon travelling vertically downwards.*

Besides the location in the Earth, the value of $\mathrm{B}_\perp$ depends on the zenith and azimuth angles of the shower. In the left panel of Fig. 5.16 we show $\mathrm{B}_\perp$ as

a function of the azimuth angle for the Auger site[3] for illustrative purposes. Note that $\phi = 0°$ corresponds to the geographical East direction following the Auger convention (unless otherwise indicated). For vertical showers ($\theta = 0°$) $B_\perp$ does not depend on azimuth and has a constant value of ~ 20 μT. At $\theta > 60°$, $B_\perp$ has an absolute minimum at $\phi \sim 87°$ and a second minimum at $\phi \sim 267°$. The difference between the values of the two minima decreases with zenith angle. However the values of the maxima are the same for all θ, and the angular separation between maxima increases with the zenith angle.

To quantify the geomagnetic deviation of the trajectory of a muon (δx), we define a set of coordinates (x, y) in the transverse plane of the shower as shown in Fig. 5.15 (x is parallel to the direction of the Lorentz force $\vec{F}$). The geomagnetic deviation of a muon produced at a height d can be expressed as:

$$\delta x = R\left[1 - \sqrt{1 \mp \left(\frac{d}{R}\right)^2}\right] \simeq \pm\frac{d^2}{2R} \simeq \pm\frac{eB_\perp d^2}{2p} \quad (d \ll R) \tag{5.15}$$

The $\pm$ sign corresponds to the sign of the charge of the muon. In Fig. 5.17, we illustrate the effect on the muon deflection of the magnetic field and the transverse momentum in the shower plane. Using the relation 5.13, the geomagnetic deviation can be expressed as:

$$\delta x = \pm\frac{0.15B_\perp d}{p_\perp}\,\overline{r} = \pm\alpha_B\overline{r} \tag{5.16}$$

where p_t is given in GeV/c, d in meters and $B_\perp$ in Tesla.

The value of α_B is a measurement of the importance of the magnetic field. It can be interpreted as the fractional deviation in terms of the distance to the shower core at which a muon would have arrived in absence of the geomagnetic field. In the right panel of Fig. 5.16 we show α_B for muons in the Auger site as a function of the azimuth angle. We have fixed the muon transverse momentum at $p_\perp \sim 0.3$ GeV and the production height at $d \sim 3.5$ km. For instance, for showers at $\theta = 60°$ the maximum value of α_B is 0.09 and as a consequence the effect of the magnetic field is not important. For very inclined showers the geomagnetic deviation is large ($\alpha_B \gg 1$) as one can see in Fig. 5.16. The importance of the magnetic field increases with θ and therefore, strong asymmetries of the muon lateral distributions are expected at very large zenith angles.

[3]The geomagnetic field used in this work corresponds to the data of May 2006 extracted from the IGRF database [93]. The strength of the field is 24.472 μT, the inclination angle below the horizon is 35.29° and the declination angle with respect to the geographical North is 2.91°.

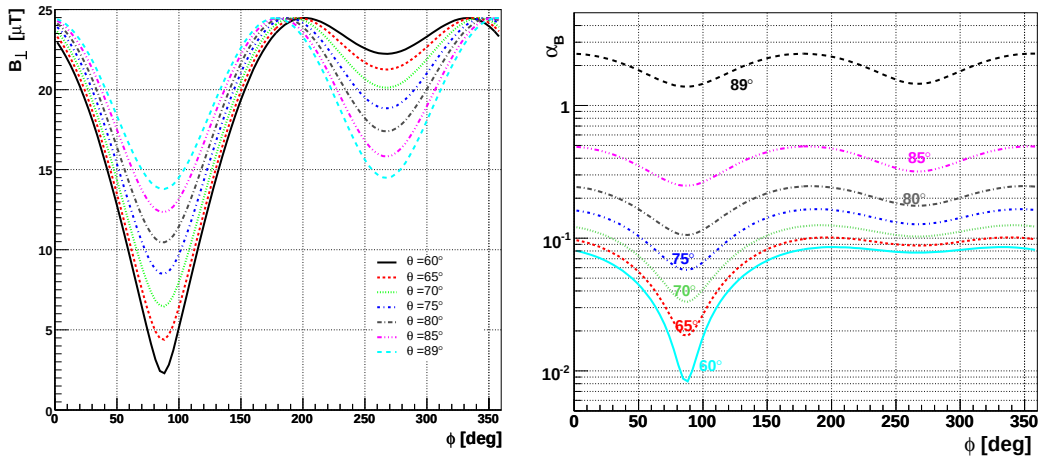

Figure 5.16: *Left panel: Component of the geomagnetic field perpendicular to the show axis as a function of the shower azimuth angle for the Auger site. Right panel: Geomagnetic deviation α_B as a function of the azimuth angle for muons with average transverse momentum $p_\perp \sim 0.3$ GeV and vertical production distance $d \sim 3.5$ km. Note that $\phi = 0°$ corresponds to the geographical East following the Auger convention.*

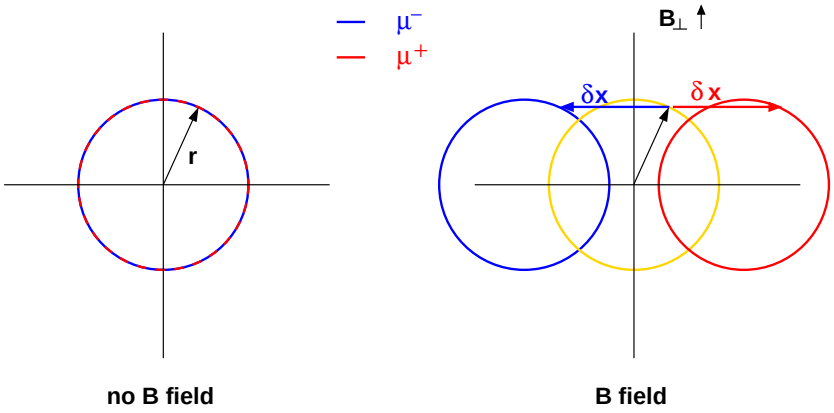

Figure 5.17: *Sketch illustrating the deviations of a muon due to transverse momentum and to the geomagnetic field in the shower plane. The left graph illustrates the case of no magnetic field. The right graph illustrates how the magnetic field deviates positive and negative muons into opposite directions along the x axis (perpendicular to* $\mathrm{B}_{\parallel}$*).*

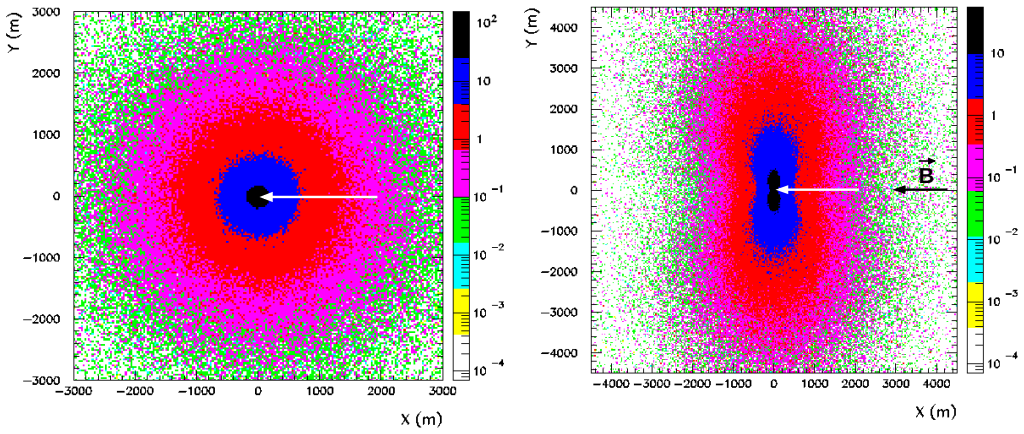

Figure 5.18: *Map of the muonic signal in the shower plane for* 10 *EeV proton induced shower with a zenith angle of* 86° *and azimuth angle* $\phi = 90°$. *Left panel: Map without the effect of the geomagnetic field. Right panel: Map with geomagnetic field. The white arrow indicates the shower direction and the black arrow shows the direction of the magnetic field.*

The main effect of the geomagnetic field is to distort the patterns of the muon densities (and consequently also the muon signal maps) in the shower plane. The patterns exhibit elliptical or even 2-lobed shapes if α_B is sufficiently large, instead of the circular shapes in the absence of magnetic fields. The two lobes that may appear at each side of $\mathrm{B}_\perp$ correspond to the negatively and positively charged muons deviating in opposite directions. As an example, in Fig. 5.18 we show a muon signal map simulated with AIRES using proton showers with $E = 10$ EeV, $\theta = 86°$ and $\phi = 0°$ without (left panel) and with (right panel) geomagnetic field. One can clearly observe the two lobes produced by the deviation of μ^- and μ^+ in opposite directions.

The geomagnetic field causes two distinct types of deflection in the particle trajectories as illustrated in Fig. 5.19, which in turn produce different patterns in the shower plane depending on the zenith and azimuth angles. The patterns can be very complex showing asymmetries between lobes and changes of the orientation with respect to the arrival direction of the shower. To study the two types of deflection, we define Ψ as the angle between $\vec{\mathrm{B}}_\perp$ and the direction parallel to the ground plane (see Fig. 5.19). We use this angle to decompose $\vec{\mathrm{B}}_\perp$ into a component parallel to the early-late direction in the shower plane ($\zeta = 0°$ and $180°$) which we denote as $\mathrm{B}^s_\perp$, and another component perpendicular to this direction (along $\zeta = \pm 90°$) denoted as $\mathrm{B}^g_\perp$. In Fig. 5.19 we show this decomposition. $\mathrm{B}^g_\perp$ deflects the particles along the early-late direction ("vertical deflection"), and is responsible for asymmetries

with respect to the semi-minor axis of the ellipse because it removes part of the muons from the ground in the late region of the shower as can be seen in Fig. 5.19. On the other hand, $B^s_\perp$ deflects the particles along the $\zeta = \pm 90°$ direction ("horizontal deflection"). Under the assumption that a shower at large zenith angles has an ellipsoidal shape, the length of the semi-minor axis of the ellipse is determined by the strength of this component.

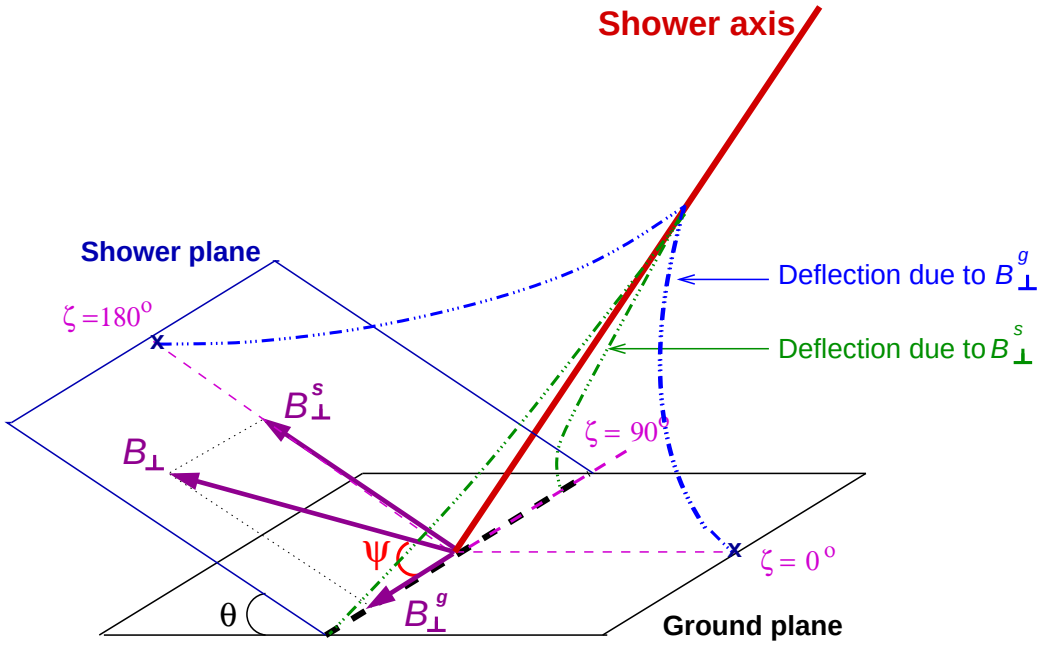

Figure 5.19: *Illustration of the two types of deflection in the muon trajectories due to the effect of the geomagnetic field* $B_\perp$.

In Fig. 5.20 we show the components $B^g_\perp$ and $B^s_\perp$ at the Auger site as a function of the azimuth angle for different zenith angles. $B^g_\perp$ is independent of the zenith angle and is 0 at $\phi = 87°$ and $\phi = 267°$. Therefore, one expects a mirror symmetry on the muon distributions in the shower plane with respect to the early-late line ($\zeta = 0°$ and $180°$) in showers arriving at these two azimuth angles. On the other hand, this component reaches a maximum at $\phi = 177°$ and $\phi = -3°$. At these angles one expects that the asymmetry induced by the geomagnetic field between the early and late parts of the shower is strongest.

The component $B^s_\perp$ is always greater than 0 for $\theta \geq 60°$ and moreover it depends on the zenith angle. The amplitude of the oscillation of its intensity decreases as the zenith angle rises, becoming less dependent on the azimuthal angle. For instance, at $\theta = 70°$ the amplitude is $\pm$ 7 μT (65% of the central

value) while at $\theta = 86°$ it is $\pm$ 1.5 μT (11% of the central value). The central value of the oscillation increases with the zenith angle. By inspecting Fig. 5.20, we expect the horizontal deflection to be minimum at $\phi = 87°$ and maximum at $\phi = 267°$ (the same azimuth angles at which $B^g_\perp = 0$).

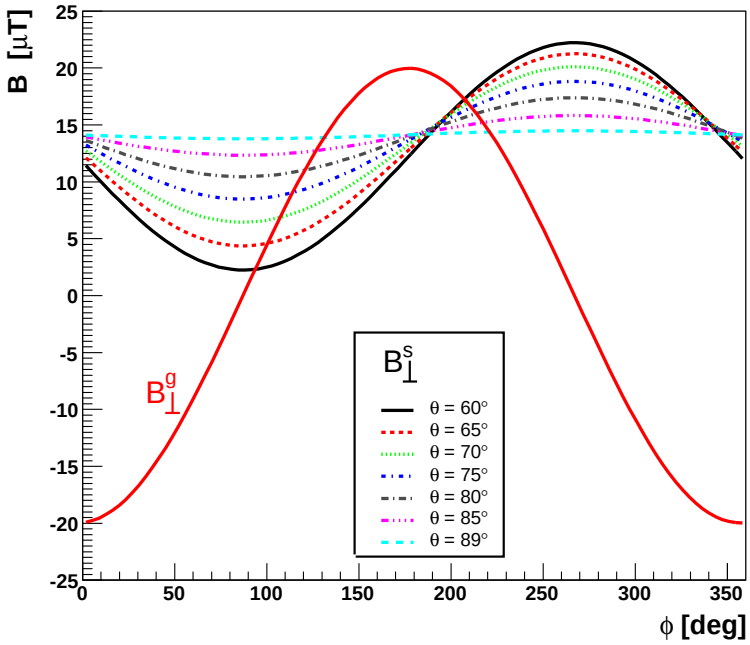

Figure 5.20: *The components* $B^g_\perp$ *and* $B^s_\perp$ *of* $B_\perp$ *plotted as a function of the azimuth direction of the shower for different zenith angles ranging from* 60° *to* 89°. *Note that* $B^g_\perp$ *is independent of* θ.

To illustrate how both types of deflection affect the shape of the signal maps, we show in Fig. 5.21 the muon (on the left-hand side) and electromagnetic (on the right-hand side) signal maps in the shower plane for 10 EeV proton induced showers at $\theta = 86°$ and different shower azimuthal directions (assuming the Auger convention with $\phi = 0°$ corresponding to the geographical East). We choose $\theta = 86°$ because the geomagnetic deviation of muon trajectories is expected to be very important at this angle (see the right panel of Fig. 5.16). In Fig. 5.20 one can also see that the strength of $B^s_\perp$ varies very little with the azimuthal angle for $\theta = 86°$ (the length of the semi-major of the ellipse will not change much) and as a consequence, the change with ϕ of the shape of the muon maps will mostly depend on the intensity of $B^g_\perp$. For instance, at $\phi = 0°$ (top panels) and 180° (bottom panels) the shower is

practically arriving perpendicular to the direction of the geomagnetic field. By inspecting Fig. 5.20 one can observe that both the vertical and horizontal deflections are relevant at both azimuthal angles. The "horizontal deflection" is the cause of the lobular structure and the "vertical deflection" produces the asymmetry in the size of the lobes. The sign of $B^g_\perp$ determines which of the two lobes has a higher muon density. At $\phi = 0°$ the component $B^g_\perp$ is < 0, so that a fraction of the negative muons are removed from the ground and consequently the μ^- lobe becomes smaller (see Fig. 5.21). On the contrary, at $\phi = 180°$ the component $B^g_\perp$ is > 0 and a fraction of positive muons are deviated away from the ground, turning the μ^+ lobe into the one with the smallest muon density.

In the middle panel of Fig. 5.21, we show the muon map for a shower at $\phi = 90°$. In this case, the only relevant deflection is the horizontal one ($B^g_\perp = 0$) and therefore, the map exhibits a mirror symmetry with respect to the arrival direction of the shower, i.e. both lobes have the same size.

In the panels on the right-hand side of the Fig. 5.21, we show the signal maps of the electromagnetic component for the same showers. These maps exhibit a similar behaviour to their corresponding muon maps. This is due to the fact that the electromagnetic particles at large zenith angles come mostly from muon decay and therefore, preserve to some extent the muon spatial distribution. However, the electromagnetic maps have less sharp patterns than the muon maps because the deflection of electrons and positrons is dominated by multiple Coulomb scattering.

It is clear that the lateral distribution of the S_{EM}/S_μ ratio averaged over all ζ should be strongly modified by the presence of the geomagnetic field at very large zenith angles. We can infer from Figs. 5.16 and 5.20 what is the effect of the geomagnetic field on the lateral distribution of S_{EM}/S_μ depend on the shower zenith and azimuth angle. On one hand, the effect of the geomagnetic field is expected to be more relevant the larger the zenith angle. On the other hand, one expects the difference in the lateral distribution of S_{EM}/S_μ with and without geomagnetic field to be minimum in a shower with $\phi = 90°$ and maximum at 180°. For this reason, we study the effect of the geomagnetic field on the S_{EM}/S_μ lateral distribution of showers induced at different zenith angles and at $\phi = 90°$ and 180° for each θ.

In the left panels of Figs. 5.22 and 5.23 we show the lateral distribution of S_{EM}/S_μ in the presence of the geomagnetic field for proton induced showers at different θ arriving at $\phi = 90°$ and 180° in each case. In the same panels, we also show the corresponding lateral distribution obtained neglecting the geomagnetic effect. We also plot in the right panels of Figs. 5.22 and 5.23 the relative difference between the distributions with and without the geomagnetic field, taking as reference the case without field (*Rt* in the figure

designates the ratio S_{EM}/S_{μ}) as a function of the distance to the shower core. In Fig.5.22 one can see that the relative differences are $\lesssim 20\%$ for the two azimuthal angles and for $\theta \leq 80^{\circ}$ and $log_{10}r > 1.5$, and as a consequence the effect of the geomagnetic field remains negligible at $\theta \leq 80^{\circ}$. In Fig. 5.23 one can see that the geomagnetic effect starts to be relevant at $\theta = 82^{\circ}$ for the case of $\phi = 180^{\circ}$ (maximum deviation) where the relative difference is $> 20\%$ for $log_{10}r < 2$, whereas at $\phi = 90^{\circ}$ (minimum deviation) the relative difference remains smaller than 20% for $log_{10}r > 1.5$. At larger angles the situation changes and the geomagnetic field has a strong effect on the S_{EM}/S_{μ} distribution, even for the azimuth angle of the shower at which the effect is expected to be minimum. For instance, at $\theta = 86^{\circ}$ the relative difference is much larger than 20% at $\phi = 180^{\circ}$ in all the range of distances to the shower core, and also at $\phi = 90^{\circ}$ for $log_{10}r < 2.5$. S_{EM}/S_{μ} increases the most near the shower core when the geomagnetic field is included. The reason is that only the highest energy muons are not significantly deflected by the geomagnetic field and there are more likely to suffer hard interactions where an EM shower is produced. As a consequence S_{EM} increases and at the same time S_{μ} decreases because lower energy muons are being moved away from the core with the overall effect of increasing S_{EM}/S_{μ}.

In conclusion, for the purposes of event reconstruction the effect of the geomagnetic field on the S_{EM}/S_{μ} lateral distribution must be taken into account only when $\theta \gtrsim 86^{\circ}$.

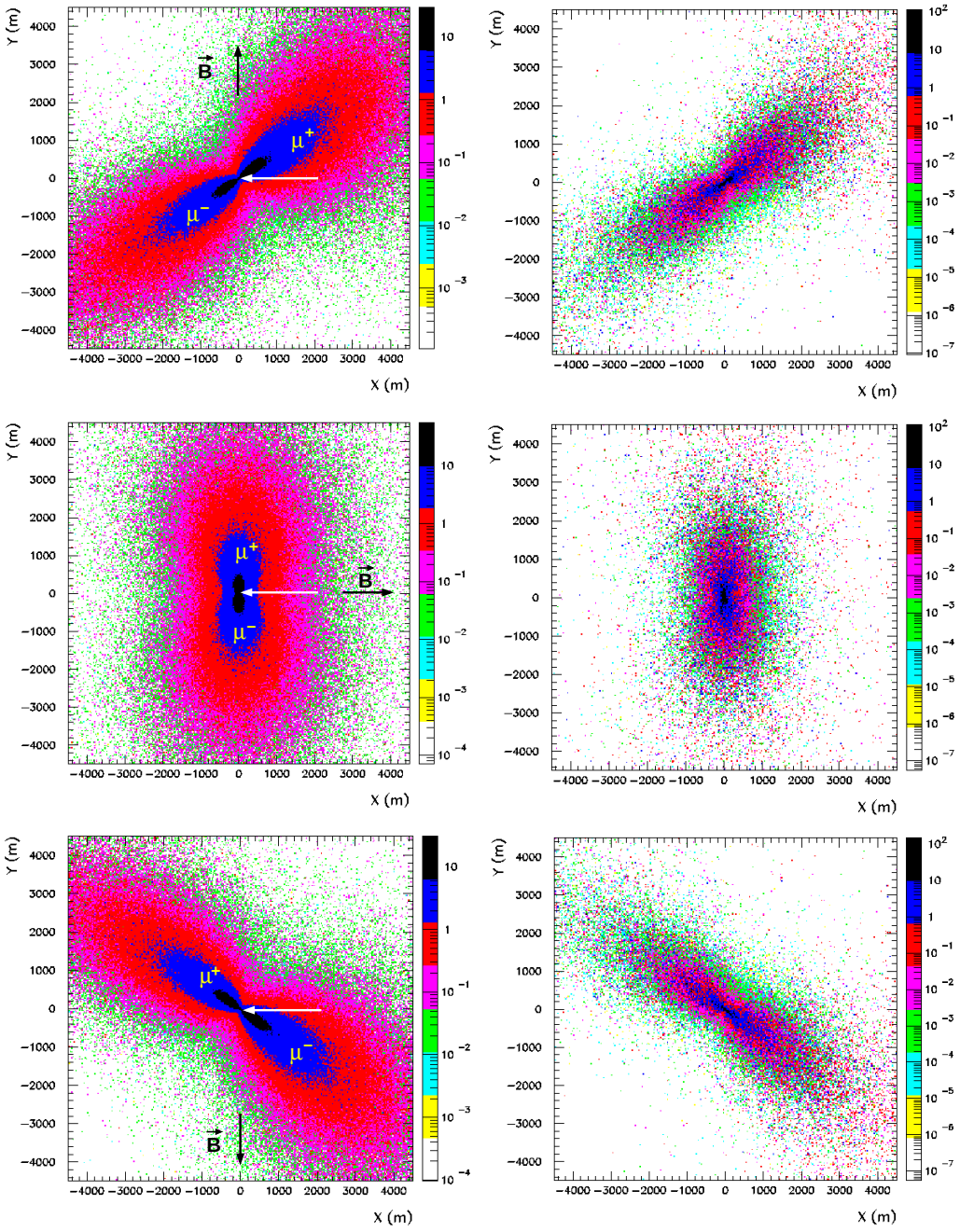

Figure 5.21: *Muon (left) and electromagnetic (right) signal maps in the shower plane for* 10 *EeV proton showers with an incident zenith angle of* 86° *as obtained in AIRES simulations for the following azimuthal angles in the Auger convention:* 0° *(top),* 90° *(middle) and* 180° *(bottom). The reference system has the x-axis pointing out in the shower direction (white arrow). The black arrow indicates the direction of* $\vec{\mathrm{B}}$*. Note that* $\vec{\mathrm{B}}$ *indicates the total field (and not only the component of it perpendicular to the shower axis that is responsible for the muon and EM deflection).*

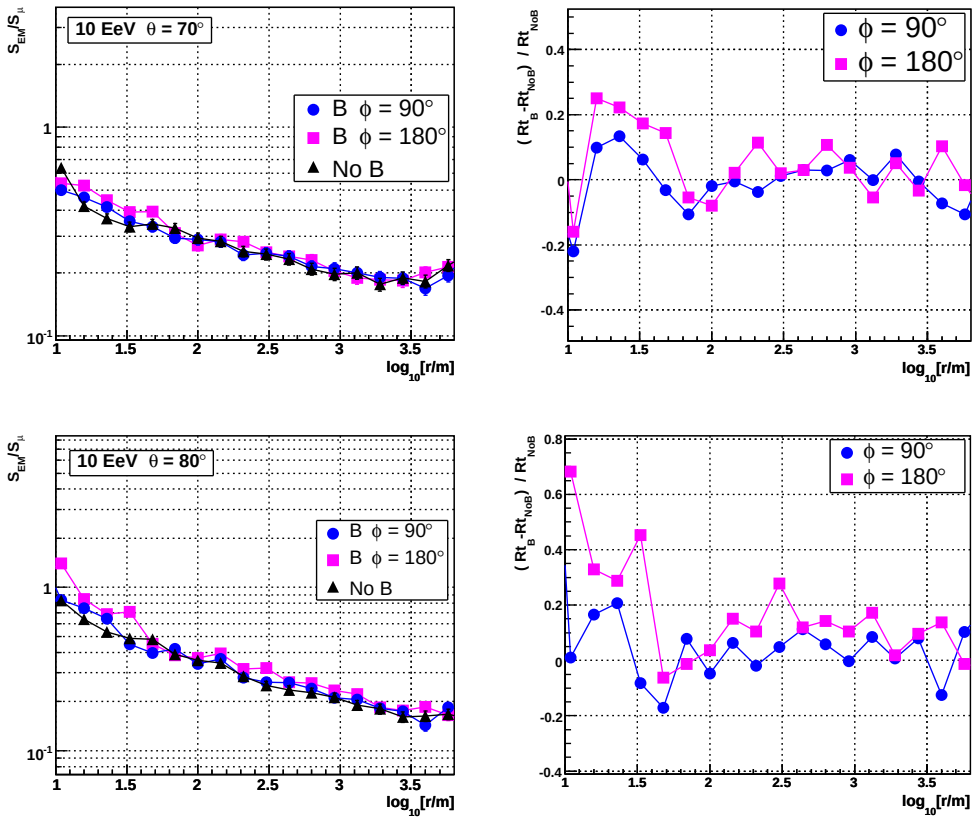

Figure 5.22: *Left panel: The lateral distribution of the ratio of the electromagnetic to muon signals in the shower plane for showers at* $\phi = 90°$ *(circles) and* $\phi = 180°$ *(squares) under the presence of the geomagnetic field, compared with the distribution without the effect of the geomagnetic field. Right panel: The relative differences between the distributions without and with geomagnetic field effect (see text) for showers at* $\phi = 90°$ *(circles) and* $\phi = 180°$ *(squares). The distributions correspond to the average of 100 proton showers with 10 EeV simulated with AIRES + S1000 USC code at* $\theta = 70°$ *(top) and* $80°$ *(bottom).*

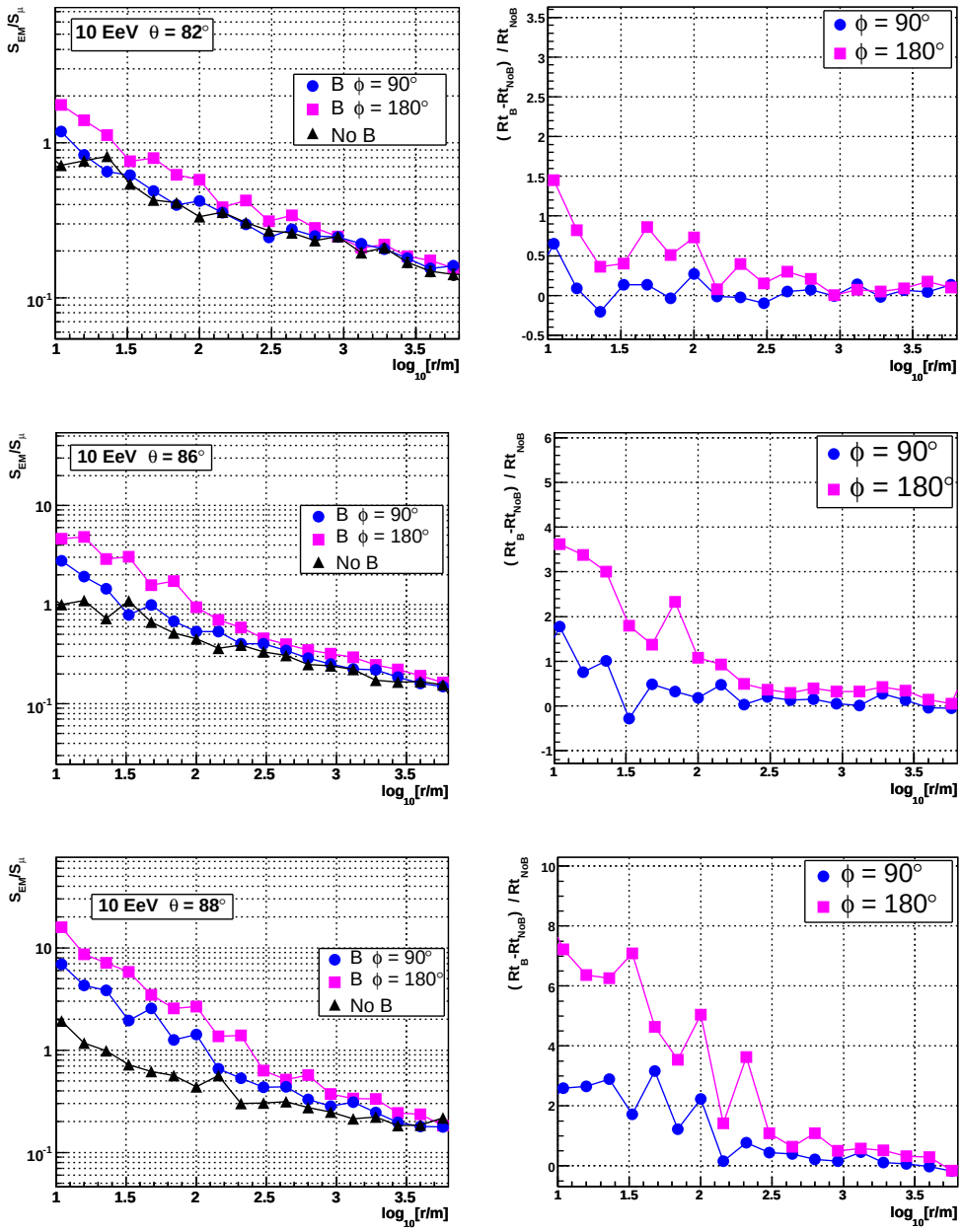

Figure 5.23: *Left panel: The lateral distribution of the ratio of the electromagnetic to muon signals in the shower plane for showers at* $\phi = 90°$ *(circles) and* $\phi = 180°$ *(squares) under the presence of the geomagnetic field, compared with the distribution without the effect of the geomagnetic field. Right panel: The relative differences between the distributions without and with geomagnetic field effect (see text) for showers at* $\phi = 90°$ *(circles) and* $\phi = 180°$ *(squares). The distributions correspond to the average of 100 proton showers with 10 EeV simulated with AIRES + S1000 USC code at* $\theta = 82°$ *(top),* $86°$ *(middle) and* $88°$ *(bottom).*

Chapter 6

Identification of Neutrino Candidates in surface detector of the Pierre Auger Observatory

The main experimental challenge in the detection of neutrino-induced showers with the surface detector of the Pierre Auger Observatory is to identify them in the background of showers initiated by nucleonic cosmic rays. Deeply penetrating highly energetic particles such as neutrinos, can initiate showers very close to the ground level while protons, heavier nuclei and photons interact shortly after entering the atmosphere. As suggested almost 30 years ago, the observation of inclined showers enhances the difference between these two types of showers [53]. Therefore the main signature of down-going neutrino events are inclined showers that interact deep in the atmosphere (Deep Inclined Showers from now on).

6.1 Selection of Inclined Events in the data set recorded by the Surface Detector

Down-going neutrino showers are searched among the inclined data set registered with the Surface Detector (SD) of the Pierre Auger Observatory. An efficient selection of inclined events in the data set is crucial for the subsequent identification of neutrino candidates.

The SD data set consists of all T3 level triggers acquired by the Central Trigger System (see Section 3.3.2). The higher levels of trigger (T4 and T5 levels) developed for vertical showers to select real events, are not suitable for

inclined showers. In the case of inclined showers, the selection of real showers in the data set can be made *a posteriori* by means of algorithms of station selection and event reconstruction.

We have developed an event selection for inclined showers that follows a *bottom-up* procedure applied to the data set collected at the surface detector and that consists of several steps: preselection of time-constrained configurations of stations; selection of a reconstruction seed; selection of candidate stations studying the space-time compatibility with the seed, and reconstruction of the resulting configuration of candidate stations which is finally accepted as a physical event if the reconstruction succeeds.

The selection procedure presented here is aimed at obtaining an optimum efficiency in the selection of inclined showers produced by neutrinos. The advantage with respect to the current algorithms used to select conventional nucleonic showers [71], is that the algorithms presented here have been developed taking into account the topological characteristics of the neutrino events obtained in Monte Carlo simulations, in order to minimize the rejection of potential neutrino candidates. Also the tolerances of the tank selection have been optimized to avoid rejecting the earliest stations in the event, which as we will show below are crucial for neutrino identification. However and despite this fact, the algorithms presented here still share many of the ideas developed by the inclined shower group of the University of Santiago de Compostela [101, 67] to select conventional nucleonic inclined showers.

6.1.1 Station selection

Developing criteria for station rejection is essential to select physical events. These criteria have been developed taking into account the particular timing and topological characteristics of inclined showers.

The spatial configuration of the stations in an inclined event can be of two types: non-aligned or aligned, which have to be treated with different selection algorithms.

In the following, the different steps used to select candidate stations are described in the same order they are applied to real data. The first four algorithms are common to non-aligned and aligned configurations, whereas the remainder are different for each type of configuration.

Rejection of Engineering Array stations

The Engineering Array (EA) is a small subset of 100 stations originally built for testing the design of the observatory at the beginning of the project. The stations that belong to the EA are different from the ones currently being

deployed (components, electronics,...). All the remaining stations have the same characteristics. Due to this, the stations belonging to the EA must be removed from the event. This is easy since each of the stations of the Surface Detector is identified with an unique identifier number (ID), which is less than 100 for the stations belonging to the EA.

Treatment of twin stations

If both stations of a twin pair [1] belong to the same event, the one with the higher ID is removed by default from the event because this station is not part of the central trigger system.

Selection of time clusters

The main aim here is to preselect configurations of stations that will be tested by the subsequent algorithms until a satisfactory configuration is found. A good criterion to build them up is to look for time-constrained configurations, called time clusters. The procedure to build up a time cluster is as follows.

After applying the two previous criteria, the remaining stations are sorted by increasing start-time. We begin with the earliest station and check if the next one in time is closer than 16 μs. If this is the case both stations are grouped into the same cluster. We keep adding stations to this cluster applying the same procedure to the following stations in time. If we find one station farther than 16 μs from its predecessor, a new and different cluster is built up using that station as starting point.

If multiple time clusters are found, these are sorted by increasing quality. The quality score is based on compactness in time of the stations belonging to the cluster. The score is defined as the number of stations whose start-time difference is less than 6 μs.

At the end of this procedure, we have a set of time clusters sorted by increasing quality.

Selection of the best seed

The main aim here is to find a good seed of three tanks which is used afterwards as the base for selecting the candidate stations that will be involved in the event reconstruction. The selection of the seed should be robust enough

[1] A twin pair are two stations that are separated by around 11 meters, which serve the purpose of studying the accuracy of the angular and signal determination. The default separation between tanks in the surface array is 1.5 km.

to guarantee its reliability, because a wrong choice of the seed could involve losing real events or selecting fake events.

In this step, the time clusters are studied in decreasing order in quality to find the best seed. The loop over the time clusters is stopped when a good seed for the reconstruction is obtained.

The time clusters can contain accidental stations[2] that do not belong to the shower and which are typically triggered by small showers or by single muons not belonging to the event. A first step to avoid these "noisy" stations is to reject the so-called isolated stations. A station is considered to be isolated if it does not have at least two stations within a distance of 5000 m. These large tolerances are aimed at keeping the peripheral stations in very inclined events. At this stage some accidentals might still be accepted but they will be rejected in the subsequent selection steps when applying the conditions on space-time compatibility among stations described later in this chapter.

After removing the isolated stations, the next step is to look for the best seed of three stations that provides a preliminary angular reconstruction of the event and that represents the point of reference to select more candidate stations by means of a *bottom-up* procedure based on the space-time compatibility of the station with the seed.

At this stage, it is not known whether the configuration of stations is non-aligned or aligned. So, the simplest approach to find a good seed, is firstly to look for a non-aligned seed. If this is not found the next step is to look for an aligned seed. This latter procedure will be particularly important for the neutrino search.

The seed of a non-aligned configuration

The main aim here is to select 3 non-aligned stations that are compatible with a plane shower front propagating at the speed of light. In an event, there are a lot of possible seeds that can be found fulfilling the previous condition. Among them, one possibility could be to select as seed the 3 stations with the highest possible signal sizes, because their start-times should be better defined. However, a large accidental signal (for instance due to a muon not belonging to the shower) could appear in a tank of the seed and this would make it a bad choice. Due to this, the signal size is only an indicator of the quality of the seed, but it is not enough to guarantee the selection of the best seed. It is better to introduce another indicator, namely, the number of compatible stations in the event. The objective is to choose as seed the 3 non-aligned stations with as many stations compatible with it and large

[2]Accidental stations are triggered stations that do not belong to the event.

signal size as possible. Also the seed triangle must be compatible with a plane shower front propagating at the speed of light.

The procedure to count the number of compatible stations with each station is as follows. Every set of three stations (i,j,k) in the event, is accepted as compatible if certain conditions (see below) are fulfilled. In this case each station of the triplet gains a bonus score that is weighted with the signal size of the station. In this way if at the end of the procedure, two stations have the same number of compatible stations, the station with the largest signal typically has a larger score than the other. The stations with bonus ≥ 1 are candidate stations to form the seed. The conditions are the following:

- Time compatibility between the triangle stations: The time compatibility for a pair (i,j) of tanks is studied using the apparent transmission speed of the signal between them defined as,

$$v_{ij} = \frac{d_{ij}}{\Delta t_{ij}} \tag{6.1}$$

  where d_{ij} is the distance between stations i and j on the ground, and Δt_{ij} is the difference between the signal start-times. In the case of vertical showers, the apparent transmission speed of the signal takes values higher than the speed of light. It tends to infinite in the extreme case of a shower with $\theta = 0°$ because the shower front plane hits a pair of tanks roughly at the same time. However, the apparent speed of the signal is tightly concentrated around c in the case of almost horizontal showers. For instance, in the case of a shower with $\theta = 90°$ the difference between the time at which the shower front hits the earliest station and the time at which it hits the following station is given by $\Delta t_{ij} = d_{ij}/c$. So, the apparent transmission speed of the signal must be equal or greater than the speed of light. Hence, the condition of time compatibility is chosen to be,

$$v_{ij} \geq 0.9c \tag{6.2}$$

- Compacity: The sides of the triangle have to be less than 5000 meters. In events with a small number of stations, typically 3 or 4, the number of compatible stations is not a good enough indicator to ensure the quality of the seed, so certain compacity requirements are necessary.

- Non-aligned configuration: This is tested by requiring that the absolute value of the difference between the azimuth angles of the lines joining stations (i,j) and stations (i,k) is larger than 5 deg.

- Physical values for the angular reconstruction of the seed: The reconstruction procedure is based on requiring compatibility of the 3 stations with a plane shower front propagating at the speed of light along the shower axis. We choose the first station of the triplet as the local origin (labeled as 1) and assumed that the stations all lay in the same plane ($z_i << x_i, y_i$). Therefore, the time $t(\vec{r_i})$ at which the shower plane passes through the position of station i, $\vec{r_i} = (x_i, y_i)$ is given by,

$$c(t_i - t_1) = -\vec{a}\,(\vec{r_i} - \vec{r_1}) \qquad \text{for } \; i \in \{1, 2, 3\} \tag{6.3}$$

  where $\vec{a} = (u, v)$ is a unit vector in the forward direction of the propagation of the shower front. We obtain two independent equations,

$$\begin{aligned} ct_{12} &= \vec{a}\,\vec{r_{21}} \\ ct_{13} &= \vec{a}\,\vec{r_{31}} \end{aligned} \tag{6.4}$$

  The values of the directional cosines (u,v) are obtained by solving this linear system analytically. From the solution (u, v) the angles can be obtained,

$$\tan\theta = \sqrt{\frac{u^2 + v^2}{1 - u^2 - v^2}} \;\; , \;\; \tan\phi = \frac{v}{u} \tag{6.5}$$

  The solution is accepted as 'physical' if the fit results on a physical azimuth angle and $u^2 + v^2 \leq 1.1$.

Once the score of each station is determined, the next step is to select the 3 non-aligned stations with as large bonus score as possible between the seed candidates. The stations are first sorted in decreasing order of score. A triangle of stations (i,j,k) is accepted as seed if the fit to a plane performed using these 3 stations results in physical values of zenith and azimuth angles (using Eq. 6.5). This test is applied first to the 3 stations having the 3 largest scores. If this first choice is not accepted, the remaining configurations with three stations are tested until one is found. If at the end of this set of tests, we have not find a non-aligned seed, an aligned seed is searched for as described below.

The seed of an aligned configuration

In the case of configurations where the stations are quasi or completely in line, the procedure to obtain the seed is different to the non-aligned case.

In this case, we choose the signal size as indicator to select the candidate stations to form the seed. The seed stations should be the three stations with the largest signals in which the start-time should be better defined. The main aim here is to obtain three aligned stations with as high signals as possible and compatible with a plane shower front propagating at the speed of light. An aligned triplet of stations (i,j,k) is accepted as a valid seed if the following conditions are fulfilled:

- Time compatibility between the stations: This is defined as in the non-aligned case (see Eqs. 6.2 and 6.1).
- Aligned configuration:
  - The area of the triangle subtended by the 3 stations is smaller than 0.6 km^2.
  - The aligned configuration of the three stations is tested by requiring that the differences between the azimuth angles of the lines joining stations (i,j), (i,k) and (j,k) are all smaller than 5 deg.
- Once we have determined that the stations are in a line, their position in the array must be in increasing order of start-time. The assumption here is that in aligned events the shower direction projected on the ground lies along the line of triggered tanks. This means, we expect that the earliest station is at an extreme in the line of tanks, the following station in time is located in the second position in the line of tanks, etc... The procedure to check if the positions of the seed stations are ordered in start-time is as follows. We calculate the vector from the position of the earliest station (I) to the position of the second station in time (J) and the vector from the second to the position of the third station (K). If the positions of the stations are ordered in time, these vectors have the same direction and therefore their dot product is greater than 0,

$$\vec{IJ} \cdot \vec{JK} > 0 \tag{6.6}$$

- Physical value for the zenith and azimuth angles of the seed: The angular reconstruction based on a fit to a plane travelling at the speed of light is not possible in the case of an aligned seed. Instead the azimuthal direction can be approximated as the direction of the line of triggered tanks which is calculated as the average value of the relative azimuth angles subtended between the vectors $\vec{IJ}$, $\vec{IK}$ and $\vec{JK}$ and the $x-$axis of the coordinate system of the observatory,

$$\phi_{seed} = \frac{\phi_{ij} + \phi_{ik} + \phi_{jk}}{3} \tag{6.7}$$

Once the azimuthal direction of the shower axis is determined, the apparent transmission speeds of signal between tanks are calculated along this direction.

Under the assumption that the shower front is a plane front moving with the speed of light along the shower axis, the apparent transmission speed between tanks also provides an estimate of the zenithal direction of the shower. As previously mentioned, the apparent transmission speed is equal to the speed of light for a shower with $\theta = 90^\circ$ with its value increasing for decreasing θ. For instance, let us consider two tanks i and j that are separated by a distance d on the ground. For a shower with $\theta = 90^\circ$ the apparent transmission speed of the signal is c and therefore the difference of start-times is $t_{90^\circ} = d/c$. As Fig. 6.1 illustrates, for a shower with a given θ the difference of start-times is $t_\theta = t_{90^\circ} \sin\theta_{ij}$. As a result, the apparent transmission speed of the signal becomes,

$$v_{ij} = d/t_\theta = d/(t_{90^\circ} \sin\theta_{ij}) = c/\sin\theta_{ij} \tag{6.8}$$

Therefore, an estimate of the "relative" zenith angle θ_{ij} can be obtained as,

$$\sin\theta_{ij} = \frac{c}{v_{ij}} = \frac{c}{d}\, t_\theta \tag{6.9}$$

where t_θ is measured and d (distance between stations projected onto the shower axis on the ground) is known.

The zenith angle of the seed is calculated as the average value of the relative zenith angles of the three possible combinations of the seed stations,

$$\theta_{seed} = \frac{\theta_{ij} + \theta_{ik} + \theta_{jk}}{3} \tag{6.10}$$

θ_{seed} is only accepted if the difference between the 3 "relative" angles in Eq. 6.10 do not differ by more than 20 degrees. The tolerance may seem very large but it is needed to allow for variations of the apparent transmission speeds of the signal because of the variable curvature of the shower front. This variation is very large in the case of neutrino showers, where the early region ("upstream" side) of the shower can have a significant curvature, whereas the late region ("downstream" side) tends to planarity. Since there is not any condition about the maximum distance between the seed stations, it could be that two stations belong to the early (late) part and the other one belongs to the late (early) part, and in this case a significant difference between

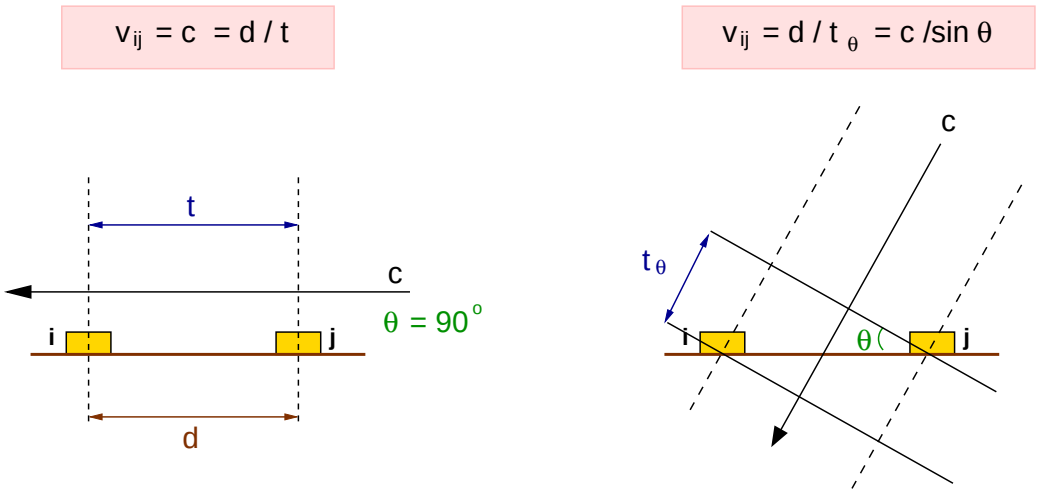

Figure 6.1: *Schematic picture illustrating the dependence of the apparent transmission speed of the signal on the zenith angle of the shower. Left panel: The apparent transmission speed of the signal between two tanks, v_{ij}, is equal to the speed of light for a shower with $\theta = 90°$. Right panel: The dependence of the apparent transmission speed of the signal on θ follows Eq. 6.9.*

their zenith angles is obtained. The difference between the zenith angle obtained using only the early tanks of an event and the one obtained using only the late tanks was tested with Monte Carlo simulations.

Moreover the tolerance in θ_{seed} has to be large because we assume the shower direction lies along the line of triggered tanks and this is in general not true.

This procedure provides a robust seed for the selection of stations in the case of an aligned event. Even if the event is not aligned, this method provides a good approach to find an aligned seed.

Selection of configurations

The outcome of the previous algorithm is a preliminary angular reconstruction of the shower axis given by the seed angles θ_{seed} and ϕ_{seed}. The proper event selection starts now under the idea of building up the set of candidate stations by compatibility with the seed, rejecting the stations of the time cluster that are not space-time compatible with the seed. We test this compatibility using the angular reconstruction performed for the seed $(\theta_{seed}, \phi_{seed})$. Once again, the selection algorithm will be different in the cases of non-aligned and aligned configurations.

Non-aligned configuration

In the case of a non-aligned seed, we study the compatibility of a station i with the seed using the zenith (θ_{seed}) and azimuth angles of the seed (ϕ_{seed}). For every station i, different from the seed stations, Eqs. (6.4) and (6.5) are applied to estimate the shower angles from the triangle formed by station i and the 2 stations in each side of the seed (θ_{il}, ϕ_{il} with $l = 1, 2, 3$ labeling the sides of the triangle). For each side, we check if the station i is in line with the side l of the seed. If this is not the case, the angles θ_{il} and ϕ_{il} are considered to be compatible with the angles of the seed if

$$|\sin\theta_{il} - \sin\theta_{seed}| < 0.2$$

$$|\phi_{il} - \phi_{seed}| < 10 \text{ deg} \tag{6.11}$$

If these conditions are fulfilled for one of the sides of seed, the station gains a score. Finally, station i is accepted as a station of the event if its final score is at least 2.

Aligned configuration

In the case of configurations in which the seed stations are in line, a different procedure is applied to check the space-time compatibility of a station. It is based on the fact that the apparent transmission speed of the signal between any two stations along the shower direction should not vary significantly for whatever couple of stations in the event.

For every station i different from the seed stations, we test its compatibility with the apparent transmission speed of the signal in the seed, given by $v_{seed} = c/\sin\theta_{seed}$. Eq. (6.8) is applied to calculate the apparent transmission speed of the signal between the station i and each seed station (v_{il} with $l = 1, 2, 3$ labeling the stations of the seed). For each station of the seed, we first check if the position of station i is ordered in start-time with the seed station following the procedure described in the previous section (see Eq. 6.6). If this is the case, a speed v_{il} is considered to be compatible with v_{seed} if,

$$\frac{|v_{il} - v_{seed}|}{v_{seed}} < 0.16 \tag{6.12}$$

The 16% tolerance allows small variations of the apparent transmission speeds of the signal because of the variable curvature of the shower front in the shower direction. For instance, for a pair of stations in the early region of the shower the apparent speed of the signal may be larger than that for a pair of stations in the late region. Station i is accepted as a station of the

event if the 3 apparent transmission speeds of the signal between it and the seed stations are compatible with v_{seed}.

Finally, the linearity of the full event is tested using as reference value the azimuth angle of the seed ϕ_{seed} and the same tolerance as in the previous cases. If the number of aligned stations is equal the total number of selected stations, the event is labeled as "completely aligned".

Second treatment of isolated stations

After selecting the set of candidate stations, the algorithm for rejecting isolated stations is applied again. The aim is to avoid accidental stations that were not removed by the previous algorithms and that can affect the angular reconstruction. One should note that the rejected stations may belong to the event, but it is better to be restrictive rather than to introduce "noisy" stations in the analysis, especially in the case of low multiplicity configurations.

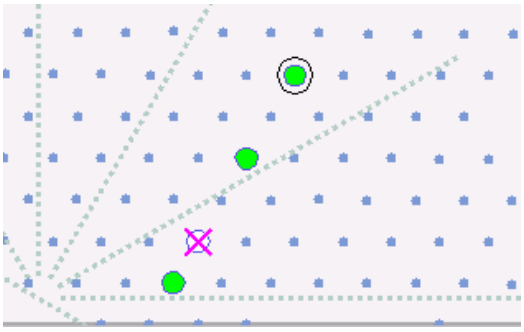

Figure 6.2: *Footprint of an aligned event where the stations that remain after the selection procedure are too much separated in the array.*

It is also possible that after applying this algorithm the accepted configuration is not an event. An example is shown in Fig. 6.2 in which two of the selected stations (those at the two ends along the line of tanks) do not have at least 2 stations within 5000 m and they are rejected. As a consequence the final configuration does not pass any of the T3 trigger conditions.

6.1.2 Angular reconstruction

After selecting the candidate stations, the next step is the angular reconstruction needed in our work to select inclined events. The reconstruction follows two different methods depending on the event configuration:

- Non-aligned configuration: non-aligned event with either an aligned or a non-aligned seed.
- Aligned configuration: the event is "completely aligned".

Non-aligned configuration

In the case of non-aligned events, the "standard" angular reconstruction can be used to determine the direction of the shower.

Plane Fit: non-linear solution

The direction of the shower axis is estimated from the start-time of the selected stations under the basic assumption that the shower front is a plane front moving with the speed of light along the shower axis. Thus, the time $t(\vec{r_i})$ when the shower plane passes through a given position $\vec{r_i} = (x_i, y_i, z_i)$ on the ground is given by,

$$ct(\vec{r_i}) = ct_0 - \vec{a}\,\vec{r_i} \tag{6.13}$$

where t_0 is the time at which the impact point of the shower axis reaches ground and $\vec{a} = (u, v, w)$ is a unit vector in the forward direction of the shower axis.

Assuming that the positions of the stations are given with no uncertainty and that the only source of uncertainty is that due to the uncertainty σ_i in the start-time (obtained from [102]), we can obtain the parameters (t_0, u, v, w) by minimizing the squares of the differences between the measured start-time and the predicted times, given by Eq. (6.13),

$$\chi^2 = \sum_{i=1}^{N} \left(\frac{t_i - t(\vec{r_i})}{\sigma_i} \right)^2 \tag{6.14}$$

where N is the number of selected stations.

In order to get a good numerical precision, it is better to sum over quantities with small absolute values, so the positions and times of the stations are referred to the signal-weighted barycenter of the candidate stations, which is set as the origin.

In reality the ground is not exactly a plane. The curvature of the Earth can be taken into account by projecting the z_i coordinate of each station i onto a plane tangential to the ground located at the impact point of the shower axis, assuming again the signal-weighted barycenter of the event as the origin. The coordinate z_i is shifted by

$$\delta z_i = -r_i^2/2R \tag{6.15}$$

where r_i is the distance of the station i from the origin and R is the radius of curvature that is assumed constant and equal to radius of the Earth.

After this correction, the following non-linear system is obtained,

$$\chi^2 = \sum_{i=1}^{N} \left(\frac{ct_i - ct_0 + x_i u + y_i v + z_i w}{c\sigma_i} \right)^2 \tag{6.16}$$

with the constraint $u^2+v^2+w^2 = 1$ and therefore 3 independent parameters: t_0, u, v.

The procedure to solve this system is iterative and converges to an unique solution if the stations are not all along the same straight line. The solution (u, v) corresponds to a physical direction (zenith and azimuth angles) if $u^2 + v^2 \leq 1$ using Eq. (6.5). The uncertainties are obtained propagating the uncertainties on the directional cosines into the angles (for details see [106]).

We use this algorithm to reconstruct the shower direction when searching for neutrino candidates. A more elaborated angular reconstruction requires knowing the position of the shower core and fitting the start-times after correcting them with (for instance) a model of the time delay of muons described in [30]. The aim of our work is however to identify neutrino candidates without a previous knowledge of the core, because current algorithms designed for reconstruction of the core of nucleonic inclined showers are in principle not suitable to determine the core of a neutrino-induced shower.

Aligned configuration

The angular reconstruction in the case of an aligned configuration is just an estimate of the zenith and azimuthal angles of the shower. The procedure is simple and robust. For every pair of candidate stations (i,i+1) sorted by increasing time, the apparent transmission speed of the signal is calculated along the shower direction given by the azimuthal angle of the seed. The zenith angle corresponding to each pair of stations (θ_j) is calculated using Eq. 6.9. The corresponding azimuth angle (ϕ_j) is calculated as the angle subtended between the vector given by the position of stations (i, i+1) and the x-axis. The mean values of these angles corresponding to different pairs of stations give an estimate of the shower zenith and azimuth,

$$\theta = \frac{\sum \theta_j/\sigma^2_{\theta j}}{\sum 1/\sigma^2_{\theta j}}$$

$$\phi = \frac{\sum \phi_j/\sigma^2_{\phi j}}{\sum 1/\sigma^2_{\phi j}} \tag{6.17}$$

The angular uncertainties $\sigma_{\theta j}$ and $\sigma_{\phi j}$ are obtained assuming that the positions of the stations have no uncertainty, and that the only source of uncertainty is that associated to the start-time (obtained from [102]).

In general the reconstructed azimuthal angle is different from the azimuthal angle of the seed assumed to be given by the direction of the line of triggered tanks. Due to this the reconstructed zenith angle of an aligned configuration tends to be smaller than the actual zenith angle.

6.2 Characterization and identification of down-going neutrino showers

The first step in the study of the possibility of identifying down-going neutrino events in the background of ordinary proton and nuclei showers, is to characterize the neutrino-induced showers using Monte Carlo (MC) simulations.

The interaction of a neutrino with atmospheric nuclei may result in a "purely hadronic" or in a "mixed" shower depending on the neutrino flavour, type of interaction (charged current or neutral current) and on the fraction of the energy of the neutrino carried by the secondary particles in the detector (Section 2.3.2).

6.2.1 Simulation of ν-like events

At the present stage of this study, we have assumed that proton primaries interacting deep in the atmosphere produce showers equivalent to the hadronic showers resulting from NC interactions of neutrinos of all flavours, or CC interactions of ν_μ or ν_τ (neglecting both the possible shower initiated by the μ or the τ). The resulting hadronic shower is assumed to carry 20% of the neutrino energy. The validity of this approximation has been studied by comparing proton-induced showers with ν-induced showers in which the interaction of the neutrino is simulated with the Monte Carlo code HERWIG [103], and then the products of such interaction are propagated in CORSIKA [104]. For instance, in Fig. 6.3 we show the comparison of the signal map in the transverse plane of proton- and $\nu_\mu-$induced showers with $\theta = 80^\circ$, injected at a slant depth measured from the ground $\Delta X = 910$ g cm^{-2} and for a proton energy or an energy carried by the hadronic shower $E_p = E_{sh} \simeq 10^{18}$ eV. The agreement between both maps is good at the $\sim 20\%$ level, although this value depends on the distance to the shower core. This is confirmed in Fig. 6.4 where we show the comparison of the muon and electromagnetic contributions to the tank signal as a function of the distance from the shower axis

for the proton-induced and $\nu_\mu-$induced showers. From this plot, no significant difference is appreciable between hadronic showers induced by protons and ν_μs if the showers carry approximately the same energy. This result is in agreement with the detailed study performed in [105].

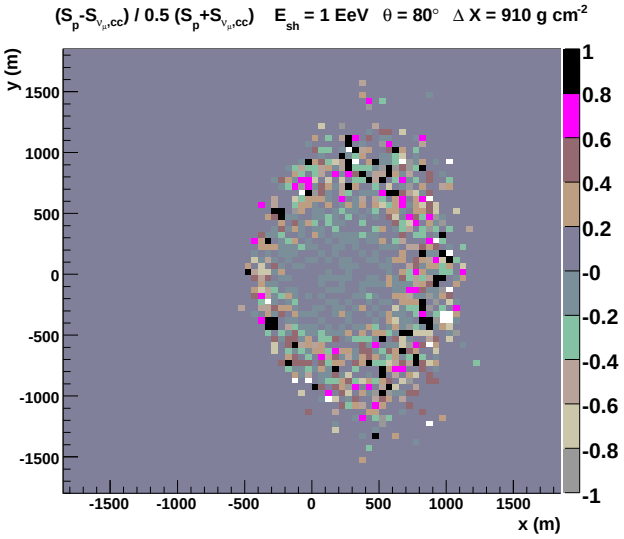

Figure 6.3: *Comparison between the signal map in the transverse plane of proton-induced showers and $\nu_\mu-$induced showers in CC interactions at $\theta = 80°$, $\Delta X = 910$ g cm^{-2} and with an energy going into the hadronic shower $E_{sh} \simeq 10^{18}$ eV. Each map is obtained as the average of 10 showers simulated with CORSIKA + S1000 USC code. The neutrino interaction is simulated with HERWIG. The coloured scale indicates the relative difference between both maps $(S_p - S_{\nu_\mu})/0.5(S_p + S_{\nu_\mu})$.*

We have generated a library of proton showers using the shower propagation Monte Carlo code AIRES 2.6.0. and the hadronic interaction model QGSJET01. We used a 10^{-6} thinning level that gives a good compromise between CPU time consumption per shower and artificial fluctuations due to the statistical sampling of particles.

Showers were generated with energies ranging from 0.1 to 10 EeV, at different incident zenithal angles (from 75° to 89°) and injection points[3] chosen so that the slant atmospheric depth crossed by the shower from the injection point to the ground (ΔX) is as large as 5000 g cm^{-2} (measured along the shower axis).

The simulations were performed in the conditions of the southern site of the Pierre Auger Observatory, neglecting the effect of the geomagnetic

[3]The injection point is the vertical depth of the first interaction point

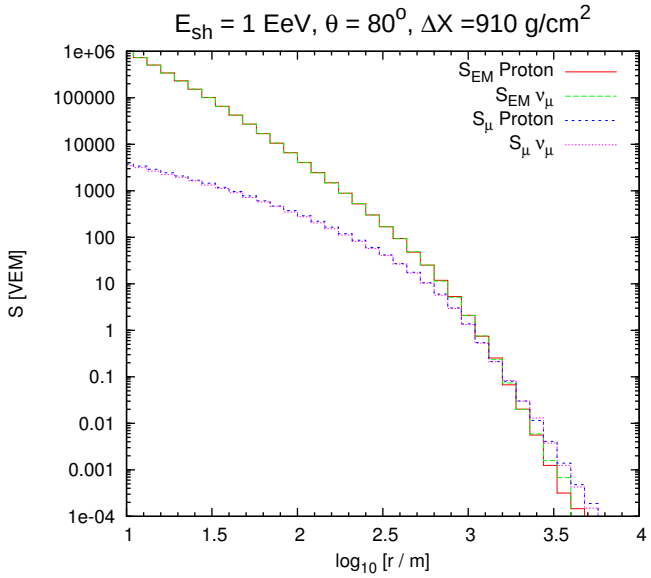

Figure 6.4: *Muon and electromagnetic contributions to the tank signal in VEM as a function of the distance from the shower axis in the shower plane for proton-induced showers and $\nu_\mu-$induced showers at $\theta = 80°$, $\Delta X = 910$ g cm^{-2} and with an energy going into the hadronic shower $E_{sh} \simeq 10^{18}$ eV.*

field. Although the magnetic deviations of the muons are very important for ordinary inclined showers, in the case of showers produced deep in the atmosphere the path lengths traveled by muons are in general not large enough to be significantly affected by the geomagnetic field.

The simulation of the Surface Detector (SD) of the Pierre Auger Observatory has been performed using the standard modules of the Auger Offline Framework [94] using as input the ground particle files produced by the AIRES code. The response of the tank has been simulated with the Geant4 fast tank simulator [72]. The current Surface Detector central trigger configuration [98] has been applied to select the showers that would trigger the detector using the Central Trigger Simulator module. We have assumed an infinite array, so that the shower is always fully contained inside the array.

In those cases in which we only needed the average signal in an Auger tank, we used the S_{1000} USC code to obtain it. This code provides a fast response to the electromagnetic and muonic components of the shower at the ground, although no time information of the signals can be obtained (see Chapter 4).

6.2.2 Signals produced by ν-showers at the ground

The current picture of a shower induced by a neutrino interacting deep in the atmosphere close to the ground, is that of a "young" shower sharing many characteristics with vertical showers induced by hadrons. According to this image, the signals in *all* the triggered surface detectors should exhibit signatures of the presence of a significant electromagnetic component. However, our simulations have shown that this is not quite correct when the resulting shower from the neutrino interaction is an inclined purely hadronic shower or a mixed shower with a relatively large hadronic component.

In fact in inclined showers, the azimuthal asymmetries on the time structure and signal size at the ground are very important, and our simulations show that in the case of a ν inducing a deep inclined hadronic shower one should expect signals with EM characteristics only in the early part of the shower as we will show below.

Azimuthal asymmetries in deep inclined showers

In inclined showers, there is an azimuthal asymmetry in the signal due to the combination of several effects, the most important being the geometric effect, the longitudinal development effect and ground screening (for a description of these effects see Section 5.2).

The geometric effect can be quite important for inclined nucleonic showers, but for ν-showers the most relevant effects for ν identification are the longitudinal development effect, and the ground screening effect as will be discussed in the following.

In Fig. 6.5 we show a sketch of an inclined shower hitting two detectors at the same distance from the core at the ground. We also display three different planes that correspond to three different values of atmospheric depth crossed by the particles in the shower, and therefore three different stages of shower development. From this illustration it is evident that the tank in the early region is hit by a younger stage on the evolution of the shower than the tank in the late region.

To quantify the difference between the three depths defined above for a shower of zenith angle θ initiated at ΔX from the ground (in slant depth), we use a simple geometrical approach. The slant depth crossed by the shower core ΔX, and the difference with the corresponding depth for the early plane ΔX_E (late plane ΔX_L) is denoted by d_E (d_L), measured along the shower axis (see Fig. 6.5). d_E corresponds to an early tank ($\zeta = 0°$) at a distance r_E from the core and d_L corresponds to a late tank ($\zeta = 180°$) at a distance r_L from the core. They can be obtained as:

$$d_E = r_E \sin\theta$$
$$d_L = r_L \sin\theta \tag{6.18}$$

Thus, the slant depth crossed by the early plane and late planes are:

$$\Delta X_E = \Delta X - d_E$$
$$\Delta X_L = \Delta X + d_L \tag{6.19}$$

The angles subtended between the shower axis and the paths from the injection point to the early and late tanks are given by:

$$\alpha_E = \theta - \arctan\left(\tan\theta - \frac{r_E}{h(\Delta X)}\right)$$
$$\alpha_L = \arctan\left(\frac{r_L \cos\theta \cos\theta}{h(\Delta X_L)}\right) \tag{6.20}$$

where $h(\Delta X)$ and $h(\Delta X_L)$ are the vertical heights as measured in meters corresponding to ΔX and ΔX_L, respectively.

Therefore, the depth crossed by the early and late planes along the straight lines from the injection point to the tanks (not parallel to the shower axis) are:

$$\Delta X_E^* = \frac{\Delta X_E}{\cos\alpha_E}$$
$$\Delta X_L^* = \frac{\Delta X_L}{\cos\alpha_L} \tag{6.21}$$

It is important to remark that this simple geometrical model is only approximate but helps understanding the difference between the early and late regions of the shower. Their predictions work better for muons than for electrons, because e electrons do not travel in straight lines due to multiple scattering.

As a result of the effect described above, for certain ranges of r and ΔX the early region corresponds to a younger stage in the shower development with a significant electromagnetic component, so most of the particles arriving at ground are electrons, positrons and gammas from the cascading processes. However the late region has to cross a much larger atmospheric depth, being in an older stage of evolution where the electromagnetic component becomes more attenuated and only muons and the electromagnetic halo component produced by muon decay and muon interactions arrive at the ground. In Fig. 6.6, we plot the depths ΔX_E^* and ΔX_L^* crossed by the

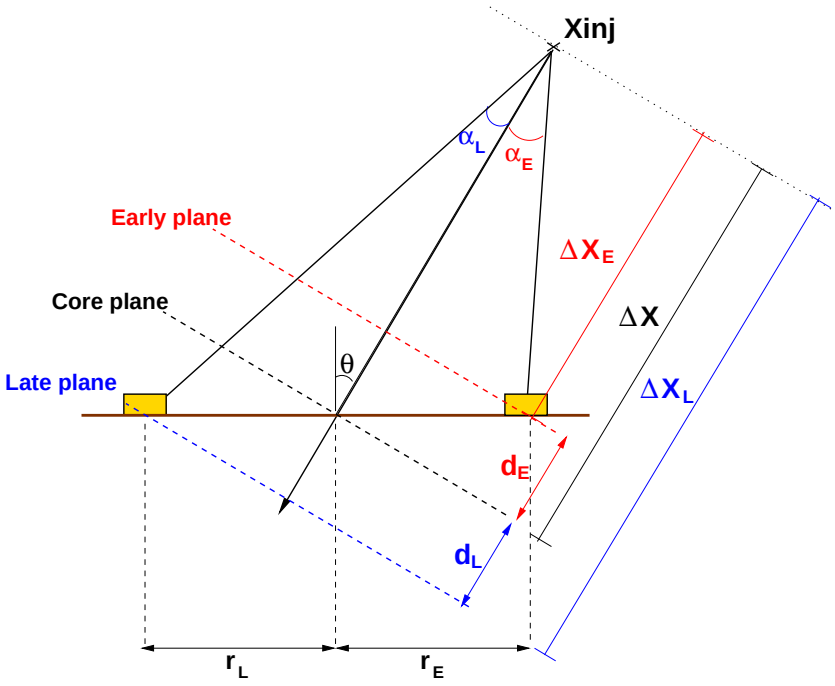

Figure 6.5: *Geometrical model of an inclined shower reaching the ground. Three planes are displayed intersecting the ground plane, each one at different depths along the shower development: early (red), late (blue) and core (black) planes. The last one is also called shower plane.*

shower particles hitting an "early" tank and a "late" tank at r =4.5 km from the core, as a function of ΔX. From this figure, we can see that for instance the particles in a $\theta = 85°$ shower initiated at $\Delta X \sim 1500$ g cm^{-2}, hit an "early" tank at a distance $r_E = 4.5$ km after crossing $\Delta X^*_E \simeq 1000$ g cm^{-2} and a "late" tank, at the same distance $r_L = 4.5$ km, after crossing $\Delta X^*_L \simeq$ 1950 g cm^{-2}. This means that for example if the shower is produced by a 10 EeV proton, we infer from Fig. 5.1 that the particles hitting the "early" tank correspond to a stage in which the electromagnetic component is at its maximum, while those hitting the "late" tank correspond to a stage in which the electromagnetic component is largely attenuated and the muonic component starts to dominate in the total signal.

The additional atmosphere crossed by the late region with respect to the early one clearly depends on the distance from the core for a given θ and ΔX as shown in Fig 6.7 where we show the difference $\Delta X^*_L - \Delta X^*_E$ as a function of the distance from the core when the shower axis travels along $\Delta X = 1500$ g cm^{-2}. In this simple geometrical model, $\Delta X^*_L - \Delta X^*_E$ increases linearly with r, for example increasing from 640 g cm^{-2} at $r = 3$ km to 960 g cm^{-2}

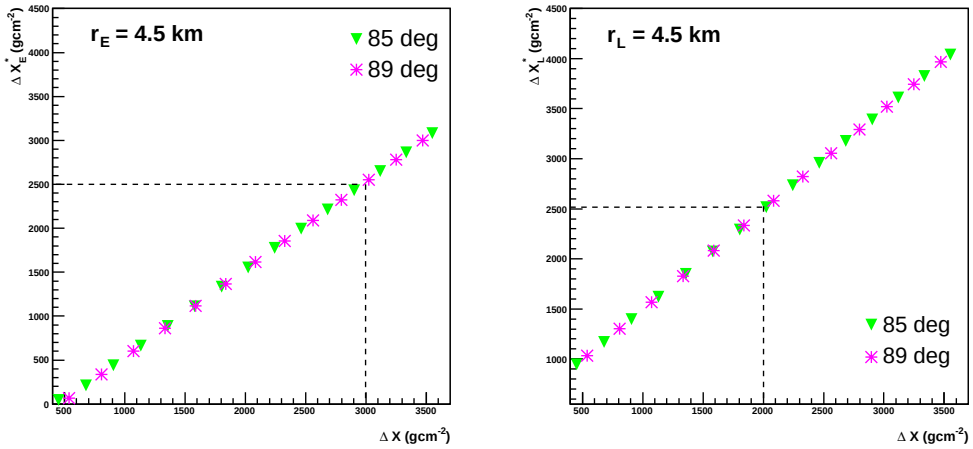

Figure 6.6: ΔX_E^* *and* ΔX_L^* *depths crossed by a plane that hits a tank at a distance of 4.5 km from the core as a function of* ΔX *for different zenith angles. Left panel: Early plane* ($\zeta = 0°$)*. Right panel: Late plane* ($\zeta = 180°$)*. The dashed lines indicate the depth* ΔX *corresponding to* $\Delta X^* = 2500$ *g cm*$^{-2}$*. From this depth, the electromagnetic component would be attenuated in 10 EeV shower in accordance with Fig. 5.1 .*

at r =4.5 km for a shower of $\theta = 85°$.

The geometric effect together with the absorption of the shower core after the impact of the shower on the ground (screening effect) also lead to the supression of the electromagnetic component in the late region (except for the electromagnetic halo). This supression is the main signature of deep inclined showers, such as those induced by neutrinos when the resulting shower is hadronic or mixed with a relatively large hadronic component. This is illustrated in Fig. 6.8 where a sketch of the development of a ν-shower is shown.

As a consequence, an asymmetry is expected on the electromagnetic content and time structure of the signal depending on the position of the the tank in the ground. In Figs. 6.9 and 6.10 we illustrate the asymmetry on the muonic or EM character of the signal, by plotting maps of the fraction of the total signal that is due to the electromagnetic and muonic component in 1 EeV proton-induced showers with $\Delta X = 1500$ g cm^{-2} for two zenith angles θ =85° and 89°. In the top panels, we show the maps of S_{EM}/S_{total}, from which it can be seen that the EM component dominates the early region and it becomes strongly supressed in the late region. In the bottom panels we show the maps of S_μ/S_{total}. It can be seen that the muonic component dominates in the late region, and it reaches considerably longer distances to the core than the early one. The difference in the length of the early and late

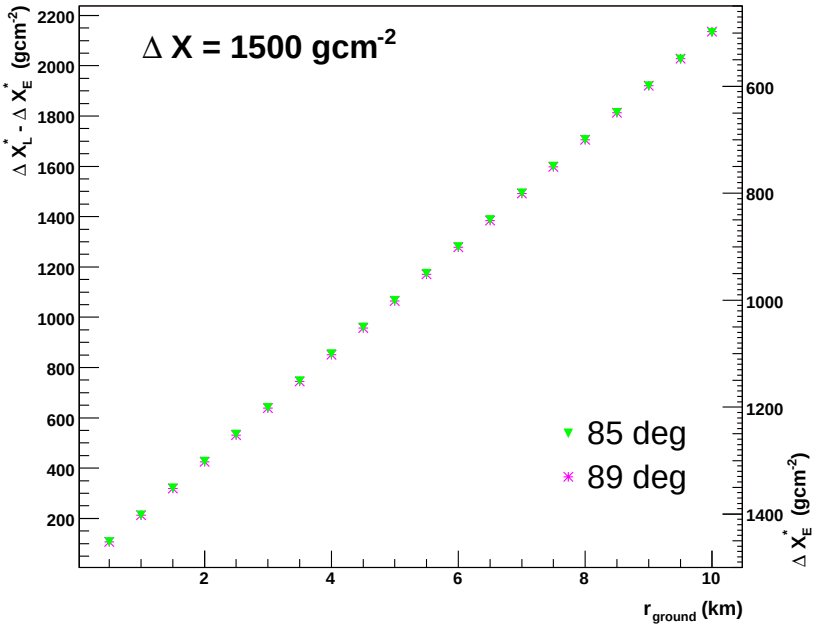

Figure 6.7: *The difference in depth crossed by the early and late planes (see Fig. 6.5) as a function of the distance from the core when the depth crossed by the shower axis is* $\Delta X \sim 1500$ *g cm*$^{-2}$*. On the right axis we show the value of the corresponding* ΔX^*_E*.*

regions along the direction of the shower axis, is mainly due to the geometric effect that increases with zenith angle.

The asymmetry is more significant around $\zeta = 0°$ and 180°. As the footprint of these events is quite elongated, we can convert the previous maps to one dimensional distributions and plot the fraction of electromagnetic and muonic signals as a function of the distance from the core to the early and late tanks. In Fig. 6.11 we show the distributions of the average ratio S_{EM}/S_{total} for both zenith angles. For showers at 85° (top graph), the ratio S_{EM}/S_{tot} decreases from $\sim 60\%$ in the earliest tanks (the tanks furthest from the core in the early region) to $\leq 20\%$ in the latest tanks. This behaviour can be easily understood knowing that the maximum of a 1 EeV shower is at a depth $\sim$700 g cm^{-2} and using the predictions of Eq. (6.21). The earliest tanks in the plot correspond to a stage of evolution of the shower around maximum. As the distance of the early tank to the shower core decreases, the shower becomes older and therefore the EM component suffers more atmospheric attenuation. After the core, the shower is in an old stage of evolution where the EM component only comes from muon processes.

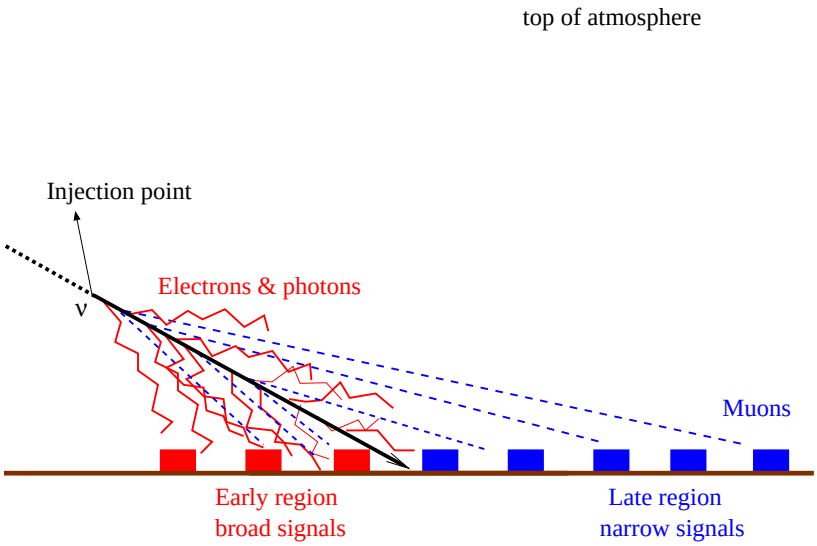

Figure 6.8: *Schematic representation of the development of a ν-shower*

In the bottom panel of Fig. 6.11 we show the same distribution for showers at 89°. In this case the earliest tanks in the shower correspond to a stage in the longitudinal evolution before shower maximum It is interesting to see that near the core in the late region ($r < 4$ km), the shower is in a stage in which there is still $\sim 30\%$ of EM component. At larger distances r the shower is again in an old stage in which the EM component is largely attenuated.

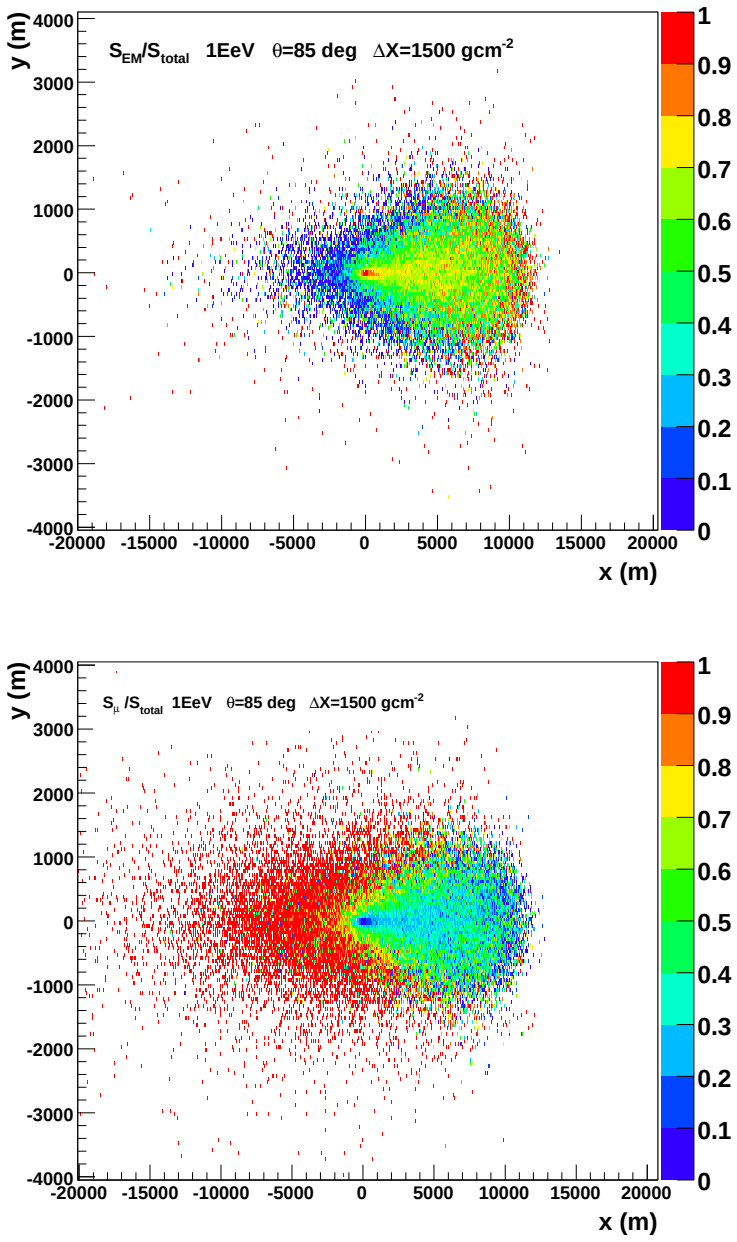

Figure 6.9: *Top panel: Map of the ratio S_{EM}/S_{total}. Bottom panel: Map of the ratio S_{μ}/S_{total}. Both correspond to the signals produced by a 1 EeV proton induced shower at 85° and ΔX = 1500 g cm^{-2}. The shower is coming from the "right" parallel to the x-axis and the shower axis impacts on the ground at (x, y)=(0,0). The response of the tank was simulated with the S1000 USC program [73]. Notice the different scale in the x and y axes.*

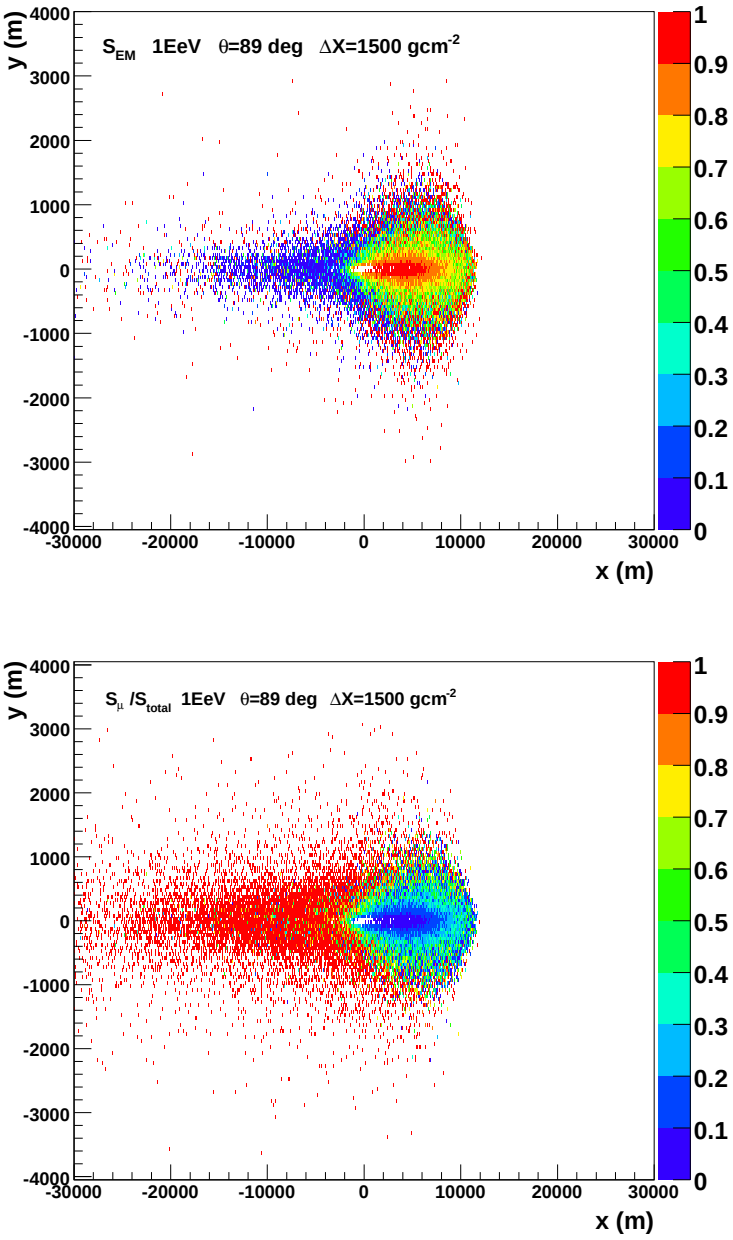

Figure 6.10: *Top panel: Map of the ratio S_{EM}/S_{total}. Bottom panel: Map of the ratio S_{μ}/S_{total}. Both correspond to the signals produced by 1 EeV proton induced shower 89° and $\Delta X = 1500$ g cm^{-2}. The mean tank response was simulated with the S1000 USC program [73] . Note the different scale in the x and y axis.*

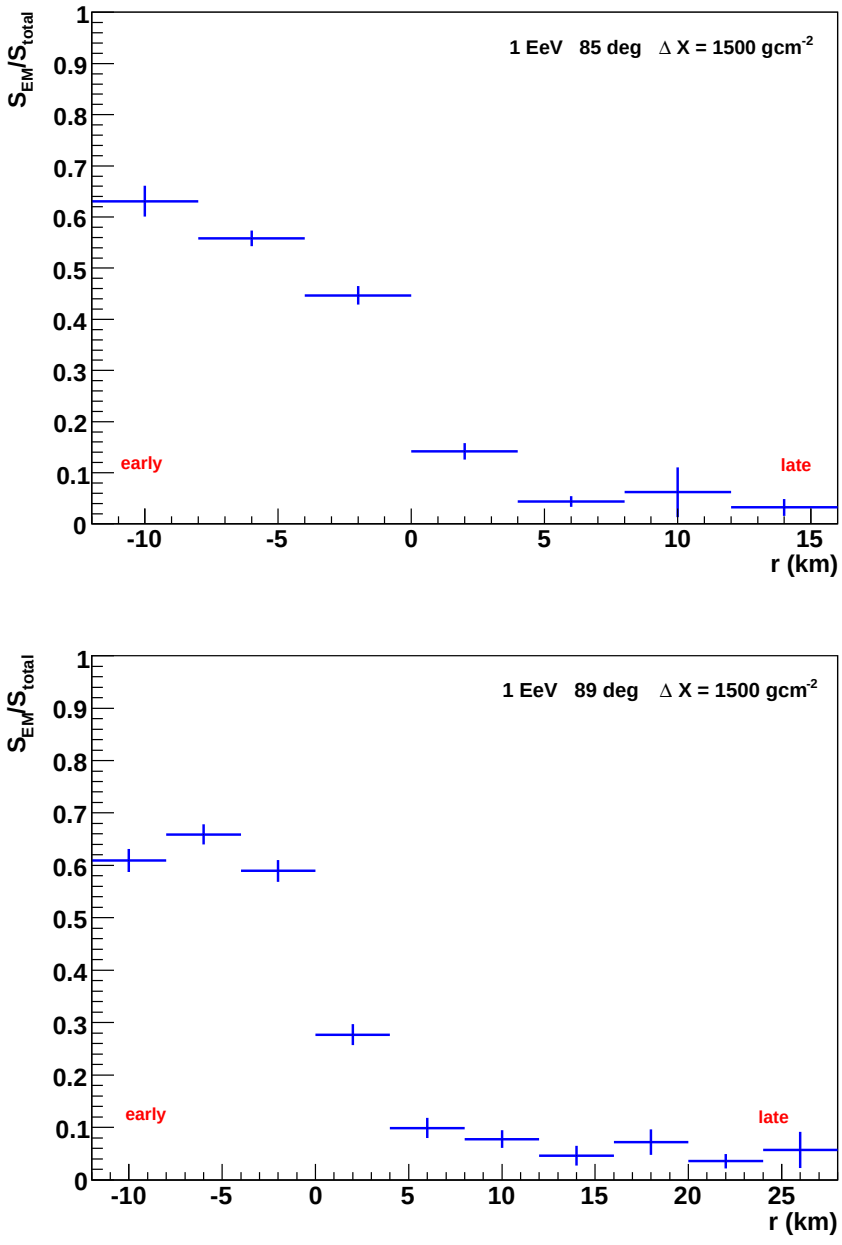

Figure 6.11: *Ratio of the electromagnetic signal to the total signal as a function of the distance from the core in the early (negative r) and late (positive r) tanks for a 1 EeV proton shower with* $\Delta X = 1500$ *g cm*$^{-2}$. *Top panel: Proton shower at 85°. Bottom panel: Proton shower at 89°. The response of the tank was simulated with the S1000 USC program.*

Both cases are examples of neutrino showers that should be easily identified, because they show a clear signature: the early region is in a young stage of development with a significant EM component, the shower front is broad and curved and therefore "slow" signals in time are expected to be recorded in the early tanks. The late region is in an older stage of evolution in which the shower front is thin and closer to a plane as in the case of ordinary inclined showers, and therefore "fast" signals in time are expected to be recorded in the tanks. This signature is the basis of the criteria of identification described in the following section.

As we predicted in the geometrical approach, the asymmetry depends on ΔX at a given distance from the core as well as on the zenith angle. When the neutrino interacts in an intermediate region of the atmosphere the slant depth crossed by the particles that hit an early tank at a given distance is large enough for the electromagnetic component to be absorbed before reaching the ground. For instance, in Fig. 6.12 we show the average ratio S_{EM}/S_{total} as a function of ΔX in early and late tanks for showers at 85° (top panel) and 89° (bottom panel). The ratio in the early tanks decreases with ΔX for both distances and zenith angles, until beyond ΔX ∼2500 g cm^{-2} the EM component is less than 20% of the total signal, a value similar to the one expected for the EM halo (see Section 5.1) and therefore, there is not a noticeable early-late asymmetry on the electromagnetic content. These numbers depend on the zenith angle. For example at 89° there is still a significant EM component near the core in the late region as shown in the bottom panel of Fig. 6.12 for $r_L = 3$ km. This component decreases with ΔX and becomes $< 20\%$ beyond ∼1500 g cm^{-2}. For $r_L > 5$ km the ratio is $< 20\%$ for all ΔX.

As mentioned at the beginning of this chapter, the current reconstruction algorithms for inclined events determine the core position under the assumption that the events are ordinary nucleonic showers. These algorithms are not suitable for neutrino-induced showers and for this reason we can not use the tank distance from the core as a variable to develop identification criteria. The solution is to study the asymmetry in the earliest tanks of the event regardless of their distance to the core. In Fig. 6.13 we show the ratio S_{EM}/S_{tot} in the earliest tank of simulated neutrino showers with 1 EeV energy as a function of ΔX. In a shower at 85° the ratio is $\leq 20\%$ beyond ΔX ∼2500 g cm^{-2}, while at 89° the EM component dominates up to ΔX ∼3500 g cm^{-2}. The reason for this is purely geometrical. The more inclined the shower, the closer to the ground the shower axis is, and the further away from the ground can the neutrino interact and still induce a shower with a significant EM component. This is illustrated in the sketch of Fig. 6.34.

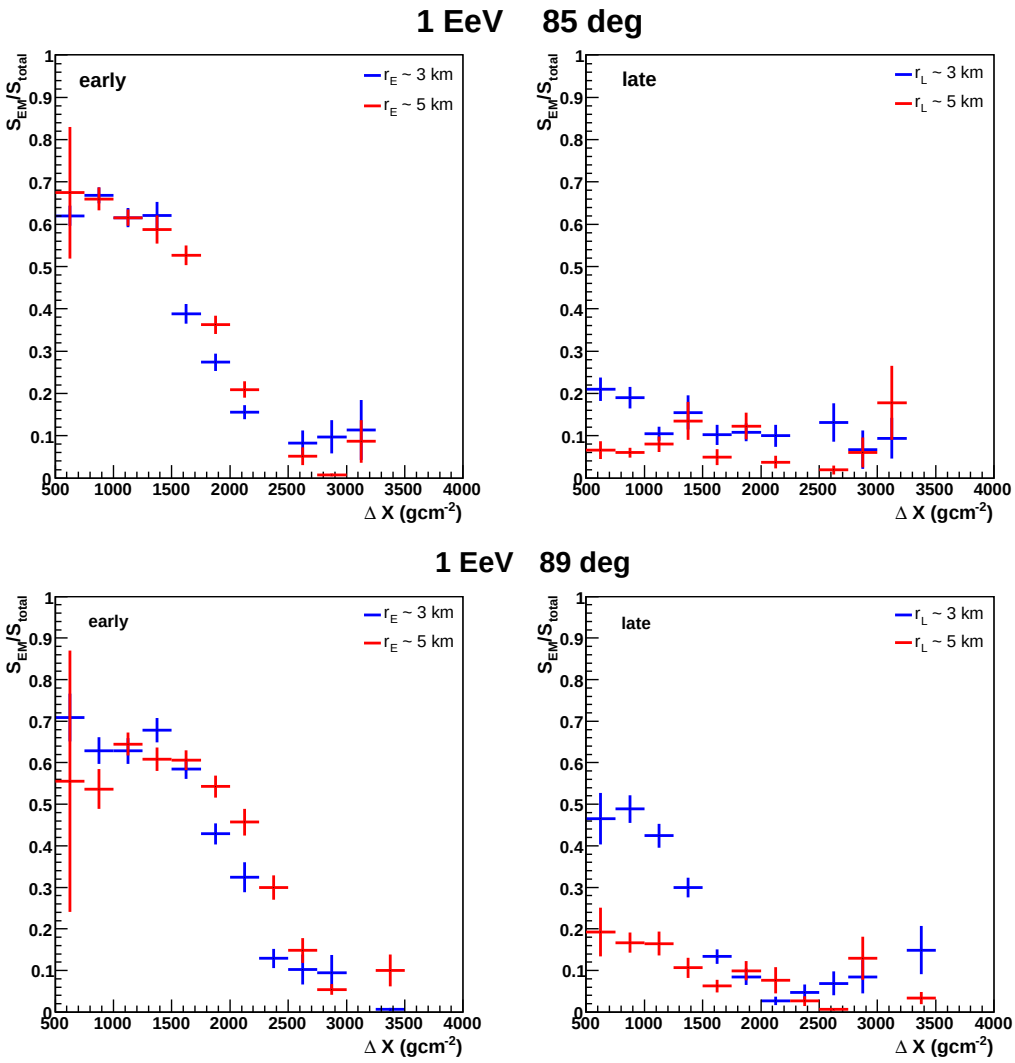

Figure 6.12: *Ratio of the electromagnetic signal to the total signal as a function of* ΔX *in tanks located at two distances from the core: r =3 km and 5 km. Top panels: Distributions corresponding to the early (left) and late (right) regions for a proton shower of 1 EeV and 85°. Bottom panels: Distributions corresponding to the early (left) and late (right) regions for a shower at 1 EeV and 89°.*

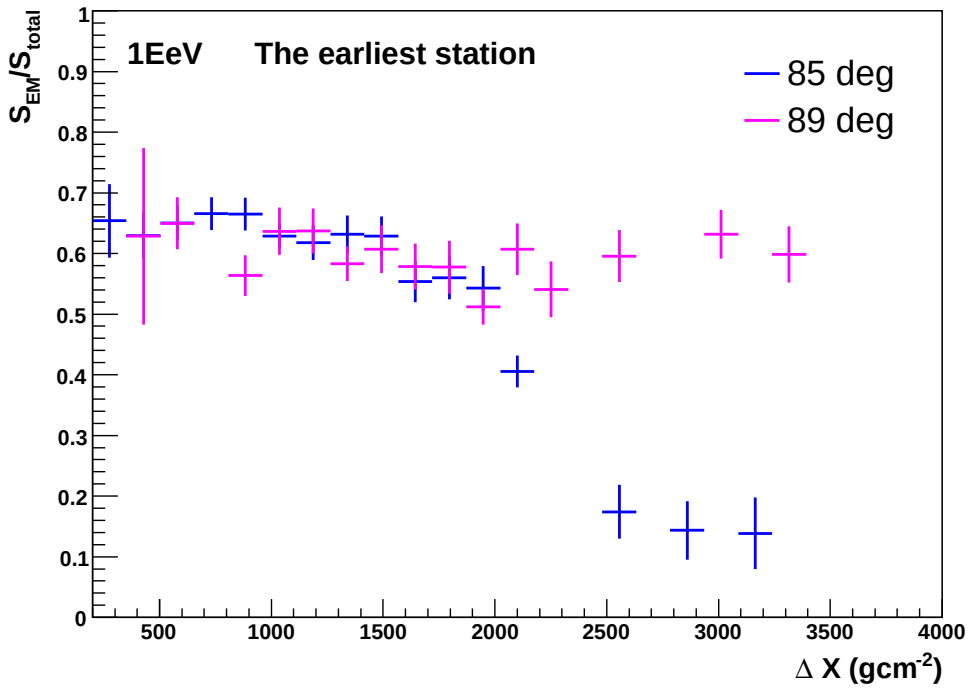

Figure 6.13: *Ratio of the electromagnetic signal to the total signal as a function of* ΔX *for the earliest tank in 1 EeV proton induced showers at* $\theta = 85°$ *and* $89°$.

When the resulting shower induced by a ν is a "mixed" shower, we expect a significant EM signal in the early region and little signal or even no signal at all in the late region depending on the relative contribution of the EM and hadronic showers to the mixed shower. Moreover, if ΔX is very large and the EM character of the shower is very significant, the events will typically not trigger the SD array.

For neutrinos interacting far from the ground, there is not a noticeable asymmetry in the relative contribution of the EM to the total signal, but the asymmetry in the shower front curvature between the early and late regions is still present [34], and in fact it might serve as an identification criterium for not so deep showers with a largely attenuated EM component. This is out of the scope of this thesis.

6.3 Selection Criterion

The selection criteria for identifying neutrino candidates in the inclined data set are based on the physical characteristics of deep $\nu-$like showers obtained from simulations. The key is in the time structure of the signals recorded in the FADC traces, that contains information about shower development, and reflects the significant electromagnetic component at the ground in the early region, and the dominance of the muonic component in the late region expected in deep inclined showers induced by neutrinos.

The digitization of the signals collected in the Surface Detector through the FADC traces allows to obtain some physical and measurable parameters that are indicators of the time structure which at the same time will allow us to discriminate between "old" showers and "young" ones. Signal observables as the risetime and falltime represent very promising quantities to establish a ν selection criterion.

6.3.1 Early-late asymmetry on the time structure of the signals in deep inclined showers.

The risetime of the signal (RT) is defined as the time interval in which between 10% and 50% of the total integrated signal is recorded. The falltime of the signal (FT) is correspondingly defined as the time interval in which the tank records between the 50% and 90% of its total integrated signal. The values of RT and FT depend on the "thickness" of the shower front and reflect the time delay between the different particles arriving at the detector.

Muons in a shower accumulate time delays with respect to a particle traveling at the speed of light along the shower axis due to their subluminal velocities, to their geometrical paths (deviations from shower axis) and to deviations produced by the geomagnetic field. For muons the effect of multiple Coulomb scattering is expected to be very small. However, electrons have larger cross sections than muons to multiple scattering and bremstrahlung. As a result, muons are the particles arriving earliest at the tank, and they arrive in a short period of time depending mainly on the distance to the shower core. Small values of risetime ($\sim$ 40 ns) are indicators of a thin shower front, a signature of "old" showers in which the signals are due to muons produced very far away from ground, and therefore have little time delays with respect to a shower front travelling at the speed of light. On the other hand, large values of risetime are indicators of a broad shower front, a signature of "young" showers constituted mainly by electrons.

Similarly, small values of falltime ($\sim$ 100 ns) indicate the presence of "old" showers in which the muonic component dominates and the muons

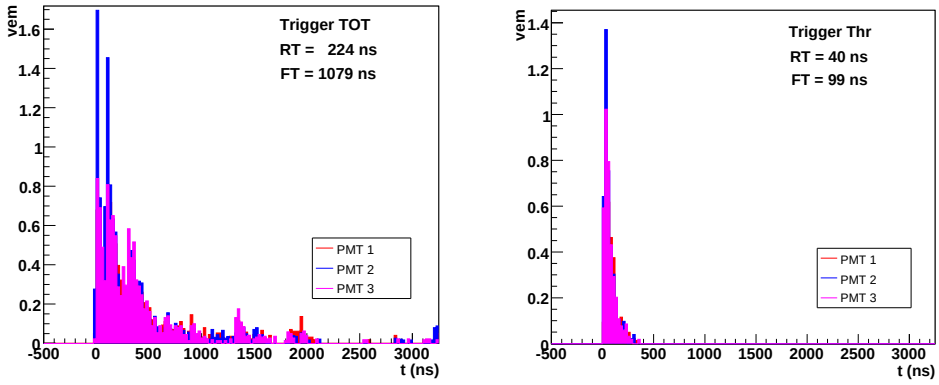

Figure 6.14: *Simulated FADC traces of an electromagnetic (left) and muonic (right) shower front. FADC traces with a significant EM component are slow on time, and usually fulfil the trigger condition called "Time Over Threshold" (TOT). FADC traces dominated by the muonic component are fast on time and usually fulfill the trigger condition called "Threshold" (Thr).*

arrive in a short period of time and large values of falltime are indicators of a broad shower front.

In Fig. 6.14 we show two examples of Offline simulated FADC traces having a significant electromagnetic (left panel) and muonic (right panel) components. In the left panel, the trace is "slow" because $\sim$ 50% of the signal is due to electromagnetic particles, and in consequence the RT and the FT have large values. In the rigth panel, there are only muons so the FADC trace is "fast" and has $RT = 40$ ns and $FT = 99$ ns.

In summary, a muonic shower front produces fast signals because the muons suffer few interactions and not much multiple scattering, characterised by small values of the risetime and falltime. An electromagnetic shower front produces slow signals due to the significant multiple scattering suffered by $e^{\pm}$ characterised by large values of the risetime and falltime. Therefore, the observables risetime and falltime supply information of the content of muonic and EM components in the shower front.

To prove the ability of the RT and FT to discriminate deep inclined showers from conventional nucleonic inclined showers we plot in figure 6.15 the average bulk-time ($RT + FT$) as a function of the signal start-time in simulated deep proton showers (top panel) and real inclined events (bottom panel). The start-time t_i is normalized as $(t_i - t_{earliest})/(t_{latest} - t_{earliest})$ in order to compare events with different interval of time between the earliest

and latest stations. For real data, we averaged ($RT+FT$) over inclined events with $\theta \geq 75^\circ$ and multiplicity ≥ 5 in the period from January 1st 2004 to December 31st 2006. For the simulated events, we averaged over showers induced by 1 EeV protons at 85° and two slant depths measured from the injection point to the ground: ΔX =1500 and 2900 g cm^{-2}.

At $\theta \geq 75^\circ$, ordinary inclined showers arrive at the ground as a muonic shower front accompanied by an electromagnetic halo (S_{EM}/S_{total} less than 15% as demonstrated in Chapter 5), so the signals recorded in the tanks are fast traces that have small values of RT and FT regardless of the start-time of the station (i.e. regardless of whether the station belongs to the early or the late region of the shower). However, for deep showers such as the simulated events with $\Delta X = 1500$ g cm^{-2} of Fig. 6.15, the asymmetry in the amount of electromagnetic component between the early and the late regions of the shower reflects itself in an asymmetry of the bulk-time. The $RT + FT$ decreases with the start-time illustrating the attenuation of the electromagnetic component of the shower front from the earliest to the latest station in the event, producing broader (narrower) signals in the early (late) part of the shower. As a consequence, the earliest stations have large values of both risetime and falltime and the latest stations have small values similar to those seen in ordinary nucleonic events. When the showers are generated far from the ground ($\Delta X = 2900$ g cm^{-2} in Fig. 6.15), the asymmetry in the time structure is negligible and the behaviour of the bulk-time is essentially the same as in ordinary inclined showers. These showers are not distinguishable from ordinary nucleonic showers using the information provided by the risetime and falltime.

Examples of individual simulated deep proton events are shown in Fig. 6.16. In the left panels, we show two events in the array produced by 1 EeV deep proton showers at 85° at different injection points. In the right panels, we plot the time structure of their signals (RT, FT, $RT+FT$) as a function of the tank start-time, referred to the time of the earliest station in the event. The event in the top panels corresponds to a shower induced deep in the atmosphere ($\Delta X \sim 1500$ g cm^{-2}), and as we discussed above, the earliest tanks have high values of the RT and FT and local "TOT" triggers, which is signature of a significant EM component. The event shown in the bottom panels of Fig. 6.16 was induced not so deep in the atmosphere ($\Delta X \simeq 2900$ g cm^{-2}) and the electromagnetic component is completely attenuated along all the event in the ground. This dominance of the muonic component is reflected on the low values of RT and FT and on the local "Threshold" triggers in all the stations. The time structure of this event is not distinguishable from an ordinary inclined nucleonic shower like the one shown in Fig. 6.17.

From the observed asymmetry, in principle one needs to rely on the time

information of the earliest tanks in the event for neutrino identification. We have obtained from the simulations that using the two earliest tanks is enough for this purpose. If we only use one tank we could missidentify an ordinary nucleonic shower as being produced by a deeply penetrating particle, because in a real event any tank may be triggered by an accidental muon with a probability $P_{1\mu}$ of $\sim 1.8\%$ [4] that artificially increases the RT or/and the FT. However, if we use the time structure of the two earliest tanks for ν identification the probability that there is an accidental muon in both tanks at the same time is expected to be $P_{2\mu} < 0.03\%$. An example of an ordinary inclined event in which the earliest tank has a double peak in the FADC trace due to an accidental muon, is shown in Fig. 6.18. In the right panel we show the FACD trace with the double peak. In the left panel we show the time structure of the signals as a function of the tank start-time. Except for the earliest tank, the remaining tanks have small values characteristic of inclined nucleonic events, namely, $RT \sim 40$ ns and $FT \sim 100$ ns.

Another indication that one of the peaks in a station exhibiting a double-peaked FADC is due to an accidental muon is the following. If the double peak in a FACD trace is due to two (inclined) single muons that belong to the same shower, both peaks should exhibit the same behaviour with respect to the direct light (DL) in each PMT. This is due to the direct light increasing the signal in the first bins of both peaks by roughly the same factor [86]. As a consequence, the values of RT and FT should be similar in the three PMTs. On the contrary, if one of the peaks is due to an accidental muon which, most likely, will be a vertical muon and no direct light is expected in that peak, and therefore a large asymmetry in the RT and FT between the three PMTs of the station should appear. For instance, in the case shown in Fig. 6.18 there is indeed a large asymmetry between the RT and FT of the 3 PMTs, $(RT_{max} - RT_{min})/(RT_{max} + RT_{min}) \sim 85\%$ and $(FT_{max} - FT_{min})/(FT_{max} + FT_{min}) \sim 77\%$.

[4] $P_{1\mu} = R_{single\ \mu} * t_{window} = 3\text{kHz} \times 6\mu\text{s}$ [107], where $R_{single\ \mu}$ is the rate of single muons and t_{window} is the integration time of the signal in a tank.

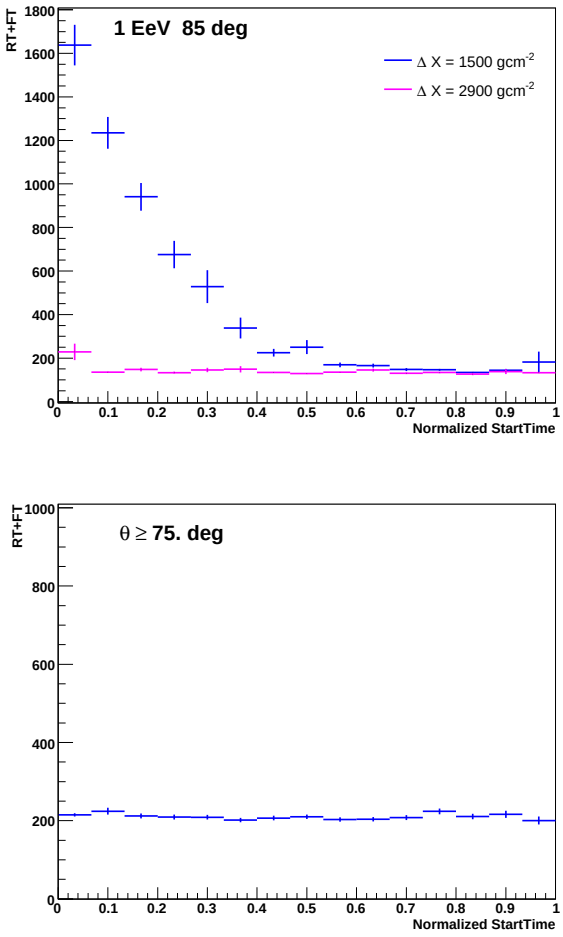

Figure 6.15: *Average $RT + FT$ as a function of the normalized start-time (see text). Top panel: Average over simulated 1 EeV proton induced showers at 85° and two different ΔX. Bottom panel: Average over inclined events corresponding to three years of SD data.*

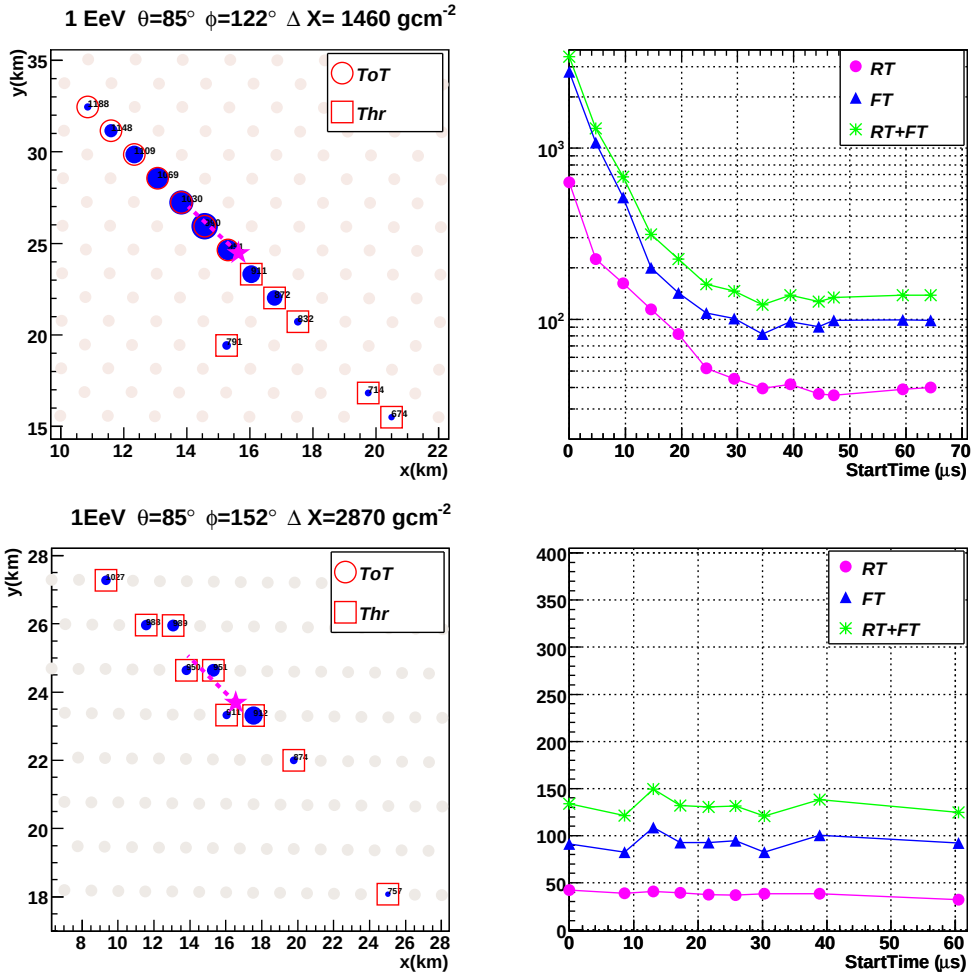

Figure 6.16: *Top: Simulated event produced by a deep shower induced at* $\Delta X \sim 1500$ *g cm*$^{-2}$ *from the ground (left) and the time structure of their signals as a function of the tank start-time (right). Bottom: Event produced by a deep shower induced at* $\Delta X \sim 2900$ *g cm*$^{-2}$ *from the ground (left) and the time structure of their signals as a function of the tank start-time (right). The triggered stations are in blue with the type of trigger indicated. The arrow shows the shower direction and the star shows the core position.*

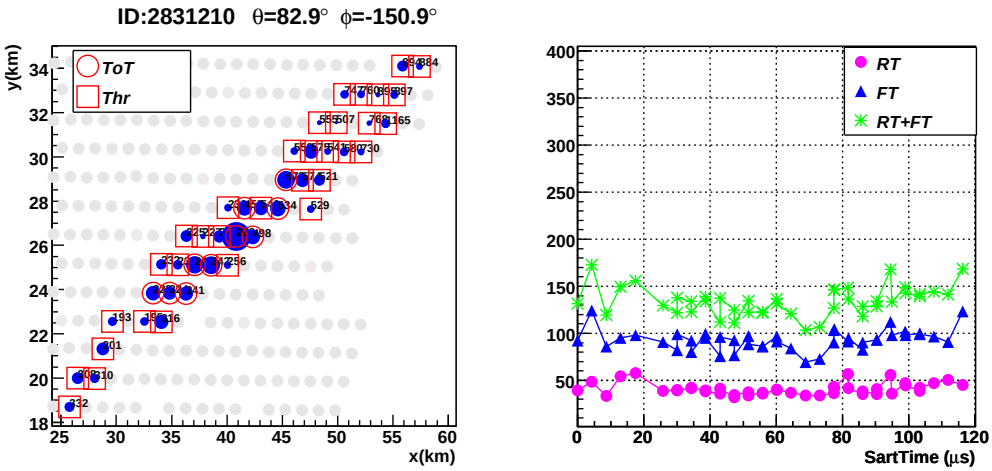

Figure 6.17: *Left panel: Ordinary inclined event (real data). Right panel: The time structure of its signals as a function of the tank start-time. The triggered stations are in blue with the type of trigger indicated.*

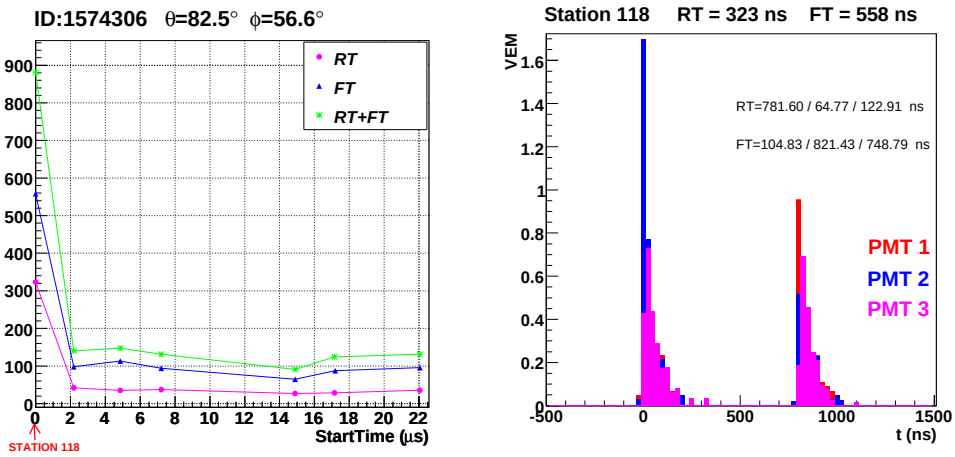

Figure 6.18: *Example of an ordinary inclined event whose earliest station has a FADC trace with a double peak due to an accidental muon entering the tank in coincidence with a muon from the shower. Left panel: The time structure of the signals of the event as a function of the tank start-time. Right panel: FADC trace of the earliest station. Also indicated is the risetime and the falltime of PMT1, PMT2 and PMT3.*

6.3.2 Choosing the cuts for neutrino identification

The first step in the search for neutrinos in the data is to apply a set of cuts on the zenith angle and multiplicity of the tanks in the events. We select events with a reconstructed zenith angle greater than 75° in the period from January 1st 2004 to December 31st 2006. For angles above 75°, if an event is due to an ordinary nucleonic shower, its electromagnetic component is expected to be sufficiently attenuated in the ground and in principle it should be easy to reject it as a neutrino candidate. In the nucleonic-initiated events the triggered tanks should all have muonic signals. We also require that the event is 5-fold or larger. The motivation for this cut is that in events with a smaller number of tanks, if either one of them is an accidental trigger (that was not rejected during the selection) or is hit by an accidental muon arriving earlier than the actual particles of the shower, the angle might be misreconstructed. In fact, we have found several 4-fold vertical events in which the zenith angle is misreconstructed as being larger than 75°, and the event was missclassified as a neutrino candidate.

In the following we estimate the best values of the RT and FT that allow the separation between neutrino induced showers and hadron induced showers. For that purpose, we have studied the distributions of the RT and FT parameters in ν-simulated events and real events.

Firstly, we show the distributions of the risetime and falltime in the simulated events before passing them through the same algorithms of tank selection and angular reconstruction that are applied to the real data. We do this to study the discrimination power of the RT and FT as a function of zenith angle, energy and injection point of the primary proton.

In Fig. 6.19, we show the distributions of the risetime of the earliest tank in simulated events of 10 EeV, 80° and multiplicity ≥ 5. In each panel, we plot the $\log_{10}RT$ distributions in different ΔX intervals, along with the distribution of the corresponding risetime of the earliest tank in the real inclined events. The distributions of real and simulated events are well separated below $\Delta X = 2000$ g cm^{-2}, while beyond this value there is a significant overlap between both distributions. The same behaviour occurs in the case of the falltime distribution, as can be seen in Fig. 6.20. The degree of overlap (i.e. the discrimination power of the RT and FT observables) depends on zenith angle and energy. For instance, in Fig. 6.21 we show that the larger the zenith angle, the less overlap between the RT distributions of data and simulations occurs. Also for a fixed zenith angle, the smaller the energy, the distributions have their maxima closer to the maximum in the data distribution and the degree of overlap is larger as shown in Fig. 6.22.

From all the previous figures, it can be deduced that the larger the energy

and the zenith angle, the larger the ΔX injection range in which the discrimination between neutrino showers and nucleonic showers will be possible. The increase with angle is due to a a purely geometrical effect explained before and easy to understand with the aid of Fig. 6.34

The goal now is to choose the cuts in RT and FT that maximize the neutrino identification efficiency in the largest possible range of energy, zenith angle and injection depths. The previous plots show that optimising the cuts is a very complex task given the dependence of RT and FT on E, θ and ΔX. For this reason we have chosen to select cuts that give a large identification efficiency at low energy $E \leq 1$ EeV for all primary zenith angles and injection points. The assumption here is that if these cuts give a good ν identification efficiency at low energy, they will also produce a good discrimination at high energy where the distributions of RT and FT in simulations and data tend to be better separated (see Fig. 6.22). Besides it is important to have a good ν identification efficiency at lower energies where the neutrino flux is expected to be highest according to current models of neutrino production. For that purpose we compare in Fig. 6.23 the distributions of the risetime and falltime of the two earliest tanks in simulated deep events with $E \in [0.1,1.]$ EeV, $\theta \in [75°,89°]$ and $\Delta X \in (0, 2500)$ g cm^{-2}, and real events after applying the tank selection and angular reconstruction algorithms as well as the cuts $\theta_{rec} \geq 75°$ and ≥ 5 selected tanks to both the data and the simulations. The chosen values for the cuts in RT and FT are those where the distribution of simulated deep events cuts the one of real events.

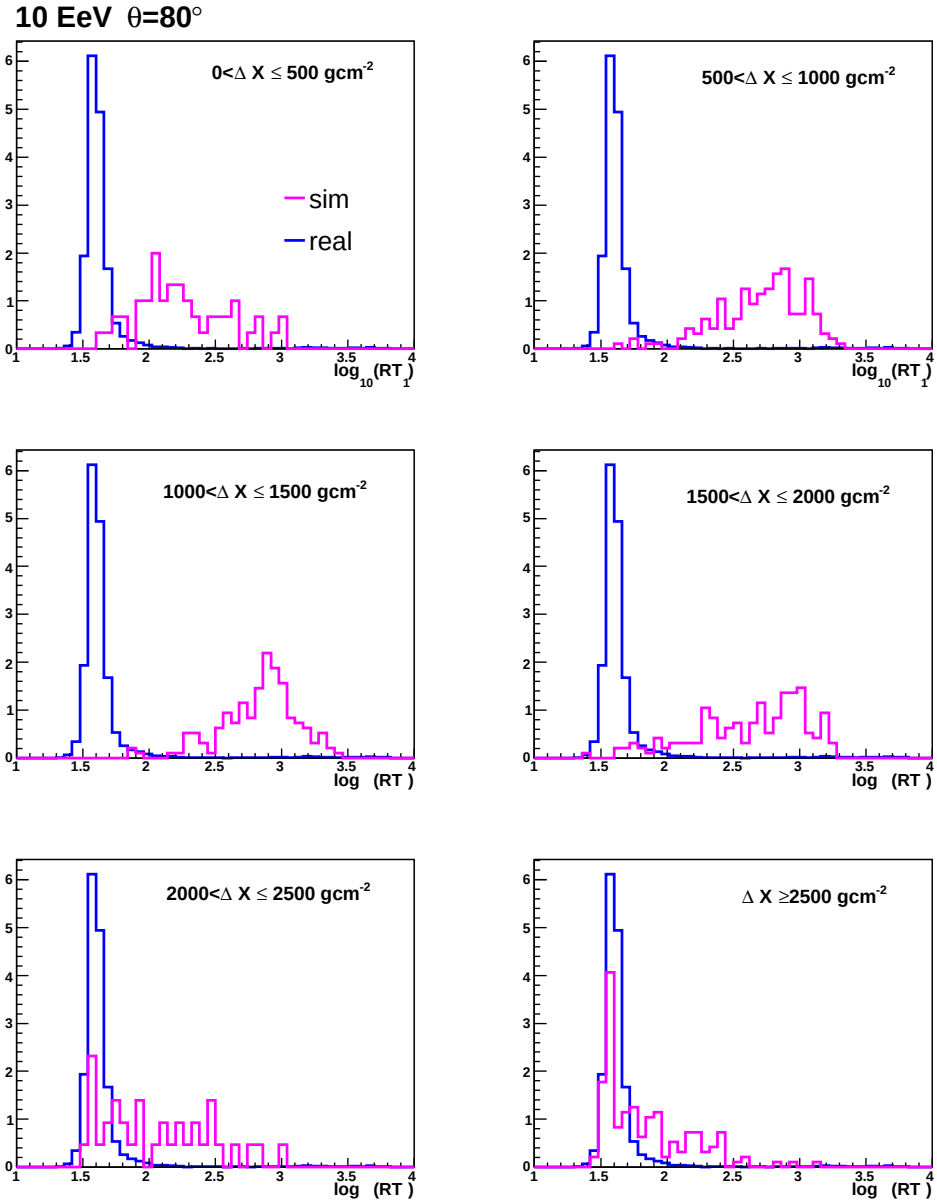

Figure 6.19: *Distributions of risetime in the earliest tank in real inclined events ($\theta \geq 75°$, 5-fold or larger) and in simulated events at 10 EeV, 80° and different ΔX intervals. The distributions are normalized to the total number of events.*

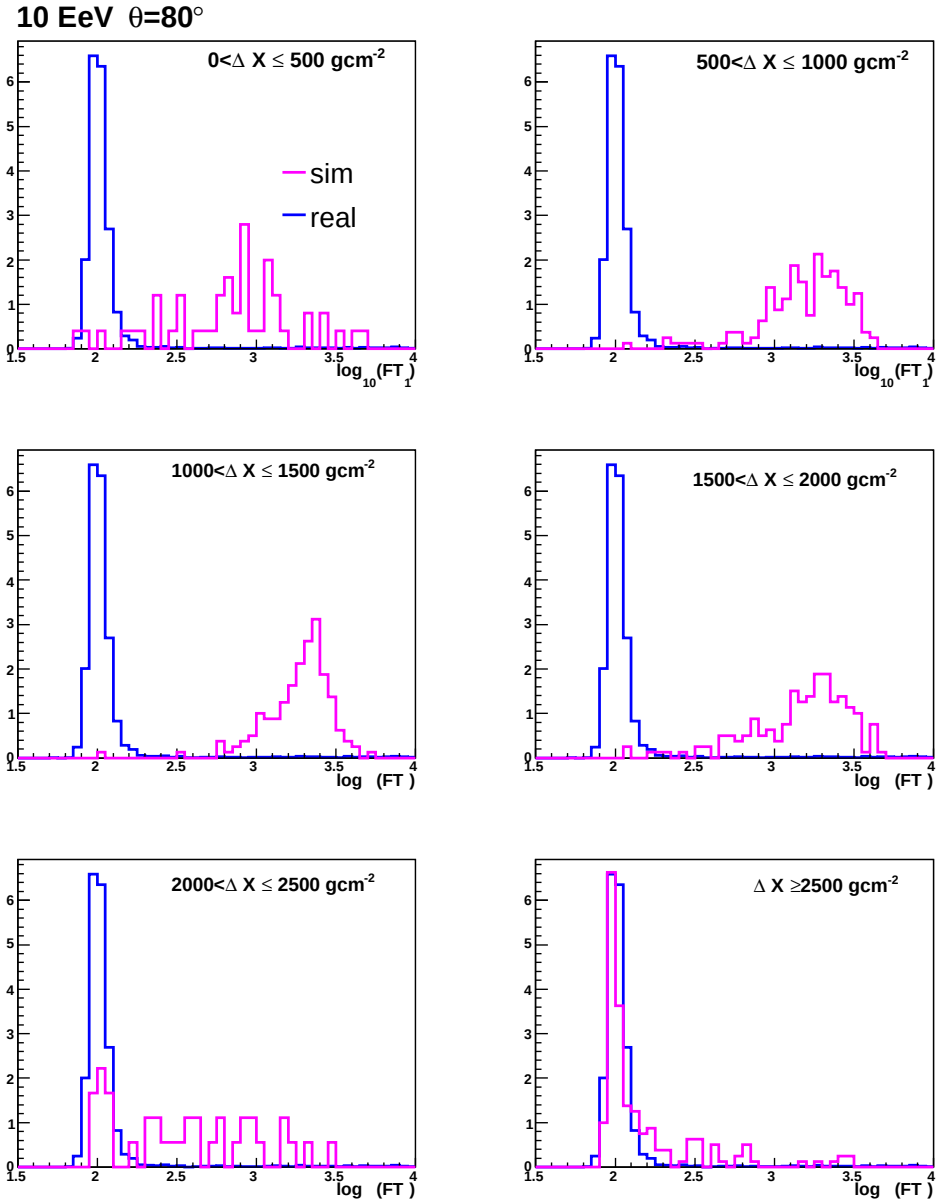

Figure 6.20: *Distributions of falltime in the earliest tank of real inclined events ($\theta \geq 75°$, 5-fold or larger) and simulated events at 10 EeV, 80° and different ΔX intervals. The distributions are normalized to the total number of events.*

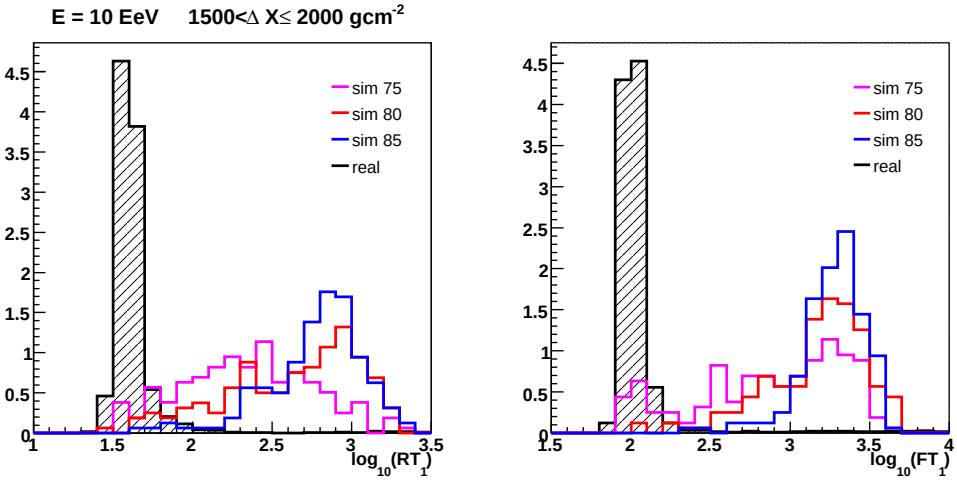

Figure 6.21: *Distributions of risetime (left) and falltime (right) distributions in the earliest tank in simulated events at 10 EeV,* $\Delta X \in (1500, 2000)\ gcm^{-2}$ *and different zenith angles, compared to the distribution for real inclined events (shaded histograms).The distributions are normalized to the total number of events.*

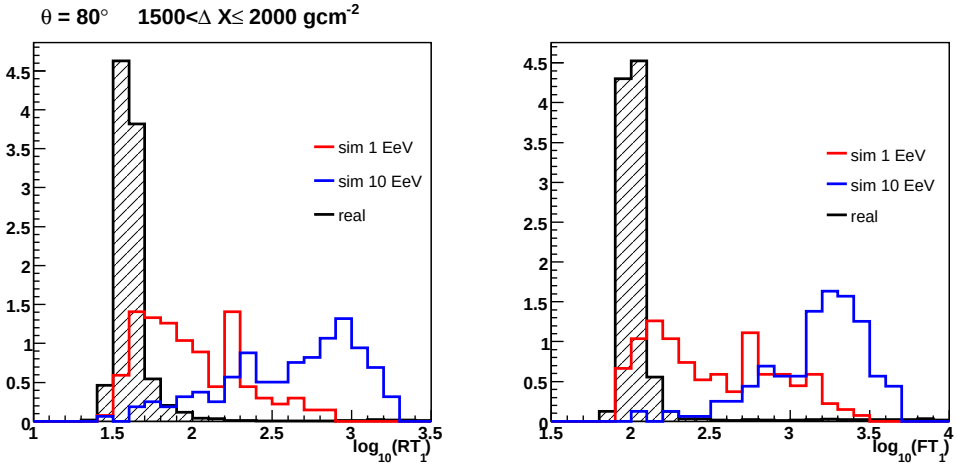

Figure 6.22: *Distributions of risetime (left) and falltime (right) distributions in the earliest tank in simulated events at 80°,* $\Delta X \in (1500, 2000)\ gcm^{-2}$ *and different shower energies, compared to the distribution for real inclined events (shaded histograms). The distributions are normalized to the total number of events.*

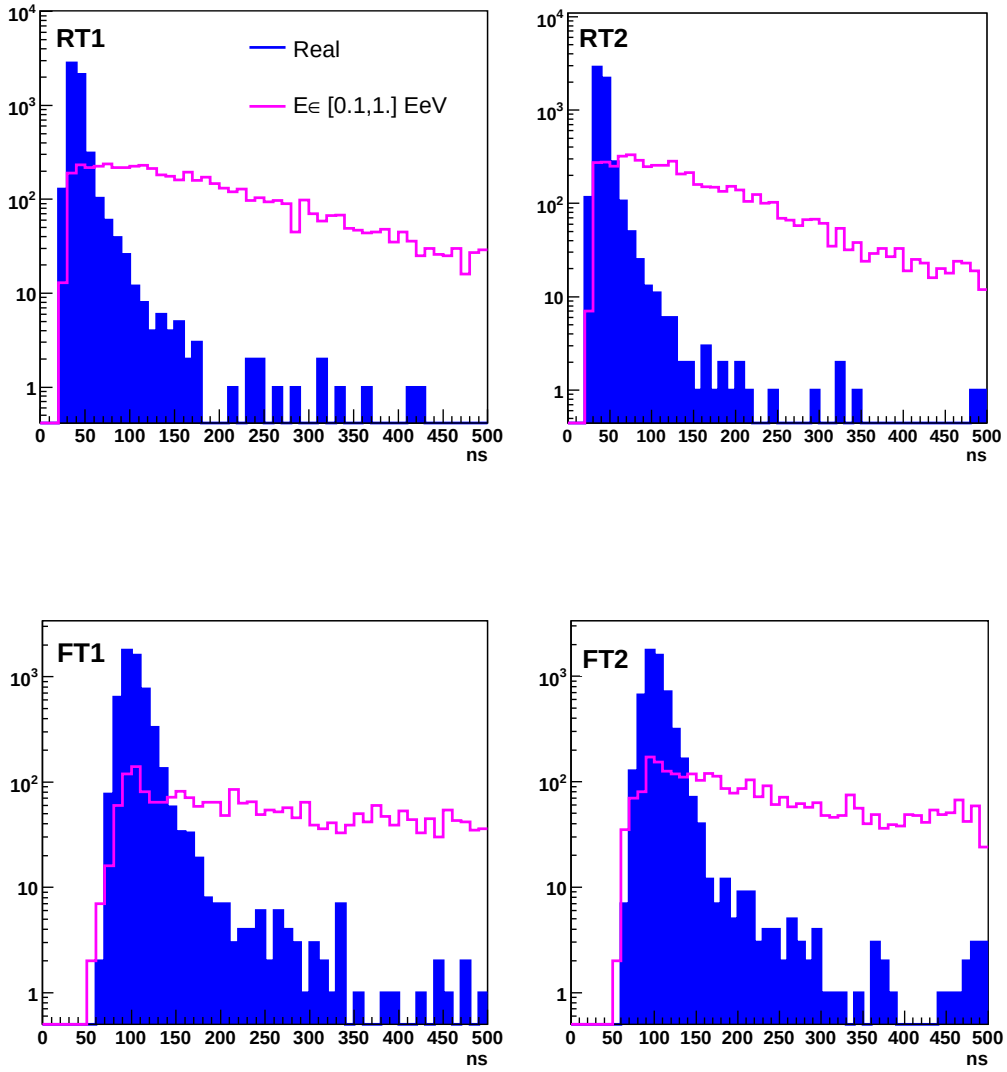

Figure 6.23: *Distributions of risetime (top) and falltime (panel) for simulated neutrino showers with* $E \in [0.1, 1.]$ *EeV,* $\theta \in [75°, 89°]$ *and* $\Delta X \in (0, 2500)$ *g cm*$^{-2}$ *and real events after the station selection and after applying the cuts on the reconstructed zenith angle* ($\theta_{rec} \geq 75°$) *and multiplicity* (≥ 5 *tanks). The labels 1 and 2 correspond to the first and second tanks in time in the event, respectively.*

Finally, we will identify as deeply penetrating inclined showers those T3 events passing the following cuts:

- 5 or more tanks after the selection described in Section 6.1.1.
- Reconstructed zenith angle $\theta_{rec} \geq 75^{\circ}$ after applying the reconstruction algorithm in Section 6.1.2.
- $\mathrm{RT}_1 > 60$ ns and $\mathrm{FT}_1 > 150$ ns
- $\mathrm{RT}_2 > 60$ ns and $\mathrm{FT}_2 > 150$ ns

with the earliest tank in the event labeled as 1 and the second tank in time labeled as 2.

Once the optimal values of the cuts have been estimated, the next step is to compute the efficiency of neutrino identification when the cuts are applied to the simulated events.

6.4 Trigger and Selection Efficiencies for Neutrino Showers

The calculation of the acceptance of the Pierre Auger Surface Detector to neutrino induced showers, requires knowing the efficiency of the array to trigger, reconstruct and identify neutrino induced showers as a function of E, θ and interaction depth of the neutrino.

The data recording in the surface detector started nearly four years ago while the observatory was being constructed. This means that the configuration of the working tanks has been changing continuously and therefore, this should be taken into account for a detailed calculation of the efficiencies. In this thesis, we have calculated the trigger, selection and neutrino identification efficiencies under the approximation of considering an ideal and infinite SD array (the showers are always fully cointained inside the array) without "holes" and without non-working stations.

6.4.1 Trigger efficiency for Neutrino Showers

The first step is calculating the efficiency of neutrino induced showers of passing any of the two T3 trigger conditions currently in use in the surface detector of the Pierre Auger Observatory, which are based on the $TOT - 2C1\&3C2$ and $2C1\&3C2\&4C4$ crown conditions (see Section 3.2.2).

The procedure to calculate the trigger efficiencies is as follows. We throw the simulated neutrino induced showers (see Section 6.2.1.) on the ideal, infinite array with a random core position and azimuthal angle. The detector response to these showers is performed using the SD simulation modules of the Auger Offline Framework (DrEvil 2.0) [95, 94]. The current CDAS Central Trigger algorithm [98] is evaluated using the Central Trigger Simulator module. This algorithm searches for events fulfilling the T3 trigger level and writes the proper flags of the stations to specify if the stations belong to the trigger.

In Fig. 6.24, we show the fraction of deeply initiated proton showers triggering the array (Trigger efficiency) as a function of the slant injection depth measured from the ground (ΔX) for different zenith angles and shower energies when the number of triggered tanks is 3 or more. Note that the energy corresponds to shower energy, not neutrino energy. The efficiencies typically grow with energy and zenith angle. For showers produced very close to the array (ΔX small), the efficiency drops dramatically since the showers do not cross enough grammage to spread out laterally and do not trigger the minimum number of tanks (3 or 4) required by the two T3 trigger conditions.

One can see that the more energetic the shower, the higher the efficiency and also the wider the range of slant injection depths where the showers can trigger the array. Therefore, above about $3{\times}10^{18}$ eV the efficiency is practically 100% for all the zenith angles above 75°, and at all the injection points from $\Delta X \sim 300 - 400$ g cm^{-2} up to the top of the atmosphere. Regarding the behaviour of the trigger efficiencies with zenith angle, firstly, as the zenith angle increases the trigger efficiency saturates at lower energy. Also for a fixed shower energy, the injection range where the trigger efficiency is 100% increases as θ increases. Both behaviours are essentially due to a combination of two geometrical effects. One is associated to the projection of the array on the shower plane that makes the tanks look closer to each other from the point of view of the incoming shower as $sec\theta$ increases, increasing the trigger probability. The other one is due to the fact that as θ increases the shower develops closer to the ground and it is easier to trigger the array (see Fig. 6.34). For instance, while the trigger efficiency is very small at 10^{17} eV for $\theta = 75°$ and has non-zero values in a ΔX range $\sim$ 500 g cm^{-2}, this efficiency increases remarkably when $\theta = 89°$ and is different from zero in a wider range of ΔX of the order of 3000 g cm^{-2} .

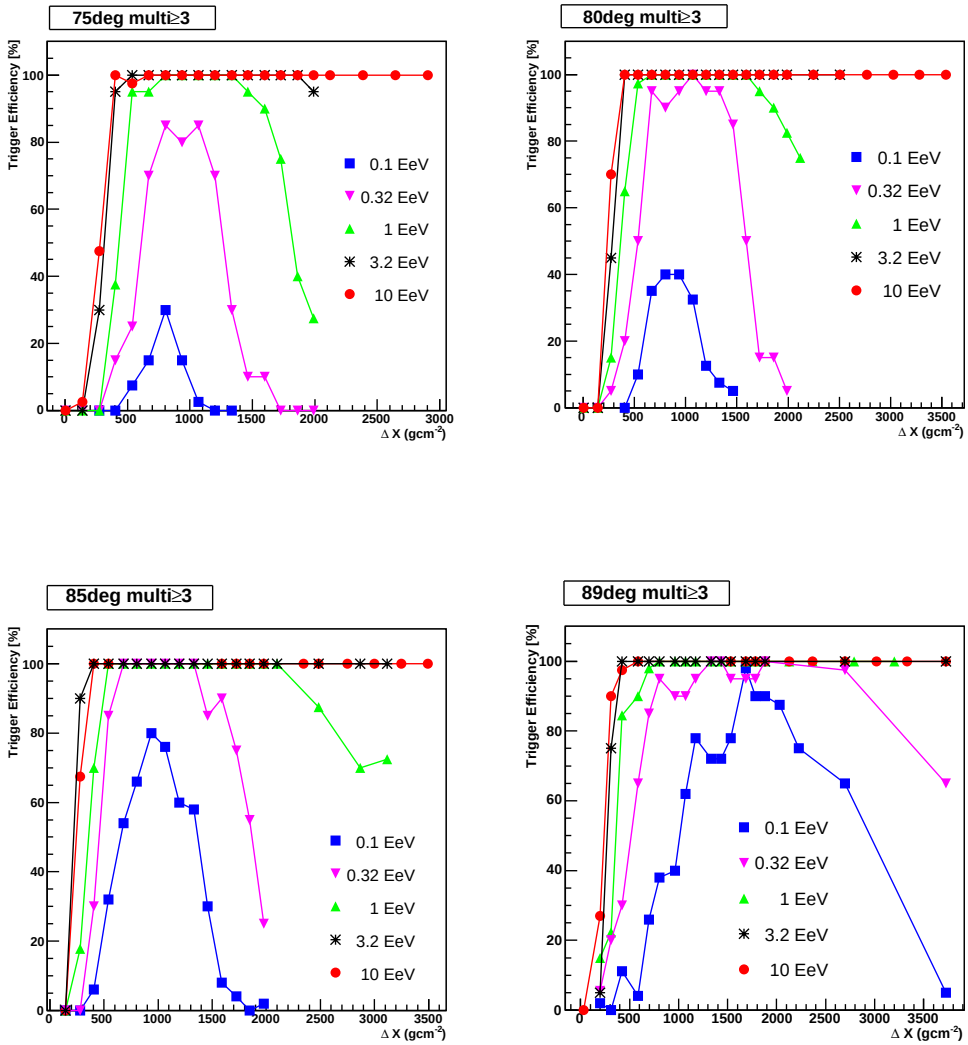

Figure 6.24: *Trigger efficiencies of 3-fold events or larger (see text) for down-going neutrinos as a function of the slant injection depth measured from the ground, for different zenith angles and different shower energies. Note that* $\Delta X = 0$ *g cm*$^{-2}$ *corresponds to the ground level.*

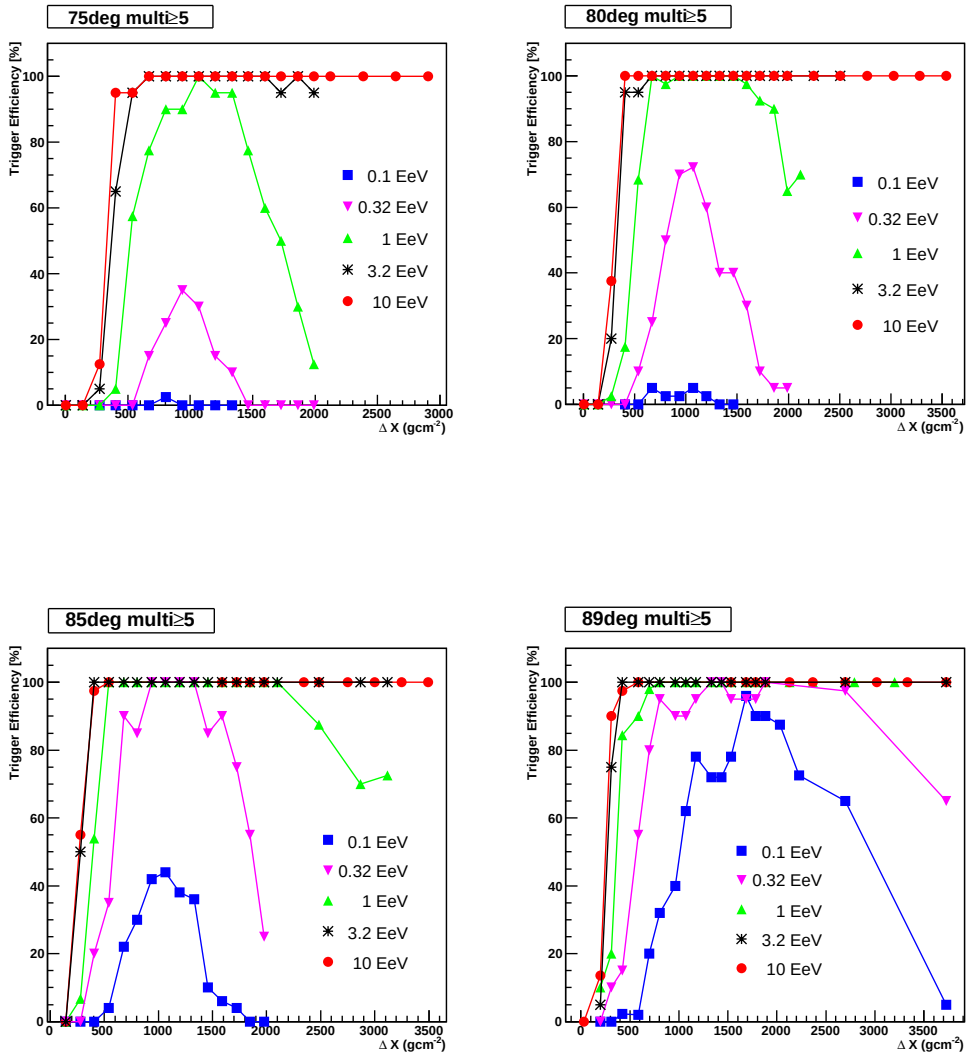

Figure 6.25: *Trigger efficiencies of 5-fold events or larger (see text) for down-going neutrinos as a function of the slant injection depth measured from the ground, for different zenith angles and different shower energies. Note that* $\Delta X = 0$ *g cm*$^{-2}$ *corresponds to the ground level.*

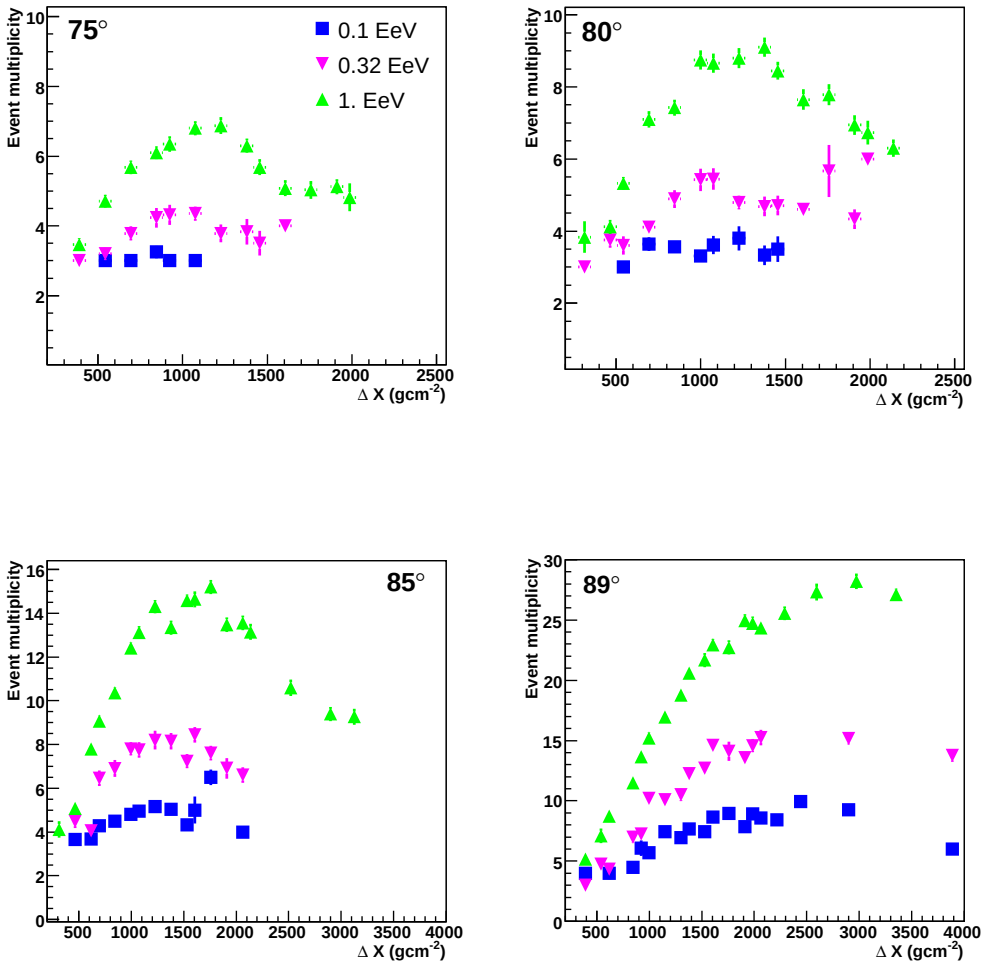

Figure 6.26: *Average number of triggered tanks per event (event multiplicity) as a function of the slant injection depth measured from the ground, for different primary zenith angles and shower energies from 0.1 to 1 EeV. Note that* $\Delta X = 0$ *g cm*$^{-2}$ *corresponds to the ground level.*

As discussed in the previous section, we require 5 or more tanks in the event. In Fig. 6.25 we plot the trigger efficiencies for the events fulfilling this requirement. This cut on the multiplicity reduces the trigger efficiencies for the less energetic showers (below 1 EeV) and with smaller zenith angle (below 85°) with respect to the case in which at least 3 tanks were required in the triggered event. However the effect on showers above 1 EeV or above $\theta \sim 85°$ is very small (compare Figs. 6.24 and 6.25). This behaviour is easy to understand: For a fixed ΔX, the showers with smaller shower energy have a smaller number of particles at ground producing less signal in the tanks at a fixed distance to the shower core, and therefore they typically trigger on less tanks. On the other hand, and for fixed energy and ΔX, the larger the zenith angle, the closer to each other in the shower plane the tanks are from the point of view of the incoming shower, and the larger the number of triggered tanks. In Fig. 6.26 we plot the average number of triggered tanks per event as a function of ΔX for the less energetic showers (E $\in$ [0.1,1.] EeV) at different zenith angles. For a fixed angle, the multiplicity increases with energy. The number of triggered tanks behaves qualitatively in the same way as the trigger efficiencies calculated before. One can also see that for 0.1 EeV showers, although the multiplicity increases with θ, it is practically always smaller than 5 for all θ and ΔX, except at 89° where the apparent shrink of the array along the shower direction due the projection onto the shower plane is large enough to increase the number of triggered tanks.

6.4.2 Selection and Reconstruction efficiency for Neutrino Showers

The simulated neutrino events fulfilling the 5-fold or larger trigger condition are stored in the same format as real data. Then the selection of candidate stations and angular reconstruction algorithms, developed in section 6.1, are applied to them, and as a result we end up with events having a reconstructed zenith angle greater than 75° and with 5 or more stations participating in the angular reconstruction. In the following we compute the efficiency with which the simulated events are reconstructed as having $\theta_{rec} \geq 75°$.

In Fig.6.27, we show the fraction of triggered events with 5 or more tanks that are selected as having $\theta_{rec} \geq 75°$ as a function of the slant injection depth measured from the ground (ΔX) for different zenith angles and shower energies from 1 to 10 EeV. By comparing Figs. 6.25 and 6.27 one can see that there is a very important loss of selected events with $\theta_{sim} = 75°$ for all the energies. For $\theta_{sim} > 75°$, the fraction of selected events with respect to the case shown in Fig. 6.25, only decreases near the ground. To explore which are

the reasons for such decreases we plot in the top and left panels of Fig. 6.28 the total fraction of rejected events for 1 EeV showers at two zenith angles $\theta = 75^\circ$ and 89°, and in the other 3 panels we show the fractions of rejected events due to three different reasons:

- Panel A: Fraction of events not reconstructed at all by our algorithm.
- Panel B: Fraction of reconstructed events fulfilling the requirement of ≥ 5 stations participating in the angular reconstruction but which are reconstructed with $\theta_{rec} < 75^\circ$.
- Panel C: Fraction of reconstructed events fulfilling the requirement of $\theta_{rec} \geq 75^\circ$, but with < 5 stations participating in the angular reconstruction.

In panel A, one can see that for $\theta_{sim} = 89^\circ$ the main reason for rejecting events is that close to the ground ($\Delta X < 1000$ g cm^{-2}) around 30% of events are not reconstructed. The remaining fraction of events are rejected because the number of selected stations is less than 5 as seen in panel C.

In panel B, one can see that for $\theta_{sim} = 75^\circ$ the main reason for the large rejection fraction of events is that the reconstructed zenith angle is smaller than 75°. This is due to the shower zenith angle being reconstructed systematically with $\sim 2^\circ$ less than θ_{sim}. The bias can be seen in Fig. 6.29, where we plot the difference between the simulated θ_{sim} and reconstructed θ_{rec} zenith angles as a function of the slant injection depth measured from the ground, for different primary energies and primary zenith angles. One can see in Fig. 6.29 that θ_{rec} is systematically $\sim 2^\circ$ smaller than θ_{sim} at essentially all angles. The effect on the selection efficiencies is largest for $\theta_{sim} = 75^\circ$ simply because it is the angle closer to the angular cut above which we select the events.

The sign of $(\theta_{sim} - \theta_{rec})$, that indicates whether the reconstructed angle is larger or smaller than the simulated angle θ_{sim}, depends on the ratio of stations between the early and late regions in the event and on the configuration of the stations in both regions. In the early region the shower front has a larger curvature that tends to push the reconstructed angle towards smaller than θ_{sim} values. In the late region the shower front is flatter and this tends to push the reconstructed angle towards values larger than θ_{sim}. In Fig. 6.30 we show two examples of 1 EeV energy events that are reconstructed with larger and smaller zenith angle than the simulated ones. In the event in the top panel, $\theta_{sim} - \theta_{rec} \simeq -1^\circ$, because there are 2 tanks in the early region and 4 tanks in the late one, so the curvature of the late region is weighting more in the angular fit producing a larger zenith angle. On the contrary, the event

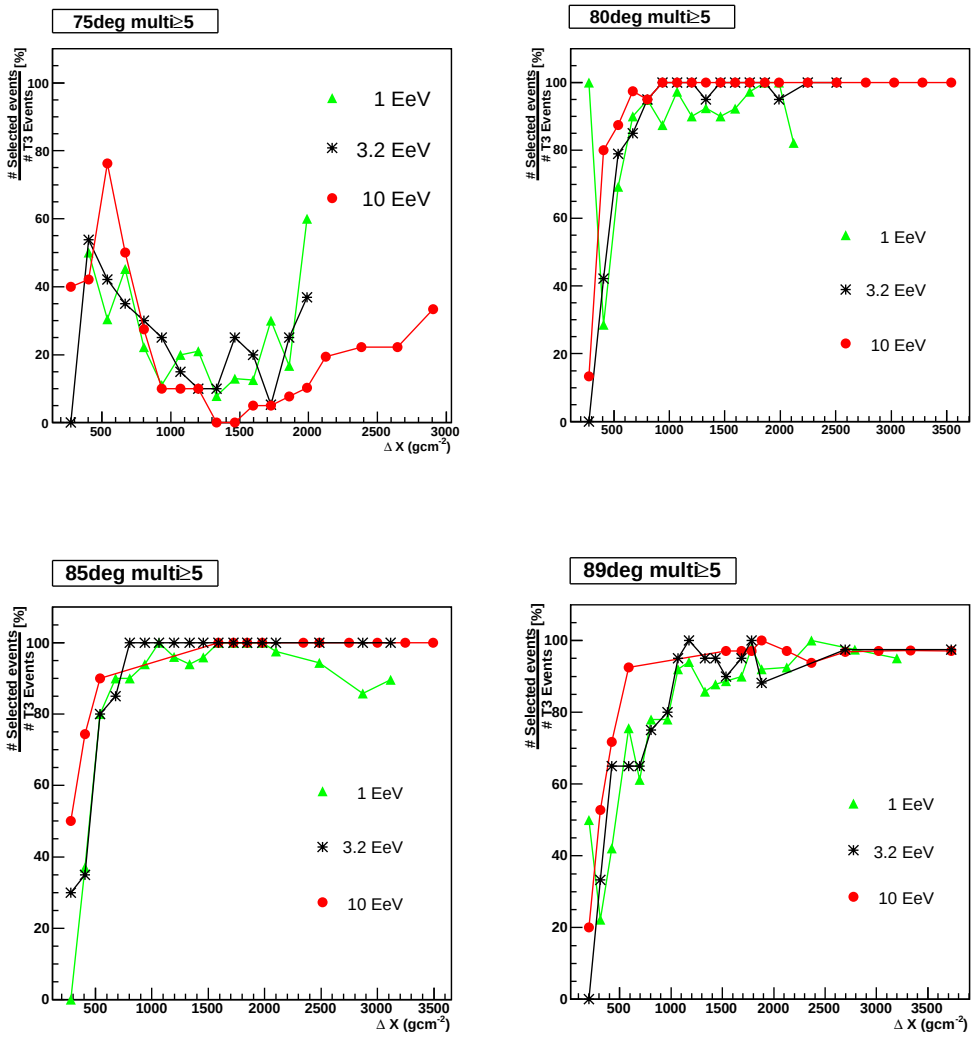

Figure 6.27: *Fraction of simulated triggered events (5-fold or more) selected as having* $\theta_{rec} \geq 75°$ *as a function of the slant injection depth measured from the ground, for different zenith angles and shower energies from 1 to 10 EeV.* $\Delta X = 0$ *g cm*$^{-2}$ *corresponds to the ground level.*

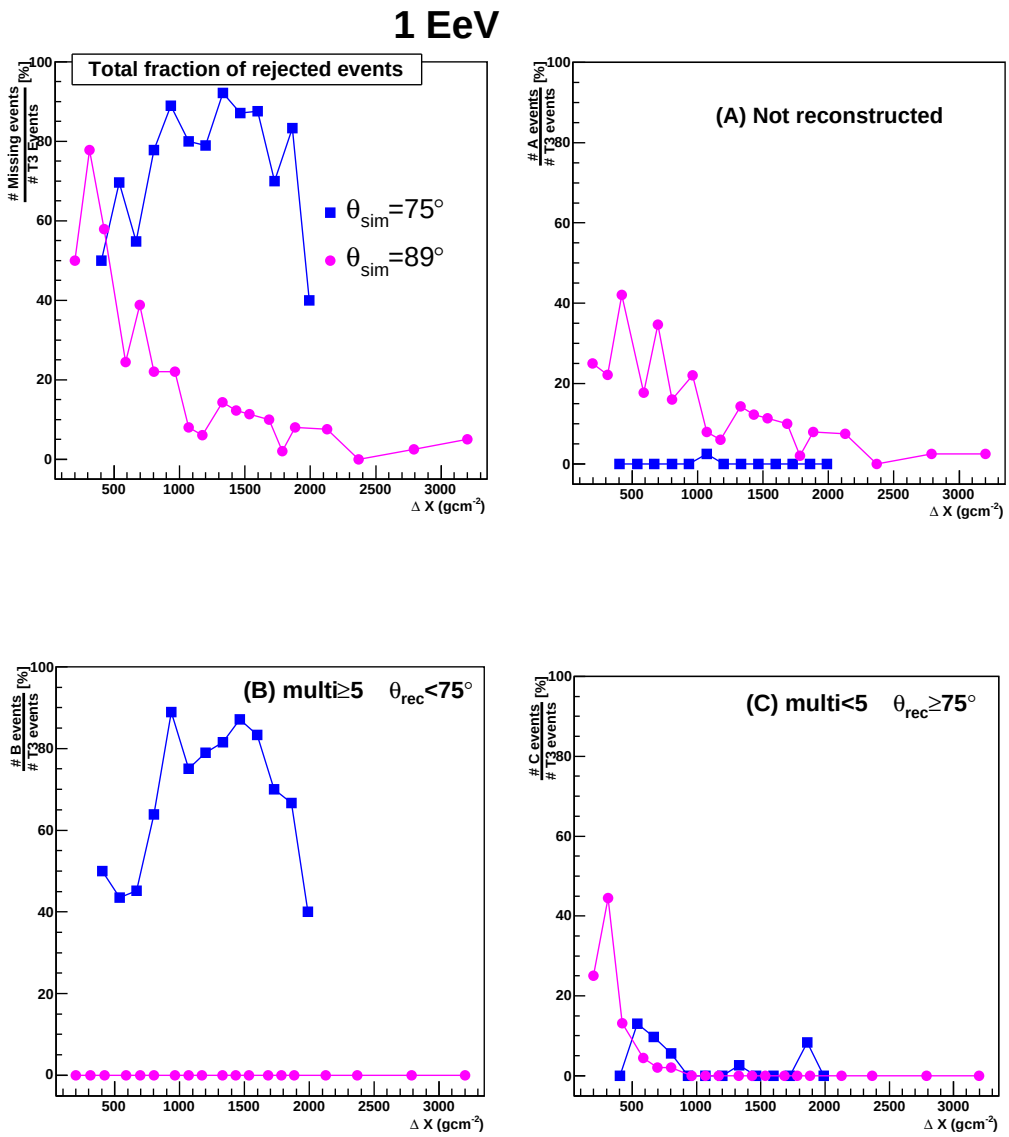

Figure 6.28: *Total fraction of rejected T3 events for 1 EeV showers at* 75° *and* 89° *after event reconstruction. Panel A: Not reconstructed events. Panel B: Reconstructed events with multiplicity* ≥ 5 *and* $\theta_{rec} < 75°$*. Panel C: Reconstructed events with multiplicity* < 5 *and* $\theta_{rec} \geq 75°$*.*

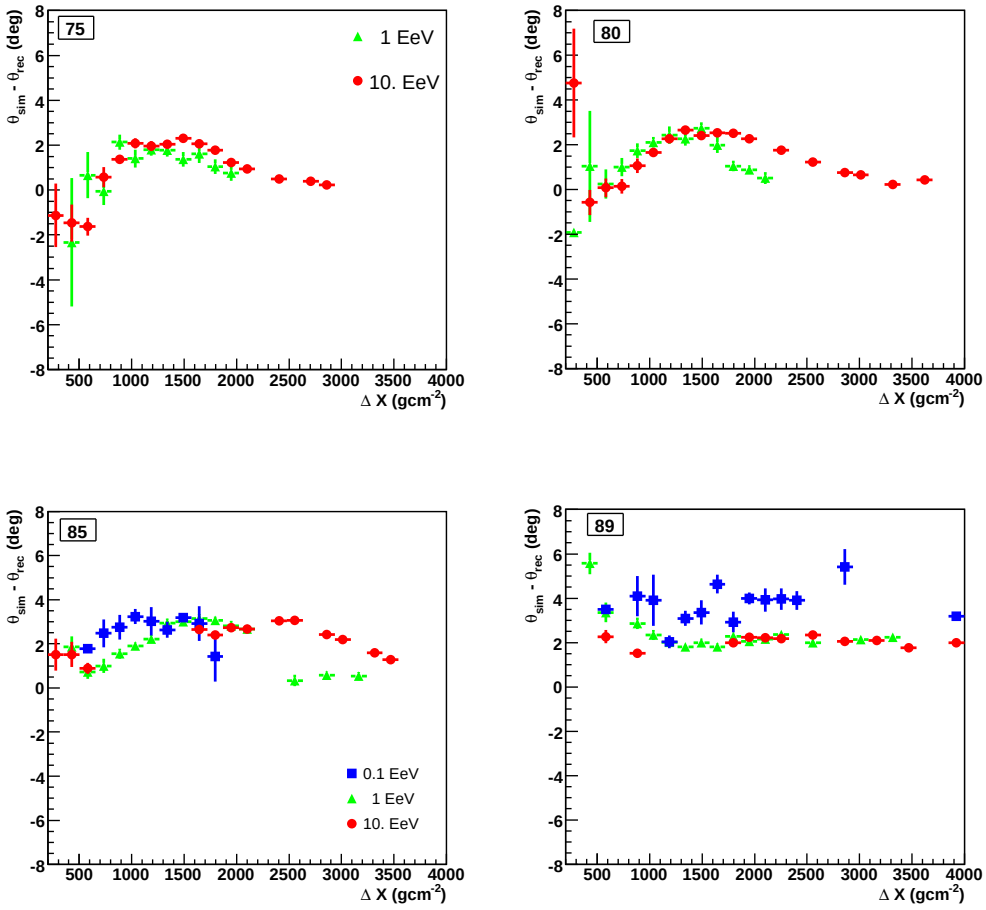

Figure 6.29: *Difference of the simulated zenith angle (θ_{sim}) and the reconstructed zenith angle (θ_{rec}) as a function of the slant injection depth measured from the ground, for different primary shower energies. Each panel corresponds to a different value of the primary zenith angle.*

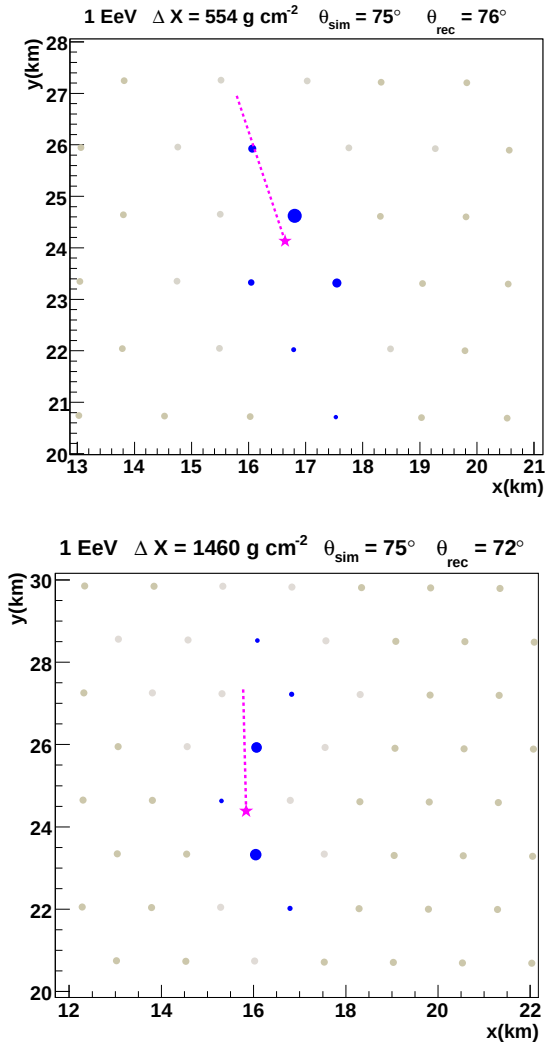

Figure 6.30: *Examples of two neutrino induced events of shower energy $E_{sh} = 1$ EeV at $\theta_{sim} = 75°$. Top panel: Event reconstructed with larger θ. Bottom panel: Event reconstructed with smaller θ. The selected stations are in blue, the arrow shows the shower direction and the star shows the core position.*

shown in the bottom panel has 4 tanks in the early region and 2 tanks in the late region, so that the curvature of the shower front in the early region weights more in the angular fit and $\theta_{sim} - \theta_{rec} \simeq 3°$. This fact explains the behaviour shown in Fig. 6.29 for $\theta_{sim} = 75°$ events, in which $\theta_{sim} - \theta_{rec}$ takes negative values near the ground because there are more stations in the late region than in the early one (checked with our MC simulations). For larger ΔX the number of stations in the early region is larger than the number of stations in the late one and $\theta_{sim} - \theta_{rec} < 0$.

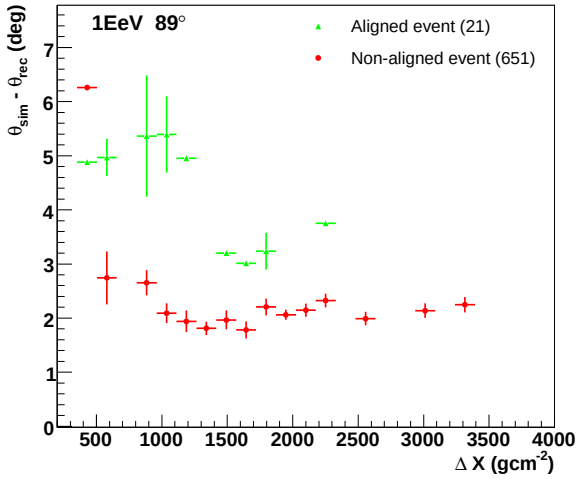

Figure 6.31: *The difference between θ_{sim} and θ_{rec} performed by the standard and the aligned reconstruction methods (see Section 6.1.2) for $\theta_{sim} = 89°$ as a function of the slant injection depth measured from the ground and for 1 EeV shower energy.*

When $\theta_{sim} \geq 85°$, $\theta_{sim} - \theta_{rec} > 0$ for all energies and slant injection depths because the early tanks weight more in the angular fit for all injection points (this has been checked with MC simulations). The systematic difference between θ_{rec} and θ_{sim} is also present in the case of aligned events, as can be seen in Fig. 6.31, where we plot $\theta_{sim} - \theta_{rec}$ for 1 EeV and 85° for completely aligned and not aligned events. In this case the approximation of taking the direction of the shower along the line of tanks tends to produce smaller values of θ_{rec} (see Section 6.1.2).

The systematic difference between the reconstructed and simulated angles indicates that the angular reconstruction needs to be improved for neutrino showers, because they typically exhibit a large difference in curvature between the early and late regions. The improved reconstruction should aim at avoiding that the event configuration shifts the θ_{rec} with respect to θ_{sim}.

Finally, in Fig.6.32 we summarize our results by showing the fraction of simulated deeply initiated proton showers having $\theta_{rec} \geq 75^{\circ}$ and multiplicity ≥ 5 (Selection efficiency) as a function of the slant injection depth measured from the ground (ΔX) for different zenith angles and energies of the shower.

6.4.3 Efficiency of the Identification Criterion for Neutrino Showers

The last step is the calculation of the identification efficiency for neutrino showers. For that purpose we compute the fraction of 5-fold or more events reconstructed with $\theta_{rec} \geq 75^{\circ}$ passing the deep shower cuts on the risetime and falltime of the two earliest tanks in the event.

In Fig. 6.33, we show the fraction of selected events after the reconstruction passing the deep shower cuts for different zenith angles and shower energies from 1 to 10 EeV. As expected the fraction of identified events drops for showers initiated far away from the ground because the electromagnetic component of the shower is absorbed even in the early region of the shower, and the risetime and falltime in the two earliest tanks in the event drop to values characteristic of conventional nucleonic showers. It is important to note that the range of injection depths where the identification is possible increases with zenith angle for a fixed energy. This is mainly due to a geometrical effect namely to the fact that for a fixed slant injection depth and energy, the more inclined a shower is the smaller the height above ground of its injection point. A sketch of this effect is shown in Fig. 6.34, where we illustrate that the more inclined a shower, the EM component of the early part can reach the ground earlier in the event because it attenuates less. As a result the electromagnetic signals in the event involve a larger number of tanks increasing the chances of identifying deeply penetrating particles. Also if the slant injection depth is small, this geometrical effect could produce the opposite behaviour, that is, the early part could be too young and in this case the shower front would not be thick enough to fulfill the cuts on risetime and falltime.

Finally, in Fig. 6.35 we show the fraction of simulated showers passing all the cuts ($\theta_{rec} \geq 75^{\circ}$, 5 or more tanks and RT and FT cuts) (Identification efficiency) as a function of ΔX for different zenith angles and shower energies.

The resulting identification efficiencies can be integrated in injection depth to obtain the total identification efficiencies as a function of zenith angle at different shower energies, which are shown in Fig. 6.36. The probability increases with zenith angle and with energy as explained before.

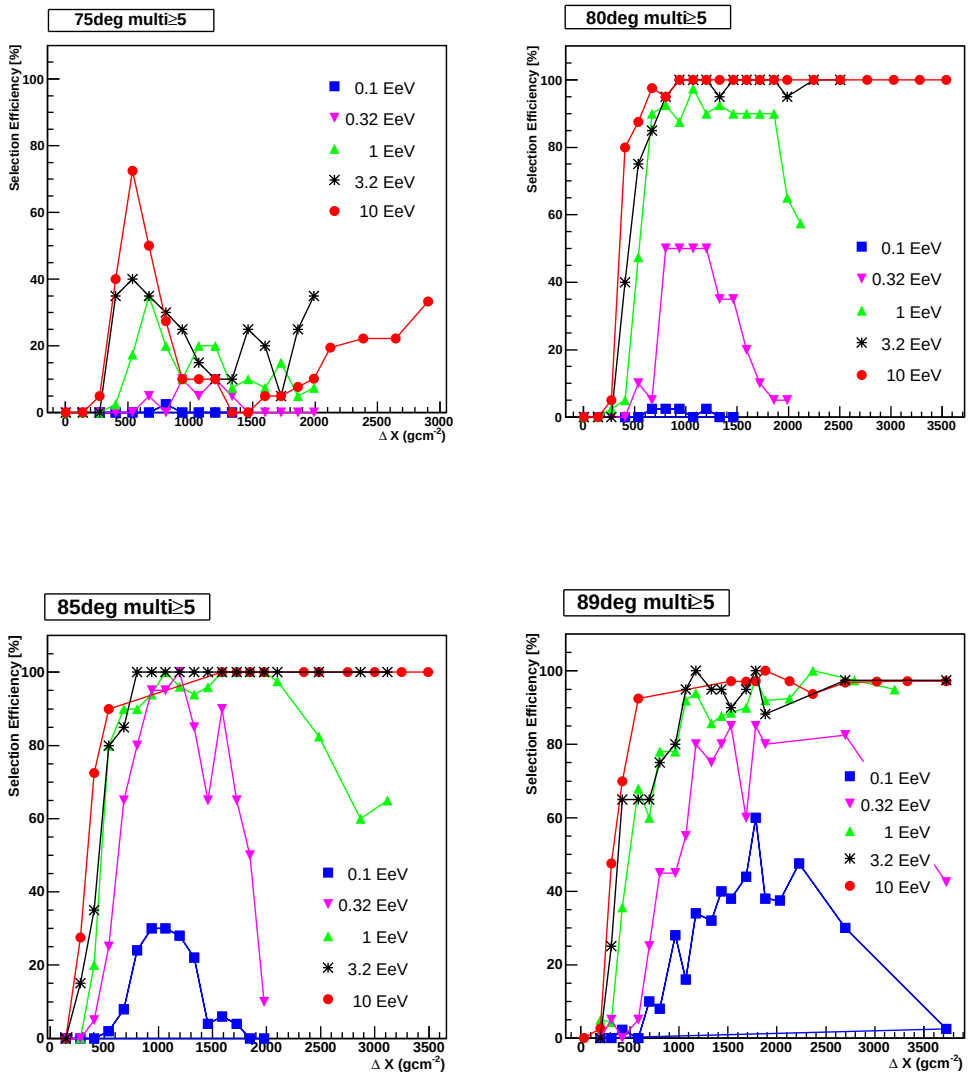

Figure 6.32: *Selection efficiencies (see text) for down-going neutrinos as a function of the slant injection depth measured from the ground, for different zenith angles and different shower energies.* $\Delta X = 0$ *g cm*$^{-2}$ *corresponds to the ground level.*

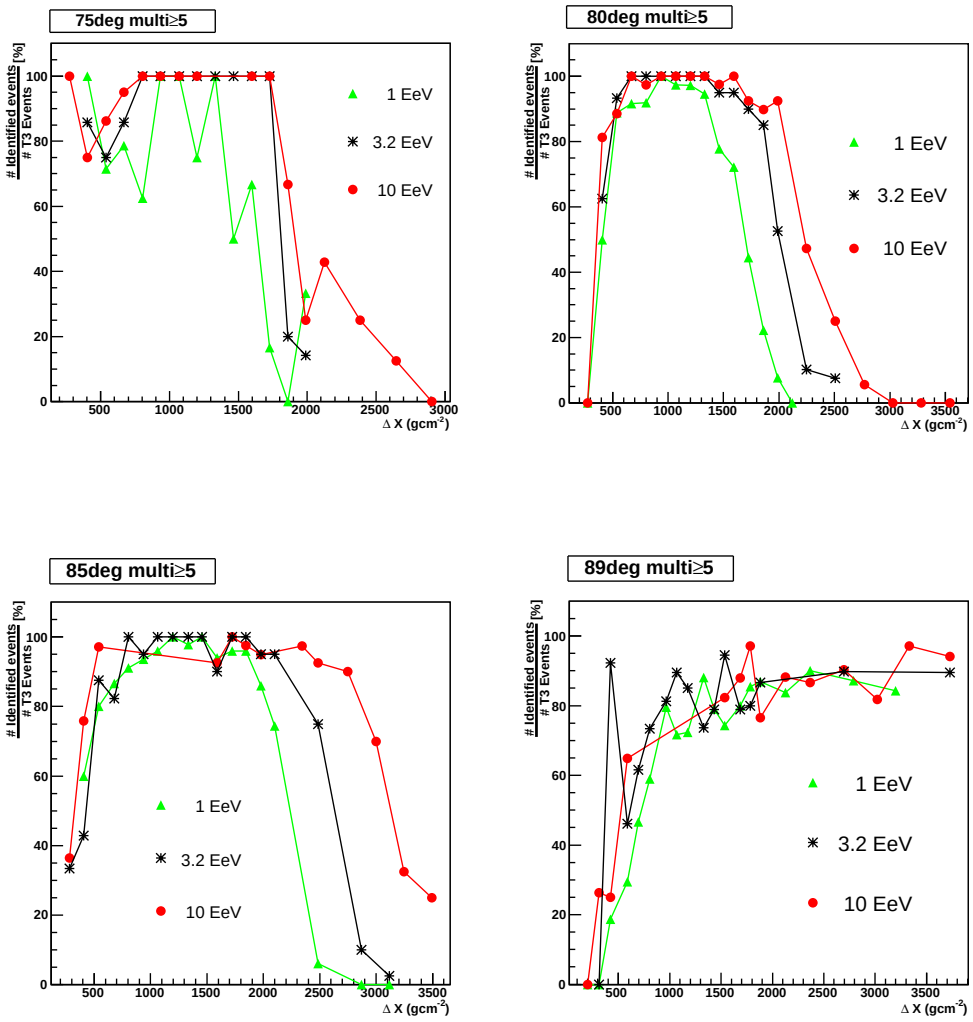

Figure 6.33: *Fraction identified events after the reconstruction passing the deep shower cuts as a a function of the slant injection depth measured from the ground, for different zenith angles and shower energies from 1 to 10 EeV.* $\Delta X = 0$ *g cm*$^{-2}$ *corresponds to the ground level.*

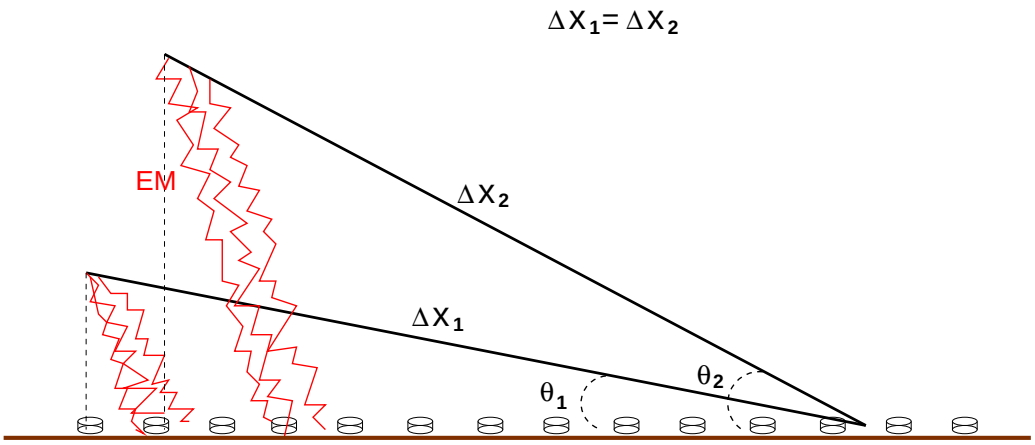

Figure 6.34: *Schematic illustration of the zenith angle effect on the identification efficiencies for down-going neutrinos for a fixed energy and slant injection depth from the ground (see text).*

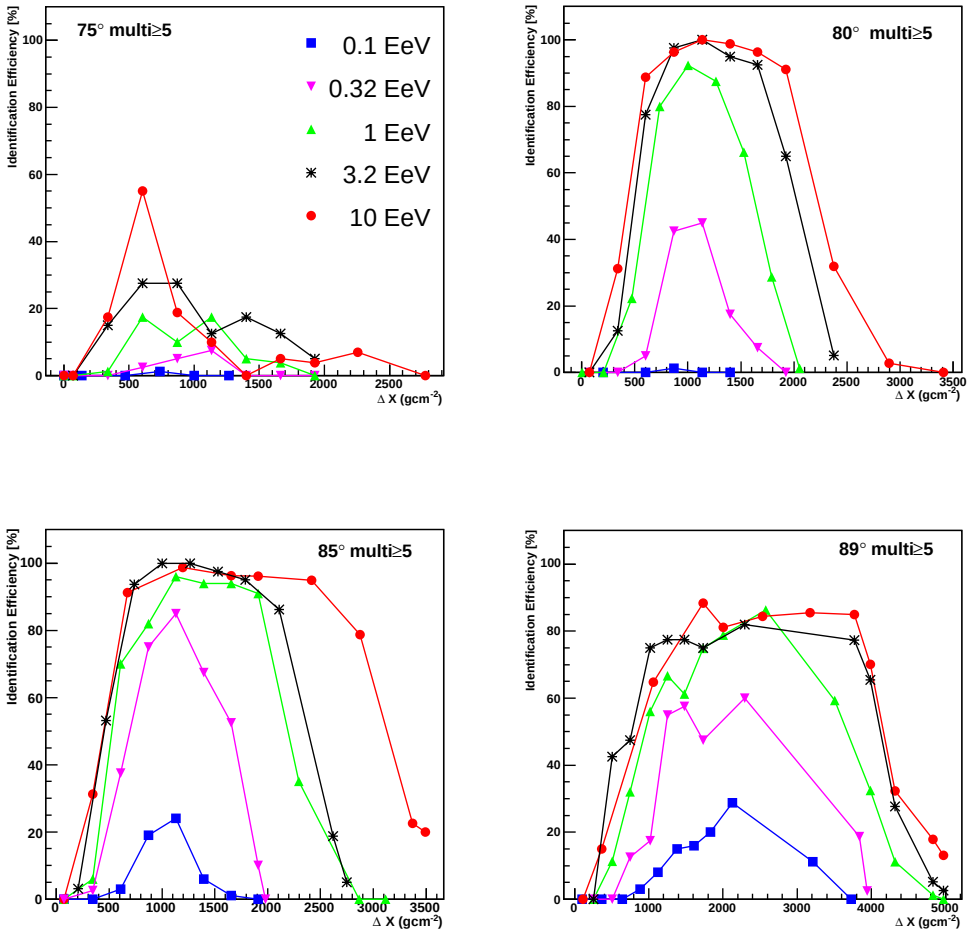

Figure 6.35: *Identification efficiencies (see text) for down-going neutrinos as a function of the slant injection depth measured from the ground, for different zenith angles and different shower energies.* $\Delta X = 0$ *g cm*$^{-2}$ *corresponds to the ground level.*

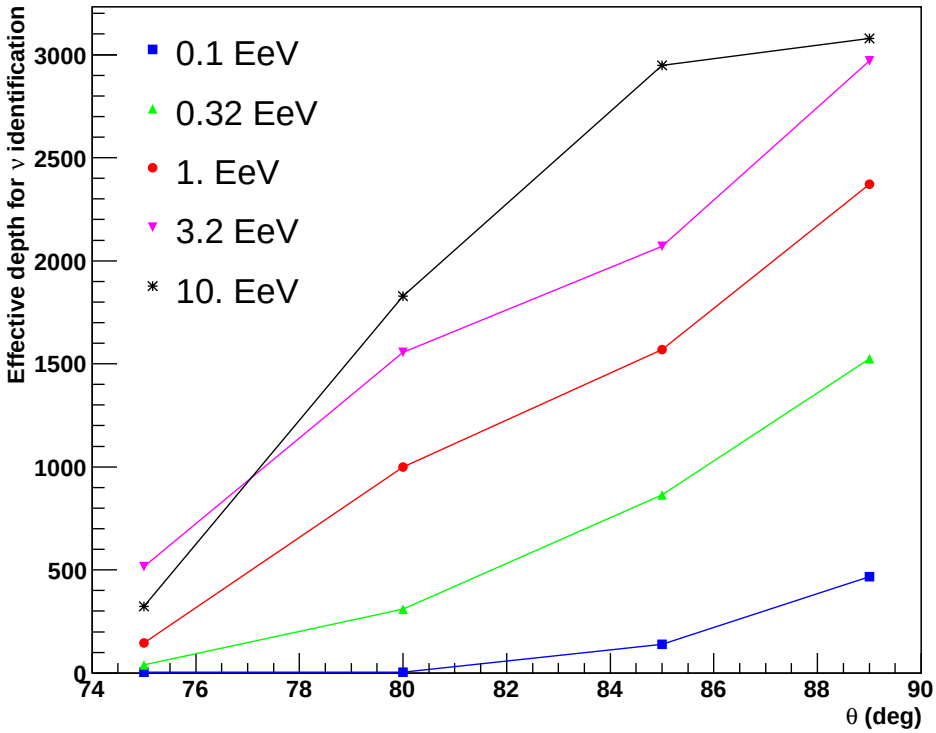

Figure 6.36: *Effective depth for down-going neutrino identification (see text) as a function of the shower zenith angle for different shower energies.*

Chapter 7

A limit to the diffuse flux of UHE Neutrinos with down-going showers from the Pierre Auger Observatory

7.1 Search for neutrino candidates in the Auger data

In this section, we apply the criteria for identifying neutrino candidates described in the previous chapter to the data collected at the surface detector of the Pierre Auger Observatory from January 1st 2004 to September 3rd 2007.

Firstly, we have selected inclined events having a reconstructed zenith angle above 75°. For this purpose, we have applied the procedure for station selection and event reconstruction described in Section 6.1. We found a total of 18486 events fulfilling this requirement. Then we selected those events with 5 or more stations participating in the angular reconstruction and we obtained 14741 events ($\sim$ 80 % of the total number). Finally, we applied the criteria to select deep events described in Section 6.3.2, namely the risetimes of the two earliest tanks $>$ 60 ns and the falltimes $>$ 150 ns. We end up with 2 events surviving all the selected cuts over the period analyzed.

The potential neutrino candidates are the events with identifier numbers (ID) 1452015 and 1956182. We have performed a careful analysis of these 2 events to study if they can be considered as neutrino candidates.

Data set	$\theta \geq 75°$	+ multi ≥ 5	+ $RT\&FT$ cuts
2004	2149	1725	0
2005	4459	3543	1
2006	6345	5049	1
2007	5533	4424	0
Total	18486	14741 (79.7%)	2 (0.01%)

Table 7.1: *Number of events surviving the cuts for identifying neutrino candidates. In the second column we show the events passing the cut of $\theta_{rec} \geq 75°$. In the third column we indicate the number of events having ≥ 5 stations participating in the angular reconstruction. In the fourth column we display the number of events also passing the cuts of deep showers.*

7.1.1 Event 1452015

Event 1452015 triggered the Surface Detector on June 18$^{\text{th}}$ 2005. In the left panel of Fig. 7.1 we display this event in the surface array, where the blue circles correspond to the 26 triggered stations that were selected to participate in the angular reconstruction. The two earliest stations of the event are stations 175 and 176 labeled as 1^{st} and 2^{nd} in the figure. Assuming the event is induced by a proton it is reconstructed with $\theta = 78.6°$, $\phi = 117.7°$ and $E = 20.4$ EeV [1].

Firstly, we study the time structure of the signals in the event to compare it with the expected structure in neutrino events (see section 6.3.1). In the right panel of Fig. 7.1, we plot the risetime, falltime and their sum ($RT+FT$) as a function of the start-time of the signal in the stations of the event. The start-time of each tank is referred to the time of the earliest station in each event. One can see that except for the two earliest stations, all the stations have $RT < 60$ ns and $FT < 150$ ns. This is not the usual time structure of the signals expected in neutrino showers. In fact, by looking at a sample of simulated deep proton showers with $\theta = 80°$, $E = 10$ EeV (close to the reconstructed energy and zenith angle), different ΔX and with similar multiplicity (number of triggered stations ≥ 20) to event, we have found that only 0.4% of them have the two earliest stations passing our RT and FT cuts, whereas the rest of tanks do not pass them. Moreover, the simulated events with a time structure similar to the real one are those that have to cross a grammage of $\Delta X \simeq 2500$ g cm^{-2} to reach the ground. However, the fact that there is just a small fraction of simulated deeply penetrating events with a

[1]The energy reconstruction is performed using the standard Auger algorithms for reconstruction of inclined events [67]

time structure similar to that of event 1452015 is not enough reason to reject or accept it as a neutrino candidate.

In fact, by inspecting the FADC traces of the two earliest stations in the event 1452015 (Fig. 7.2) one can see that both traces exhibit a signal with a structure of several fast peaks ($RT_{peak} < 50$ ns and $FT_{peak} < 80$ ns) separated by a very short time. This type of structure is expected to be found in detectors triggered by a muonic shower front with a significant curvature due to the arrival time delay of the muons. Therefore, showers induced by protons can produce this type of structure in stations located at large distances from the shower core. However, showers induced by neutrinos far from the ground can also arrive at the ground as a muonic shower front with a significant curvature and therefore, they can produce signals in the tanks that exhibit a structure of several fast peaks separated by a very short time. In fact, in the simulated neutrino events (see above) that had the same time structure as that of event 1452015, the earliest stations also have 2 or 3 muon peaks separated by a very short time. In conclusion, it is still possible that the event was produced by a neutrino interacting at $\Delta X \simeq 2500$ g cm^{-2} from the ground.

Further information on the event can be obtained using the model of the time distribution of muons in air showers developed in [30]. This model relates the depth development of the muonic component in air showers to the arrival time of individual muons at ground. As a result, the arrival time distributions of muons at ground level can be converted into distributions of muon production distance from the ground in inclined showers, and viceversa. Therefore, this model allows the reconstruction of the distribution of production distance of muons using the signal start-time in stations that are not very close to shower axis. This could allow us to determine if an event was produced by an ordinary inclined shower or a deep inclined shower. This model was tested for ordinary inclined showers in [30], and here we have also tested it using the signal start-time of neutrino simulated events finding that the model reproduces with a good accuracy the distribution of muon production distance obtained directly from the neutrino simulations (the mean and RMS values of the distributions are reproduced with a $\sim 2.5\%$ accuracy).

We applied the model to event 1452015, and we obtained that the probability distribution of muon production distance peaks at 67.1 km ($\Delta X \sim$ 3698.24 g cm^{-2}) with a RMS of 8.6 km. The expected mean value of the muon production distance for 10 EeV proton showers interacting at the top of the atmosphere with $\theta = 78°$ is 67.8 km and the RMS is 15.5 km as obtained from MC simulations. As a consequence, the mean depth of muon production of the event 1452015 is compatible with that expected for an ordinary proton shower, which allows us to conclude that very likely 1452015 is not a

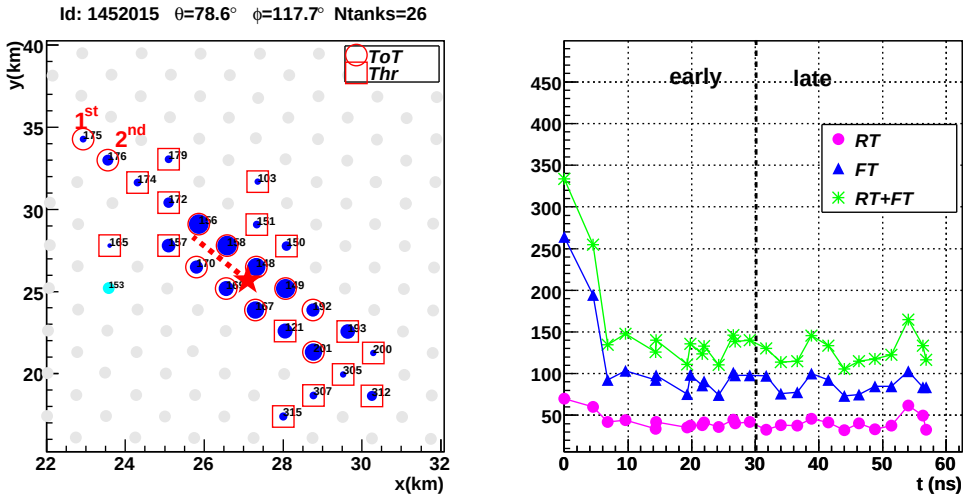

Figure 7.1: *The SD event labeled as 1452015 that passes all the cuts for selection of neutrino candidates. Left panel: The stations of the event in the surface array are indicated by blue circles, whose radius is proportional to the signal size. The two earliest stations are labeled as* 1^{st} *and* 2^{nd}*. The arrow shows the shower direction and the star indicates the barycenter position. The type of trigger in each station is also indicated. Right panel: The time structure of the signals in the event as a function of the tank start-time with* $t = 0$ *corresponding to the first triggered station. The early an late regions are indicated.*

neutrino candidate.

Analysis of the FADC traces

A very relevant question is why the two earliest stations of this inclined event passed the cuts that select FADC traces with a significant electromagnetic component. In Fig. 7.2 we show the FADC traces of the two earliest stations, both exhibit a signal with a time structure of approximately 2 or 3 fast peaks ($RT_{peak} < 50$ ns and $FT_{peak} < 80$ ns) separated by a very short time. This type of time structure is expected to be found in inclined events with high multiplicity of triggered stations, such as 1452015, where the earliest tanks are usually far from the core. In fact in this event, station 175 is at $r \sim 9.54$ km from the core of the event in the ground plane and station 176 at ~ 8.1 km, assuming the barycenter of the signal footprint of the event is close to the shower core.

We can try to reproduce this time structure using again the model for the arrival time distribution of muons developed in [30]. Under the assumption that the candidate event 1452015 is induced by a proton or a nucleus and

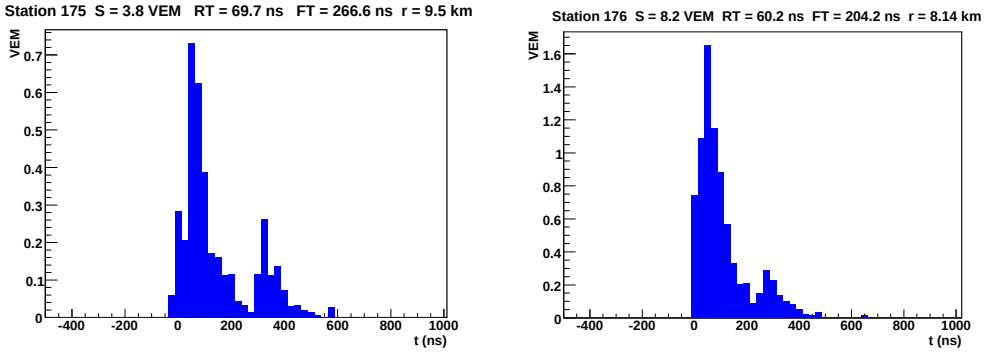

Figure 7.2: *FADC traces of the two earliest selected stations of the event 1452015. Left panel:* 1^st *station. Right panel:* 2^nd *station. The trace corresponds to the mean trace of the three PMT.*

assuming each peak seen in the FADC traces is produced by a single muon, we can apply the model to calculate several useful quantities related to the time structure of the signal, such as Δt the time separation between the arrival of the first and the last muon at each station, the probability of having a time separation between muons larger than the time separation seen in each FADC of the earliest stations, and also the probability that a given number of muons produces FADC traces with a risetime > 60 ns and a falltime > 150 ns.

By inspecting the FADC trace of station 175 (left panel of Fig. 7.2) we can assume 3 muon peaks produce the FADC, and we obtain that the first and last muons are arriving with a time separation of $\Delta t \sim 320$ ns. From the model, we have obtained the distribution of Δt the difference in arrival time between the first and last muons in a detector placed at the same coordinates (r, ζ) as station 175. The distribution is very broad with a mean $\langle \Delta t \rangle \sim 62$ ns and a RMS of 150 ns. The probability of having a Δt larger than 320 ns is only 1% ($\pm 0.5\%$), and decreases to 0.7% if only 2 muon peaks are assumed. In the case of station 176 (right panel of Fig. 7.2), we assume 2 muon peaks separated by $\Delta t \sim 250$ ns. From the model, we have obtained a mean arrival time difference of $\langle \Delta t \rangle \sim 31$ ns with a RMS of 45 ns, and a probability of having a time separation larger than 250 ns of $\sim 0.7\%$ ($\pm 0.3\%$).

Using the model we have also calculated the probability that the number of assumed muons in each of the 2 earliest stations produced a risetime > 60 ns and falltime > 150 ns. This is 1.4% ($\pm 0.8\%$) for station 175 and 0.7% ($\pm 0.2\%$) for station 176.

In consequence and according to the model in [30], although it is not very likely it is still possible that a conventional nucleonic inclined shower

produced a time structure similar to what is observed in event 1452015. The model does not seem to be very helpful here but this could be due to the assumptions on the number of muons in the FADC trace and on the assumption about the core position (we have used the barycenter of the footprint of the event) which determines the distance to the stations.

7.1.2 Event 1956182

Event 1956182 triggered the Surface Detector on January 28$^{\text{th}}$ 2006. In the left panel of Fig. 7.3 we display this event in the surface array, which has 33 triggered stations that were selected to participate in the angular reconstruction. The two earliest stations of the event are stations 581 and 768 and are labeled as 1^{st} and 2^{nd} in the figure. Assuming the event is induced by a proton it is reconstructed with $\theta = 76.0°$, $\phi = -39.9°$ and $E = 33.2$ EeV.

We have analyzed this event in detail following the same steps as in the previous event. Firstly, in the right panel of Fig. 7.3 we plot the risetime, falltime and their sum ($RT + FT$) as a function of the start-time of the signal in the stations of the event. One can see that besides the two earliest stations, there are other two stations with $RT > 60$ ns and $FT > 150$ ns (stations 679 and 683 indicated with arrows in the figure). These stations are the 12$^{\text{th}}$ (in the early region) and the 22$^{\text{nd}}$ (in the late region) stations in time. They have a large RT and FT most likely because either they are relatively close to the core and triggered by multiple muons (see Fig. 7.5) or because one of the peaks was produced by an accidental muon interfering with the signal and artificially increasing the RT and FT. Neglecting stations 679 and 683, we end up with the same situation as in the previous event. Event 1956182 might in principle be a neutrino shower produced far from the ground at $\Delta X \simeq 2500$ g cm^{-2}.

As in the previous event, we have applied the model [30] and we have obtained that the probability distribution of muon production distance peaks at 47.4 km ($\Delta X \sim 2870.17$ g cm^{-2}) with a RMS of 3.7 km. The expected mean value for 10 EeV proton showers interacting at the top of the atmosphere with $\theta = 76°$ is 55.2 km and the RMS is 12.5 km. As a consequence, the mean depth of muon production of the event 1956182 is compatible with that expected for an ordinary proton shower, which allows us to conclude that very likely event 1956182 is not a neutrino candidate.

Analysis of the FADC traces

By inspecting the FADC traces of the two earliest stations (see Fig. 7.4), we find that both exhibit a signal with a time structure of 3 fast peaks

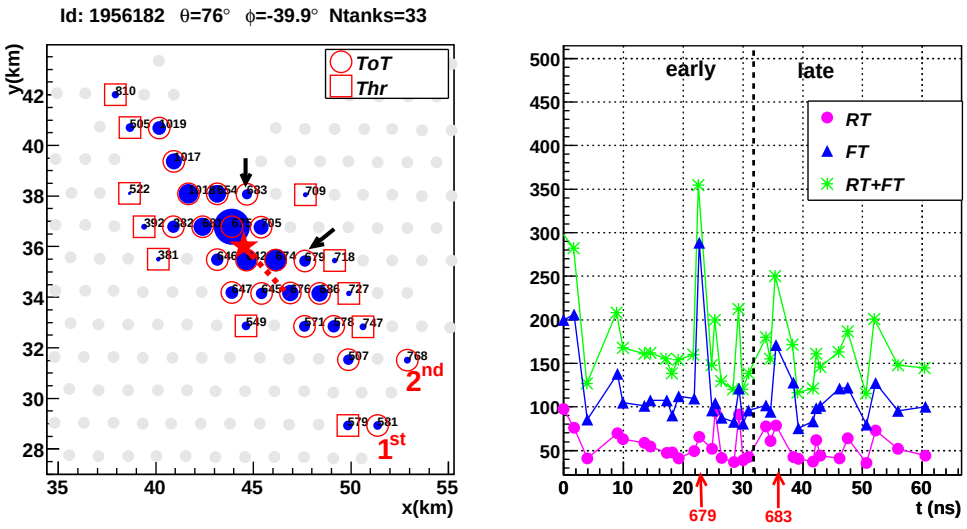

Figure 7.3: *The SD event labeled as 1956182 that passes all the cuts for selection of neutrino candidates. Left panel: The stations of the event in the surface array are indicated by blue circles, whose radius is proportional to the signal size. The two earliest stations are those labeled as* 1^{st} *and* 2^{nd}*. The black arrows indicate two other stations that also pass the RT and FT cuts. The red arrow shows the shower direction and the star indicates the barycenter position. The type of trigger is also indicated. Right panel: The time structure of the signals in the event as a function of the tank start-time with* $t = 0$ *corresponding to the first triggered station. The early an late regions are indicated.*

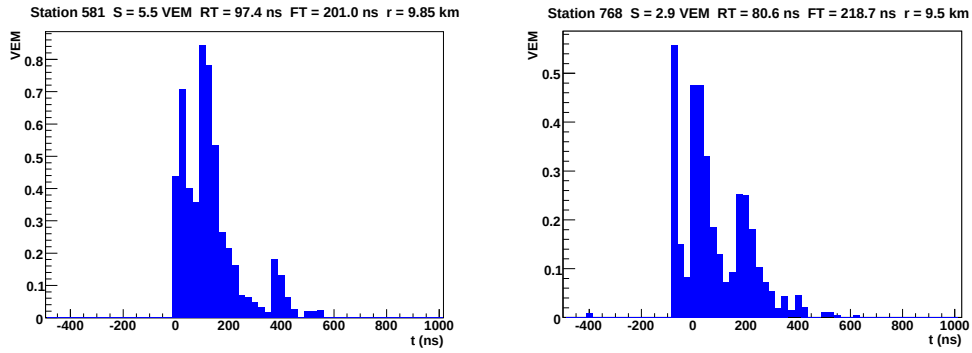

Figure 7.4: *FADC traces of the two earliest selected stations of the event 1956182. Left panel:* 1^{st} *station. Right panel:* 2^{nd} *station. The trace corresponds to the mean trace of the three PMT.*

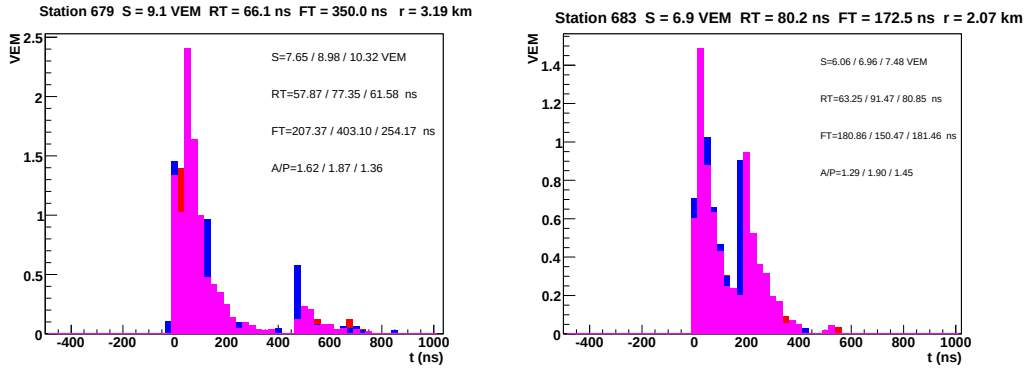

Figure 7.5: *FADC traces of two selected stations different from the earliest stations, which also pass the RT and FT cuts in event 1956182. Left panel: station 679. Right panel: station 683. The different colour of the histograms corresponds to the trace of each PMT.*

($RT_{peak} < 50$ ns and $FT_{peak} < 80$ ns) separated by a very short time. As in the previous event, 1956182 has a very high multiplicity and the two earliest stations are far from the shower core. Station 581 is at $r \sim 9.85$ km from the event core in the ground plane and station 768 at $r \sim 9.5$ km, assuming again that the barycenter of the signal footprint of the event is close to the shower core.

Under the assumption that event 1956182 is induced by a proton or nucleus and assuming each peak seen in the FADC traces is produced by a single muon, we applied the model [30] to obtain the same quantities related to the time structure of the signal as obtained for event 1452015.

In station 581 (left panel of Fig. 7.4) we assume 3 muon peaks, and we assume the first and last muons are arriving with a time separation of $\Delta t \sim 370$ ns. From the model, we have obtained the distribution of Δt the difference in arrival times between the first and last muons. The distribution is broad with a mean $\langle \Delta t \rangle \sim 143$ ns and a RMS of 255 ns, and the probability of having a Δt larger than 370 ns is 3.2% ($\pm 0.8\%$). For station 768 (right panel of Fig. 7.4), we also assume 3 muon peaks separated by ~ 230 ns. The distribution of the difference in arrival time predicted by the model has a mean of $\langle \Delta t \rangle \sim 130$ ns and a RMS of 116 ns, and the probability of having a Δt larger than 230 ns is 9.7% ($\pm 3.8\%$).

We also calculated the probability that the 3 muons assumed in each of the two earliest stations produced a risetime > 60 ns and a falltime > 150 ns in each one of the 2 earliest stations. This is 10.1% ($\pm 0.4\%$) for station 581 and 8.2% ($\pm 2.3\%$) for station 768. In consequence and according to the model in [30] it is possible that a conventional nucleonic inclined shower produces

a time structure similar to what is observed in event 1956182. Note again that the predictions of the model depend on the assumption on the number of muons, distance of the stations to the core,...etc.

As a final comment, the fact that the 2 events that pass the neutrino identification criteria are large multiplicity events but they are not very likely induced by neutrino interactions, seems to be indicating that a further refinement of the identification criteria is needed. A possibility could be to use n tanks in the criteria with n increasing with the multiplicity of the event. This possibility has not been explored in this thesis.

7.2 Acceptance calculation

The calculation of the aceptance of the surface detector to inclined showers is a very complicated task. Firstly, the surface array is growing with time, its configuration is not regular (holes, non-working stations,...) and changes even at the second level. Furthermore, the inclined showers typically have very elongated patterns on the ground, and can fall well outside the array but part of the shower may still trigger the surface detector. This prevents the use of a simple geometrical calculation of the acceptance as is done in the case of vertical showers [108]. Moreover, for deep inclined showers the acceptance depends on the shower energy, zenith angle and injection depth.

Therefore, the calculation of the acceptance would require Monte Carlo techniques in which the rapidly changing configuration of the array is taken into account. Then simulated showers at different energies, zenith angles and injection points have to be thrown at the configuration of the array at each instant of time. The physics trigger conditions and the algorithms of selection and reconstruction should also be applied to the simulated showers. The program to calculate the acceptance to deep inclined down-going showers following this procedure is work in progress within the Pierre Auger Collaboration [109]. In this work we will only calculate the potential of the Surface Detector of the Pierre Auger Observatory for the detection of down-going ν-induced showers. For this purpose we will assume:

- A constant with time geometrical area $A = 3000$ km^2 that corresponds to the estimated surface area covered by the full SD array (1600 tanks) when it is completed, working continuously and uniformly for a time period of 1 year.

- The efficiences of identification for neutrino showers $\epsilon(E, \theta, X_{inj})$ (obtained in Section 6.4.3) calculated assuming an infinite ideal array.

We define the effective aperture or area for a given energy and a slant injection depth ΔX (measured from the ground) as:

$$A_{eff}(E, \Delta X) = \int_0^{2\pi} d\phi \int_{\theta_{min}}^{\theta_{max}} d\theta \sin\theta \cos\theta \;\; A \;\; \epsilon(E, \theta, \Delta X) \;\; [\mathrm{km}^2\,\mathrm{sr}] \qquad (7.1)$$

where the integral over the zenith angle goes from $\theta_{min} = 75^\circ$ to $\theta_{max} = 89^\circ$.

Integrating the effective aperture over the slant injection depth, we obtain the effective volume inside which if a neutrino interacts it will be identified. This effective volume for a fixed shower energy is given by:

$$V_{eff}(E) = \frac{f}{\rho_{air}} \int_{\Delta X_{min}}^{\Delta X_{max}} d\Delta X \;\; A_{eff}(E, \Delta X) \quad [\mathrm{km}^3\,\mathrm{sr}] \qquad (7.2)$$

where the integral over the injection depth goes from $\Delta X_{min} = 0$ g cm^2 (ground) to $\Delta X_{max} = 5000$ g cm^2, and we take $\rho_{air} = 1.210^{-3}$ g cm^{-3} as the density of air assumed constant. $f = 10^{-5}$ is just a factor converting cm into km.

The exposure can be defined as the effective volume multiplied by the observation time Δt :

$$Exp(E) = V_{eff}(E)\ \Delta t \qquad [\mathrm{km}^3\,\mathrm{sr\,yr}] \qquad (7.3)$$

In Fig. 7.6 we show the exposure as a function of shower energy for one year. The exposure increases from 0.22 km^3 w.eq. sr at 0.1 EeV to 9.9 km^3 w.eq. sr at 10 EeV[2]. Above this energy, the exposure increases very slowly due to the saturation of the identification efficiencies. The behavior of the exposure at high energies is only approximate since we do not account for the possibility of high energy neutrino-induced showers falling outside the array but still triggering.

7.3 Upper bound to the diffuse flux of UHE neutrinos

Given that we found no neutrino candidates, we can obtain an upper limit to the diffuse flux of ultra-high energy neutrinos. In particular we will asses

[2]In units of km^3 water equivalent.

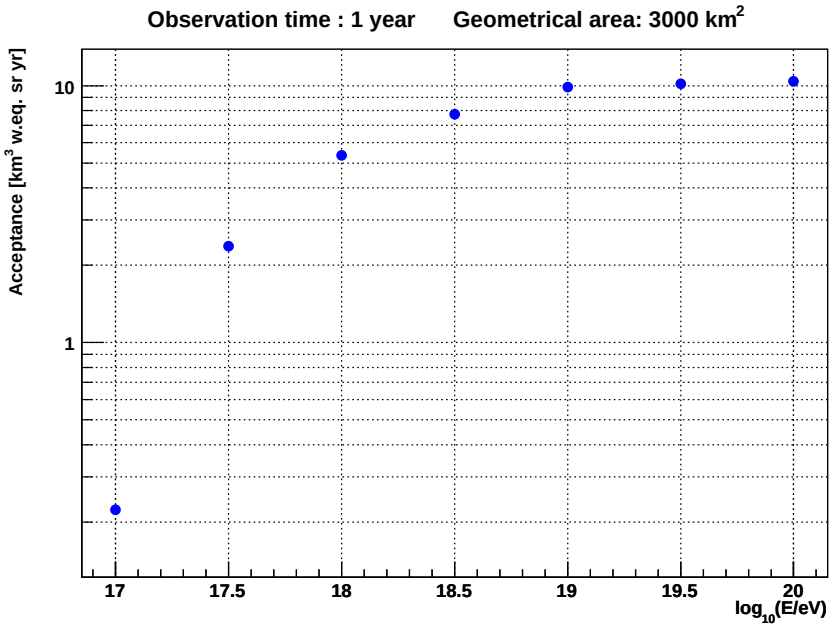

Figure 7.6: *The acceptance of the Surface Detector of the Pierre Auger Observatory for down-going neutrino showers for one year and assuming a constant geometrical area* $A = 3000\ km^2$ *as a function of shower energy.*

the potential of the Surface Detector of the Pierre Auger Observatory to constrain the diffuse fluxes of UHE neutrinos.

The simplest approach to obtain the limit consists of calculating the expected event rate given the exposure of the surface detector, for an assumption on the spectral shape of a neutrino flux $\Phi_\nu\ (E_\nu)$. We can establish a 90% C.L. bound for the assumed flux shape, simply finding the normalization of the flux (K) that would produce 2.3 events given the exposure computed above.

In this thesis, we have used proton primaries interacting deep in the atmosphere under the assumption that the resulting showers are equivalent to the hadronic showers induced by any neutrino flavour in a Neutral Current (NC) interaction, or by a muon or a tau neutrino in a Charged Current (CC) interaction (neglecting both the possible shower initiated by the muon or the tau lepton) with energy $E_\nu \sim\ E/ < y > =\ 5 \times E$, where E is the shower energy and y is the fraction of energy transferred to the nucleon in the laboratory frame. Therefore, we only assume that these two channels contribute to the down-going neutrino rates, neglecting the channel of electron neutrinos in CC interactions whose importance will be estimated below.

The expected shower rate N_{sh}^{had} induced by any of the contributing channels is given by:

$$N_{sh}^{had} = \rho_{air}\ N_A \int_{E_\nu^{min}}^{E_\nu^{max}} dE_\nu \int_0^1 dy\ \Phi_\nu(E_\nu)\ \frac{d\sigma^{NC(CC)}}{dy}(E_\nu, y)\ Exp(E) \qquad (7.4)$$

Here E is the shower energy given by $E = yE_\nu$, N_A is the Avogadro's number and $d\sigma^{NC(CC)}/dy$ is the differential neutrino cross-section for NC or CC interactions. The neutrino cross-section at the energies of interest must be deduced from the extrapolation of the parton distribution functions (pdfs) into unmeasured regions. The pdfs are obtained from parametrizations of the data of accelerator experiments. Several sets of parametrizations have been developed which lead to different cross-section calculations. In this work, we use the CTEQ6 [111] set of structure functions as a reference. In Fig. 7.7 we show the neutrino cross-section as a function of the neutrino energy in CC and NC interactions.

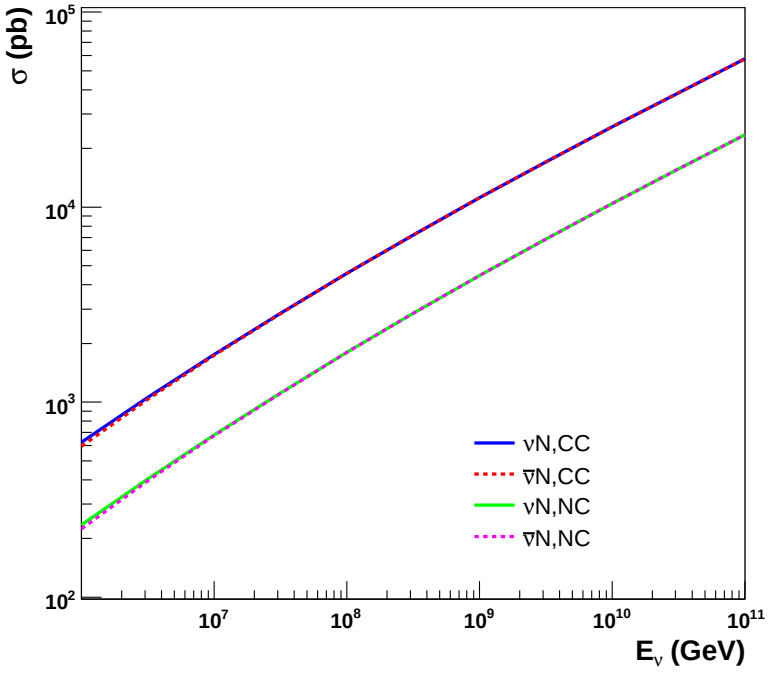

Figure 7.7: *The neutrino-nucleon (and antineutrino-nucleon) cross-section in CC and NC interactions obtained using the CTEQ6 set of parton distribution functions.*

As a first example we assume a neutrino flux with a constant spectral index of -2, the same index as the Waxman-Bahcall theoretical bound [110] corresponding to a limit to the $\nu_\mu + \overline{\nu}_\mu$ flux at production[3]. After oscillation over cosmological distances, the total neutrino flux can be approximately obtained multiplying the $(\nu_\mu + \overline{\nu}_\mu)$-flux at production by a factor 0.5 times the number of contributing ν flavours.

We calculate the NC and CC contributions to the shower rate separately using Eq. 7.4. A high energy cutoff has been introduced and we do not consider showers above 10^{20} eV. This implies a soft cutoff of the flux at $E_\nu^{max} \sim 5 \times 10^{20}$ eV. Also, the minimum energy that a shower must have to be identified as being produced by a ν is $\sim 10^{17}$ eV which implies $E_\nu^{min} \sim 5 \times 10^{17}$ eV. The corresponding bounds for both channels (K_{90}^{NC} and K_{90}^{CC}) and the total bound (K_{90}) for all the channels are shown in Fig. 7.8, assuming 2.3 events in each bin of half a decade in neutrino energy. One can see in Fig. 7.8 that the best sensitivity is reached at $E_\nu \sim 10^{18}$ eV. At energies lower than this the sensitivity is worse because the ν identification efficiencies are very small (see Fig. 6.35). At higher energies the sensitivity decreases as E_ν increases because although the ν identification efficiencies increases with E_ν (see Fig. 6.35) and the $\nu-$nucleon cross-section increases with $\sim E_\nu^{1/3}$ the flux of UHE neutrinos drops rapidly as E_ν^{-2}. Also one can see that the contribution of the ν_μ or ν_τ in CC interaction ($K_{90}^{CC}/2$) is roughly equal to the contribution of all ν flavours in NC interaction because the factor 3 in the number of flavours compensates roughly the 3 times larger CC cross-section compared the NC one.

Integrating over the energy range from $E_\nu^{min} = 5 \times 10^{17}$ eV to $E_\nu^{min} = 5 \times 10^{20}$ eV, the 90% C.L. limit is $E_\nu^2 \Phi_\nu(E_\nu) < 1.2\ 10^{-6}$ GeV cm^{-2} s^{-1} sr^{-1}. This limit is shown in Fig. 7.9. For this calculation, we have considered the 3 neutrino flavours in NC interactions and ν_μ and ν_τ in CC interactions.

We can estimate by how much the limit will improve if the channel of ν_e in CC interactions is included. For this purpose, we assume that the identification efficiencies of ν_e-induced showers are approximately equal to the efficiencies obtained for deep proton showers (the accuracy of this approximation is studied in [109]). Under this assumption the limit improves by more than a factor 2 down to $E_\nu^2 \Phi_\nu(E_\nu) < 4.7\ 10^{-7}$ in the energy range 5×10^{17} -10^{20} eV. The effect of this channel is very important because the induced showers carry all the energy of the electron neutrino ($E = E_\nu$) in the CC interaction.

In Fig. 7.9 we show the results of this work compared to other upper limits to a E^{-2} diffuse neutrino flux. All limits are still 1 to 2 orders of magnitude

[3] $E_\nu^2 \Phi_\nu(E_\nu) = 4.5\ 10^{-8}$ [GeV cm^{-2} s^{-1} sr^{-1}].

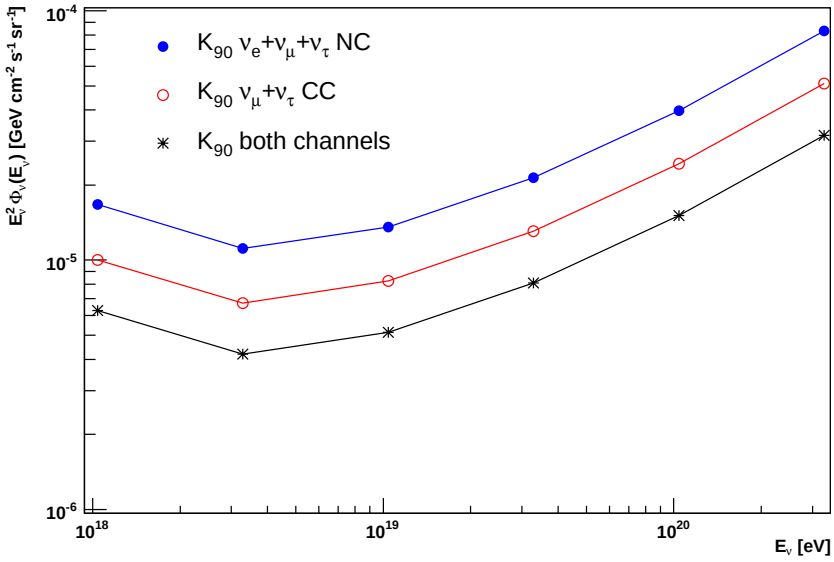

Figure 7.8: *Sensitivity of the Surface Detector of the Pierre Auger Observatory to an E^{-2} diffuse neutrino flux at 90% C.L. The full circles correspond to the sensitivity obtained considering only the NC contributions of all neutrino flavours. The empty circles correspond to the sensitivity obtained considering only the CC contributions of the muon and tau neutrinos. The stars correspond to the total sensitivity considering the 2 contributing channels. All of them have been obtained assuming less than 2.3 events in each half a decade in neutrino energy.*

higher than the reference Waxman-Bahcall theoretical bound. We have included in the figure the limit on ν_τ presented in [115] and also obtained with the surface detector of the Pierre Auger Observatory. One must keep in mind that this is a different limit to the one presented here, obtained using Earth-skimming tau neutrinos. After a correct acount for all the approximations done to obtain our prospective limit, including the very important ν_e CC channel, we expect the sensitivity of the Surface Detector of the Pierre Auger Observatory to down-going ν interactions to be comparable to the sensitivity to Earth-skimming ν_τs. The larger efficiency of ν_τ to τ conversion inside the Earth compared to the low rate of interactions of downg-going neutrinos in the dilute atmosphere, is partially offset in down-going ν events by a larger solid angle (75-89 deg versus 1 or 2 deg for Earth-skimming neutrinos), and by the fact that with down-going events we are sensitive to all neutrino flavours and CC as well as NC interactions. Earth-skimming events are also not very sensitive to the highest energies above 10^{19} eV because the

Earth attenuates the ν_τ flux strongly except in a very narrow angular range just below the horizon. Moreover in the limit obtained with Earth-skimming tau neutrinos, events with 3 or more stations were selected. However our prospective limit was obtained using only events with 5 or more selected stations. Given that the mean multiplicity of low energy showers ($E < 1$ EeV) is $\sim$ 3-4 stations for showers with $\theta > 85^\circ$ (see Fig. 6.26), requiring 5-fold or larger events induces a reduction of acceptance at low energies ($\sim$ 50% at $E_\nu^{min} = 5 \times 10^{17}$ eV) or equivalently an increase of the neutrino energy threshold. This in turn implies an important reduction of the limit since for a E^{-2} neutrino spectrum, the shower rates in the lowest energy bins represent an important contribution to the total neutrino rate. To illustrate the contribution to the limit of the different energy bins, we plot in Fig. 7.10 the limit obtained integrating from $E_\nu^{min} = 5 \times 10^{17}$ eV to different E_ν^{max} energies. One can see the fast improvement of the limit in the lowest energy bins.

Finally it is worth reminding once again that the 90% C.L. limit on downgoing neutrinos $E_\nu^2 \Phi_\nu(E_\nu) < 1.2\ 10^{-6}$ GeV cm^{-2} s^{-1} sr^{-1} is only a prospective value. Several assumptions have been made in our calculations, such as using deep proton induced showers instead of ν induced showers, using an infinite ideal array for the simulations, assuming a constant aperture with time, and neglecting the ν_e CC channel. A more accurate calculation accounting for all these approximations is work in progress within the Pierre Auger Collaboration [109].

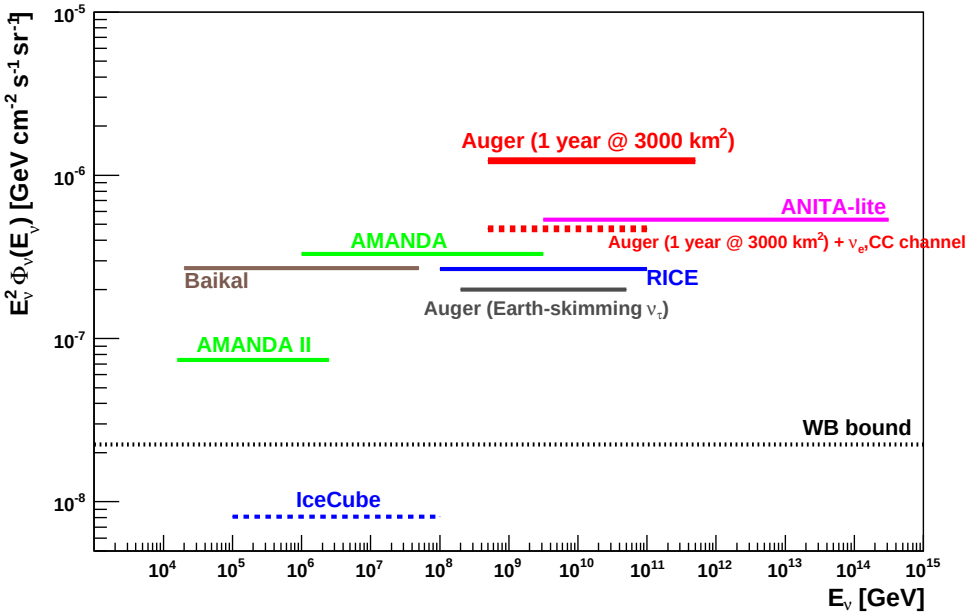

Figure 7.9: *Upper limits at 90% C.L. for an E^{-2} diffuse neutrino flux corresponding to a single flavour assuming a 1:1:1 ratio of the 3 neutrino flavours. From top to bottom: Auger (assuming a surface detector of constant geometrical area $A = 3000$ km^2 and 1 year of operation, and all ν flavours in NC interaction and $\nu_\mu + \nu_\tau$ in CC interactions), ANITA-lite limit [112], AMANDA-B10 all flavour limit [113], limit in Auger considering all the flavours in both CC and NC interactions, i.e. including the ν_e CC channel (see text), the Baikal five year limit [45], the RICE six year limit [114], Auger limit using Earth-skimming showers (real array acceptance corresponding to roughly 1 year of the full array) [115], AMANDA-II upper limit on the ν_μ flux [116], Waxman-Bahcall upper limit [110], sensitivity for 1 year of IceCube [117].*

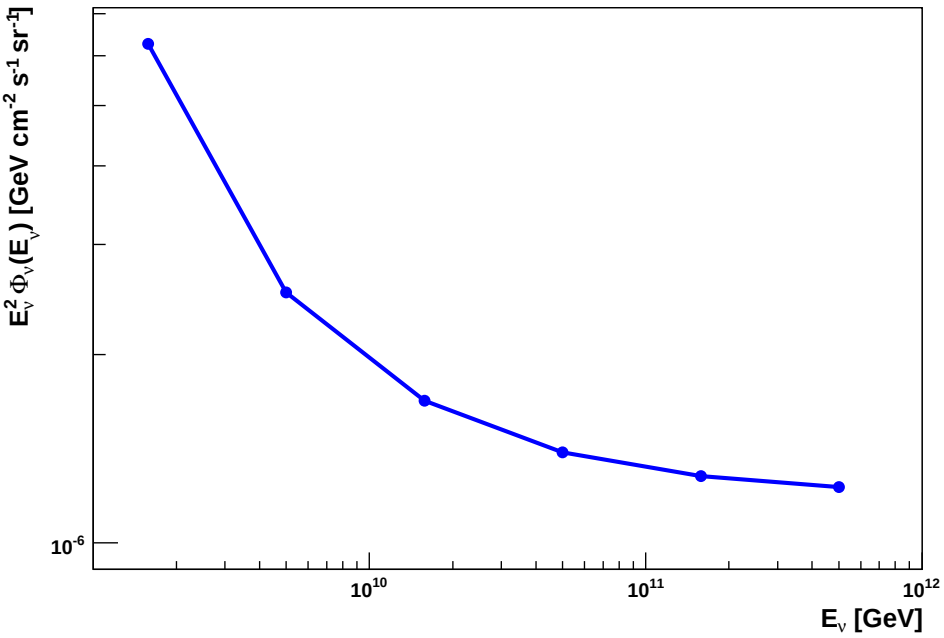

Figure 7.10: *The upper limit at* 90% *C.L. for an* E^{-2} *diffuse neutrino flux integrating the event rate from* $E_\nu^{min} = 5 \times 10^{17}$ *eV up to* E_ν *plotted as a function of* E_ν.

Chapter 8

Summary and conclusions

The most relevant contributions presented in the thesis are summarized in the following.

8.1 Chapters 4 and 5

In the first part of the thesis we study the signals in the Surface Detectors of the Pierre Auger Observatory with the aim of characterizing the electromagnetic (EM) component of inclined ($60^\circ < \theta < 90^\circ$) showers, of great importance in the reconstruction of inclined events. Inclined showers mainly consist of muons at the ground level with an accompanying EM component (the so-called EM halo) which is mainly produced by muon decay and hard muon interactions.

Firstly, we have developed an alternative fast method to calculate the mean response of the Auger tanks to shower muons, electrons, positrons and gammas. The method named $S(1000)$ USC code is based on the conversion of shower particle tracklengths inside the tank to signals in Vertical Equivalent Muon units (VEM). As a first approximation to the tracklength we use the geometrical tracklengths of a muon and the total tracklength produced by an EM particle induced shower assuming it is fully contained inside the tank, and assuming the particles entering in the tank travel parallel to the shower axis. These tracklengths are then corrected and converted into effective tracklengths accounting for a number of physical effects in the muonic and electromagnetic components. In the case of the muonic signal we account for efficiency in Cherenkov emission depending on the velocity of the muons, muon energy loss and muon decay, and $\delta-$rays and pair production. The corrections to the electromagnetic component include: Containment of the electromagnetic subshower in the tank, departure of EM tracklength from

linear scaling with energy because electrons lose energy rapidly at low energy and inefficiencies in Cherenkov emission. There are also corrections that affect both the muonic and the electromagnetic components namely, particle energy loss inside the wall of the Auger tank, direct light in the tank and particle deviations from the shower axis. With this method we quantify the relative importance of each of the effects on the tank response. The most important correction to the electromagnetic component is due to fact that the subshower induced by an EM particle entering the tank is not always completely contained inside the tank. For the muonic component, the most important corrections are the muon energy loss and inefficiencies in the Cherenkov yield due to subluminal velocities.

We have compared the $S(1000)$ USC code with an accurate and well-tested simulator of the passage of particles through matter such as Geant4. For this purpose, we have performed a comparative study of the response of both codes to vertical and inclined individual particles for different particle kinetic energies and angles. The agreement between both codes is generally good with differences of less than 10% for muons and 20% for electromagnetic particles, which are within the statistical uncertainty of the Geant4 output.

We have applied the $S(1000)$ USC method to study the ratio of the electromagnetic signal to the muon signal in inclined showers. We have studied the dependence of the ratio S_{EM}/S_{μ} on the shower zenith angle and distance from the shower axis. The conclusions of this study are:

- Near the core ($r < 1$ km), S_{EM}/S_{μ} decreases with zenith angle up to $\theta \sim 72^{\circ}$ and then increases due to hard muon processes being more important in very inclined showers in which higher energy muons are expected.

- S_{EM}/S_{μ} is compatible with an almost constant value far from the core ($r > 1$ km).

- The larger the zenith angle, the smaller the distance to the shower core at which the electromagnetic halo and the muonic component are equal.

We have also performed a parameterization of S_{EM}/S_{μ} as a function of the distance from the shower axis and the shower zenith angle assuming no azimuthal asymmetry of the signal on the ground. This parameterization is used in the reconstruction of inclined nucleonic events.

We have also studied the azimuthal asymmetry in the lateral distributions of the electromagnetic and muonic components of the signal and the azimuthal asymmetry in the ratio S_{EM}/S_{μ} in absence of the geomagnetic

field. The azimuthal asymmetry is due to the combination of several effects: the geometric effect, the longitudinal development effect and ground screening. The conclusions of this study are:

- At $\theta \geq 60^\circ$ there is a small early-late asymmetry in the muonic signal that increases slowly with distance to the core. This is due to the long attenuation length of the muons in the atmosphere.

- At $\theta < 70^\circ$ there is an important early-late asymmetry in the EM signal that increases rapidly with r. However, at $\theta \geq 70^\circ$ the asymmetry increases slowly with r in the same way as the asymmetry in the muonic signal since the EM component comes mainly from muon decay.

- The ratio S_{EM}/S_μ has a clear azimuthal asymmetry at $\theta < 70^\circ$ and an almost circular symmetry at $\theta \geq 70^\circ$, in agreement with the asymmetries obtained for the muon and electromagnetic components.

For purposes of reconstruction of inclined events, we have performed a parameterization of the ratio S_{EM}/S_μ as a function of the distance from the shower axis, zenith angle and azimuthal angle taking into account the azimuthal asymmetry (but neglecting the effect of the geomagnetic field) for showers with $\theta < 70^\circ$. For showers with $\theta > 70^\circ$ the azimuthal asymmetry is expected to be small and the parameterization without accounting for the asymmetry could be used.

Finally, we have studied the effect of the geomagnetic field in the ratio S_{EM}/S_μ and we have concluded that:

- The effect of the geomagnetic field on the ratio S_{EM}/S_μ depends strongly on the shower zenith and azimuth angles of the shower as expected.

- The effect of the geomagnetic field on the ratio S_{EM}/S_μ must be taken into account for the purpose of event reconstruction when the shower zenith angle $\theta \gtrsim 86^\circ$. For $\theta < 86^\circ$ the effect is less than 20% with respect to the case in which the geomagnetic field is not accounted for.

8.2 Chapters 6 and 7

The second part of the thesis is aimed at defining criteria to identify neutrino candidates in the data recorded by the Surface Detector of the Pierre Auger Observatory. After applying the selection criteria to the surface detector data sample, no neutrino candidates were found. The prospects of the surface detector of the Pierre Auger Observatory to constrain the diffuse flux of UHE neutrinos was established.

Firstly, we have developed different algorithms of station selection and event reconstruction depending on the spatial configuration of the stations in the event with two distinct cases: non-aligned or aligned event. Applying these algorithms we have selected inclined showers among the data recorded at the surface detector of the Pierre Auger Observatory.

Then we have characterized neutrino-induced showers using proton showers simulated with the Monte Carlo code AIRES 2.6.0 and the hadronic interaction model QGSJET01. We have checked that proton primaries interacting deep in the atmosphere produce showers equivalent to the hadronic showers induced by any neutrino flavour in a Neutral Current (NC) interaction, or by a muon or tau neutrino in a Charged Current (CC) interaction (neglecting both the possible shower initiated by the muon or tau lepton) as long as the neutrino energy is ~ 5 times greater than the shower energy. The main conclusions of this study are:

- The main signature of neutrino showers are inclined showers where the early region of the shower is in a young stage of development having a significant EM component, and the late region is in an older stage of evolution having a muonic front.

- The asymmetry in the electromagnetic content of the signal between the early and late regions at a given distance from the core depends on the shower zenith angle and the atmospheric grammage crossed by the shower from the injection point to the ground.

We have obtained a set of selection criteria for identifying neutrino candidates in the inclined data set collected at the surface detector. The criteria are based on the physical characteristics of the simulated neutrino showers. In particular we have studied the potential of the risetime and falltime of the signal as discriminant observables to select neutrino candidates. The criteria for identifying events induced by deeply penetrating particles consists of looking for showers that pass the following cuts:

- 5 or more tanks participating in the angular reconstruction.

- Reconstructed zenith angle $\theta \geq 75°$.

- The two earliest stations in the event must have risetime greater than 60 ns and falltime greater than 150 ns.

We have computed the efficiencies to trigger, reconstruct and identify neutrino showers with the Surface Detector of the Pierre Auger Observatory using the simulated deep proton showers. The efficiencies have been obtained

as a function of the slant injection depth measured from the ground for different zenith angles and shower energies. We have also studied the effect of the different cuts on the identification efficiency. The main conclusions of this study are:

- For showers produced very close to the array the efficiency drops since they do not produce enough signal to trigger the minimum of 5 tanks required by the criterion.
- For showers simulated at $\theta = 75°$, the reconstruction efficiency decreases by a significant factor in all the energy range due to the shower zenith angle being systematically reconstructed with $\sim 2°$ less than the angle at which the shower was simulated.
- The identification efficiency drops for showers initiated far away from the ground since in these showers the EM component is largely absorbed and they are difficult to distinguish from conventional nucleonic showers.
- The range of injection depths in which the identification of a deep shower is possible increases with energy and zenith angle.

We have searched for neutrino candidates in the data collected by the Surface Detector of the Pierre Auger Observatory from January 1$^{\text{st}}$ 2004 to September 3$^{\text{rd}}$ 2007 and we conclude that there is not a single event that can be considered as neutrino candidate over this period.

Assuming the calculated efficiencies and a constant with time geometrical area $A = 3000$ km^2, we have computed the effective volume of the surface detector of the Pierre Auger Observatory, inside which if a neutrino interacts it will be identified.

Given that there are not ν candidates and assuming a E_ν^{-2} diffuse neutrino flux, we have obtained the 90% C.L. prospective limit for one year of operation of the full surface detector of the observatory:

$$E_\nu^2 \Phi_\nu(E_\nu) < 1.2 \times \ 10^{-6} \ \text{GeV cm}^{-2} \ \text{s}^{-1} \ \text{sr}^{-1}$$

This limit is valid in the energy range from from $E_\nu^{min} = 5 \times 10^{17}$ eV to $E_\nu^{min} = 5 \times 10^{20}$ eV. For this calculation, we have considered the 3 neutrino flavours in NC interactions and $\nu_\mu + \nu_\tau$ in CC interactions. This limit is only a prospective value due to the several assumptions made in our calculations. A more accurate calculation accounting for all the approximations made in this thesis and including the ν_e CC channel is expected to improve the sensitivity of the Surface Detector of the Pierre Auger Observatory to down-going ν interactions.

Bibliography

[1] P. Auger and R. Maze, Compt. Rend. Acad. Sci. (Ser. II) **207** (1938) 228.

[2] J. Linsley, Phys. Rev. Lett. **10** (1963) 146-148.

[3] T. Abu-Zayyad [High Resolution Fly's Eye Collaboration], Astropart. Phys. **23** (2005) 157-174.

[4] R. Abbasi *et al.* [HiRes Collaboration], arXiv:astro-ph/0703099.

[5] K. Shinozaki [AGASA Collaboration], Nucl. Phys. Proc. Suppl. **151** (2006) 3.

[6] A. V. Olinto, Phys. Rept. **333** (2000) 329.

[7] W. M. Yao *et al*, J. Phys. G **33** (2006) 1.

[8] M. Nagano and A. A. Watson, Rev. Mod. Phys. **72** (2000) 689.

[9] J. R. Hörandel, astro-ph/0508014.

[10] J.R. Hörandel, Astropart. Phys. **19** (2003) 193.

[11] R. U. Abbasi *et al.* [The High Resolution Fly's Eye Collaboration], Astrophys. J. **622** (2005) 910.

[12] A. A. Watson, Nucl. Phys. Proc. Suppl. **151** (2006) 83.

[13] J. Abraham *et al.* [Pierre Auger Collaboration], arXiv:astro-ph/0606619.

[14] F. A. Aharonian and J. W. Cronin, Phys. Rev. D **50** (1994) 1892.

[15] M. Ave, N. Busca, A. V. Olinto, A. A. Watson and T. Yamamoto, Nucl. Phys. Proc. Suppl. **136** (2004) 159.

[16] P. Bhattacharjee and G. Sigl, Phys. Rept. **327** (2000) 109.

[17] A. M. Hillas, Ann. Rev. Astron. Astrophys. **22** (1984) 425.

[18] E. Fermi, Phys. Rev. **75** (1949) 1169.

[19] R. D. Blandford and J. P. Ostriker, Astrophys. J. **221** (1978) L29.

[20] A. R. Bell, Mon. Not. Roy. Astron. Soc. **182** (1978) 147.

[21] Y. A. Gallant and A. Achterberg, arXiv:astro-ph/9812316.

[22] W. Heitler,*The Quantum Theory of Radiation*

[23] J. Matthews, Astropart. Phys. **22** (2005) 387.

[24] T. K. Gaisser,*Cosmic Rays and Particles Physics*

[25] M. V. S. Rao and B. V. Sreekantan, *Extensive Air Showers.*

[26] K. Greisen, *Prog. in Cosmic Rays Phys.* ed. J. G. Wilson, Vol. III, p.1, North Holland Publ. Co. (1656).

[27] V. Avati *et al.*, Eur. Phys. J. C **34** (2004) S255.

[28] G. Anelli *et al.* [TOTEM Collaboration], arXiv:hep-ex/0602025.

[29] T. K. Gaisser and A. M. Hillas, *Proc. 15th I.C.R.C.*, Plovdiv, Bulgaria, **8** (1977) 353.

[30] L. Cazón, Ph. Thesis *Modeling the muon time distribution in extensive air showers*, 2004.

[31] K. Kamata and J. Nishimura, Prog. Theor. Phys. (Kyoto) Suppl. **6** (1958) 93.

[32] M. Ave, R. A. Vazquez, E. Zas, J. A. Hinton and A. A. Watson, Astropart. Phys. **14** (2000) 109.

[33] P. Billoir and P. Sommers, Comptes Rendus Physique **5** (2004) 495.

[34] L. Cazon, R. A. Vazquez and E. Zas, Astropart. Phys. **23** (2005) 393.

[35] R. Mirzoian *et al.*, Nucl. Instrum. Meth. A **351** (1994) 513.

[36] T. C. Weekes, AIP Conf. Proc. **558** (2001) 15.

[37] K. Green, J. L. Rosner, D. A. Suprun and J. F. Wilkerson, Nucl. Instrum. Meth. A **498** (2003) 256.

[38] J. L. Rosner and D. A. Suprun, AIP Conf. Proc. **579** (2001) 81.

[39] S. Yoshida, H. y. Dai, C. C. H. Jui and P. Sommers, Astrophys. J. **479** (1997) 547.

[40] F. W. Stecker, C. Done, M. H. Salamon and P. Sommers, Phys. Rev. Lett. **66** (1991) 2697 [Erratum-ibid. **69** (1992) 2738].

[41] P. Meszaros and S. Razzaque, arXiv:astro-ph/0605166.

[42] K. S. Hirata *et al.* [Kamiokande-II Collaboration], Phys. Rev. D **44** (1991) 2241 [Erratum-ibid. D **45** (1992) 2170].

[43] K. Hirata *et al.* [KAMIOKANDE-II Collaboration], Phys. Rev. Lett. **58** (1987) 1490.

[44] R. Gandhi, C. Quigg, M. H. Reno and I. Sarcevic, Astropart. Phys. **5** (1996) 81.

[45] V. Aynutdinov *et al.* [BAIKAL Collaboration], Astropart. Phys. **25** (2006) 140.

[46] A. Kouchner and f. t. A. collaboration, "The ANTARES neutrino telescope: a status report", *Prepared for 30th International Cosmic Ray Conference (ICRC 2007), Merida, Mexico (2007).*

[47] J. D. Zornoza [IceCube Collaboration], Nucl. Phys. Proc. Suppl. **165** (2007) 196.

[48] P. A. Toale [IceCube Collaboration], arXiv:astro-ph/0607003.

[49] G. Aggouras *et al.* [NESTOR Collaboration], Nucl. Instrum. Meth. A **567** (2006) 452.

[50] R. Coniglione [NEMO Collaboration], Nucl. Phys. Proc. Suppl. **168** (2007) 271.

[51] R. Gandhi, C. Quigg, M. H. Reno and I. Sarcevic, Phys. Rev. D **58** (1998) 093009.

[52] E. Zas, New J. Phys. **7** (2005) 130.

[53] V. S. Berezinsky and A. Yu. Smirnov, Astrophys. Space Science **32** (1975) 423.

[54] S. Yoshida *et al.*, "A Search For Horizontal Air Showers Induced By Extremely High Energy Cosmic Neutrinos Observed By Akeno Giant Air Shower Array" *Prepared for 27th International Cosmic Ray Conference (ICRC 2001), Hamburg, Germany (2001).*

[55] M. Ave, R. A. Vazquez, E. Zas, J. A. Hinton and A. A. Watson,"Near horizontal showers detected with the Haverah Park Array", *Prepared for 26th International Cosmic Ray Conference (ICRC 99), Salt Lake City, Utah (1999).*

[56] R. M. Baltrusaitis *et al.*, AIP Conf. Proc. **126** (1985) 307.

[57] M. M. Guzzo and C. A. Moura, arXiv:hep-ph/0312119.

[58] C. Aramo, A. Insolia, A. Leonardi, G. Miele, L. Perrone, O. Pisanti and D. V. Semikoz, Astropart. Phys. **23** (2005) 65.

[59] X. Bertou, P. Billoir, O. Deligny, C. Lachaud and A. Letessier-Selvon, Astropart. Phys. **17** (2002) 183.

[60] B. R. Dawson [Pierre Auger Collaboration], "Hybrid Performance of the Pierre Auger Observatory", *Prepared for 30th International Cosmic Ray Conference (ICRC 2007), Merida, Mexico (2007).*

[61] J. Abraham *et al.* [Pierre Auger Collaboration], Nucl. Instrum. Meth. A **523** (2004) 50.

[62] X. Bertou *et al.* [Pierre Auger Collaboration], Nucl. Instrum. Meth. A **568** (2006) 839.

[63] M. Mostafa, Nucl. Phys. Proc. Suppl. **165** (2007) 50.

[64] D. Allard *et al.*, "A guide-line to the Auger Surface Detector Analysis", Internal Note for the Pierre Auger Collaboration, GAP 2006-024.

[65] M. Ave [Pierre Auger Collaboration], "Reconstruction accuracy of the surface array of the Pierre Auger Observatory", *Prepared for 30th International Cosmic Ray Conference (ICRC 2007), Merida, Mexico (2007).*

[66] P. Bauleo [Pierre Auger Collaboration], "Absolute calibration of the Auger fluorescence detectors" , *Prepared for 29th International Cosmic Ray Conference (ICRC 2005), Pune, India (2005).*

[67] D. Newton [Pierre Auger Collaboration], "Selection and reconstruction of very inclined air showers with the Surface Detector of the Pierre Auger Observatory", *Prepared for 30th International Cosmic Ray Conference (ICRC 2007), Merida, Mexico (2007).*

[68] G. Rodríguez Fernández, PhD Thesis, Universidad de Santiago de Compostela (2007).

[69] P. Sommers [Pierre Auger Collaboration], "First Estimate of the Primary Cosmic Ray Energy Spectrum above 3 EeV from the Pierre Auger Observatory", *Prepared for 29th International Cosmic Ray Conference (ICRC 2005), Pune, India (2005).*

[70] M. Roth [Pierre Auger Collaboration], "Measurement of the UHECR energy spectrum using data from the Surface Detector of the Pierre Auger Observatory",, *Prepared for 30th International Cosmic Ray Conference (ICRC 2007), Merida, Mexico (2007).*

[71] P. Facal San Luis [Pierre Auger Collaboration], "Measurement of the UHECR spectrum above 10^{19} eV at the Pierre Auger Observatory using showers with zenith angles greater than 60°", *Prepared for 30th International Cosmic Ray Conference (ICRC 2007), Merida, Mexico (2007).*

[72] M. G. Pia [Geant4 Collaboration], Nucl. Phys. Proc. Suppl. **125** (2003) 60.

[73] J. Alvarez-Muñiz, G. Rodriguez-Fernandez, I. Valiño and E. Zas. Allison, "An Alternative Method for Tank Signal Response and S(1000) Calculation", Internal Note for the Pierre Auger Collaboration, GAP 2005-054.

[74] http://www.fisica.unlp.edu.ar/auger/aires/eg_Aires.html

[75] D. Heck, J. Knapp, J.N. Capdevielle, G. Schatz, and T. Thouw, "CORSIKA: A MonteCarlo Code to Simulate Extensive Air Showers", **FZKA 6019** (1998) (http://www-ik.fzk.de/corsika/)

[76] A. M. Hillas, Nucl. Phys. Proc. Suppl. **52B** (1997) 29.

[77] P. Billoir, "Reconstruction of showers with the Ground Array: status of the prototype program", Internal Note for the Pierre Auger Collaboration, GAP 2000-025.

[78] E. Zas, F. Halzen and T. Stanev, Phys. Rev. D **45** (1992) 362.

[79] J. Alvarez-Muniz, E. Marques, R. A. Vazquez and E. Zas, Phys. Rev. D **68** (2003) 043001 [arXiv:astro-ph/0206043].

[80] D. E. Groom, N. V. Mokhov and S. I. Striganov, Atom. Data Nucl. Data Tabl. **78** (2001) 183.

[81] E. Zas, private communication.

[82] http://geant4.web.cern.ch

[83] http://pdg.lbl.gov/2007/AtomicNuclearProperties/index.html

[84] A. Lopez-Aguera, V.M. Olmos-Gilbaja, G. Rodríguez Fernández., "Direct light in inclined showers" , Internal Note for the Pierre Auger Collaboration, GAP 2003-112.

[85] A. Lopez-Aguera, V.M. Olmos-Gilbaja, G. Rodríguez Fernández., "Direct light Impact parameter dependence in a Cherenkov water tank", Internal Note for the Pierre Auger Collaboration, GAP 2004-026.

[86] A. Lopez-Aguera, V.M. Olmos-Gilbaja, G. Rodríguez Fernández., "Removing Direct light Impact from HAS", Internal Note for the Pierre Auger Collaboration, GAP 2004-061.

[87] G. Rodríguez Fernández, private communication.

[88] M. Ave, R. A. Vazquez and E. Zas, Astropart. Phys. **14** (2000) 91.

[89] M. Ave, J. Knapp, J. Lloyd-Evans, M. Marchesini and A. A. Watson, Astropart. Phys. **19** (2003) 47.

[90] C. Pryke, "Asymmetry of Air Showers at Ground Level", Internal Note for the Pierre Auger Collaboration, GAP-98-034.

[91] X. Bertou and Pierre Billoir, "On the origin of the asymmetry of ground densities in inclined showers", Internal Note for the Pierre Auger Collaboration, GAP 2000-017.

[92] M. T. Dova [Pierre Auger Collaboration], *Prepared for 28th International Cosmic Ray Conference (ICRC 2003), Tsukuba, Japan (2003).*

[93] A. Cillis and S. J. Sciutto, J. Phys. G **26** (2000) 309.

[94] S.. Argiro *et al.*, Nucl. Instrum. Meth. A, In Press.

[95] http://www.ifi.unicamp.br/AUGER/projects/dpa/software/distribution/index.html

[96] P. Skelton, "Speeding up the Gean 4 Tank Simulator", Internal Note for the Pierre Auger Collaboration, GAP 2004-066.

[97] G. Rodríguez Fernández *et al*, "Surface Detector Response Using Lookup Table Based on Geant4 Simulation", Internal Note for the Pierre Auger Collaboration, GAP 2004-045.

[98] S. Dagoret-Campagne, "The Central Trigger, User Guide and Reference Manual", Internal Note for the Pierre Auger Collaboration, GAP 2004-020.

[99] M. Ave, J. A. Hinton, R. A. Vazquez, A. A. Watson and E. Zas, Phys. Rev. D **67** (2003) 043005.

[100] L. Cazon, R. A. Vazquez, A. A. Watson and E. Zas, Astropart. Phys. **21** (2004) 71.

[101] Inclined shower reconstruction group, Univ. de Santiago de Compostela, talk given at the Pierre Auger Collaboration Meeting, Malargüe, Argentina, March 2004, and private communication.

[102] V.M. Olmos-Gilbaja, private communication.

[103] G. Corcella *et al.*, arXiv:hep-ph/0210213.

[104] O. Pisanti, private communication.

[105] M. Ambrosio *et al.*, "Corsika + Herwig Monte Carlo Simulation of Neutrino Induced Atmospheric Air Showers", Internal Note for the Pierre Auger Collaboration, GAP 2003-013.

[106] P. Billoir, "Reconstruction of first year EA events from the Surface Detector", Internal Note for the Pierre Auger Collaboration, GAP 2002-044.

[107] P. S. Allison, "Origin on the Time over Threshold trigger rate dependence on water quality and the Time over Threshold background", Internal Note for the Pierre Auger Collaboration, GAP 2005-040.

[108] D. Allard [Pierre Auger Collaboration], "Aperture calculation of the Pierre Auger Observatory surface detector", *Prepared for 29th International Cosmic Ray Conference (ICRC 2005), Pune, India (2005).*

[109] J. Alvarez-Muñiz, Y. Guardincerri, D. N. Newton, S. Pastor, R. Piegaia, T. Pinto, O. Pisanti, I. Valiño, J. Tiffemberg, R. A. Vazquez, A. A. Waton, and E. Zas, Internal Note for the Pierre Auger Collaboration in preparation.

[110] J. N. Bahcall and E. Waxman, Phys. Rev. D **64** (2001) 023002.

[111] J. Pumplin, D. R. Stump, J. Huston, H. L. Lai, P. Nadolsky and W. K. Tung, JHEP **0207** (2002) 012.

[112] S. W. Barwick *et al.* [ANITA Collaboration], Phys. Rev. Lett. **96** (2006) 171101.

[113] M. Ackermann *et al.*, Astropart. Phys. **22** (2005) 339.

[114] I. Kravchenko *et al.*, Phys. Rev. D **73** (2006) 082002.

[115] O. Blanch [Pierre Auger Collaboration], "Limits to the diffuse flux of UHE neutrinos at EeV energies from the Pierre Auger Observatory", *Prepared for 30th International Cosmic Ray Conference (ICRC 2007), Merida, Mexico (2007).*

[116] A. Achterberg [IceCube Collaboration], Phys. Rev. D **76** (2007) 042008.

[117] J. Ahrens *et al.* [IceCube Collaboration], Astropart. Phys. **20** (2004) 507.

Appendix A

Resumen de la tesis

Los Rayos Cósmicos son partículas relativistas que están continuamente llegando a la tierra desde todas las direcciones y con energías que van desde 10^9 eV hasta energías superiores a 10^{20} eV. En la actualidad, el descubrimiento del origen, de la composición y del espectro energético de los Rayos Cósmicos con energías superiores a 10^{19} eV representa uno de los mayores retos para la Física de Astropartículas.

Dentro del estudio de los Rayos Cósmicos, la detección de neutrinos cósmicos tiene un especial interés pues estas partículas proporcionan una ventana única al conocimiento del origen de los Rayos Cósmicos, dado que pueden viajar distancias cosmológicas a lo largo del universo desde las fuentes donde se originaron hasta la tierra sin interaccionar ni desviar sus trayectorias.

A estas energías tan altas el flujo de Rayos Cósmicos es muy bajo y su detección se realiza de forma indirecta a través de la observación de la cascada de partículas secundarias que se produce tras la interacción del rayo cósmico primario con un núcleo atmosférico. En la colisión la energía del primario se distribuye entre las partículas resultantes de la colisión. Posteriormente éstas continúan propagándose y produciendo tras varias generaciones una cascada atmosférica. Las componentes fundamentales de una cascada, cada una con distinto poder de penetración en la materia son: un core de hadrones de alta energía, componente electromagnética (electrones, positrones y fotones), componente muónica y componente de neutrinos.

A.1 El Observatorio de Rayos Cósmicos Pierre Auger

El Observatorio Pierre Auger está dedicado a la detección de rayos cós-micos de energías superiores a 10^{19} eV para investigar su dirección de llegada, composición y espectro energético. Este experimento fue diseñado para proporcionar una cobertura completa del cielo mediante la construcción de un observatorio en cada uno de los hemisferios terrestres. El Observatorio del hemisferio Sur se encuentra en la etapa final de su construcción en Malargüe, Argentina, mientras que en el hemisferio Norte está planificada la construcción de un observatorio en Colorado, EEUU.

El Observatorio Pierre Auger es un detector híbrido que combina dos técnicas de detección de cascadas atmosféricas: una red de detectores de superficie y 4 telescopios de fluorescencia. La observación simultánea de cascadas usando ambas técnicas permite identificar las fuentes de errores sistemáticos en cada técnica, y medir de forma independiente algunas de las propiedades de la partícula que inicia la cascada.

El detector de superficie está compuesto por una red de 1600 detectores tipo Cherenkov en agua cubriendo un área de 3000 km^2. Cada detector es un tanque de 3.6 m de diámetro y 1.55 m de altura lleno de 12 toneladas de agua purificada. En la parte superior del tanque, en contacto óptico con el agua, se colocan 3 tubos fotomultiplicadores. Las partículas cargadas que se propagan en el tanque emiten luz Cherenkov que tras ser reflejada en las paredes del tanque es recogida por los fotomultiplicadores. La señal obtenida en los fotomultiplicadores es digitalizada y guardada en discos duros junto con el tiempo en el que fue detectada para su posterior análisis. Cada tanque es un sistema autónomo pues tiene dos paneles solares y dos baterías que suministran energía al sistema electrónico y a los fotomultiplicadores. El tanque también consta de una antena que permite la comunicación con el Sistema Central de Adquisición de Datos.

El detector de fluorescencia consiste en 4 "ojos", cada uno alojado en un edificio distinto situado en el borde del detector de superficie. Cada ojo consta de 6 telescopios y cada uno de ellos abarca un campo visual de 28.6° en elevación y 30° en acimuth. Cada telescopio tiene además 440 tubos fotomultiplicadores. Estos telescopios miden la luz fluorescente emitida por las moléculas de nitrógeno de la atmosféra al desexcitarse previamente excitadas tras el paso de las partículas de la cascada.

Un rayo cósmico genera una cascada poco despues de entrar en la parte superior de la atmósfera a un cierto ángulo cenital con respecto a la normal. A las energías a las que trabaja Auger una cascada alcanza su número

máximo de partículas secundarias a una profundidad aproximadamente de unos 800 g cm^{-2}. Atendiendo al ángulo cenital θ se distingue entre cascadas verticales, aquellas con $0° < \theta < 60°$, y cascadas horizontales (inclinadas), aquellas con $60° < \theta < 90°$. La diferencia entre cascadas verticales y horizontales se debe a la diferente profundidad de atmósfera que tienen que atravesar antes de llegar al suelo, y que será la causa de que el número de partículas que llegan al suelo y su especie sean diferentes según el ángulo cenital. En las cascadas verticales, la mayoría de las partículas que llegan al suelo son electrones, positrones y fotones, producidos en subcascadas electromagnéticas iniciadas principalmente en desintegración de π^0s. Sin embargo en las cascadas horizontales, las partículas tienen que recorrer mayor profundidad atmósferica antes de llegar al suelo, por lo que la componente electromagnética es prácticamente absorbida en la atmósfera (debido fundamentalmente a procesos electromagnéticos de baja energía y al efecto fotoeléctrico en la atmósfera) y sólamente llegan al suelo muones acompañados por un halo electromagnético debido fundamentalmente a la desintegración de los muones de más baja energía.

El análisis de cascadas horizontales tiene un interés especial entre otros motivos porque constituyen el fondo más importante para la detección de cascadas iniciadas por neutrinos. La idea de detectar neutrinos de alta energía a través de cascadas horizontales está basada en que los neutrinos de alta energía pueden inducir cascadas horizontales a mayor profundidad en la atmósfera que serían en principio fácilmente identificables porque tendrían componente electromagnética en el suelo.

El trabajo desarrollado en esta tesis está enmarcado dentro del estudio de cascadas horizontales. La primera parte de la tesis está orientada al estudio de las señales de las cascadas horizontales en el detector de superficie del Observatorio Pierre Auger con el fin de caracterizar el halo electromagnético que juega un papel importante en la reconstrucción de cascadas horizontales. La segunda parte de la tesis está orientada al estudio de la capacidad del detector de superficie del Observatorio Pierre Auger para detectar e identificar cascadas de neutrinos.

El trabajo realizado se encuentra recogido desde el capítulo 4 al 7, y las conclusiones obtenidas están detalladas en el capítulo 8. A continuación se hace un breve resumen de estos capítulos.

A.2 Estudio de las señales en el Detector de Superficie del Observatorio Pierre Auger

El estudio de la respuesta al paso de las partículas de la cascada (muones, electrones, positrones y fotones) de un tanque del detector de superficie del Observatorio Pierre Auger es una tarea compleja que requiere el uso de sofisticadas técnicas de simulación. Dado que estas simulaciones tan detalladas necesitan un gran tiempo de cómputo, hemos desarrollado un método alternativo y rápido para calcular la respuesta promedio del tanque. Este método denominado código $S(1000)$ USC está basado en el hecho físico de que la señal producida por un muón es proporcional a la longitud de su traza dentro del tanque, y en que una partícula electromagnética (electrón, positrón o fotón) induce una subcascada electromagnética dentro del tanque que produce una señal proporcional a la longitud total de las trazas de los electrones y positrones de la subcascada. Por tanto, la idea básica de este método es convertir una longitud de traza a señal en unidades de VEM [1]. Como una primera estimación de la traza, hemos usado la longitud geométrica de traza de un muón y la longitud total de las trazas producidas por una subcascada electromagnética que suponemos en primera aproximación que está siempre completamente contenida dentro del tanque. También se supone por el momento que las partículas que inciden en el tanque lo hacen paralelamente al eje de la cascada a la que pertenecen. Posteriormente, se calcula la longitud effectiva de la traza teniendo en cuenta los differentes procesos físicos sufridos por las partículas dentro del tanque y que no fueron considerados hasta el momento. Agrupamos las correcciones en aquellas específicas a muones; aquellas específicas a electrones, positrones y fotones; y finalmente aquellas que afectan a ambas componentes.

Las correcciones a la señal muónica incluyen:

- La eficiencia Cherenkov y la pérdida de energía del muon. Al perder los muones energía su velocidad disminuye, por lo que se convierten en menos eficientes en la producción de luz Cherenkov, hasta que su energía es menor que la energía umbral de emisión Cherenkov y cesan de emitir luz.

- Electrones $\delta-$rays. Los muones pueden producir electrones secundarios llamados $\delta-$rays. Estos electrones secundarios suelen tener suficiente energía como para producir también luz Cherenkov en el tanque.

[1] Un VEM (Vertical Equivalent Muon) es la señal producida por un muón que incide en el centro del tanque totalmente vertical con respecto a la normal a la superficie

- Los muones puede sufrir interacciones duras tales como bremsstrahlung, producción de pares e interacciones nucleares. La producción de pares se convierte en una contribución relevante para muones muy energéticos.

- Desintegración de los muones en el tanque. Para esta corrección se asume que los muones sólo se desintegran si se paran dentro del tanque y que el electrón resultante de la desintegración tiene una energía promedio de 37 MeV. Este electrón produce una subcascada electromagnética dentro del tanque.

Las correcciones a la señal electromagnética incluyen:

- La subcascada electromagnética iniciada por electrones, positrones o fotones secundarios no siempre está contenida completamente en el tanque. De hecho, para los fotones es posible atravesar totalmente el tanque sin producir ninguna señal.

- La proporcionalidad entre la energía de la partícula y la longitud total de la traza de la subcascada electromagnética no es válida a bajas energías (< 0.1 GeV) pues los electrones pierden energía muy rápidamente a baja energía.

- Eficiencia Cherenkov. Los electrones y positrones secundarios también están sujetos a ineficiencias de producción luz Cherenkov debido a que sus energías y por tanto velocidades decrecen a medida que la subcascada se desarrolla en el tanque.

Las correcciones que afectan tanto a la señal muónica como a la electromagnética son:

- Los muones, electrones y positrones pierden energía al atravesar la pared del tanque.

- Luz directa en el tanque. Si el ángulo de incidencia de las partículas en el tanque es mayor que el complementario del ángulo Cherenkov en agua, una fracción de la luz emitida por la partícula llega directamente al tubo fotomultiplicador produciendo una señal adicional en el tanque que no es proporcional a sus trazas correspondientes.

- Las partículas no viajan paralelas al eje de la cascada, sino que se desvian un cierto ángulo del eje.

Tras cuantificar la importancia relativa de cada efecto, concluímos que la corrección más importante para la componente electromagnéti-ca es que la

subcascada EM puede no estar completamente contenida dentro del tanque. Las correcciones más importantes para muones son la pérdida de energía del muón y las ineficiencias en la emisión Cherenkov.

Finalmente, hemos comparado el código $S(1000)$ USC con el software Geant4, el cual permite simular con precisión el paso de las partículas a través de la materia. Hemos realizado un estudio comparativo de la respuesta de ambos códigos a partículas individuales de distintas energías incidiendo a distintos ángulos cenitales en el tanque. El acuerdo entre ambos códigos es bueno con diferencias menores que el 10% para muones y del 20% para electrones, positrones y fotones. Dichas diferencias están dentro de la incertidumbre estadística de la respuesta del tanque obtenida con Geant4.

A.3 Estudio de las señales en cascadas horizontales: caracterización del halo electromagnético

Hemos aplicado el código $S(1000)$ USC al estudio del halo electromagnético en cascadas horizontales. En concreto, hemos estudiado el cociente entre la señal electromagnética y la señal muónica (S_{EM}/S_μ) pues es una cantidad muy importante en la reconstrucción de eventos inclinados.

Para este estudio, se han utilizado cascadas de protones generadas con energía 10 EeV y ángulos cenitales entre 60° y 88°. Para cada energía y ángulo cenital se han simulado 100 cascadas con el programa Monte Carlo AIRES 2.6.0 y el modelo hadrónico QGSJET01.

Hemos estudiado el comportamiento de S_{EM}/S_μ con la distancia al eje de la cascada y con el ángulo cenital de la cascada. Cerca del core de la cascada ($r < 1$ km), el cociente entre señal electromagnética y señal muónica disminuye con el ángulo cenital hasta $\theta \sim 72°$ y luego aumenta debido a las interacciones duras sufridas por el muon. Este incremento es más importante en cascadas muy inclinadas en las cuales se esperan muones muy energéticos cerca del core. Lejos del core ($r \sim 1$ km), S_{EM}/S_μ tiene un valor prácticamente constante pues la señal electromagnética es producida por el halo electromagnético que proviene principalmente de la desintegración de muones, y por tanto muestra un comportamiento análogo al de la señal muónica. Por otro lado, cuanto mayor es el ángulo cenital, menor es la distancia al core a la cual el halo electromagnético comienza a dominar sobre la componente electromagnética debida a la desintegración de los π^0 es decir, la distancia a la cual el cociente S_{EM}/S_μ adquiere un valor constante.

Hemos realizado una parametrización de S_{EM}/S_μ como función de la

distancia al eje de la cascada y del ángulo cenital, suponiendo en primera instancia que la señal es acimutalmente simétrica. Esta parametriza-ción es útil en la reconstrucción de eventos inclinados.

El siguiente paso es estudiar la asimetría acimutal en las distribuciones laterales de las componentes electromagnética y muónica de la señal y la consecuente asimetría acimutal en el cociente S_{EM}/S_{μ} en ausencia de campo geomagnético. La asimetría acimutal es debida a la combinación de varios efectos: el efecto geométrico, el efecto del desarrollo longitudinal de la cascada y el efecto del "apantallamiento" del suelo.

El efecto geométrico proviene del hecho de que las partículas entran en los detectores de la región temprana de la cascada (el tiempo de trigger de los detectores es anterior al tiempo correspondiente al impacto del núcleo hadrónico de la cascada en el suelo) con un ángulo más vertical que en los detectores de la región tardía de la cascada (el tiempo de trigger de los detectores es posterior al tiempo correspondiente al impacto del núcleo hadrónico de la cascada en el suelo). Se espera que esta asimetría sea más importante para bajos ángulos cenitales.

El efecto del desarrollo longitudinal proviene de que partículas a la misma distancia del core en el plano de la cascada, pero a diferentes ángulos acimutales con respecto a la dirección de la cascada, viajan diferentes caminos antes de llegar al suelo, por lo que se encuentran en diferentes etapas en la evolución de la cascada. La asimetría debida a este efecto es más importante para la componente electromagnética debida a la desintegración de los π^0.

El efecto de "apantallamiento" del suelo es debido a la absorción del core hadrónico de la cascada después de impactar en el suelo. Como consecuencia, el core hadrónico deja de alimentar las componentes electromagnética y muónica de la señal en una porción de la región tardía de la cascada.

La combinación de todos estos efectos hace que a $\theta \geq 60^{\circ}$ haya una pequeña asimetría acimutal en la señal muónica que aumenta lentamente con la distancia al core. La asimetría es pequeña debido a la gran longitud de atenuación de los muones en la atmósfera. Para $\theta < 70^{\circ}$ hay una importante asimetría acimutal en la señal electromagnética, la cual aumenta rápidamente con la distancia al core. Sin embargo a $\theta \geq 70^{\circ}$ la asimetría en la componente electromagnética aumenta lentamente con la distancia al core de la misma forma que la asimetría de la señal muónica. Como consequencia el cociente entre ambas señales (S_{EM}/S_{μ}) tiene una clara asimetría acimutal a $\theta < 70^{\circ}$ y una simetría casi circular a $\theta \geq 70^{\circ}$.

Con el fin de poder aplicar este estudio en la reconstrucción de eventos inclinados hemos realizado una parametrización del cociente S_{EM}/S_{μ} como función de la distancia al eje de la cascada, del ángulo cenital y del ángulo acimutal para cascadas con $\theta < 70^{\circ}$. Para cascadas con $\theta > 70^{\circ}$ la

asimetría acimutal en S_{EM}/S_μ es pequeña con lo que se puede utilizar la parametrización realizada sin tener en cuenta esta asimetría.

Finalmente, hemos estudiado el efecto del campo geomagnético en la razón entre la señal electromagnética y la señal muónica. El efecto del campo geomagnético es más importante para muones, pues estas partículas recorren grandes distancias desde donde se originan hasta llegar al suelo. El campo geomagnético desvía a lo muones en direcciones opuestas según el signo de su carga eléctrica haciendo que las las densidades de los muones muestren un patrón elipsoidal en el plano de la cascada que sería circular en ausencia del campo geomagnético. Incluso a grandes angulos cenitales la desviación es tan grande que se orgina una estructura lobular en los patrones de muones.

Se pueden separar las desviaciones de las trayectorias de los muones por efecto del campo geomagnético en dos tipos. Por un lado, existe una componente de la fuerza en la dirección perpendicular a la dirección de la cascada en el plano de la cascada y paralela al plano del suelo. De la intensidad de esta desviación depende la extensión de la densidad de muones a lo largo del semi-eje mayor del patrón elipsoidal que forman en el suelo. Esta componente además desvía a parte de los muones alejándolos del suelo en la región tardía de la cascada. Por otro lado, existe una componente de la fuerza geomagnética perperdicular a la dirección de llegada de la cascada en el plano de la cascada y perpendicular a su vez a la fuerza anterior. Esta componente origina una asimetría especular de los lóbulos con respecto al semi-eje mayor del patrón elipsoidal.

Tras caracterizar los tipos de desviación de las trayectorias de los muones en el campo geomagnético, hemos estudiado como afectan a la razón S_{EM}/S_μ. El efecto del campo geomagnético depende de los ángulos cenital y acimutal de la cascada. Dicho efecto debe ser tenido en consideración para fines de recontrucción de eventos sólo cuando $\theta \geq 86^\circ$. Para $\theta < 86^\circ$ el efecto es menor que el 20% en todas las distancias del core relevantes en la reconstrucción de eventos.

A.4 Identificación de candidatos a cascadas inducidas por neutrinos en el Observatorio Pierre Auger

Primero, hemos desarrollado diferentes algoritmos para la selección de estaciones y para la reconstrucción de la dirección de llegada de los eventos inclinados. Estos algoritmos fueron desarrollados teniendo en cuenta las características temporales y topológicas de los eventos inclinados y han sido op-

timizados para la selección eficiente de posibles eventos candidatos a neutrinos. La selección sigue un procedimiento de "abajo a arriba" pues parte de la selección de una semilla de estaciones que se utiliza para estudiar la compatibilidad espacio-temporal del resto de estaciones y de esta manera seleccionar aquellas que formen parte de los eventos. Posteriormente se realiza una reconstrucción angular con todas las estaciones seleccionadas y se aceptan como eventos físicos (cascadas) aquellos que hayan sido reconstruídos. Además, se utilizan algoritmos de selección y reconstrucción específicos según la configuración espacial del las estaciones en el evento, la cual puede ser de dos tipos: evento alineado o no-alineado. Posteriormente, hemos aplicado estos algoritmos para seleccionar cascadas inclinadas entre los datos recogidos en el detector de superficie del Observatorio Pierre Auger.

Despues de ésto, hemos caracterizado las cascadas inducidas por neutrinos asumiendo que protones interaccionando a profundidades grandes en la atmósfera producen cascadas equivalentes a las cascadas hadrónicas inducidas por neutrinos 5 veces más energéticos que los protones. Hemos comprobado que esta aproximación es válida para cualquier sabor en una interacción de corriente neutra o para un ν_μ o ν_τ en interacción de corriente cargada (despreciando en ambos casos la posible cascada iniciada por el μ ó τ).

Para este estudio hemos generado una librería de cascadas de protones usando el programa Monte Carlo AIRES 2.6.0 y el modelo hadrónico QGSJET01. Las cascadas fueron generadas con energías desde 10^{17} eV hasta 10^{20} eV, a diferentes ángulos cenitales desde 75° hasta 89° y diferentes puntos de inyección del protón elegidos de forma que la cantidad de atmósfera atravesada por la cascada medida desde el suelo llegue hasta 5000 g cm^{-2}.

Hemos encontrado que la principal característica que presentan las cascadas de neutrino es que son cascadas inclinadas en las que la región temprana de la cascada está en una etapa joven de desarrollo que se traduce en la presencia de una importante componente electromagnética en el suelo, mientras que la región tardía está en una etapa de evolución más vieja en la que la cascada llega al suelo como un frente muónico. La asimetría en el contenido de componente electromagnética en la señal entre las regiones temprana y tardía para una distancia fija del core depende del ángulo cenital de la cascada y de la profundidad de atmósfera atravesada por la cascada desde el punto de inyección al suelo.

Basándonos en las características físicas de las cascadas de neutrino simuladas, hemos desarrollado un criterio de selección para identificar candidatos a cascadas inducidas por neutrino en el conjunto de eventos reales inclinados. Hemos demostrado el potencial del "risetime" (intervalo temporal en el cual entre el 10% y el 50% de la señal total integrada es grabada) y del "falltime" (intervalo temporal en el cual entre el 50% y el 90% de la señal

total integrada es grabada) de las señales como observables para seleccionar candidatos a neutrinos, pues los valores de estos parámetros dependen del contenido electromagnético en la señal. Finalmente, hemos establecido un posible criterio para identificar eventos inducidos por partículas altamente penetrantes. Dicho criterio consiste en buscar eventos que pasen los siguientes cortes:

- 5 o más estaciones participando en la reconstrucción angular.
- Evento reconstruido con un ángulo cenital $\theta \geq 75^{\circ}$.
- Las dos primeras estaciones en tiempo del evento tienen que tener "risetime" mayor que 60 ns y "falltime" mayor que 150 ns.

Una vez establecido un criterio de identificación, hemos calculado las eficiencias del detector de superficie del Observatorio Pierre Auger para detectar, reconstruir e identificar cascadas inducidas por neutrinos. Estas eficiencias han sido obtenidas como función del punto de inyección para diferentes ángulos cenitales y energías de la cascada.

También hemos estudiado el efecto de los diferentes cortes del criterio en la eficiencia de identificación. Para cascadas producidas muy cerca del array de detectores, la eficiencia es muy baja ya que estas cascadas no producen suficiente señal como para producir trigger en al menos 5 estaciones como requiere el criterio. Por otro lado, para cascadas simuladas a $\theta = 75^{\circ}$ la eficiencia de reconstrucción disminuye de manera importante en todo el rango de energías, pues el ángulo cenital de la cascada es sistemáticamente reconstruido con $\sim 2^{\circ}$ menos que el ángulo al cual fue simulada y las cascadas entonces no pasan el corte $\theta > 75^{\circ}$. Para cascadas iniciadas lejos del suelo la eficiencia de identificación también es muy baja debido a que en estas cascadas la componente electromagnética es en gran parte absorbida, y por tanto estas cascadas son difíciles de distinguir de cascadas convencionales originadas por protones o núcleos. El rango de profundidades de inyección donde la identificación de cascadas de neutrinos es posible aumenta con la energía y con el ángulo cenital fijo.

A.5 Límite al flujo difuso de neutrinos UHE usando cascadas atmosféricas inclinadas en el Observatorio Pierre Auger

Hemos buscado candidatos a eventos producidos por neutrinos entre los datos recogidos en el detector de superficie del Observatorio Pierre Auger entre el

período comprendido entre el 1 de Enero del 2004 y el 3 de Septiembre del 2007. Aunque dos eventos en este período pasaron los cortes del criterio, un estudio exhaustivo de dichos eventos revela que no son candidatos reales a neutrinos. Por tanto, ningún evento puede ser considerado como candidato a neutrino en el período analizado. Este hecho permite calcular un límite superior al flujo difuso de neutrinos a muy altas energías ($> 10^{17}$ eV).

Primero, hemos calculado el volumen efectivo dentro del cual si el neutrino interacciona será identificado. Para ello hemos asumido las eficiencias obtenidas en el capítulo anterior y el área geométrica del detector completo (3000 km^2), suponiendo que no varía en uno varía en un intervalo de un año.

Finalmente asumiendo un flujo difuso de neutrino con una forma espectral E_ν^{-2}, hemos obtenido que el límite al 90% de nivel de confianza para un año de operación del detector es:

$$E_\nu^2 \Phi_\nu(E_\nu) < 1.2 \times \ 10^{-6} \ \text{GeV cm}^{-2} \ \text{s}^{-1} \ \text{sr}^{-1}$$

Este límite es válido en el rango de energía entre $E_\nu^{min} = 5 \times 10^{17}$ eV y $E_\nu^{max} = 5 \times 10^{20}$ eV. Para este cálculo, hemos considerado los tres sabores de neutrino en interacciones de corriente neutra y $\nu_\mu + \nu_\tau$ en interacciones de corriente cargada, suponiendo equipartición de sabores. Este límite es solo una estimación de la sensibilidad del detector de superficie Observatorio Pierre Auger debido a la varios supuestos realizados en nuestros cálculos. Un cálculo más preciso que incluya el canal de ν_e en interacciones de corriente carga mejorará la sensibilidad del Observatorio Pierre Auger a cascadas inducidas por neutrinos tras interaccionar en la atmósfera.